Silicon and Carbon-Based Anode Materials for Lithium and Sodium-Ion Rechargeable Batteries

by

Elmira Memarzadeh Lotfabad

A thesis submitted in partial fulfillment of the requirements for the degree of

Doctor of Philosophy

In
Materials Engineering

Department of Chemical and Materials Engineering
University of Alberta

Abstract

This thesis is focused on the Si-based anode materials for lithium-ion batteries (LIBs) as well as biomass-derived carbons for LIBs and sodium-ion batteries (NIBs). In our first attempt we investigated the effect of the support growth substrate as well as of aluminum coating layers on the electrochemical performance of the silicon nanowires. We observed improved cycling performance in the Si nanowires coated with 3 and 8 wt.% aluminum, as compared to the uncoated nanowires. The aluminum shell helps maintain the mechanical integrity of the coated parts of the nanowires, thereby slowing down capacity degradation. A solid electrolyte interphase (SEI) that was stable under the beam in a transmission electron microscope (TEM) was observed only on bare parts of a nanowire. Nanowires grown on a TiN underlayer not only demonstrated a higher specific capacity during cycling but also significantly improved coulombic efficiency with respect to nanowires grown directly on stainless steel, which is attributed mainly to a difference in size distribution.

In our second attempt, we conformally coated the Si nanowires with TiO_2 using atomic layer deposition (ALD), in which it showed a remarkable performance improvement. The coulombic efficiency is increased to ~99%, among the highest ever reported for Si nanowires, as compared to 95% for the baseline uncoated samples. The capacity retention after 100 cycles for the nanocomposite was twice as high as that of the baseline at 0.1 C (60% vs. 30%), and more than three times higher at 5 C (34% vs. 10%). We also demonstrated that the microstructure of the coatings was critically important towards achieving this effect. Titanium dioxide coatings with an as-deposited anatase structure are nowhere near as effective as amorphous ones, the latter proving much more resistant to delamination from the Si nanowires core. We used TEM to

demonstrate that upon lithiation the amorphous coating developed a highly dispersed nanostructure comprised of crystalline $LiTiO_2$ and a secondary amorphous phase.

In our third attempt, we explored the use of ALD of TiO_2, TiN and Al_2O_3 on the inner, the outer, or both surfaces of hollow Si nanotubes (SiNTs) for improving their cycling performance. We demonstrated that all three materials enhanced the cycling performance, with optimum performance being achieved for SiNTs conformally coated on both sides with 1.5 nm of Li active TiO_2. Substantial improvements wer achieved in the cycling capacity retention (1700 mAh/g vs. 1287 mAh/g for the uncoated baseline, after 200 cycles at 0.2C), and steady-state coulombic efficiency (~100% vs. 97-98%). TEM and other analytical techniques were employed to provide new insight into the lithiation cycling-induced failure mechanisms that turned out to be intimately linked to the microstructure and the location of these layers.

In our last attempt, we showed that Banana peel pseudographite (BPPG) offers superb dual functionality for NIBs and LIBs anodes. The materials possessed low surface areas (19 - 217 m^2 g^{-1}) and a relatively high electrode packing density (0.75 g cm^{-3} vs. ~ 1 g cm^{-3} for graphite). Tested against Na, BPPG delivered a gravimetric capacity of 355 mAh/g after 10 cycles at 50 mA/g. A nearly flat ~ 200 mAh/g plateau that is below 0.1 V, and a minimal charge/discharge voltage hysteresis, made BPPG a direct electrochemical analogue to graphite but with Na. A charge capacity of 221 mAh/g at 500 m/Ag was degraded by 7% after 600 cycles, while a capacity of 336 mAh/g at 100 mA/g was degraded by 11% after 300 cycles, in both cases with ~ 100% cycling coulombic efficiency. For LIB applications BPPG offered a gravimetric capacity of 1090 mAh/g at 50 mA/g. The reason that BPPG worked so well for both NIBs and LIBs was that it uniquely contained three essential features: a) dilated intergraphene spacing for Na intercalation at low voltages; b) highly accessible near-surface nanopores for Li metal filling at low voltages; and c) substantial defect content in the graphene planes for Li adsorption at higher voltages. The < 0.1 V charge storage mechanism was fundamentally different for Na versus for Li. A combination of XRD and XPS demonstrates highly reversible Na intercalation rather than metal underpotential deposition. By contrast, the same analysis proved the presence of metallic Li in the pores, with intercalation being much less pronounced.

Preface

Chapter 2 of this thesis has been published as E.L. Memarzadeh, W.P. Kalisvaart, A. Koandehghan, B. Zahiri, C.M.B. Holt, D. Mitlin, "Silicon Nanowire Core Aluminum Shell Coaxial Nanocomposites for Lithium Ion Battery Anodes Grown with and without a TiN Interlayer", *J. Mater. Chem.*, 2012, **22**, 6655-6668.

Chapter 3 of this thesis has been published as E. Memarzadeh Lotfabad, P. Kalisvaart, K. Cui, A. Kohandehghan, M.Kupsta, B. Olsen, D. Mitlin, "ALD TiO_2 Coated Silicon Nanowires for Lithium Ion Battery Anodes with Enhanced Cycling Stability and Coulombic Efficiency", *Phys. Chem. Chem. Phys.*, 2013, **15**, 13646-13657.

Chapter 4 of this thesis has been published as E. Memarzadeh Lotfabad, P.Kalisvaart, K. Cui, A. Kohandehghan, Kai Cui, Martin Kupsta, Behdokht Farbod, D. Mitlin, "Si Nanotubes ALD Coated with TiO_2, TiN or Al_2O_3 as High Performance Lithium Ion Battery Anodes", *J. Mater. Chem. A*, 2014, **2**, 2504-2516.

Chapter 5 of this thesis has been published as E. Memarzadeh Lotfabad, J. Ding, Kai Cui, Alireza Kohandehghan, Peter Kalisvaart, D. Mitlin, "High Density Sodium and Lithium Ion Battery Intercalation Anodes from Banana Peels", *ACS Nano*, 2014, DOI: 10.1021/nn502045y.

I was responsible for the data collection and analysis as well as the manuscript composition. Prof. David Mitlin was the supervisory author and was involved with concept formation and manuscript composition.

Acknowledgments

I would like to thank my supervisor, Prof. David Mitlin, for supporting me throughout this research with his knowledge and patience, and also for giving me the freedom and resources I required. Prof Mitlin's enthusiasm and encouragements never faltered during my graduate school career, and were sources of continual motivation. I feel very fortunate to have been his student, and to have had such a successful, fulfilling graduate school experience. His creativity and teaching style are truly unique, and I wish him the best of luck in his faculty career. I look forward to seeing many more great discoveries coming out of his lab.

I would also like to thank my group members for their help, support, and friendship. I am so honored to have been able to work alongside and become acquainted with so many bright and talented people. I look forward to seeing all the great things I am sure these people will accomplish. Being in an interdisplinary group was a great experience for me. A big thanks to every member of Mitlin Group for their invaluable and unconditional help; Thank you Peter Kalisvaart, Alireza Kohandehghan, Tyler Stephenson, Xuehai Tan, Brian Olsen, Behdokht Farbod, Beniamin Zahiri, Michael Hazelton and Jia Ding.

I would like to thank all of the helpful technicians and staff members of the Chemical and Materials Engineering Department, National Institute for Nanotechnology and Cross-Cancer Institute at University of Alberta. Not only do these helpful and resourceful people assist with equipment training, but they also bring their wealth of experience and knowledge and are always willing to participate in data interpretation. The support from these staff members has made my graduate school experience so much more pleasant.

I would also like to thank my family. My parents have given me their never-ending support throughout my entire life and have made countless sacrifices to ensure that I could attend my college of choice and freely pursue my career.

Table of Contents

List of Figures

List of Tables

1 Introduction

Currently, ~80% of the global energy consumption relies mostly on the usage of non-renewable fossil fuel with serious energy, environmental, health and climate concerns, and therefore, it is non-sustainable. Thus, the arrival of a new era of green renewable energy including solar and wind powers is expected to support a more sustainable economic growth. [1-8] However, it is difficult to use these kinds of energy for transportation such as vehicles due to their uneven energy production. One promising alternatives is driving electric vehicles which can significantly relieve the environmental pollution. [6,8,10,11] However, the utilization of electric cars requires highly efficient energy storage devices. In this regard, lithium- ion batteries (LIBs) can play an important role. [5-8,12] LIBs have been widely used in portable electronic devices such as computers, tablets, mobile phones, and medical microelectronic devices due to their high energy density and long cycle life. However, there are still many existing problems to be overcome for their broad and practical applications in stationary energy storage and electric vehicles. [5,612-14] For example, the amount of energy density they provide is still not enough to be competitive with liquid fuels and the driving range of most full electric cars is still well below the one of gasoline-powered vehicles. [15] Therefore, it is demanding to further increase their energy and power densities, improving their safety, and lowering the cost. [5,14,16]

1.1 Batteries

Batteries use a driving force, which is the difference in oxidation or reduction potential, to accept or give away electrons, between two species or electrodes. The two species consist of a metallic current collector allowing the electron flow from the external circuit to the electrodes in which they provide useful work, for example power a portable device such as a cellular phone or an electric vehicle. The two electrodes are separated, physically and electronically, by an ionically conducting and electronically insulating electrolyte. In order to mechanically separate electrodes and to prevent short-circuits, a separator is also used, which is made of glass, cellulose, or polymer fibers. The electrode with stronger reducing potential to give up electrons and become oxidized is the negative electrode (anode). Lithium is the strongest reductant on the periodic table with a standard reduction potential of -3.04 V. The electrode which accepts the electrons from the negative electrode and become reduced is the positive electrode (cathode).

During discharge, an electrochemical oxidation reaction proceeds at the negative electrode and at the same time an electrochemical reduction reaction proceeds at the positive electrodes by accepting the electrons passing through the external circuit. The electron transfer process will occur until the potential difference between the two electrodes becomes too low. At this point, the cell is fully discharged. [17,18] The change from electronic current to ionic current occurs at the electrode/electrolyte interface. Faraday's Law, which is the relationship between the equivalent quantities of chemical reactants and electrical charge, governs this change. In secondary batteries, the reverse process can be performed using external energy, known as the charge. During the charge process, the electrons flow from positive to the negative electrode and the potential difference between the two electrodes can be reinstated. In both cases, the transfer of electrons through the circuit from one electrode to another is balanced by the transfer of positively charged ions (cations) in the electrolyte.

There are two main types of batteries: primary batteries (non-rechargeable batteries) and secondary batteries (rechargeable batteries). In a secondary battery, the redox reactions and structural changes can be reversed by running a current into the cell with a battery charger to recharge it, regenerating the chemical reactants and allowed to discharge again. Primary batteries usually have good shelf time, energy and power density, and low cost and are typically used as hearing aides, watches, smoke alarms, and some portable electronics such as cameras. However, the secondary batteries with lower total cost of use and environmental impact have become the most commonly used batteries todays and are now a common place in all cell phones, laptops, digital cameras, and mp3 players.

Among the various existing technologies (Figure 1.1), Li-based batteries currently outperform other types of secondary batteries due to their high gravimetric and volumetric energy densities and design flexibility.[18] This allows them to be lighter and take up less space. Moreover, with superior power densities, they can recharge more quickly than other types of batteries. These advantages result from using the light-weight lithium containing compounds and a non-aqueous electrolyte that can allow for a larger voltage range between the two electrodes. Because the energy density is related to this voltage range, a large voltage will yield a higher energy density. They account for 63% of worldwide sales values in portable batteries. [19] This explains why they receive most attention at both fundamental and applied levels.

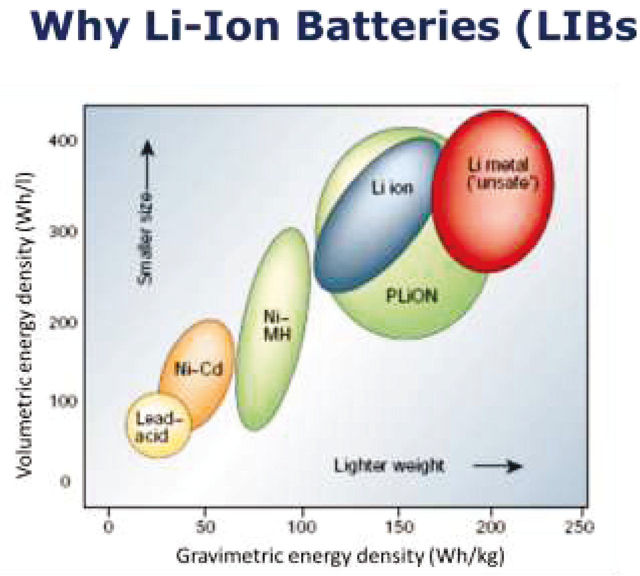

Figure 1.1: Comparison of the different battery technologies in terms of volumetric and gravimetric energy density. (adapted from 18).

1.1.1 Lithium-ion batteries

Lithium batteries are characterized by the transfer of Li ions and electrons in order to balance the charge. Certain materials have interstitial sites into which these Li ions can insert. In 1972, Exxon [20,21] embarked on a large project using TiS_2 as the positive electrode, Li metal as the negative electrode and lithium perchlorate in dioxolane as the electrolyte. TiS_2 was the best intercalation compound available at the time, having a very favourable layered-type structure. However, it was soon discovered that the dendrite formation and continiuos shape change of the electrode plague the electrodeposition of Li. [22] Rather than the Li ions re-depositing at the location where they originated, they would plate out at different locations. Moreover, more plating would occur at locations that already had deposition. This resulted in the formation of long, dendritic fibers, which could grow long enough to penetrate the separator and make contact with the positive electrode, which would cause a short circuit. Such a short circuit could be disastrous, as large amounts of current combined with a flammable organic electrolyte could lead to thermal runaway, fire, and explosions.

The discovery that graphite, [23] which was used as the negative electrode instead of more dangerous Li metal was a fortuitous one as it could reversible intercalate Li ions. Since graphite has a layered structure, Li ions can insert in between the graphene layers, at a maximum of 1 Li^+

per every 6 C atoms. This leads to a theoretical capacity of 372 mAh/g. Moreover, as the Li insertion occurs at about 0.1 V vs. Li/Li$^+$, there is the added benefit of a safer operating potential, while still maintaining a high cell voltage and energy density.

A schematic of a lithium battery with a graphite negative electrode and a lithium metal oxide ($Li_{1-x}CoO_2$) positive electrode, which are connected through an external circuit, has been illustrated in Figure 1.2. During discharging, lithium ions diffuse from a lithiated graphite (Li_xC_6) structure (negative electrode) into a delithiated $Li_{1-x}CoO_2$ structure (the cathode) with concomitant oxidation and reduction of the two electrodes, respectively. Accordingly, the negative electrode contracts as lithium ions are deintercalated from graphite and inserted in the positive electrode through the electrolyte, while electrons flow towards the positive electrode through an external circuit. During charging process, electrons are driven from the positive electrode to the negative electrode through the external circuit by an external power source. For maintaining the neutrality, lithium ions are displaced from the positive electrode towards the negative electrode through the electrolyte. The expansion of the negative electrode takes place by lithium ions insertion.

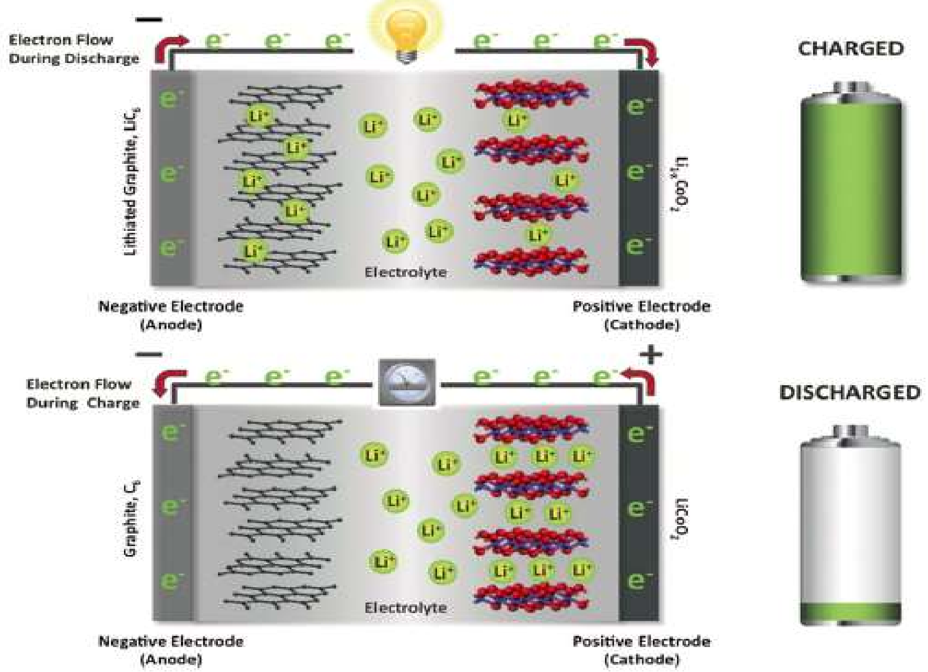

Figure 1.2: A schematic illustration of the working principles of a $Li_xC_6/Li_{1-x}CoO_2$ lithium-ion cell. (adapted from 24).

1.1.2 Important parameters for evaluating battery electrode materials

1.1.2.1 Voltage

The difference between the standard Gibbs free energy of formation (ΔG°_{f}) of the products and the reactants is the driving force for a reaction which follows as:

$$\Delta G^{\circ}_{rxn}=\Sigma\,\mu^{\circ}\,(\text{products})-\Sigma\,\mu^{\circ}\,(\text{reactants}) \tag{1}$$

This chemical driving force is equivalent to an electrostatic driving force (-nEF) where, E is the voltage between the electrodes, n is the stoichiometric number of electrons involved in the reaction and F is the Faraday's constant. Accordingly, a theoretical voltage for that reaction equals to:

$$\mathrm{E} = \frac{-\Delta\mu^{\circ}_{\mathrm{rxn}}}{\mathrm{nF}} \tag{2}$$

The voltage of a battery in Li-ion batteries is equivalent to the difference in chemical potential of lithium in each electrode. The voltage between the two electrodes when the cell is at open circuit and not discharged yet equals to:

$$V_{oc} = \frac{-[\mu_{Li}^{(+)} - \mu_{Li}^{(-)}]}{nF} \tag{3}$$

Where, $\mu_{Li}^{(-)}$ and $\mu_{Li}^{(+)}$ is the chemical potential of Li in the negative and positive electrode, respectively. When the cell is fully charged, $\mu_{Li}^{(-)} > \mu_{Li}^{(+)}$ and the voltage is positive. Li^{+} ions transfer from the higher chemical potential in the negative electrode to the lower chemical potential in the negative electrode when current flows upon closing the circuit. Upon discharging, chemical potential change for lithium in each electrode when a reaction occurs can be expressed by the Nernst equation:

$$\mu_i = \mu_i^{\circ} + RTlna_i \tag{4}$$

Where, μ_i° is the chemical potential of species i in its standard state, a_i is the activity of species, T is the temperature and R is the ideal gas constant (8.314 J/mol.K). Since the activity of a species is its effective concentration, the Nernst equation indicates that the chemical potential and subsequently, the voltage changes as a function of the amount of Li in each electrode. Typically the potential change is monitored over time. Accordingly, the capacity can be determined from the potential-time relation.

There are two groups and three different types of lithium reaction with a metal or alloy, which could be divided as: A: 1) solid-solution reaction and 2) addition reaction; B: 3) displacement or conversion reaction. [25] When lithium ions are added in the reactant phase without displacing components from the reactant, it is referred to group A reaction which follows as:

$$Li + xM \leftrightarrow LiM_x \tag{5}$$

Where, M can be element or a compound. Group A can be divided into solid-solution and addition reactions depending on whether or not a phase transformation occurs in the reactant M when lithium ions are inserted into the structure. When a phase change occurs from M to LiM_x, it is referred to an addition reaction. For example, lithium insertion/extraction in crystalline Si, Al and Sn are addition reactions since lithium has a very limited solubility in these elements. In displacement reaction, lithium reacts with one component of the reactant, while the other component, which could be active or inactive towards lithium, is displaced or extruded from the reactant. The corresponding reaction follows as:

$$Li + xMN_y \rightarrow LiM_x + xyN \tag{6}$$

Some displacement reactions are irreversible and the displaced element does not participate in the subsequent reactions and acts as a buffering matrix. Accordingly, the reaction becomes an addition reaction for the other element. When the displaced element is active, it reacts with lithium at potential lower than that the other element and the reaction becomes an addition reaction for the active element as well as a displacement reaction according to the reaction (6).

The Gibbs phase rule is useful for understanding why a voltage curve can be so important for understanding the electrochemical reactions of a material. The Gibbs phase rule for non-reactive processes states that:

$$F=C-P+2 \tag{7}$$

Where, F is the number of degree of freedom, C is the number of independent components and P is the number of phases in the system. The quantity of F indicates the number of intensive thermodynamic parameters to define the system and its related properties e.g. the chemical potential and thus, voltage. For a solid-solution reaction, the degree of freedom equals to three. Concerning that the electrochemical reactions are measured at specific temperature and pressure, only one parameter is required for defining the system. Since lithium is added to the system, its concentration in LiM_x changes during the reaction. So the concentration of lithium in LiM_x could be the final parameter. Based on this, the potential, where only one phase exists, varies with the lithium concentration at constant temperature and pressure. In this case, the voltage profile has a sloping shape. For an addition reaction in a binary system, the chemical potential is two degree of freedom. At constant temperature and pressure, there is no parameter to be defined and thus, the potential is independent of the lithium concentration. The voltage profile is a constant plateau. Finally, the equilibrium potential of a displacement reaction in a ternary system Li-M-N, where three phases exist, is independent of the lithium concentration.[25]

1.1.2.2 Capacity

The amount of charge that material can store is defined as the capacity of an electrode. Typically, capacities are reported in terms of gravimetric specific capacities, or the amount of stored charge normalized by the mass of the material. For the applications where the size of the battery is more important than its weight, the volumetric specific capacities are used. Capacities are often reported in units of ampere-hours per gram for batteries. Because an ampere is a Coulomb/sec, an ampere-hour is just another way of representing the charge.

The capacity of an electrode for LIBs can be calculated if the stoichiometry of the lithiated material, Li_xA is known as one electron is transferred for every Li ion. The specific (gravimetric) capacity, C_G, and volumetric capacity, C_v, can be calculated from the following equations:

$$\mathrm{C_G} = \frac{\mathrm{1000xF}}{\mathrm{3600M_w}}\ \mathrm{mAh/g} \tag{8}$$

$$C_v = \rho C_G\ \frac{Ah}{L} or\ mAh/cm^3 \tag{9}$$

Where *F* is Faraday's constant (9.64853 x 10^4 C), and M_w and ρ are the molecular weight and density, respectively, of the host material *A, and x* is the amount of Li in Li_xA*,* The Coulombic efficiency (CE) is ratio (expressed as a percentage) between the energy removed from a battery during discharge compared with the energy used during charging to restore the original capacity:

$$CE(\%) = \frac{C_{G,D}}{C_{G,C}} \times 100 \quad (10)$$

The Coulombic efficiency shows the reversibility of the lithiation process. The CE lower than 100% means some charge is lost and used for processes other than the reversible lithiation/delithiation reactions such as the irreversible trapping of Li in the host material and the formation of solid electrolyte interphase (SEI) due to the decomposition of the electrolyte at low potentials. However, this irreversible capacity loss is observed only in the first few cycles after which, the lithiation process becomes more reversible and the SEI layer has passivated the surface of the material, leading to very little irreversible capacity loss and high CE in subsequent cycles. It is worth noting that the electrolyte is reduced prior to lithiation for the formation of the passivating SEI layer on negative electrode surfaces to inhibit electron transfer between the electrolyte and electrode. [17] The large volume change in silicon negative electrodes leads to the SEI breakage and continual growth resulting in large irreversible capacity loss.

1.1.2.3 Energy density

The specific energy, *E,* of an electrode material can be calculated from the specific capacity and the average potential at which the reaction with lithium occurs, *V.*

$$E = VC_G \quad (11)$$

The specific energy (gravimetric energy density) is typically reported in units of Wh/kg while the volumetric energy density is reported in Wh/L. According to the equation above, there are two options to increase the energy of the battery, 1. Increase the specific capacity or 2. Increase the voltage. When considering only the active materials of the positive and negative electrodes, the energy densities of ~560 Wh/kg are obtained for $LiCoO_2$, $LiMn_2O_4$, or $LiFePO_4$ against graphite. However, the gravimetric energy density of the entire battery is lower by about 50-70% than the theoretical one as the weight of the electrolyte, separator, current collectors, and other inactive components must be considered.[26]

It should be noted that if the potential changes dramatically during the lithiation/delithiation process, then the energy density will also change. Some electrode materials that display high specific capacities have poor voltage characteristics, resulting in minimal improvements in the energy density. Thus, it is always important to consider both the voltage and specific capacity when looking at possible new electrode materials.

1.1.2.4 Power

The power a battery can supply is related to the magnitude of the current drained during the discharge. Typically, the larger the current, the higher the IR losses and polarization effects. Moreover, the problem could be related to the phase transformations and solid-state diffusion in the active materials. All of these factors may change the shape of the discharge curve as well as lower the capacity and voltage the battery can deliver. Therefore, batteries are typically measured at different currents. "C" rates are used to identify the currents used in galvanostatic (constant current) measurements. 1C is defined as the amount of current needed to fully discharge the battery in one hour. This can be calculated from the theoretical capacity, C_G, and the mass of available material, m:

$$1C = mC_G \tag{12}$$

1.1.3 Silicon as a LIB negative electrode

Silicon is one of the most promising negative electrode materials owing to its large charge storage capacity of 3590 mAh/g, corresponding to $Li_{15}Si_4$, which is ten times higher than graphite (372 mAh/g corresponding to the formation of LiC_6) [27-32] Silicon is also the second most abundant element on earth. Because of these attributes, a great deal of attention has been given to using Si as a Li ion cell negative electrode material. Wen and Huggins [33] in an early study have shown that at 415 °C, the electrochemical reaction of lithium with silicon follows the equilibrium Li–Si phase diagram. Based on the phase diagram in Figure 1.3(a), the reaction products are $Li_{12}Si_7$, Li_7Si_3, $Li_{13}Si_4$ and $Li_{22}Si_5$ with the onset potentials of 332, 288, 158, and 44 mV, respectively. The final phase gives a specific discharge capacity of about 4200 mAh/g based on the weight of Si However, the Li–Si reaction at room temperature does not appear to follow this scheme.

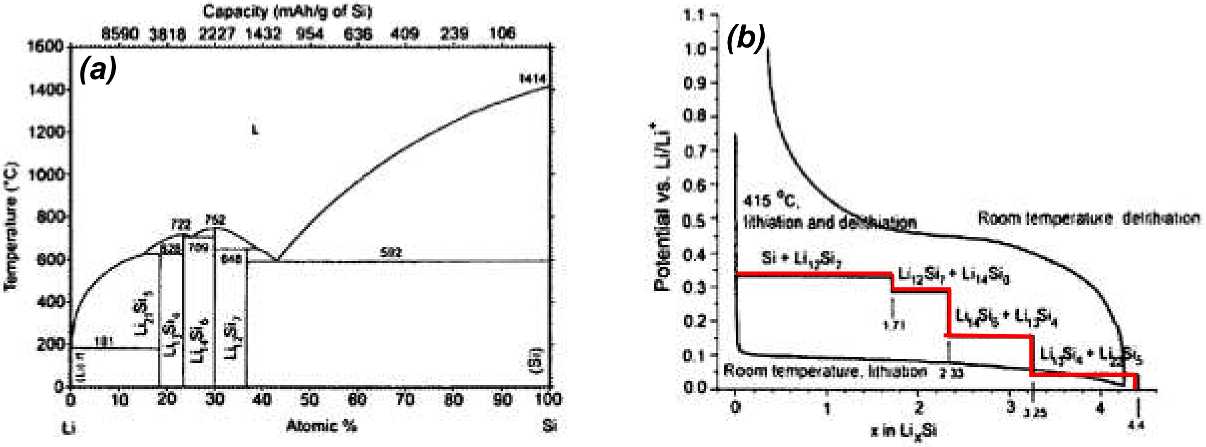

Figure 1.3: Li-Si system, (a) Equilibrium phase diagram, (adapted from 34) (b) Voltage profile of the reaction of Li with Si at 415 °C (red). (adapted from 33). The voltage profile of the room temperature lithiation and delithiation of Si is also shown (black).

In 1999, Huggins et. al. investigated the system at room temperature using the stoichiometric equilibrium phases.[33] They found out the delithiation of these compounds occurred in two-phase regions, but the expected voltage profile for the formation of increasingly Li-poor phases was not observed (see Figure 1.3(b)). Instead, the two-phase region was maintained until most of the Li was removed. During delithiation, a voltage hysteresis of about 0.4 V was observed. Interestingly, Li could be re-inserted into the discharged Si in two sloping voltage regions. Moreover, the cycling voltage curves are influenced by both the Si particle size and the depth of lithiation.[35] The typical voltage curves observed for Si negative electrodes with the particle sizes of few microns is shown in Figure 1.4. [36-40]

The first lithiation curve exhibits a single flat plateau at around 0.1 V, indicating a two-phase addition reaction rather than the multi-phase reactions predicted by the equilibrium Li–Si phase diagram. Moreover, the subsequent lithiation shows sloping plateau voltage curves. Meanwhile, there is a strong dependence between the cut-off potential of lithiation and delithiation voltage curves. If the negative electrode is fully lithiated to 0 V, the delithiation curves exhibit a single flat plateau at around 0.4 V in all the cycles, followed by an upwardly sloping region (Figure 1.4(a)). However, if the negative electrode is lithiated to above 50 mV, the delithiation curves show a sloping plateau (Figure 1.4(b)).

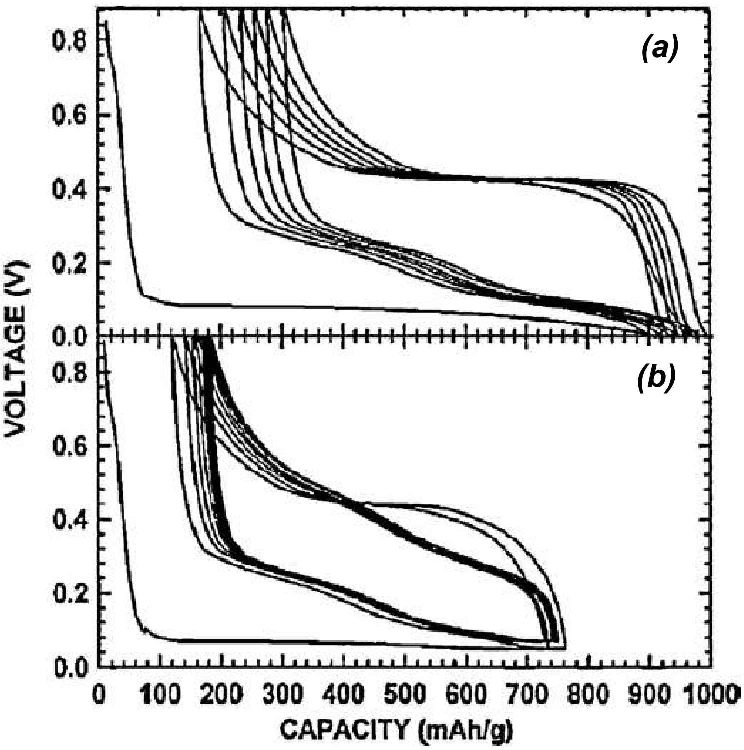

Figure 1.4: Voltage–capacity curves for $Ni_{30}Si_{70}$ alloy (a) lithiated to 0 V and (b) lithiated to 50 mV for the first two cycles and then to 70 mV for later cycles. (adapted from 38).

Detailed XRD studies [40-42] indicated that at voltages above 50 mV, the crystalline Si particles are transformed to amorphous Li_xSi in the first lithiation process. A distinct plateau is observed as it is a two-phase addition reaction. Below 50 mV, the amorphous phase is suddenly crystallized to $Li_{15}Si_4$ with the subsequent flat plateau at around 0.4 V during delithiation. Then, it is followed by a solid-solution reaction from amorphous Li_zSi to amorphous Si. [42] When the negative electrode is lithiated to above 50 mV, the formation of crystalline $Li_{15}Si_4$ phase is suppressed and the final product will be amorphous Li_xSi. Then, the subsequent delithiation process is a solid-solution reaction from amorphous Li_xSi to amorphous Si without phase change, leading to a sloping voltage curve.

Another parameter which changes the voltage profiles of Si negative electrodes is the Si particle size. For Si particles of 50–200 nm, it shows a sloping delithiation voltage profile with no distinct plateau, even if the negative electrodes are fully lithiated to 0 V. [39,43-46] Figure 1.5(a) and (b) shows the voltage profile of the micron-sized Si sample with a flat delithiation plateau at around 0.4 V but a sloping profile for the nanosized sample (10–100 nm) even after fully lithiated to 0 V. [39] When the Si particle sizes are further reduced to less than 20 nm, even the flat plateau in the first lithiation process turns to a sloping shape. [47,48] For those sloping voltage curves, two broad peaks are often observed on the corresponding differential-capacity (dQ/dV) plots in both the lithiation and delithiation branches (see Figure 1.5(b)). The peak potentials of most Si-alloys appear at ~0.06 V and ~0.25 V for lithiation, and ~0.3 V and ~ 0.5 V for delithiation.

It has been reported that the voltage curves and phase transformation in amorphous Si thin-film negative electrodes are affected by the film thickness, surface roughness and alloy additions. [41,47,48] The critical thickness for the crystalline $Li_{15}Si_4$ phase in amorphous Si films and subsequently, the appearance flat plateau in the delithiation process is ~2 µm. [41] However, it has been observed that in a multilayer amorphous Fe/Si negative electrode the crystallization occurs for the Si thickness larger than 200 nm. But the formation of crystalline $Li_{15}Si_4$ phase is suppressed when the film is deposited on a rough surface. The relatively low critical thickness for crystallization in the Fe/Si films as compared to pure Si films may be due to the promoting effect of Fe/Si interfaces on the crystallite nucleation.[47]

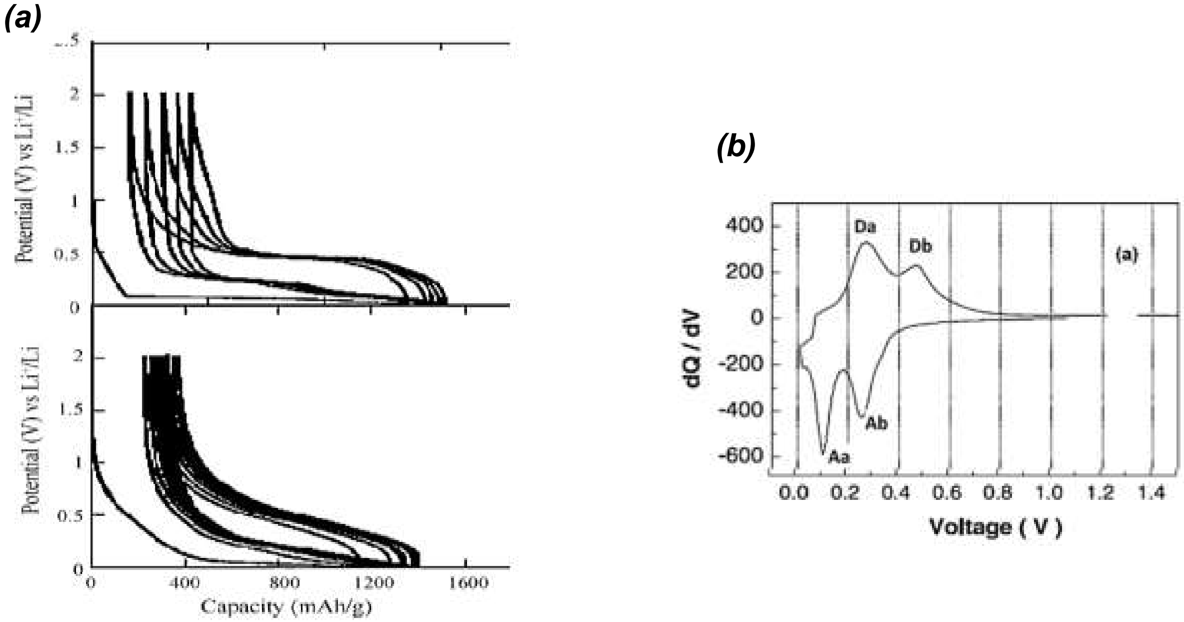

Figure 1.5: Voltage–capacity curves for (a) micronsized (1–10µm) and (b) nanosized (10–100 nm) Si-anodes.[39] (c) The differential capacity vs. potential curves for the 2nd discharge/charge cycle of a pure Si thin-film anode. (adapted from 49).

An important feature observed in silicon-based materials is the large inherent change in specific volume (>300%) associated with lithium insertion and extraction. The stresses induced by these volume changes lead to high internal stress, pulverization and electrical disconnection from the current collector. This induces a significant capacity loss and short cycle life and subsequently, limits the commercial use of silicon in lithium cells. [50-55] Many efforts have been made in recent years to improve the cycling stability, such as decreasing the structures to nanosize or using the thin films or nanoparticles. There have been a large number of studies on the electrochemical reaction of Li with Si and subsequent cycling behavior. Several electrode morphologies and architectures have been explored, including nanopillars, [56,57] particles, [58-60] porous structures,[60-65] various composite negative electrodes, [66-68] thin films, [69-72] nanowires (NWs), [73-78] and nanotubes (NTs). [79-84] As we will discuss with more details in the next part, nanosized silicon-based negative electrodes can improve cycling by accommodation the large volume change without structural degradation during lithiation/delithiation process. They could also improve cycling by exploiting short lithium diffusion distances within the electrode and large surface area resulting in high rate capability. [85,86]

1.1.4 Advantages of nanostructured or nanoscale electrodes

Nanostructured or nanoscale electrodes can provide the necessary volume of free space to accommodate alloying induced expansion/contraction. Thus, they can minimize material stress and electrode pulverization to achieve greater reversibility and cycling stability. [87-89] Nanoscale dimensions allow quick relaxation of stress, making nanoparticles more resistant to fracture than bulk particles. Comparison of the calculated misfit stress energy in partially delithiated particles (consisting of a lithiated core and delithiated shell) suggests fracture should not occur during cycling for particles having diameters of 10 nm or less.[90] As mentioned above, different Si nanostructures have been contemplated to mitigate volumetric changes of Si-based negative electrode materials. Several methods have been used to reduce the capacity fading of Si-based negative electrode materials. One strategy is the reduction of Si particle size to nanometres, which is helpful to decrease the lithium ion diffusion path length, and improve the capacity retention of Si-based negative electrodes. However, it has failed to completely exclude capacity fading. When metal nanoparticles are used as a negative electrode material, the nanoparticles undergo aggregation and pulverization during cycling.[91,92] More attractive strategy is to fabricate NWs and NTs in order to better accommodate the large volume change during lithium insertion/extraction compared to micro- and nanoparticles.

The use of nanoscale morphologies may also improve the rate capability and specific capacity. As expected, the capacity of silicon electrodes decreases at high charge/discharge rates as a result of the low lithium ionic conductivity in silicon and sluggish mass transfer at the electrode interface. By reducing the electrode dimension and increasing the surface-to-volume ratio shorter lithium diffusion distances can be provided. Thus, the electrode polarization may be reduced, allowing high capacities to be realized.[17]

1.1.4.1 Nanostructure morphologies-nanowires

The nanowire structure exhibits an excellent large strain and volume accommodation property, and electrodes comprised of 1D SiNWs have been shown to have a dramatically improved electrochemical performance. [46,93-95] Moreover, using nanowire based electrodes is very important in terms of understanding multiple important fundamental concepts involving lithium ion transportation, fracture initiation and propagation within silicon materials. Figure 1.6 illustrates the schematic of morphological changes occurring in silicon negative electrodes during electrochemical cycling. As could be seen, silicon thin films and particles are more prone to pulverize compared to SiNWs during cycling resulting in poor transport of electron as indicated by arrows. The storage capacity of the Si thin film electrode is increased using a large layer thickness. However, this could be resulted in poor capacity retention due to a fast degradation of the material as a result of delamination or pulverization. SiNW negative electrodes grown via vapor-liquid-solid (VLS) growth method on a metal current collector can accommodate large volume changes during lithium insertion and extraction with near theoretical capacities compared to planar films.

Generally, the SiNWs growth approaches could be categorized into two groups: bottom-up and top-down methods. The bottom-up approach is the most popular technique to grow Si NWs. [96] The growth mechanism of nanowires could be well elucidated by the VLS mechanism, which was first proposed by Wagner and Ellis in the 1960's [97] and further developed by Lieber et al. [98] The VLS growth mechanism is used for interpreting the nanowires growth with multiple techniques including CVD, molecular beam epitaxy (MBE), laser ablation (LA), silicon monoxide evaporation, and solution-based techniques using various kinds of catalysts, such as Au, Cu, Pt, Ni, Bi, and Co.

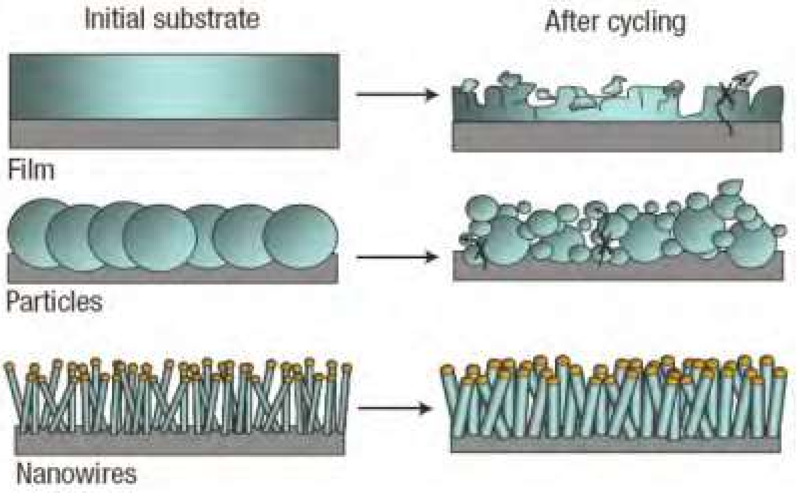

Figure 1.6.: Schematic of morphological changes that occur in Si during electrochemical cycling. (adapted from 46).

One of the most effective ways to prepare semiconducting SiNWs with controllable diameters and lengths is the bottom-up approach VLS chemical vapor deposition. The common Si sources are silane, disilane, and their chloride derivatives. At the process temperature below 600 °C, the catalyst metal and precursors which are used are limited to Au and silane (SiH_4)/disilane (Si_2H_6), respectively. At higher growth temperatures, there is much broader choice of possible VLS catalyst materials, including Cu, [99] Pt, [100] Ni, Ag, Zn, and Al. [101] The main advantage of the CVD technique is the precise control over the diameter, length, growth direction, and doping level of wires. Notably, using low-temperature CVD, the diameter and length of the Si nanowires could be further controlled down to a few nanometers. [102,103] Besides the diameters, the growth direction of Si nanowires could also be arbitrarily controlled via the CVD technique. When the diameters are above 50 nm, Si nanowires along <111> orientation could be preferentially obtained, [104] whereas <110> and <112> oriented nanowires are produced via reducing the diameters below 20 nm and in the range of 20–50 nm, respectively. [105,106]

1.1.4.1.1 Electrochemical performance of SiNWs in LIBs

The pioneering work of using Si nanowires as negative electrodes for LIBs was performed in Cui's group in 2007. [46] They prepared Si nanowires with a diameter of ~90 nm by the CVD method and vertically aligned on stainless steel substrate. It was observed that the initial coulombic efficiency was greatly improved from ~25% for 10 μm Si powder-based electrode to 73%. Moreover, the cycle life was significantly improved using these nanostructures. The improved electrochemical performances were related to the well-designed architecture of the SiNWs electrodes. They could provide sufficient space for a large volume change, robust electrical contacts between individual wires and substrate, as well as high resistance for fracture formation. [107] However, the initial and long-term coulombic efficiencies are still low, which mainly originated from the decomposition of electrolyte and the sequential formation of SEI films on the fresh high surface area of Si nanowires exposed to the electrolyte. Therefore, several approaches have been developed to increase the coulombic efficiency of SiNWs based electrodes. It has been reported that the initial coulombic efficiency of nanowires were greatly enhanced with 10 nm thick carbon coating (from ~70% for uncoated nanowires to ~83% for the coated ones). Moreover, the capacity increase from ~3125 mAh/g to ~3702 mAh/g after coating with the capacity retention of ~75% after 15 cycles.[108]

Metallic conductive coatings have been explored more recently, such as Cu coating on SiNWs, in which the initial coulombic efficiency was further improved to 90.3% with the capacity retention of ~86% after 15 cycles. [109] By contrast, Al coating could not improve the initial coulombic efficiency, but it did help to increase the capacity retention after numerous cycle. Moreover, by the application of an electrically conducting TiN barrier layer between stainless steel substrate and SiNWs, the growth of nanowires with diameter larger than 250 nm was limited with an improvement of initial coulombic efficiency from 84.3% to 93.1%. [75] An improvement of the capacity retention was also observed by coating nanowires with ~100 nm Ag/poly(3,4-ethylenedioxythiophene) (PEDOT).[110]

In order to protect the electrode surface from excessive formation of the SEI layer, the Si-based and other negative electrodes have also been coated with non-conducting coatings. The use of functional Al_2O_3, [111-114] TiN, [78] TiO_2, [77,115-117] SnO_2 [118,119] and SiO_2 [80] on the surface of silicon has shown promising outcomes in order to prevent the direct contact of the active material with the electrolyte. Thin Al_2O_3 coatings (<10 nm) obtained by atomic layer deposition

(ALD) have also been tested on thin film Si negative electrodes [111,112] and Si NWs.[113] The formation of Al-Li-O glass, which is a good Li ion conductor and an electronic insulator occurs during the first lithiation. Thus, it can act as a good substitute for the SEI layer. Although, the Al_2O_3 coating does not withstand the ~300% volume expansion of Si, it still can provide some protective patches. This leads to a 45% increase of the negative elecrode cycle life compared to the uncoated nanowires.[113]

1.1.4.1.2 Mechanisms studies through SiNWs

As mentioned before, the major obstacle limiting the application of Si-based electrodes in lithium batteries is the drastic volume change during lithiation/delithiation.[120,121] However, the nature of volume changes in Si materials has not been well understood. It has been shown that the nanowires diameter plays an important role in determining the mechanical properties of nanowires, [122] and the effect of the diameter on the electrochemical performance have been well studied.[123] The diffusion-induced stresses model on nanowires during lithiation illustrates that the tensile stress is converted to compressive stress for nanowires with diameter below a critical value. This can reduce the crack initiation.[124]

Furthermore, the "critical diameter" proposed by Ryu and co-workers for pulverization is in the regime of 220–260 nm (See Figure 1.7). The existence of "critical diameter" was confirmed by both theoretical calculation and ex situ TEM observations.[125]

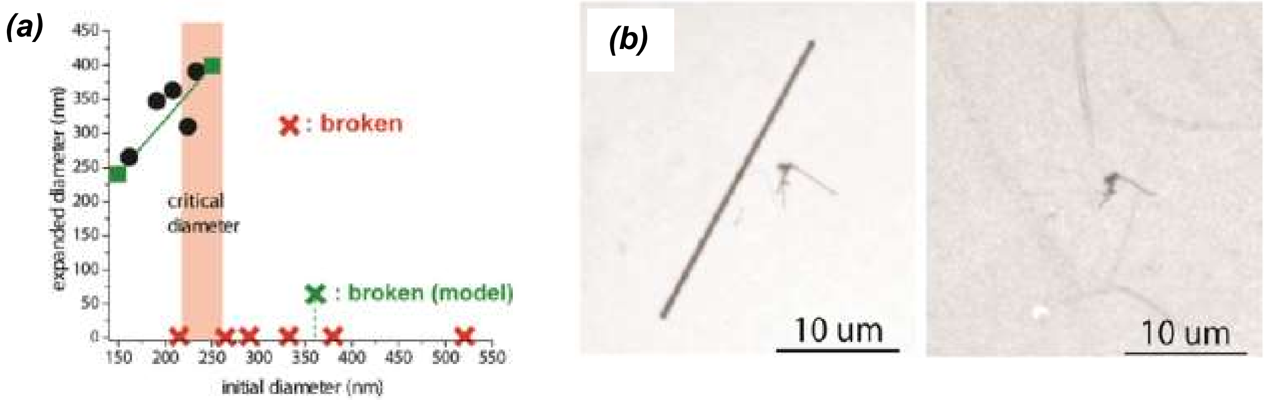

Figure 1.7: (a) A statistical plot showing critical diameters (220–260 nm) at which Si NWs start pulverizing. Green line shows the model prediction. (b) TEM images before (left) and after (right) the lithiation process to 10 mV vs. Li/Li^+. Large nanowires disappear due to pulverization during the

lithiation process, whereas the small nanowires remain in the same position.(adapted from 125).

Silicon nanowires, even when prepared under highly reducing conditions, will be ultimately exposed to some oxygen and water vapour (even if it is inside an inert glove box). Due to its very high thermodynamic stability, silicon oxide will then form. It has been demonstrated that the mechanically strong oxide shell could limit the radial expansion of SiNWs during the lithiation/delithiation process, especially for smaller nanowires with thicker oxide shells.[126]

Another important finding is studying the nature of volume changes of Si materials through studying the evolution of nanowires during lithiation/delithiation process. The in-situ study and experimental observations indicated that the diffusion of Li ions is anisotropic within Si along different crystal orientations and, the diffusion of Li ions in Si nanowires occurs layer by layer from the surface to the inner core.[127] The in situ TEM observations confirmed that the lithiated Si nanowires have a dumbbell shape with a diameter along <110> expanded by ~170%, while less than 20% along <111> directions.[128]

1.1.4.2 Nanostructure morphologies-nanotubes

SiNTs are one attractive electrode configuration that improves electrochemical performance.[80-82,84] The inside empty space within the nanotubes as well as the empty space on the outside provide free space to accommodate the volume expansion during lithiation, thus limiting the overall swelling of the structure (see Figure 1.8). Moreover, the lithium diffusion distance can be significantly shortened as both inner and outer walls of nanotubes are exposed to the electrolyte, and walls of NTs are extremely thin.

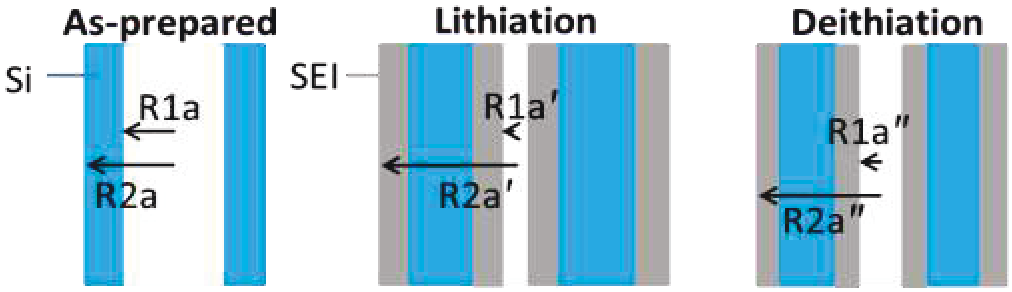

Figure 1.8: The schematic of one representative as-synthesized and cycled silicon nanotube with SEI formation on the surfaces.

Song and coworkers [82] have synthesized their nanotubes by deposition a conformal Si shell on sacrificial ZnO nanorod cores and subsequently removed the ZnO using a moderate temperature (600 °C) reduction process. They demonstrated that free expansion at the inner surface of the Si nanotubes eases the volume increase during Si lithiation. Wu et al.[80] synthesized their Si nanotubes by using sacrificial carbon fibers on which a CVD Si shell was deposited. Then, the carbon fibers were selectively removed by a 500 °C thermal treatment in air. This treatment leaves a thin protective SiO_2 coating around the nanotubes, in which it acts a mechanical clamping layer, preventing the outer expansion of the SiNTs during lithiation, while forcing the nanotubes to expand inwards into the hollow space. Because the outside surface of the Si nanotubes does not, or only slightly expands, the SEI which deposits on it is mechanically stable and serves as an efficient passivation layer.

1.1.4.2.1 Electrochemical performance of SiNTs in LIBs

Concerning the relative difficult synthesis process of SiNTs compared to the nanoparticles, nanowires and nanorods, there are only a few reports on SiNTs as LIB negative electrodes. However, SiNTs have been attracting more and more attentions by material researchers since it was first reported as LIB negative electrode by Park and co-workers in 2009. [81] In this study, they prepared the nanotubes with carbon coating with outer diameters of 200-250 nm, wall thickness of ~40 nm, and length of ~40 μ m through the decomposition of silicon precursors which were pre-deposited within porous alumina membrane. They could achieve the initial discharge capacity and coulombic efficiency of 3648 mAh/g and 89%, respectively, at a charging rate of 0.2 C. More importantly, full cells using these SiNTs as the negative elecctrode and $LiCoO_2$ as the positive electrode could deliver a capacity of more than 3000 mAh/g (based on the mass of Si) even at high rate of 5 C. Thy attributed the excellent capacity retention to the unique tubular structure of Si. The presence of the carbon on the nanotube surface could separate the Si surface from exposing to the electrolyte and promote the formation of a stable SEI layer.

Interestingly, without a carbon coating, arrays of sealed silicon nanotubes also delivered an initial high coulombic efficiency of ~90% with an impressive discharge capacity of 2924 mAh/g at 0.2 C. [82] In addition, the could retain 81% and 82% of their initial capacity after 50 cycles at a rate of 0.05 and 0.2 C, respectively. (see Figure 1.9)

Besides carbon coating, other materials such as Ge [129], SiO_x, [80] SnO_2, [9] and TiO_2, [84,130] Al_2O_3, [84] and TiN [84] have also been deposited on the inner and/or outer surface of SiNTs with a significant improvement in the cycling stability by the introduction of an extra layers of these materials on the surface of nanotubes. Moreover, an additional improvement in the initial as well as long-term coulombic efficiency may be obtained by coating the inner surface of the nanotubes as well as the outer surface. [84]

Electrochemical study on a double-walled Si/SiO_x NTs architecture showed that it could preserve 88% of initial capacity (~600 mAh/g) after 6000 cycles at a rate of 12 C. However, the initial coulombic efficiency of the initial cycle was only 76% due to the constraining SiO_x layer. [80] The extremely long cycle life was attributed to the formation of stable SEI layer associated with this unique double-walled architecture. Furthermore, the clamping SiO_x layer could force silicon to expand inward into the hollow space, and thus the outer surface remains static during both lithiation and delithiation.

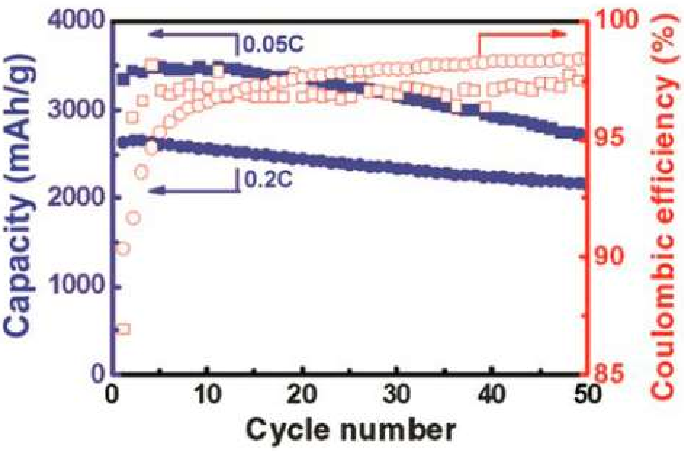

Figure 1.9: Specific capacity and Coulombic efficiency of silicon nanotubes cycled at rates of 0.05C (squares) and 0.2C (circles).(adapted from 82).

In another study on double-layered Si/Ge nanotubes, the capacity retention was 85% after 50 cycles at a rate of 0.2 C. [129]

In summary, silicon nanotubes can offer better cycling stability with a relatively high specific capacity compared to other silicon nanostructures. This could be mainly attributed to the existence of extra empty space inside the nanotubes which can accommodate the Si expansion during cycling. This will reduce the cracking of silicon and the subsequent formation of new SEI layer on the surface of fresh Si exposed to the electrolyte during cycling. A main drawback of these hollow nanostructures is a very low mass density due to the existence of high porosity in the structure. This will significantly reduce the volumetric capacity of the electrode and energy per unit volume of LIB cells. Moreover, fabrication costs of silicon nanotubes are higher compared to those of silicon nanoparticles. Thus, developing a facile method to fabricate SiNTs is highly demanding for their industrial application.

1.1.4.2.2 Mechanisms studies through Si nanotubes

SiNT negative electrodes for LIBs have demonstrated very impressive cycling stability and rate capability. The excellent electrochemical performances are closely linekd to the unique tubular structure which can provide free space for volume expansion/contraction. Moreover, the hollow structure can reduce the lithium diffusion path, which in turn can improve the rate capability.

There is a strong relationship between the length, inner and out diameters, wall thickness and the mechanical and thus the electrochemical properties of nanotubes during lithiation/delithiation process.

Wu and co-workers [131] have calculated the diffusion-induced stresses for the tubular structure. Based on their study, all stresses within tubular structure and corresponding tangential and axial fracture tendensies can be reduced by decreasing the wall thickness. On the other hand, with a fixed wall thickness and length when the radius of tubes is reduced, both tangential and axial fracture tendencies decrease. Finally, for tubes with fixed radius and wall thickness, the tangential fracture tendency is independent of the tube length, while axial fracture tendency elevates with an increased tube length. In summary, shorter tubes with smaller radius and thinner walls have better cycling stability. Furthermore, anisotropic volume expansion of SiNTs was observed, which could increase the diameter by ~150% with much less increase in length (~5%). [82] In fact, the anisotropic volume expansion of SiNTs is due to the free surface (inner and outer), which can better accommodate the expansion in the favor of radial direction rather than axial direction. Compared to silicon nanowires, the maximum stress in SiNTs is much lower due to the additional free inner surface possessed by tubular structures. [82]

Another important finding is the effect of constraining layer on the surface of the nanotubes. Based on the finite element modeling, SiNTs tend to expand outwards during lithiation. But, they are forced to expand inwards into the hollow space by the application of a mechanically rigid coating on the outer surface. This mechanical constraining effect can also provide a stable SEI layer on the outer surface which remains static during cycling. As a result, a double-walled SiNTs (SiO_2/Si) electrode showed a superior electrochemical performance. [80]

1.1.5 Sodium-ion batteries

As discussed earlier, practical applications of LIBs with the highest energy density and long cycle life have attracted great attention. However, because of the low abundance of Li in the Earth's crust and the large-scale demand for Li, it would be inevitable to consider the growing price of Li resources. The total global Li consumption in 2008 was approximately 21 280 tons; therefore, Li resources could be sustained for approximately 65 years at most from the present, considering an average growth of 5% per year.[132] Therefore, it is highly demanding to explore low cost, highly safe, and cycling stable rechargeable batteries based on abundant resources. Sodium has strongly broken into energy storage research field. This alkali is very promising to be a complement or substituting Li-based technology. Its natural abundance, easy access to sodium sources and, consequently, lower price; suitable redox potential (E^0 (Na^+/Na)=-2.71 V vs. standard hydrogen electrode, 0.3 V above that of Li) (see Table 1.1) [133-138] and similar intercalation chemistry to Li, make this element strategic in innovative research of energy storage systems. Although at this point the gravimetric and volumetric density of sodium-ion batteries (NIBs) is lower than that of LIBs, for stationary applications cost and availability are considered to be more essential.[136-138]

Table 1.1: The comparison between Na and Li elements. (adapted from 137).

	Na	Li
Cation radius	97	68
Atomic weight	23	6.9 $gmol^{-1}$
E° vs. SHE	-2.7 V	-3.04 V
Melting point	97.7 °C	180.5 °C

Abundance	23.6 x 1.3 mg kg^{-1}	20 mg kg-1
Distribution	Everywhere	70% in South America
Price	~2 RMB per kg	~40 RMB per kg

NIBs are not new. NIBs and LIBs were investigated in parallel from 1970s to the 1980s.[139-141] However, after a successful achievement in using LIBs for commercial applications in 1990s, the investigation of NIBs was significantly decreased.

Recently, research interest in Na-ion batteries operated at room-temperature has attracted more attention due to the abundance and low cost of Na. Previously, Whittingham and Hagenmuller studied the Na intercalation into layered MoS_2, TaS_2, TiS_2 and Na_xMO_2 (M=Co, Mn, etc.) during the 1970s to the 1980s.[141-143] However, searching for new electrode materials (cathode and anode) and new stable electrolytes (liquid and solid) for Na-ion battery system is necessary. Although there are numerous electrode materials for Li-ion batteries, [144,145] only a few are suitable host materials to accommodate Na ions and allow reversible insertion/deinsertion reactions; most of these are positive electrode materials.[146-148] So far, negative electrode materials are less explored and are one of the most troublesome components of the sodium-ion cell. In this work, only carbon-based negative electrode materials will be discussed.

1.1.5.1 Anode materials

Graphitic carbon materials are the most-used negative electrode material in commercial LIBs due to their high reversible capacity, low and flat potential plateau with respect to lithium metal, superior cycling behaviour, high coulombic efficiency, low cost, and good safety features.[11-14] Nevertheless, they exhibit very poor Na-ion storage properties. [149,150] Only a limited number of Na ions can be intercalated into graphite (NaC_{70}), which can be mainly attributed to the larger size of the Na ions.[150] To date, very few negative electrode materials have been reported as viable. Unlike Li metal, Na metal is not a good choice due to its high reactivity and unstable passivation layer in most organic electrolytes at room temperature. Therefore, it is very demanding to identify an negative electrode material with a proper Na storage voltage, high reversible capacity and high structural stability for the development of NIBs.

1.1.5.1.1 Carbon-based compound

In 1993, researchers first examined the Na storage behaviors in various carbon materials with PEO-$NaCF_3SO_3$ polymer as the electrolyte. Approximate compositions which were formed for graphite, petroleum coke and Shawinigan black were NaC_{70}, NaC_{30} and NaC_{15}, respectively.[151] In 2000, authors compared the electrochemical behavior of Li and Na storage in hard carbon produced from a glucose precursor.[152] They could get a high reversible capacity of 300 mAh/g in NIBs. To date, extensive carbon materials with different morphologies, such as tailor-made carbon with hierarchical porosity (Figure 1.10(b)) [153] N-doped porous carbon nanosheets, hollow carbon nanospheres, [154] and nanowires[155] have been studied for NIBs with significant improved storage performance and kinetics. Carbon based hollow nanowires[155] and hollow nanospheres[154] show improved sodium storage properties compared to their solid counterparts, as a result of a more efficient sodium diffusion within the material as shown in Figure 1.11. Hollow nanospheres showed a reversible capacity of 160 mAh/g at 100 mA/g after 100 cycles in 1 M $NaClO_4$ in PC in the voltage range 0.001–3.0 V. Hollow nanowires delivered a reversible capacity 250 mAh/g at the current denisity of 50 mA/g and over a narrower voltage range 1.2–0.01 V vs. Na/Na^+ with 82% capacity retention after 400 cycles. Interestingly, it showed excellent rate capability with 150 mAh/g at a high rate of 500 mA/g in 1 M $NaClO_4$ in EC: EMC. The excellent cycle stability and rate capability is related to the quite large average graphitic interplanar distance in the as prepared nanowires and short Na diffusion distance.

In another study, researchers examined hard carbon in various electrolytes and could obtain an initial capacity of 240 mAh/g in a voltage range of 0–2 V with an initial coulombic efficiency above 78% in 1 M $NaClO_4$/EC:DEC (1 : 1 by volume) electrolyte (Figure 1.10b).[156]

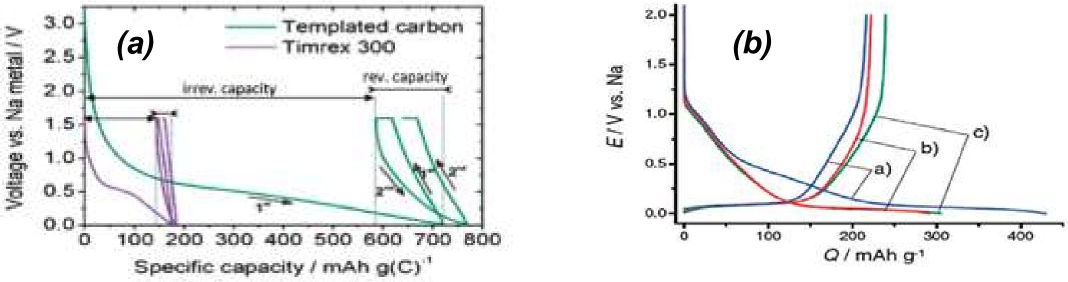

Figure 1.10: The charge–discharge profiles various carbons. (a) hierarchical porous carbon. [153] (b) Hard carbon.(adapted from 156).

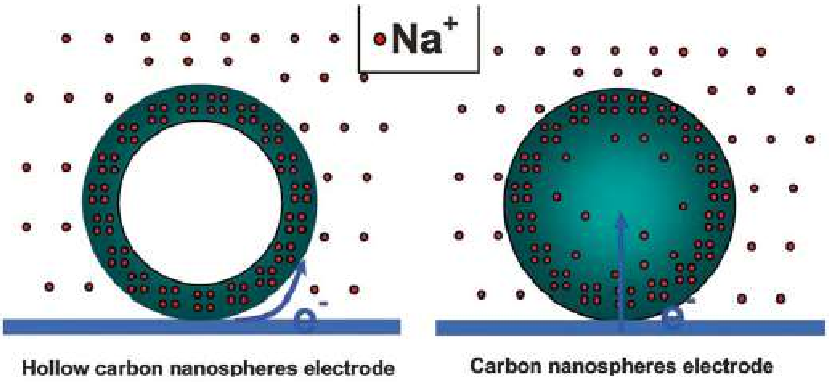

Figure 1.11: Schematic of the electrochemical reaction process of hollow carbon nanospheres and solid carbon spheres.(adapted from 154).

More recently, reduced graphene oxide (RGO) has shown an intermediate performance between that of hollow nanotubes and nanospheres in the same electrolyte, with a reversible capacity of 177 mAh/g at 200 mA/g and a capacity of 93 mAh/g after 1000 cycles (see Figure 1.12).[157] The reversible capacity delivered by interconnected nanofibres produced from annealing polypyrrole was higher than 130 mAh/g at a current density of 200 mA/g for 200 cycles and 73 mAh/g at a high current density of 20 A/g between 0.1 and 2.0 V.[158] Finally, N-doped carbon nanosheets,[159] in 1 M $NaPF_6$ EC : DMC delivered a capacity of ~300 mAh/g at 50 mA/g, but only 50 mAh/g at 20 A/g. Nevertheless the capacity retention in 10 cycles is less than 70%.

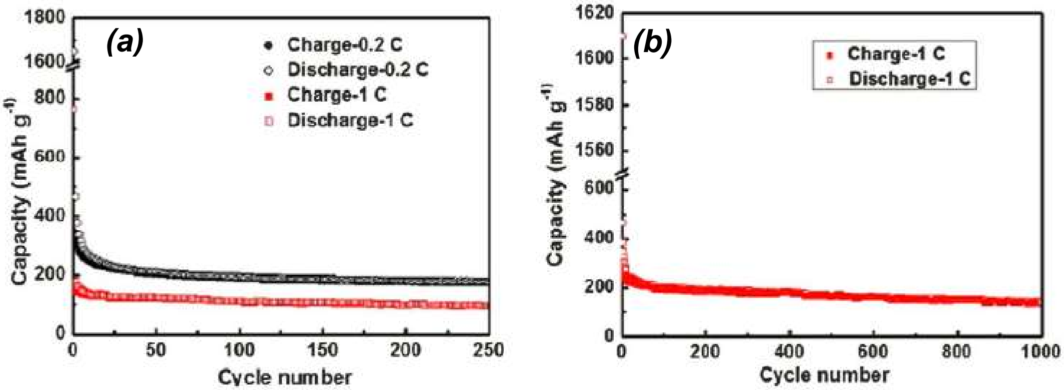

Figure 1.12: (a) Cycling performance of RGO at 0.2 C and 1 C for 250 cycles (b) cycling performance of RGO at 1 C for 1000 cycles. (adapted from 157).

These studies demonstrate that hard carbon is a promising negative electrode material for NIBs. However, reports of LIB-graphite analogues for NIBs are scarce; their performance is still far from that achieved by graphite in lithium-ion batteries and its electrochemistry towards sodium storage particularly below 0.2 V vs. Na/Na^+ remains unclear.[160] Moreover, there are few reports on cycling stability and rate capability.[154,155,160,161] Finally, as in the lithium system, efforts are also needed to increase the volumetric capacity in order to make them good candidates for negative electrodes.

1.2 The motivation and scope of this thesis

This thesis is mainly focused to improve the cycling performance of different nanostructures of silicon that suffer from SEI and volumetric expansion-induced performance losses. This is achieved by coating the Si nanostructures using different coating techniques (i.e. sputtering, atomic layer deposition). We demonstrate how different coatings using different coating techniques and on different locations in the case of hollow nanostructures can affect the electrochemical performance. What is the optimum coating thickness and optimum deposition temperature and how the resultant composite performs during cycling. The degradation mechanisms of silicon nanostructures as negative electrode materials in lithium-ion batteries are also investigated through systematic post cycle characterizations of electrode materials. Finally, the application of a biomass-derived carbon as an negative electrode for lithium and sodium ion batteries is also studied in the last chapter. We show that how the carbons' unique structure consisting of highly ordered graphite-like arrays with a relatively large interlayer spacing can substantially improve cycling performance.

In chapter 2 we investigate the effect of the support growth substrate as well as of aluminum coating layers on the electrochemical performance of silicon nanowires. We indicate that how the contact loss between the nanowires and the current collector has an important role in determining the irreversible capacity for the first charge/discharge cycle. A corrosion mechanism for the case when a bare stainless steel support was utilized for the nanowire growth is demonstrated. This corrosion mechanism is almost entirely inhibited through the use of a TiN growth underlayer. This chapter also compares the cycling performance of silicon nanowires grown on stainless steel with TiN interlayer with the nanowires grown on stainless steel. The effect of sputtered aluminum coating with different thicknesses on the cycling performance of nanowires is also studied. We also discuss the role of aluminum on reducing the crack growth rate in silicon and delaying the ultimate onset of wire decrepitation and loss of electrical contact with the underlying electrode.

In chapter three we demonstrate substantial improvement in cycling performance of silicon nanowires using a nanoscale conformal coating of TiO_2, deposited by atomic layer deposition. Using TEM electron energy loss spectroscopy (EELS) analysis, combined with complementary techniques such as focused ion beam (FIB) and X-ray photoelectron spectroscopy (XPS), we elucidate that these radical changes in cycling behaviour are directly attributed to the as deposited and the post-cycled microstructure of the coatings. We show that how the microcrystalline TiO_2 with an as-deposited anatase crystal structure does not possess the mechanical integrity or the passivation efficacy of the amorphous coatings, which upon lithiation decompose into a tough and adherent composite of Li active amorphous and nanocrystalline cubic $LiTiO_2$ phases. This chapter provides new insight into the lithiation cycling-induced failure mechanisms that turn out to be intimately linked to the growth of the secondary electrolyte interface (SEI). We put forth a unique observation of both the SEI and the active Si actually extruding through and past the coatings, to a degree that varies with the film structure.

Chapter four presents the results of our study on employing atomic layer deposition to coat TiO_2, Al_2O_3 and TiN onto hollow Si nanotubes. Such hollow structures are believed to be better able to accommodate the large volume expansion of Si upon lithiation (300% at 3590 mAh/g capacity), thus improving both cycling stability and coulomic efficiency. We use elemental mappings obtained using EELS to show the locations where SEI formation occur. We are the first to demonstrate that it is not entirely correct to assume that passivating only the outer surface is enough to achieve optimum coulombic efficiency. Rather, we show that how an additional improvement may be obtained by coating the inner surface as well. We also study the cycling performance of different coatings on different locations to find out the composite with substantial improvement in capacity retention and coulombic efficiency. A short summary and comparison with prior art is included in this chapter, which are among the best in terms of stability and efficiency ever reported for hollow Si based nanostructures. We demonstrate that only high electronic conductivity (TiN) or only high ionic conductivity (Al_2O_3) are not nearly as effective for improving high-rate capability as the TiO_2 coating that combines both. The findings of our study should provide a broadly applicable design methodology for nanoscale coatings employed to improve the cycling performance of a variety of nanostructured LIB negative electrode materials where SEI growth is universally detrimental.

In chapter five we create NIB carbons that behave electrochemically nearly identically to graphite in LIBs, demonstrating the same key advantages. The electrodes are a) volumetrically dense with a low surface area, resulting in excellent electrode packing characteristics; b) maximize the voltage window of a full cell due to a low and flat charge - discharge plateau; c) highly reversible with nearly 100% cycling coulombic efficiency and minimal voltage hysteresis; e) highly economical and "green", being obtained from a waste precursor and a simple carbonization and activation process. We demonstrate that how the carbons' unique structure consisting of highly ordered graphite-like arrays with a relatively large inter graphene spacing is a key to achieve these properties.

We then go on to examine banana peel-derived carbons for LIB applications. Overall the performance is quite excellent - among the best in literature for non-highly doped materials. We also demonstrate metal nanopore filling is primarily responsible for the sub - 0.1 V capacity, with adsorption of Li on graphene defects being important at higher voltages.

1.3 References

1. A. Midilli, I. Dincer, M. Ay, *Energy Policy,* 2006, *34*, 3623.

2. M. I. Hoffert, K. Caldeira, G. Benford, D. R. Criswell, C. Green, H. Herzog, A. K. Jain, H. S. Kheshgi, K. S. Lackner, J. S. Lewis, H. D. Lightfoot, W. Manheimer, J. C. Mankins, M. E. Mauel, L. J. Perkins, M. E. Schlesinger, T. Volk, T. M. L. Wigley, *Science*, 2002, **298**, 981.

3. K. Caldeira, A. K. Jain, M. I. Hoffert, *Science,* 2003, **299**, 2052.

4. M. E. Porter, C. Vanderlinde, *Harvard Bus. Rev.,* 1995, **73**, 120.

5. M. Armand, J. M. Tarascon, *Nature,* 2008, **451**, 652.

6. M. M. Thackeray, C. Wolverton, E. D. Isaacs, *Energy Environ. Sci.,* 2012, **5**, 7854.

7. V. Etacheri, R. Marom, R. Elazari, G. Salitra, D. Aurbach, *Energy Environ. Sci.* 2011, **4**, 3243.

8. J. B. Goodenough, *Acc. Chem. Res,* 2013, **46**, 1053.

9. N.-S. Choi, Y. Yao, Y. Cui, J. Ch, *J. Mater. Chem.*, 2011, **21**, 9825-9840.

10. T. H. Bradley, A. A. Frank, *Renew. Sust. Energy Rev.* 2009, **13**, 115.

11. J. S. Yi, T. V. Nguyen, *J. Electrochem. Soc.* 1998, **145**, 1149.

12. N.-S. Choi, Z. Chen, S. A. Freunberger, X. Ji, Y.-K. Sun, K. Amine, G. Yushin, L. F. Nazar, J. Cho, P. G. Bruce , *Angew. Chem. Int. Ed.,* 2012, **51**, 9994.

13. A. Patil, V. Patil, D. W. Shin, J.-W. Choi, D.-S. Paik, S.-J. Yoon, *Mater. Res. Bull.* 2008, **43**, 1913.

14. J. M. Tarascon, M. Armand, *Nature,* 2001, **414**, 359 .

15. M.R. Zamfir, H.T. Nguyen, E. Moyen,Y.H. Lee, D. Pribat, *J. Mater. Chem. A*, 2013, **1**, 9566.

16. B. Xu, D. Qian, Z. Wang, Y. S. Meng, *Mater. Sci. Eng. R-Rep.* 2012, **73**, 51.

17. J. R. Szczech, S. Jin, *Energy Environ. Sci.*, 2011, **4**, 56-72.

18. J.-M. Tarascon, M. Armand, *Nature*, 2001, **414**, 359-367.

19. H. Takeshita, Proc. Conf. Power, 2000, San Diego.

20. M.S. Whittingham, *Science,* 1976*,* **192,** 1226.

21. M.S. Whittingham, M. S. US Patent 4009052.

22. R.A. Huggins, *In Advanced Batteries: Materials Science Aspects,* Springer Science + Business Media, LLC: New York, 2009, 123-149.

23. R. Yazami, Ph. Touzain, *J. Power Sources,* 1983, **9 (3)**, 365-371.

24. M. M. Thackeray, C. Wolverton, E.D. Isaacs, *Energy Environ. Sci.*, 2012, **5**, 7854.

25. W.J. Zhang, *J. Power Sources*, 2011, **196**, 877-885.

26. D. Linden, T.B. Reddy, *Handbook of Batteries;* 3 ed.; McGraw-Hill: New York, 2001.

27. X. Meng, X. Q. Yang and X. Sun, *Adv. Mater.*, 2012, **24(27)**, 3589-615.

28. T. Song, D. H. Lee, M. S. Kwon, J. M. Choi, H. Han, S. G. Doo, H. Chang, W. Park, W. Sigmund, H. Kim and U. Paik, *J. Mater. Chem.*, 2011, **21**, 12619–12621.

29. T.D. Hatchard and J.R. Dahn, *J. Electrochem. Soc.*, 2004, **151**, A838.

30. V.L. Chevrier and J.R. Dahn, *J. Electrochem. Soc.*, 2010, **157**, A392.

31. L.Y. Beaulieu, T.D. Hatchard, A. Bonakdarpour, M.D. Fleischauer and J.R. Dahn, *J. Electrochem. Soc.*, 2003, **150**, A1457.

32. R.Teki, M. K. Datta, R. Krishnan, T. C. Parker, T.-M. Lu, P. N. Kumta, N. Koratkar, *small*, 2009, **5**, 2236–2242.

33. C.J. Wen, R.A. Huggins, *J. Solid State Chem*., 1981, **37**, 271.

34. R.P. Elliott, 1st Suppl., McGraw-Hill: New York, 1965.

35. W.-J. Zhang, *J.Power Sources*, 2011, **196**, 877–885.

36. J.H. Ryu, J.W. Kim, Y.E. Sung, S.M. Oh, *Electrochem. Solid-State Lett*., 2004, **7**, A306.

37. Q. Si, K. Hanai, N. Imanishi, M. Kubo, A. Hirano, Y. Takeda, O. Yamamoto, *J. Power Sources, 2009,* **189**, 761.

38. Z. Luo, D. Fan, X. Liu, H. Mao, C. Yao, Z. Deng, *J. Power Sources*, 2009, **189**, 16.

39. J. Saint, M. Morcrette, D. Larcher, L. Laffont, S. Beattie, J.P. Peres, D. Talaga, M. Couzi, J.M. Tarascon, *Adv. Funct. Mater*., 2007, **17**, 1765.

40. M.N. Obrovac, L. Christensen, *Electrochem. Solid-State Lett., 2004,* **7**, A93.

41. T.D. Hatchard, J.R. Dahn, *J. Electrochem. Soc*. 2004, **151**, A838.

42. J. Li, J.R. Dahn, *J. Electrochem. Soc*. 2007, **154**, A156.

43. G.X. Wang, J. Yao, H.K. Liu, *Electrochem. Solid-State Lett*. 2004, **7**, A250.

44. G.X. Wang, J.H. Ahn, J. Yao, S. Bewlay, H.K. Liu, *Electrochem. Commun*. 2004, **6**, 689.

45. S. Ohara, J. Suzuki, K. Sekine, T. Takamura, *J. Power Sources*, 2003, **119–121**, 591.

46. C.K. Chan, H. Peng, G. Liu, K. Mcilwrath, X.F. Zhang, R.A. Huggins, Y. Cui, *Nat. Nanotechnol.* 2008, **3**, 31-35.

47. J.B. Kim, S.H. Lim, S.M. Lee, *J. Electrochem. Soc*. 2006, **153**, A455.

48. H.Y. Lee, S.M. Lee, *Electrochem. Commun*. 2004, **6**, 465.

49. J.B. Kim, H.Y. Lee, K.S. Lee, S.H. Lim, S.M. Lee, *Electrochem. Commun*. 2003, **5**, 544.

50. T.D. Hatchard, J.R. Dahn, *J. Electrochem. Soc.*, 2004, **151 (6)**, A838-A842.

51. S.H., Ng, J. Wang, D. Wexler, K. Konstantinov, Z.P. Guo, H.K. Liu, *Angew. Chem. Int. Ed*., 2006, **45**, 6896 –6899.

52. S.H. Ng, J. Wang, D. Wexler, S.Y. Chew, H.K. Liu, *J. Phys. Chem. C*, 2007, **111**, 11131-11138.

53. R. Ruffo, S.S. Hong, C.K. Chan, R.A. Huggins, Y. Cui, *J. Phys. Chem. C***,** 2009, **113***,* 11390–11398.

54. Y.J. Cho, H.S. Kim, H. Im, Y. Myung, G.B. Bok Jung, C.W. Lee, J. Park, M.H. Park, J. Cho, H.S. Kang, *J. Phys. Chem. C*, 2011, **115**, 9451–9457.

55. L.Y. Beaulieu, K.C. Hewitt, R.L. Turner, A. Bonakdarpour, A.A. Abdo, L. Christensen, K.W. Eberman, L.J. Krause, J.R. Dahn, J. Electrochem. Soc., 2003, **150 (2)**, A149-A156.

56. S.W. Lee, M.T. McDowell, L.A. Berla, W.D. Nix, Y. Cui, *PNAS*, 2012, **109(11)**, 4080–4085.

57. S.W. Lee, M.T. McDowell, J.W. Choi, Y. Cui, *Nano Lett.*, 2011, **11**, 3034–3039.

58. J.-I. Lee, J.-H., Park, S. Lee, S. Park, *Phys. Chem. Chem. Phys.*, 2013, **15**, 7045-7049.

59. N. Liu, Z. Lu, J. Zhao, M. T. McDowell, H.-W. Lee, W. Zhao, Y. Cui, *Nature nanotechnology*, 2014, 9, 187-92.

60. H, Wu, G, Yu, L, Pan, N, Liu, M. T. McDowell, Z, Bao,Y, Cui, Nature Comm. 2014, 4, 1943.

61. M. Ge,Y. Lu, P. Ercius, J. Rong, X. Fang, M. Mecklenburg, C. Zhou, Nano Lett., 2014, 14, 261−268.

62. L. Yue, H. Zhong, D. Tang, L. Zhang, *J Solid State Electrochem*., 2013, **17**, 961–968.

63. M. Ge, J. Rong, X. Fang, A. Zhang, Y. Lu, C. Zhou, *Nano Research,* 2013, **6(3)**, 174–181.

64. M. Ge, X. Fang, J. Rong, C. Zhou, *Nanotechnologyy*, 2013, **24**, 422001.

65. Y. Zhao, X. Liu, H. Li, T. Zhai, H. Zhou, *Chem. Commun.*, 2012, **48**, 5079–5081.

66. D. Munaò, M. Valvo, J.V. Erven, E.M. Kelder, J. Hassoun, S. Panero, *J. Mater. Chem.*, 2012, **22**, 1556-1561.

67. W. Wang, M.K. Datta, P.N. Kumta, *J. Mater. Chem.*, 2007, **17**, 3229-3237.

68. J. Guo, A. Sun, X. Chen, C. Wang, A. Manivannan, *Electrochimica Acta*, 2011, **56**, 3981–3987.

69. S. Ohara, J. J. Suzuki, K. Sekine and T. Takamura, *Electrochemistry*, 2003, **71**, 1126–1128.

70. H. Jung, W. L. Yoon, H. Lee, J. S. Park, J. S. Shin, H. La and J. D. Lee, *J. Power Sources*, 2003, **124**, 76–80.

71. C. Yu, X. Li, T. Ma, J. Rong, R. Zhang, J. Shaffer, Y. An, Q. Liu, B. Wei, H. Jiang, *Adv. Energy Mater.*, 2012, **2**, 68-73.

72. P. R. Abel, Y.-M. Lin, H. Celio, A. Heller, C. B. Mullins, *ACS Nano*, 2012, **6 (3)**, 2506–2516.

73. T. D. Bogart, D. Oka, X. Lu, M. Gu, C. Wang, B. A. Korgel, *ACS Nano*, 2014, **8 (1)**, 915–922.

74. J.-H. Cho, S.T. Picraux, *Nano Lett.*, 2013, **13 (11)**, 5740–5747.

75. E. L. Memarzadeh, W. P. Kalisvaart, A. Kohandehghan, B. Zahiri, C. M. B. Holt and D. Mitlin, *J. Mater. Chem*., 2012, 22, 6655.

76. A. Kohandehghan, W.P. Kalisvaart, M. Kupsta, B. Zahiri, B. Shalchi Amirkhiz, Z. Li, E.L. Memarzadeh, L.A. Bendersky, D. Mitlin, *J. Mater. Chem. A*, 2013, 1, 1600.

77. E. Memarzadeh Lotfabad, P.Kalisvaart, K. Cui, A. Kohandehghan, M. Kupsta, B. Olsen, and D. Mitlin, *Phys. Chem. Chem. Phys.*, 2013, **15**, 13646-13657.

78. A. Kohandehghan, P. Kalisvaart, K. Cui, M. Kupsta, E. Memarzadeh Lotfabad, and D. Mitlin, *J. Mater. Chem. A*, 2013, **1**, 12850-12861.

79. Z. Wen, G. Lu, S. Mao, H. Kim, S. Cui, K. Yu, X. Huang, P. T. Hurley, O. Mao, J. Chen, Electrochem. Commun., 2013, 29, 67–70.

80. H. Wu, G. Chan, J. W. Choi, I. Ryu, Y. Yao, M. T.McDowell, S. W. Lee, A. Jackson, Y. Yang, L. Hu, and Y. Cui, *Nature Nanotechnology*, 2012, **7**, 310-315.

81. M-H Park, M. G. Kim, J. Joo, K. Kim, J. Kim, S. Ahn, Y. Cui, and J. Cho, *Nano Lett.*, 2009, **9(11)**, 3844-3847.

82. T. Song, J. Xia, J.-H. Lee, D. H. Lee, M.-S. Kwon, J.-M. Choi, J. Wu, S. K. Doo, H. Chang,

83. W. I. Park, D. S. Zang, H. Kim, Y. Huang, K.-C. Hwang, J. A. Rogers, and U. Paik, *Nano Lett.*, 2010, **10**, 1710.

84. E. Memarzadeh Lotfabad, P. Kalisvaart, A. Kohandehghan, K. Cui, M. Kupsta, B. Farbod, D. Mitlin, *J. Mater. Chem. A*, 2014, **2**, 2504-2516.

85. R. Huang, J. Zhu, J. Mater. Chem. Phys., **2010**, 121, 519–522.

86. M. Holzapfel, H. Buqa, L.J. Hardwick, M. Hahn, A. Würsig, W. Scheifele, P. Novák, R. Kötz, C. Veit, F.M. Petrat, *Electrochimica Acta*, 2006, **52**, 973–978.

87. Y. Wang, G. Cao, *Adv. Mater.*, 2008, **20**, 2251–2269.

88. A. S. Arico, P. Bruce, B. Scrosati, J.-M. Tarascon and W. van Schalkwijk, *Nat. Mater.*, 2005, **4**, 366–377.

89. H. Li, Z. Wang, L. Chen and X. Huang, *Adv. Mater.*, 2009, **21**, 4593– 4607.

90. K. E. Aifantis and S. A. Hackney, *Nanostruct. Mater. Electrochem.*, 2008, 319–347.

91. Y. Kim, H. Hwang, C. S. Yoon, M. G. Kim and J. Cho, *Adv. Mater.*, 2007, **19**, 92.

92. G. Derrien, J. Hassoun, S. Panero and B. Scrosati, *Adv. Mater.*, 2007, **19**, 2336.

93. C. K. Chan , R. N. Patel , M. J. O'Connell , B. A. Korgel , Y. Cui , *A CS Nano,* 2010 , **4**, 1443 .

94. H. Kim, J. Cho , *N ano Lett.* 2008, **8**, 3688.

95. L.-F. Cui , Y. Yang , C.-M. Hsu , Y. Cui , *Nano Lett.* 2009, **9**, 3370.

96. S. Barth, F. Hernandez-Ramirez, J. D. Holmes, A. Romano-Rodriguez, *Prog. Mater. Sci.* 2010, **55**, 563.

97. R. S. Wagner, W. C. Ellis, *A ppl. Phys. Lett.,* 1964, **4**, 89.

98. A. M. Morales, C. M. Lieber, *S cience,* 1998, **279**, 208.

99. B. M. Kayes , M. A. Filler , M. C. Putnam , M. D. Kelzenberg , N. S. Lewis , H. A. Atwater, *Appl. Phys. Lett.,* 2007, **91**, 103110

100. E. C. Garnett, W. Liang, P. Yang, *A dv. Mater.,* 2007, **19**, 2946.

101. V. A. Nebol'sin, A. A. Shchetinin, A. A. Dolgachev, V. V. Korneeva, *Inorg. Mater.* 2005, **41**, 1256.

102. Y. Wu , Y. Cui , L. Huynh , C. J. Barrelet , D. C. Bell , C. M. Lieber , *Nano Lett.,* 2004, **4**, 433.

103. T. Baron, M. Gordon, F. Dhalluin, C. Ternon, P. Ferret, P. Gentile, *Appl. Phys. Lett.,* 2006, **89**, 233111/1 .

104. E. Pollak , G. Salitra , V. Baranchugov , D. Aurbach , *J. Phys. Chem. C,* 2007, **111**, 11437 .

105. S.-H. Ng, J. Wang, D. Wexler, K. Konstantinov, Z.-P. Guo, H.-K. Liu, *Angew. Chem. Int. Ed.* 2006, **45**, 6896.

106. X. Chen , C. Li , M. Gratzel , R. Kostecki , S. S. Mao , *Chem. Soc. Rev.,* 2012, **41**, 7909.

107. H. Wu, Y. Cui, *Nano Today,* 2012, **7**, 414.

108. H.-X. Chen, Z.-X. Dong, Y.-P. Fu, Y. Yang, *J. Solid State Electrochem.,* 2010, **14**, 1829.

109. H. Chen, Y. Xiao, L. Wang, Y. Yang, *J. Power Sources,* 2011, **196**, 6657.

110. Y. Yao, N. Liu, M. T. McDowell, M. Pasta, Y. Cui, *Energy Environ. Sci.,* 2012, **5**, 7927.

111. X. Xiao, P. Lu, and D. Ahn, *Adv. Mater.*, 2011, **23**, 3911–3915.

112. Y. He, X. Yu, Y. Wang, H. Li and X. Huang, *Adv. Mater.*, 2011, **23**, 4938–4941.

113. H. T. Nguyen, M. R. Zamifir, L. D. Duong, Y. H. Lee, P. Bondavalli, and D. Pribat, *J. Mater. Chem.*, 2012, **22**, 24618.

114. X. Meng, X. Q. Yang and X. Sun, *Adv. Mater.*, 2012, **24**, 3589-615.

115. B. E. Kim, S. E. Park, J. C. Lim, and Joong Kee Lee, *Phys. Scr.*, 2010, **T139**, 014021.

116. S. K. Cheah, E. Perre, M. Rooth, M. Fondell, A. Hårsta, L. Nyholm, M. Boman, T. Gustafsson, J. Lu, P. Simon, and K. Edström, *Nano Lett.*, 2009, **9(9)**, 3230-3233.

117. G. Jeong, J.-H. Kim, Y.-U. Kim and Y.-J. Kim, *J. Mater. Chem.*, 2012, **22**, 7999.

118. X. Li, X. Meng, J. Liu, D. Geng, Y. Zhang, M. N. Banis , Y. Li , J. Yang, R. Li , X. Sun, M. Cai , M. W. Verbrugge, *Adv. Funct. Mater.* 2012, **22**, 1647–1654.

119. Y. Hwa, W-S. Kim, B-C. Yu, HS. Kim, S-H. Hong, and H-J. Sohn, *J. Mater. Chem. A*, 2013, **1**, 3733.

120. U. Kasavajjula, C. Wang , A. J. Appleby , *J. Power Sources,* 2007, **163**, 1003.

121. V. L. Chevrier, J. R. Dahn, *J. Electrochem. Soc.,* 2009, **156**, A454.

122. S. Cuenot, C. Fretigny, S. Demoustier-Champagne, B. Nysten, *Phys. Rev. B: Condens. Matter,* 2004, **69**, 165410.

123. S. T. Boles, A. Sedlmayr, O. Kraft, R. Moenig, *Appl. Phys. Lett.,* 2012, **100**, 243901.

124. R. Deshpande, Y.-T. Cheng, M. W. Verbrugge, *J. Power Sources,* 2010, **195**, 5081.

125. I. Ryu, J. W. Choi, Y. Cui, W. D. Nix, *J. Mech. Phys. Solids,* 2011, **59**, 1717.

126. M. T. McDowell, S. W. Lee, I. Ryu, H. Wu, W. D. Nix, J. W. Choi, Y. Cui, *Nano Lett.* 2011, **11**, 4018.

127. Q. Zhang, W. Zhang, W. Wan, Y. Cui, E. Wang, *Nano Lett.,* 2010, **10**, 3243.

128. X. H. Liu, H. Zheng, L. Zhong, S. Huang, K. Karki, L. Q. Zhang, Y. Liu , A. Kushima, W. T. Liang, J. W. Wang, J.-H. Cho, E. Epstein, S. A. Dayeh, S. T. Picraux, T. Zhu, J. Li, J. P. Sullivan, J. Cumings, C. Wang, S. X. Mao, Z. Z. Ye, S. Zhang, J. Y. Huang , *Nano Lett.,* 2011, **11**, 3312.

129. T. Song, H. Cheng, H. Choi, J.-H. Lee, H. Han, D. H. Lee, D. S. Yoo, M.-S. Kwon, J.-M. Choi, S. G. Doo, H. Chang, J. Xiao, Y. Huang, W. I. Park, Y.-C. Chung, H. Kim, J. A. Rogers, U. Paik, *ACS Nano,* 2012, **6**, 303.

130. J. Rong, X. Fang, M. Ge, H. Chen, J. Xu, C. Zhou, *Nano Res.,* 2013, **6**, 182.

131. Q. L. Wu, J. Li, R. D. Deshpande, N. Subramanian, S. E. Rankin, F. Yang, Y.-T. Cheng, *J. Phys. Chem. C,* 2012, **116**, 18669.

132. C.-X. Zu, H. Li, *Energy Environ. Sci.*, 2011, **4**, 2614–2624.

133. V. Palomares, P. Serras, I. Villaluenga, K. B. Hueso, J. Carretero-Gonzalez, T. Rojo, *Energy Environ. Sci.*, 2012, **5**, 5884–5901.

134. B. L. Ellis and L. F. Nazar, Curr. *Opin. Solid State Mater. Sci.*, 2012, **16**, 168–177.

135. S. W. Kim, D. H. Seo, X. H. Ma, G. Ceder and K. Kang, *Adv. Energy Mater.*, 2012, **2**, 710–721.

136. M. D. Slater, D. Kim, E. Lee and C. S. Johnson, *Adv. Funct. Mater.*, 2013, **23**, 947–958.

137. H. Pan, Y.-S. Hu, L. Chen, *Energy Environ. Sci.*, 2013, **6**, 2338.

138. V. Palomares, M. Casas-Cabanas, E. Castillo-Mart´ınez, M. H. Hanb, T. Rojo, *Energy Environ. Sci.*, 2013, **6**, 2312.

139. K. Mizushima, P. C. Jones, P. J. Wiseman, J. B. Goodenough, *Mater. Res. Bull.*, 1980, **15**, 783–789.

140. A. S. Nagelberg and W. L. Worrell, *J. Solid State Chem.*, 1979, **29**, 345–354.

141. J. P. Parant, R. Olazcuag, M. Devalett, C. Fouassie and P. Hagenmul, *J. Solid State Chem.*, 1971, **3**, 1–5.

142. J. J. Braconnier, C. Delmas, C. Fouassier and P. Hagenmuller, *Mater. Res. Bull.*, 1980, **15**, 1797–1804.

143. M. S. Whittingham, Prog. Solid State Chem., 1978, **12**, 41–99.

144. C.M. Park, J.H. Kim, H. Kim, H.J. Sohn, Li-alloy based anode materials for Li secondary batteries. *Chem. Soc. Rev.,* 2010, **39**, 3115-3141.

145. C. Liu, F. Li, L.P. Ma, H.M. Cheng, Advanced Materials for Energy Storage. *Adv. Mater.,* 2010, **22**, E28.

146. C.D. Wessells, S.V. Peddada, R.A. Huggins, Y. Cui, Nickel Hexacyanoferrate Nanoparticle Electrodes For Aqueous Sodium and Potassium Ion Batteries. *NanoLett.*, 2011, **11**, 5421.

147. S. Tepavcevic, H. Xiong, V.R. Stamenkovic, X. Zuo, M. Balasubramanian, V.B. Prakapenka, C.S. Johnson, T. Rajh, Nanostructured Bilayered Vanadium Oxide Electrodes for Rechargeable Sodium-Ion Batteries. *ACS Nano,* 2012, **6**, 530.

148. J. Qian, M. Zhou, Y. Cao, X. Ai, H. Yang, Nanosized $Na_4Fe(CN)_6$/C Composite as a Low-Cost and High-Rate Cathode Material for Sodium-Ion Batteries. *Adv. Energy Mater.*, **2012**, *2*, 410.

149. P. Ge, M. Fouletier, Electrochemical intercalation of sodium in graphite. *Solid State Ionics*, 1988, **28–30**, 1172-1175.

150. D.A. Stevens, J.R. Dahn, The Mechanisms of Lithium and Sodium Insertion in Carbon Materials. *J. Electrochem. Soc.*, 2001, **148**, A803-A811.

151. M. M. Doeff, Y. P. Ma, S. J. Visco, L. C. Dejonghe, *J. Electrochem. Soc.*, 1993, **140**, L169–L170.

152. D. A. Stevens, J. R. Dahn, *J. Electrochem. Soc.*, 2000, **147**, 1271–1273.

153. S. Wenzel, T. Hara, J. Janek, P. Adelhelm, *Energy Environ. Sci.*, 2011, **4**, 3342–3345.

154. K. Tang, L. J. Fu, R. J. White, L. H. Yu, M. M. Titirici, M. Antonietti, J. Maier, *Adv. Energy Mater.*, 2012, **2**, 873–877.

155. Y. L. Cao, L. F. Xiao, M. L. Sushko, W. Wang, B. Schwenzer, J. Xiao, Z. M. Nie, L. V. Saraf, Z. G. Yang, J. Liu, *Nano Lett.*, 2012, **12**, 3783–3787.

156. S. Komaba, W. Murata, T. Ishikawa, N. Yabuuchi, T. Ozeki, T. Nakayama, A. Ogata, K. Gotoh and K. Fujiwara, *Adv. Funct. Mater.*, 2011, **21**, 3859–3867.

157. Y.-X. Wang, S.-L. Chou, H.-K. Liu, S.-X. Dou, *Carbon*, 2013, **57**, 202–208.

158. Z. Wang, L. Qie, L. Yuan, W. Zhang, X. Hu, Y. Huang, *Carbon*, 2013, **55**, 328–334.

159. H. Wang, Z. Wu, F. Meng, D. Ma, X. Huang, L. Wang, X. Zhang, *ChemSusChem*, 2013, **6**, 56–60.

160. X. Zhou, Y.-G. Guo, *ChemElectroChem*. 2014, **1**, 83–86.

161. J. Ding, H. Wang, Z. Li, A. Kohandehghan, K. Cui, Z. Xu, B. Zahiri, X. Tan, E. Memarzadeh Lotfabad, B.C. Olsen, D. Mitlin, *ACS Nano*, 2013, **7 (12)**, 11004–11015.

2 Silicon Nanowire Core Aluminum Shell Coaxial Nanocomposites for Lithium Ion Battery Anodes Grown with and without a TiN Interlayer

Material in this chapter has been published in:

E.L. Memarzadeh, W.P. Kalisvaart, A. Koandehghan, B. Zahiri, C.M.B. Holt, D. Mitlin, *J. Mater. Chem.*, 2012, **22**, 6655-6668.

2.1 Introduction

Rechargeable lithium-ion batteries are the primary energy storage devices for a wide variety of applications, such as communication, transportation and renewable-energy sectors due to their high energy density and long cycle life. Consequently the field is attracting a great deal of exciting activity in furthering the understanding of emerging electrode materials and of their reactions with the electrolyte, e.g. [1-7]. Due to their low cost, low discharge potential and the second highest known theoretical capacity of about 3590 mAh/g after Li (3862 mAh/g), corresponding to $Li_{15}Si_4$, silicon-based materials for lithium-ion battery anodes are attracting sustained scientific attention [8-11]. However, large and anisotropic volume change (>300%) during lithium insertion and extraction leads to material pulverization along with electrical disconnection from the current collector [12-16]. The short cycle life of Si – based electrodes thus limits their practical applicability.

Many efforts have been made in recent years to improve the cycling stability. These include decreasing the dimensions of the active structures to the nanoscale using thin films [17, 18], nanoparticles [15, 19, 20], nanotubes [21, 22], or imbedding silicon nanoparticles in an inactive or active matrix [23-26]. Nanosized silicon-based anodes can accommodate the large volume change without structural degradation during the lithiation and delithiation process, resulting in an improved cycle life [27-29]. Of all shapes and forms in which silicon has been tested as a Li-ion battery anode, silicon nanowires anchored to a conductive substrate have demonstrated the largest capacity (~3000 mAh/g), as the need for additional conductive phases such as carbon which subtract from the net capacity of the system, is eliminated [30-33]. Very often, the growth substrate is a stainless steel substrate used for battery coin cell anodes [33-35]. There is always layer of chromium oxide on the surface of any stainless steel, its thickness ranging from several nanometers in the as-received state, to several microns when exposed over several hours to elevated temperatures in a water vapour containing atmosphere [36]. Previously researchers have utilized this fact to actually create in-situ conversion electrodes out of Cr_2O_3 layers present on oxidized stainless steel according to the reaction $Cr_2O_3 + 6Li \rightarrow 3Li_2O + 2\ Cr$ [37-39]. Therefore, a question remains whether lithiation/delithiation of residual oxide influences the performance of the nanowires sitting on its surface. Since the process is a conversion reaction with significant associated volume changes and the formation of new phases, one would expect for there to be an effect [38, 39]. This could be a potential way for SiNWs to get detached from the stainless steel substrate.

A recent in-situ TEM study demonstrated that charging of SnO_2 nanowires coated with carbon, aluminum, or copper could be carried out at an order of magnitude higher rate as compared with uncoated wires. In addition, during the initial lithiation cycle, the coatings mechanically confined the nanowires, fundamentally altering the accompanying expansion in favor of the longitudinal direction rather than radial [40]. Metallic coating with Cu improved capacity retention during cycling as well as the charge transfer kinetics for SiNWs [34]. However, Cu is an inactive material towards Li, which means it will detract from the storage capacity. 5 wt.% carbon coating improves cycling stability considerably, but the maximum storage capacity (372 mAh/g) is dwarfed by that of Si and thus makes no noticeable contribution to the total capacity [41]. An active Al layer, on the other hand, stores Li and contributes to the capacity in addition to placing the nanowires under compressive stress. That may suppress or at least reduce its pulverization of SiNWs during cycling. An additional advantage of an Al coating is that it serves as a barrier layer between the silicon and the electrolyte. In the case of pure Si, the continuing exposure of fresh material to the electrolyte during lithiation/delithiation would cause a progressively thickening solid electrolyte interphase (SEI) layer to form. This is accompanied by an irreversible consumption of both lithium and silicon and an increasing interfacial resistance. Both Si and its native oxide film are vulnerable to HF derived from $LiPF_6$ in the presence of trace moisture, which converts Si into electrochemically-inactive SiF_6^{2-} and results in capacity loss [42]. A study on three-dimensional macroporous silicon authors obtained improved capacity and capacity retention when the structures were coated by silver nanoparticles [43]. Coating the nanowires with a ductile and adherent Al layer may reduce this effect, though SEI formation on Al is not well understood.

The purpose of this study is to explore two effects: the role of the underlying substrate and of the Al coating on the cycling performance of silicon nanowires. We present a comprehensive microstructural characterization – based study where we examine factors like initial capacity loss and extended cycling stability. We utilize nanowires grown on TiN interlayers and compare them with nanowires grown on bare, but otherwise identically prepared stainless steel supports, as well as nanowires coated with 1-19 wt.% Al. Our findings point to the importance of the average size and size distribution in the nanowire diameters in limiting capacity loss and achieving high coulombic efficiency in the first cycle. We also show that there is a specific weight percentage where an Al coating significantly improves the cycling capacity retention of the nanowires. A mechanistic explanation of both phenomena is proposed.

2.2 Experimental

Commercial 316 L stainless steel spacers (MTI Technologies) that were polished down to Ra<50 nm using SiC paper and Alumina slurry and dried before deposition were used as support for the SiNW electrodes. Typically, Cu foil is used as the current collector for the anode in commercial batteries. However, growing SiNWs directly on Cu foil is not possible due to 1) the high reactivity of Au with Cu and 2) the high reactivity of SiH_4 with the Cu to form copper silicides. Therefore, the SiNWs growth substrate is usually a stainless steel substrate. Two 'bare' NW samples were compared to investigate the influence of the substrate: one where the Au catalyst was deposited directly onto the stainless steel and one where an interlayer of TiN was utilized. A second set of samples, which were the ones utilized for the Al coating studies, had a TiN interlayer between the stainless steel and the Au catalyst particles. The stack actually consisted of 50 nm of Ti as an adhesive layer followed by 150 nm of TiN as a conductive diffusion barrier. A 10 nm-thick Au film was utilized as the nanowire growth catalyst on TiN. On stainless steel, 50 nm Au had to be used, analogous to Chan et al. [33], in order to get sufficient NW growth, because of fast penetration of Au-containing melts into stainless steel [44]. The films were deposited using a magnetron sputtering system (AJA International Inc.). We used Ar gas with a purity of grade 5 at a sputtering pressure of $5x10^{-3}$ mbar, with a maximum base pressure of $5x10^{-8}$ mbar. The rates of deposition for Ti and Au were 0.47 and 0.38 Å/sec. The reactive sputter deposition of the TiN layer was done at DC power of 150 W and Ar pressure of 4 mTorr in a mixture of Ar and N_2 with a flow ratio of (20:1) at 250 °C. Depositions were done in a sputter-up configuration with continuous substrate rotation. Film thickness and deposition rates were obtained through the use of crystal deposition rate monitor held at the substrate plane. A separate series of experiments involving ex-situ film thickness measurements versus deposition parameters were used to cross check the thickness/rate accuracy for TiN.

A commercial Tystar CVD furnace was utilized for nanowire growth. A mixed SiH_4 and H_2 environment with SiH_4:H_2 ratio of 1:4 was utilized as the working gas. The samples were annealed under vacuum for 30 min at 525 °C just prior to growth. A chamber pressure of 100 Torr was then used along with a 2 minute growth time. For the bare SS supports, the annealing and growth temperatures were 485 °C. The total chamber pressure was 40 Torr and the growth time was 10 minutes. One would not expect the Cr_2O_3 to be reduced by the H_2 present during the Si NW growth process due to its very high thermodynamic stability {$2Cr(s) + 3H_2O(g) => Cr_2O_3(s) + 3H_2(g)$, $\Delta G° = -298.5$ kJ/mol }[36]. A slightly lower temperature and working pressure had to be used for growing the Si NWs on bare SS versus on TiN. This was done to achieve roughly the same mass loading in each case. The mass of the nanowires was about 0.33 mg, which was calculated by measuring the mass of the substrate using a microbalance (Mettler Toledo, 1µg resolution) before and after growth.

For the TiN samples an Al coating was then sputter deposited at a rate of 0.2 Å/sec onto the as-grown nanowires. The substrate was held at nominally ambient temperature. The thicknesses of the films when deposited on a planar support were 5, 10, 50, 100 and 150 nanometers. Based on the measured weight of Si and calculated mass loading of Al in each case, the nanocomposites can be addressed with weight percentage of Al. Accordingly, 5, 10, 50, 100 and 150 nm sputtered Al contain the weight percentage of 1, 3, 8, 13 and 19 wt.% Al, respectively. Because of shadowing, the Al flux did not cover the nanowires completely, and depositions corresponding to larger geometric thicknesses penetrated further down to the nanowire base. The maximum coating thickness observed by transmission electron microscopy was ~50 nm for the 13 wt.% sample, but to avoid any ambiguities we will refer to the weight percentage of Al rather than the geometrical or measured layer thickness for the remainder of the manuscript.

For the remainder of the manuscript the aforementioned specimens will be referred to as SiNWs/SS, i.e. silicon nanowires on stainless steel support; SiNWs/TiN, i.e. bare Si nanowires on titanium nitride on stainless steel; and xAl/SiNWs, i.e. x weight percentage of Al coating on the silicon nanowires on TiN on stainless steel.

Standard 2032 button half-cells were fabricated using Li metal foils as the counter electrodes, and Polyethene (MTI technologies) separator (porosity of 36-44% and mainly 0.03 μm pore size) which was soaked in electrolyte. The electrolyte was 1.0 M $LiPF_6$ in 1:1:1 (volume ratio) ethylene carbonate:dimethyl carbonate:diethyl carbonate (EC/DMC/DEC). The cells were assembled inside an Ar-filled glovebox. Cyclic voltammetry (CV) was performed on a Versa STAT 3 potentiostat using 1 mV/s scan rate in the potential range from 0.01 to 2 V (vs. Li/Li^+). Galvanostatic discharge/charge cycling was carried out on a computer controlled BT2000 Arbin potentiostat in the voltage range of 0.01 to 2 V (vs. Li/Li^+). A constant current density was used for discharge/charge experiments. The ac impedance of the half-cell electrodes was measured using Versa STAT3 frequency response analyzer (FRA) over a frequency range of 0.01 Hz to 1 MHz with an amplitude of 10 mV. After cycling, the coin cells were disassembled and the samples were rinsed with acetonitrile thoroughly and kept overnight in the glove box to remove the excess electrolyte. The as-prepared and cycled samples were characterized using scanning electron microscopy (SEM) (Hitachi S-4800) and transmission electron microscopy (TEM) (JEOL 2010, 200 kV). SiNWs/SS was characterized by X-ray diffraction (XRD) analysis on a Bruker Discover 8 diffractometer using Cu-K_α radiation in order to investigate the reactivity of the SiNWs with the substrate.

2.3 Results and Discussion

Figures 2.1(a) and 2.1(b) show representative SEM micrographs of SiNWs/SS as well as SiNWs/TiN. As compared to SiNWs/TiN, the SiNWs/SS are quite non-uniform in their geometries and dimensions. The SiNWs/SS samples also possessed a significant amount of amorphous silicon particles interspersed with the nanowires. Figure 2.1(c) shows a cross-sectional view of the SiNWs/TiN. The tallest nanowires are over 10 μm in length and have grown over a large range of angles with the substrate. The size (= diameter) distribution histogram shown in Figure 2.1(d) highlights the much narrower size distribution for the SiNWs/TiN case. The mean nanowire diameter for SiNWs/SS was 100 nm, while the mean diameter for SiNWs/TiN was 105 nm. However as can be seen from the histograms the size distributions are quite different for the two supports. For the case of the SiNWs/SS there are many finer nanowires in addition to very coarse, really micron-scale ones.

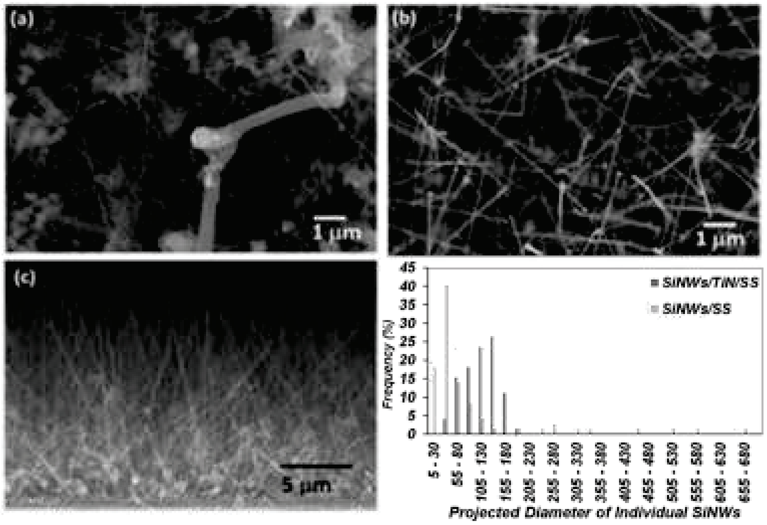

Figure 2.1: SEM image of the (a) SiNWs/SS, (b) SiNWs/TiN, (c) cross-sectional view of SiNWs/TiN, (d) histogram of the projected diameters of the individual Si NWs on TiN and on SS substrates.

The small Au droplets for growing the SiNWs as a catalyst are observed at the top of the nanowires. Figure 2.2 illustrates SEM images of a SiNW/TiN and aluminum-coated nanowires. Pristine SiNW reveals smooth surface, while the micrographs of coated samples indicate bumpy surface on the SiNWs. The morphology of the nanowires demonstrates that SiNWs are indeed coated by a thin Al layer. It can be seen in Figure 2.2(b) that the 1% Al coating layer is not continuous on the surface of the SiNWs and forms separated islands since it is too thin to form a continuous layer all around the nanowires. The Al coating layers become continuous by increasing the Al weight percentage as evident from Figure 2.2(c-e). The surface of the NWs becomes rougher with increasing Al thickness, which reflects an increase in the average grain size.[45]

TEM images of the SiNW/TiN, 3Al/SiNW and 13Al/SiNW are shown in Figure 2.3. Figure 2.3(a) shows the bright field micrograph of as-prepared SiNWs. Simulation of the selected area diffraction (SAD) pattern indicates that the SiNW is close the [112] zone axis of Si. The SiNW shown in Figure 2.3(b) is imaged using the g=111 reflection. According to HRTEM in Figure 2.3(c), exposure to air after the growth leads to the formation of less than 5 nm SiO_2 on the surface of the SiNWs. Figures 2.3(d-f) show the TEM images of the 1Al/SiNWs. The spots observed in the SAD pattern are due to the Si single crystal. The dark field image is taken from the g=111 Si. The faint continuous ring in the diffraction pattern corresponds to Al. The dark field image in Figure 2.3(f) is imaged using a portion of this ring. As it is evident from this image, Al does not form a continuous layer on the SiNW surface. Figures 2.3(g-l) demonstrate the microstructures of the as prepared 3Al/SiNW and 13Al/SiNWs. The corresponding SAD patterns from both materials consist of spotty and ring patterns. The spots are due to the Si single crystal shown in the dark field micrograph in Figures 2.3(h) and 2.3(k) (taken from the g=111 Si reflection). The simulation of the observed ring pattern indicates that the rings correspond to Al. The dark field images shown in Figure 2.3(i) and 2.3(l) are imaged using a portion the 111 Al ring. It appears that the Al coating is not conformal around all of the SiNWs and the thickness of Al layer is different around each SiNW. This is more pronounced in the 13Al/SiNW (Figure 2.3(g)). It should be noted that the surface of SiNWs is smoother with thinner Al layer, since the grain size is smaller (Figure 2.3(f)), while thicker Al layer has the larger grain size (Figure 2.3(l)) leading to a rougher surface.

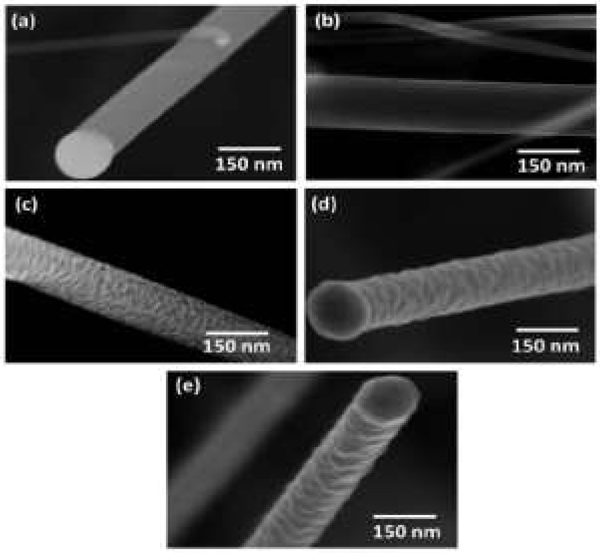

Figure 2.2: SEM images of the (a) SiNWs/TiN, (b) 1Al/SiNWs, (c) 3Al/SiNWs, (d) 8Al/SiNWs, and (e) 13Al/SiNWs.

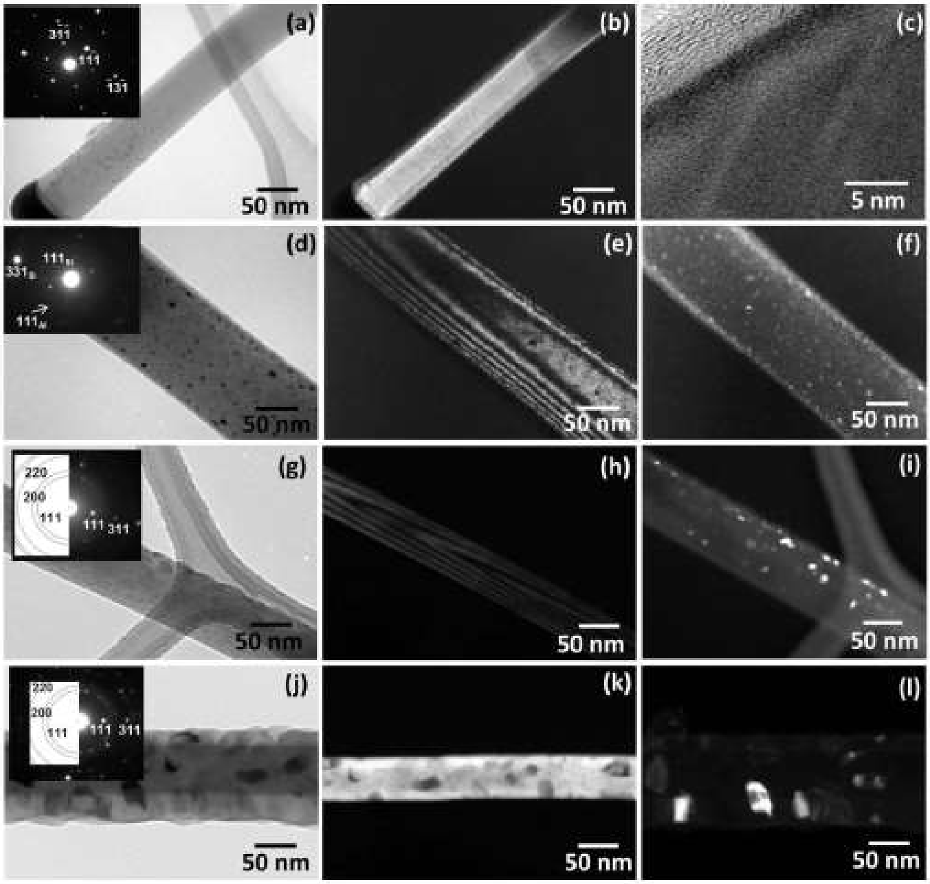

Figure 2.3: TEM micrographs of bare and coated SiNWs. (a)–(c) show TEM micrographs of the SiNW/TiN (a) bright field micrograph with corresponding indexed selected area diffraction (SAD) insert, (b) dark field micrograph, obtained using g ¼ 111Si with the wire oriented near the 112 symmetric zone axis, (c) HRTEM image of the SiNW structure. Fig. 3 (d)–(f) show 1Al/SiNW. (d) Bright field micrograph with corresponding indexed SAD insert, (e) dark field micrograph of the Si obtained using g ¼ 111Si. (f) Dark field micrograph, obtained using a portion the 111Al ring pattern. (g)–(i) show 3Al/SiNW. (g) Bright field micrograph with corresponding indexed composite SAD insert, (h) dark field micrograph of the Si obtained using g ¼ 111Si. (i) Dark field micrograph, obtained using a portion of the 111Al ring pattern, highlighting the nanocrystalline grain size of Al. Fig. 3(j)–(l) show 13Al/SiNW. j) Bright field micrograph with corresponding indexed composite SAD insert, (k) dark field micrograph of the Si obtained using g ¼ 111Si. (l) Dark field micrograph, obtained using a portion of the 111Al ring pattern, highlighting the much coarser albeit still nanocrystalline grain size of Al.

As mentioned before, TiN was used as one of the substrates to grow SiNWs on. Figure 2.4(a) clearly shows that TiN has a very low reactivity with respect to lithium-ion insertion, revealing lower storage capacity by more than an order of magnitude compared to SS (Figure 2.4(b)). Hence, it can protect the SS substrate from reaction with Li. It can be confirmed by the charge/discharge curves, since no distinct plateaus are observed on the charge/discharge curves of TiN. Therefore, the electrochemical charge/discharge response is entirely due to Al/SiNWs composites. For the SS spacer without TiN (Figure 3.4(b)) a sloped plateau centered around 0.9 V and 1.2 V for reduction and oxidation, respectively is observed indicating that the native oxide on SS does indeed reversibly react with Li.

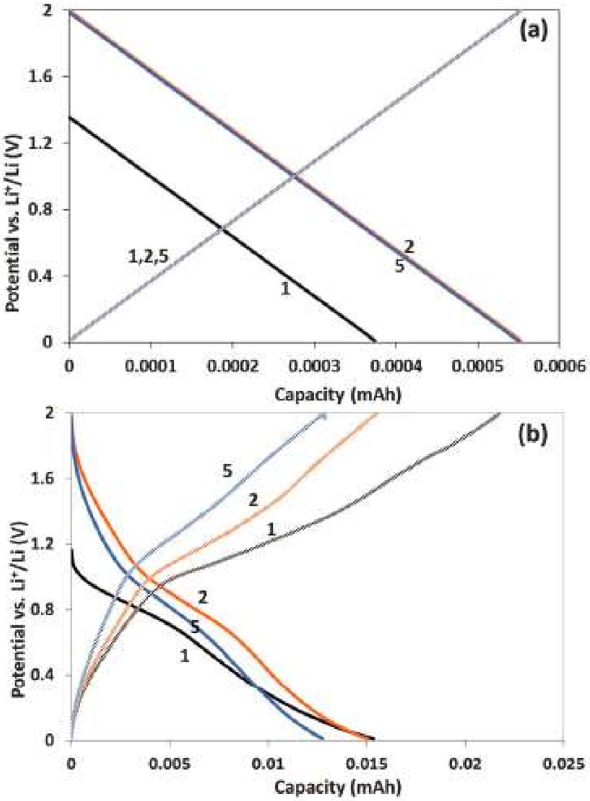

Figure 2.4: Galvanostatic discharge/charge curves of the (a) SS spacer coated with TiN layer and (b) SS spacer without any coating layer.

Figure 2.5 shows the capacity data for the SiNWs/TiN as well as SiNWs/SS cycled between 0.01 to 2 V up to 50 cycles. The first discharge capacity for the SiNWs/SS was 3050 mAh/g, which was lower compared to the SiNWs/TiN (3581 mAh/g). The first coulombic efficiency defined as CE = (delithiathion capacity/lithiation capacity) and the first discharge capacity loss were 84.3% and 14.5% for the SiNWs/SS, whereas they were 93.1% and 4% for the SiNWs/TiN, respectively. The subsequent capacity degradation rate on the other hand, is approximately the same for both SiNWs/TiN and SiNW/SS.

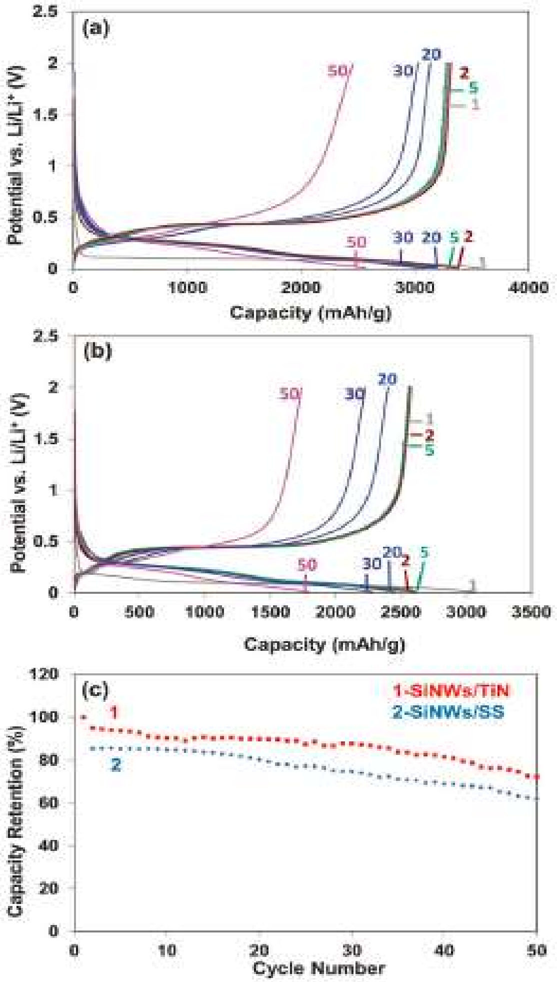

Figure 2.5: Galvanostatic discharge/charge curve of the (a) SiNWs/TiN, (b) SiNWs/SS, and (c) discharge capacity retention of the SiNWs/TiN and SiNWs/SS at 0.1 C rate.

After 50 cycles, the capacity is still ~75% of that in the second cycle. Another difference between SiNWs on TiN and SS is that for the latter, the growth temperature was lower which favors the formation of amorphous Si next to SiNWs. Before the onset of the long plateau at 0.1 V, there is a large, sloping plateau of ~600 mAh/g (see Figure 2.6) which may be related to an amorphous Si fraction that is already present in as-grown SiNWs/SS.

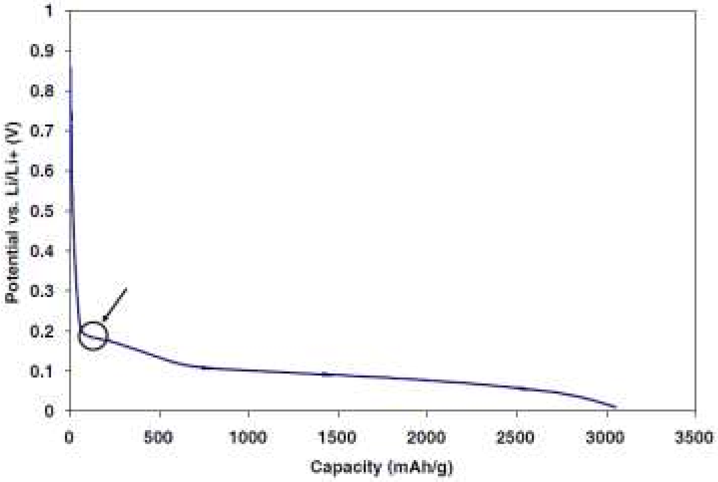

Figure 2.6: First lithiation response of SiNWs/SS highlighting the contribution of amorphous Si.

Figure 2.7 shows the XRD patterns of SiNWs/SS in the as-made condition, after lithiation to 0 V and delithiation to 2 V. For the as-made material, peaks of crystalline Si and the SS substrate are clearly visible. For the Au catalyst used for growing the nanowires, the (111), (200) and (220) reflections are visible at 38.2, 44.4 and 64.5°, respectively. A trace amount of the $FeSi_2$ intermetallic is also present. After lithiation, all Si has transformed to crystalline $Li_{15}Si_4$. Au also forms an intermetallic with Li with the exact same Li-content, $Li_{15}Au_4$, which appears to be amorphous. In fact, it is this reaction of Li with gold that causes the small plateau at ~0.15 V in the delithiation curves of Figure 2.5(b). [33] The $FeSi_2$ phase remains inactive as was also observed in previous studies. [33] After delithiation to 2 V, all Si and Au have become amorphous and only the peaks from $FeSi_2$ and SS remain.

The electrochemical response of the SiNWs/TiN, 3Al/SiNWs, 19Al/SiNWs and pure Al were investigated with cyclic voltammetry (CV) with a scan rate of 1 mV/s. The first ten scans are presented in Figure 2.8. For uncoated Si NWs in Figure 2.8(a), there is a reduction peak starting at a potential of about 0.3 V vs. Li/Li^+, which becomes quite large at about 0.1 V. This peak is associated with the insertion of lithium ion into the Si NWs and the formation of Li_xSi alloys. A double peak response is measured during lithium-ion extraction. This is consistent with previous experiments on micro-structured silicon anodes.[46]

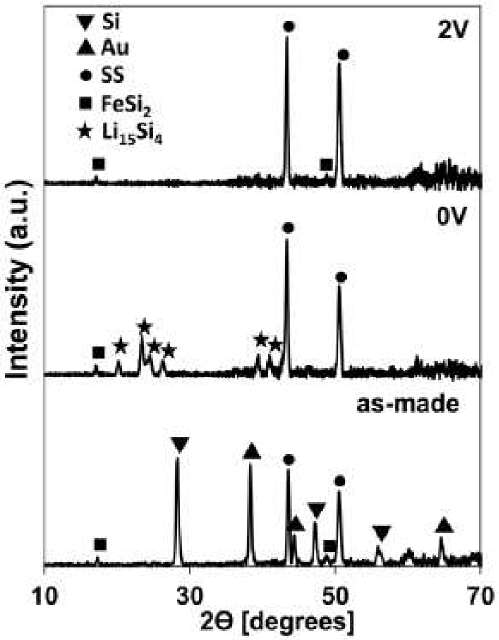

Figure 2.7: XRD patterns of SiNWs/SS in as-made, lithiated and delithiated state.

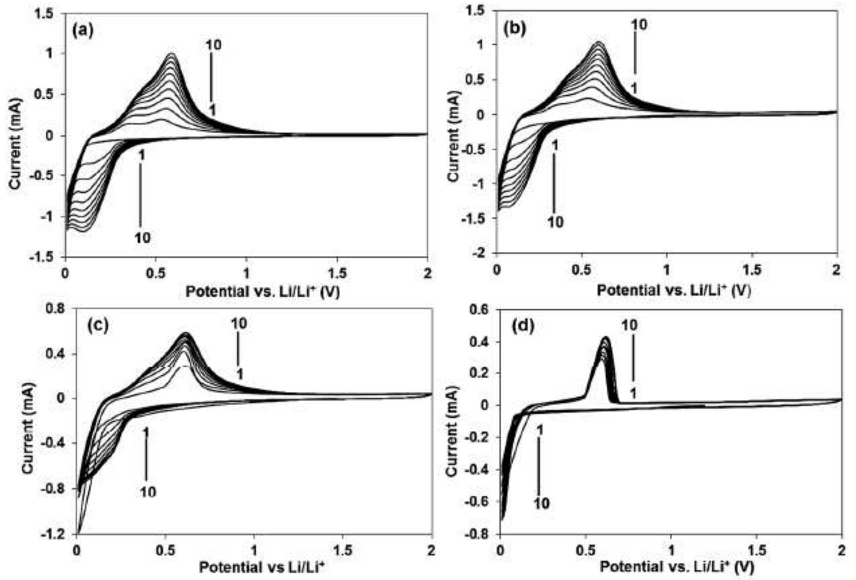

Figure 2.8: Cyclic voltammetry profiles of the (a) SiNWs/TiN, (b) 3Al/SiNWs, (c) 19Al/SiNWs, and (d) 50 nm of pure aluminum on TiN/SS substrate with the scan rate of 1 mVs^{-1}.

For 19Al/SiNWs in Figure 2.8(c), the first peak ascribed to Si at ~0.3 V is completely absent from the first two cycles. This means the large peak at ~0.6 V has to be ascribed to Al for this material. This is supported by the data in Figure 2.8(d), where a pure 50 nm Al film shows its delithiation peak at the same potential around 0.6 V. The CV curves of the 3Al/SiNWs are almost the same as that of the bare SiNWs. Since the amount of Al is only about 0.01 mg for this sample, which is much less than that of the SiNWs (~0.33 mg) and the specific capacity of Al is, at only 993 mAh/g (corresponding to LiAl formation)[47, 48], much lower than that of silicon (3590 mAh/g for the formation of crystalline $Li_{15}Si_4$ phase)[49], the reduction/oxidation peaks related to Al in 3Al/SiNWs will be too small to be distinguished in a CV curve.

The magnitude of the current peaks increases with cycling due to the activation of more materials to react with lithium with each scan. It can also be referred to an improvement of the reaction kinetics during cycling by repeatedly insertion/extraction of lithium ions in which the conductivity may improve as a result of the lithium-doping or changes in geometry.[50]

Galvanostatic charge/discharge experiments of the Al/SiNWs electrode with different Al weight percentages were carried out in the voltage range of 0.01-2 V. Uncoated SiNWs/TiN electrode was also measured for comparison. Figures 2.9(a-f) show the discharge and charge capacity data for the electrodes in order of increasing Al wt%. The curves obtained during the first charge/discharge process for uncoated and coated SiNWs show a long voltage plateau located at around 0.1 V during lithiation, which is indicative of a two-phase region where crystalline silicon is being transformed into an amorphous lithium silicide, Li_xSi. [51,52] This is analogous to the reduction peak observed in the CV experiment of SiNWs/TiN in Figure 2.8(a). The delithiation curves exhibit a single and flat plateau at about 0.4 V, which means that during lithiation the amorphous phase is transformed to crystalline $Li_{15}Si_4$. [51] If crystalline $Li_{15}Si_4$ is not formed during lithiation, there would be two sloping plateaus during the subsequent delithiation process.[53]

The formation of this phase can also be confirmed by the specific capacity observed in the first lithiation process for SiNWs/TiN (Figure 2.9(a)). As could be seen, the first discharge capacity of SiNWs is 3581 mAh/g close to the theoretical capacity of silicon (3590 mAh/g), when crystalline $Li_{15}Si_4$ is formed at full lithiation.[54] The amorphous material exhibits lower specific capacity of around 3000 mAh/g (equivalent to 3.2 Li per Si). [52] Consequently, the delithiation curves show a plateau at about 0.4 V because of the two-phase reaction from crystalline $Li_{15}Si_4$ to amorphous Li_zSi phase, which is then followed by a solid-solution reaction from amorphous Li_zSi to amorphous Si.

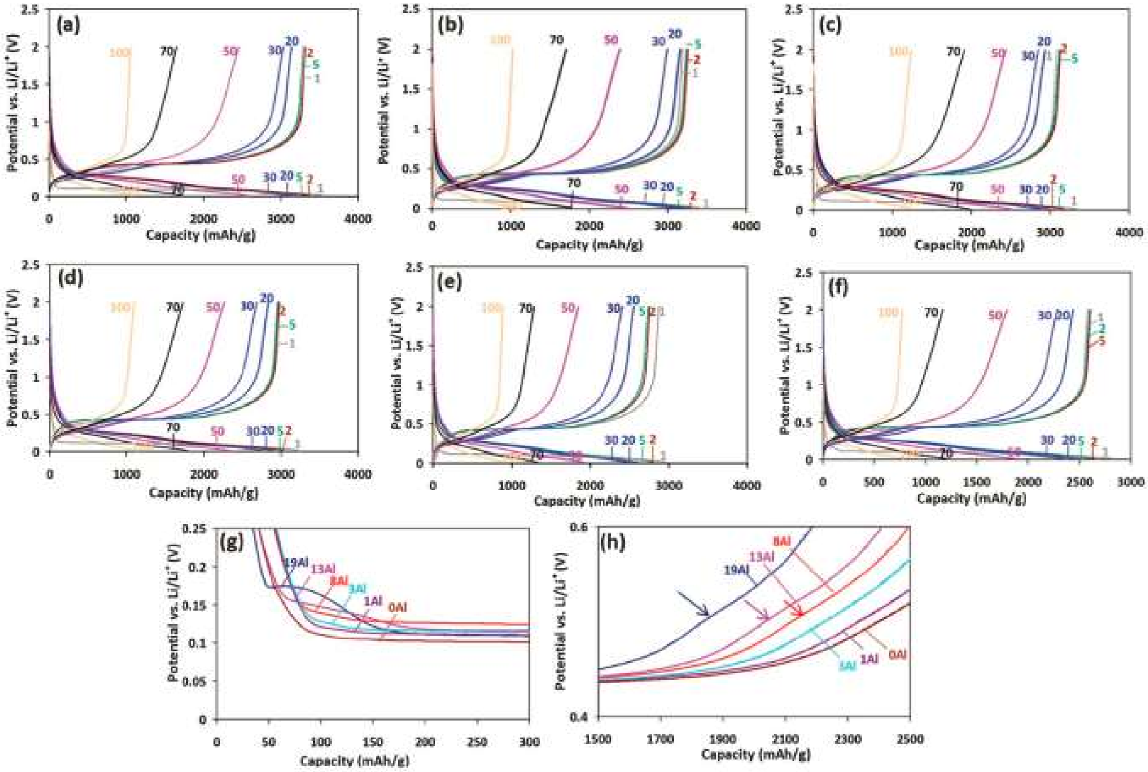

Figure 2.9: Galvanostatic discharge/charge curves of the (a) SiNWs/TiN, (b) 1Al/SiNWs, (c) 3Al/SiNWs, (d) 8Al/SiNWs, (e) 13Al/SiNWs, (f) 19Al/SiNWs, (g) first discharging, and (h) first charging cycle at 0.1 C rate. The contribution of Al to the electrochemical response is highlighted by arrows in Figure 2.9(h).

There is a small plateau in the voltage profile of the Al/SiNWs at around 0.14 V (Figure 2.9(g)), which is most pronounced for the 19Al/SiNWs, which means it corresponds to the lithium insertion into Al. [55] The small magnitude of this plateau compared to the long plateau at 0.1 V confirms the small contribution of Al in electrochemical performance of SiNW electrode. This is in agreement with the CV curves in Figure 2.8. The Al lithiation is much less obvious for the materials with lower Al thickness in Figure 2.9(g) although for 13Al/SiNWs there is still a clear feature in the potential profile between 0.15 and 0.1 V. However, from the delithiation curves the presence of Al is more obvious. Figure 2.9(h) shows a magnification of the first delithiation cycle for all our materials. There is a small sloping plateau at approximately 0.5 V, indicated by the arrows, which diminishes continuously with decreasing Al thickness.

Table 2.1 summarizes the first discharge and charge capacities as well as the coulombic efficiencies of the SiNWs/TiN as well as Al/SiNWs. Compared with the SiNWs/TiN, Al/SiNWs electrodes show a reduced capacity. As mentioned before, lithium insertion in Al leads to the formation of LiAl with a maximum capacity of 993 mAh/g on the first alloying with lithium[47, 56], which is much lower than that of silicon. Of all the materials that were tested, only the SiNWs/SS has a significantly lower coulombic efficiency in the first cycle. It should be noted that the CE in the first cycle is not significantly different between bare SiNWs on TiN and the Al-coated materials and is always between 92 and 94%, which, to the authors' knowledge, are the highest first-cycle efficiencies ever reported. The fact that the presence and also the thickness of the coating do not significantly influence the initial coulombic efficiency is surprising. Previous studies on Cu and carbon-coated SiNWs showed a large influence of the coating and the coulombic efficiency was improved from 69.5 to 90.3% and 83.2%, respectively. [34, 41] Possible reasons for these discrepancies will be discussed later.

Table 2.1: The capacity and coulombic efficiency of the SiNWs/TiN and Al/SiNWs electrodes in the first cycle

Sample	Discharge Capacity (mAh/g)	Charge Capacity (mAh/g)	CE (%)
SiNWs/SS (0.1C rate)	3050	2571	84.3
SiNWs/TiN (0.1C rate)	3581	3307	93.1
1 Al/SiNWs (0.1C rate)	3400	3185	93.6
3 Al/SiNWs (0.1C rate)	3347	3105	92.8
8 Al/SiNWs (0.1C rate)	3239	2982	92.1
13Al/SiNWs (0.1C rate)	2992	2811	93.9
19Al/SiNWs (0.1C rate)	2832	2597	92

Figures 2.10(a) and (b) show the cycle life of SiNWs/TiN and Al/SiNWs at 0.1 C rate. The first discharge capacity loss for both SiNWs/TiN and Al/SiNWs is around 4%. As can be seen, the 3Al/SiNWs and 8Al/SiNWs exhibit better cycling performance compared to the other Al thicknesses as well as the SiNWs/TiN. Both SiNWs/TiN and Al/SiNWs show a stable capacity up to 25 cycles after which it starts to drop with a higher rate for the 1Al/SiNWs as

well as SiNWs/TiN. The 3 wt.% Al coating layer has the best result on the cycling performance of the SiNWs. It gives a stable reversible capacity of approximately 1300 mAh/g after 100 cycles, a capacity retention of about 40%, while the capacity of SiNWs/TiN decays rapidly to 1090 mAh/g after 100 cycles (~30%). The biggest improvement is seen after 75 cycles where the bare and 3 wt.% coated SiNWs show 42% and 55% capacity retention, respectively. Thus, improvement of the cycling stability of SiNWs is observed after coating with Al for a certain range of wt.% Al/coating thicknesses. The 1Al/SiNWs degrades with the same rate that is observed in the SiNWs/TiN. For higher than 8wt.%Al, no additional decrease in the degradation rate is observed and only results in decrease of the total gravimetric capacity due to the high amount of Al.

Coulombic efficiency versus cycle number is shown in Figure 2.10(c) for the SiNWs/TiN and Al/SiNWs. The initial coulombic efficiency of the SiNWs/TiN is almost the same as Al/SiNWs electrodes. The slight variations in the first cycle coulombic efficiency between the samples could be related to the difference in the surface area as the SEM images in Figure 2.2 showed that thicker Al coatings increase the surface roughness. After the first cycle, the coulombic efficiency is more stable for the 3Al/SiNWs and 8Al/SiNWs throughout cycling compared to all the other samples. Although 1Al/SiNWs initially shows the highest coulombic efficiency near 100%, it drops faster at higher cycles. On the other hand, when the Al coating is too thick, the coulombic efficiency is not as stable as 3Al/SiNWs and 8Al/SiNWs. It can also be seen in Figure 2.10 that the cycles where capacity degredation is fastest coincides with those where the coulombic efficiency is lowest, as would be expected.

The dependence of discharge capacity versus cycle number for the 3Al/SiNWs at 0.2 C and 0.1 C rates is shown in Figure 2.11(a). The 0.2 C rate cycling shows slightly better cycle performance. The first coulombic efficiency is about 96% and the irreversible capacity is lower in the first cycle than that at 0.1 C rate. It can be due to the formation of less SEI layer and occurrence of the less side reactions with the electrolyte at higher charge/discharge rate since less time is spent at the potentials where these reactions occur. Moreover, the first charge curve shows sloping profile at 0.2 C rate, although there is still an indication of a plateau (Figure 2.11(b)).

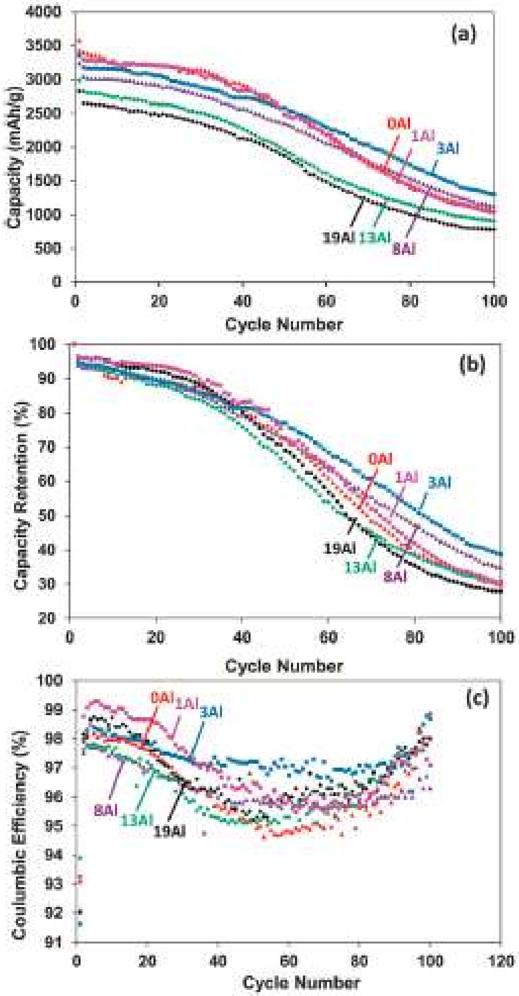

Figure 2.10: (a) Cycle life, (b) discharge capacity retention, and (c) coulombic efficiency of the uncoated and aluminum-coated SiNWs/TiN at 0.1 C rate.

At 0.1 C rate, the charge curve exhibits a single plateau at about 0.4 V, which is followed by an upwardly sloping region. As discussed earlier, if $Li_{15}Si_4$ phase is formed during the lithiation, the subsequent charge curves include a plateau at about 0.4 V, since there is a two-phase reaction from the crystalline to amorphous phase. It seems that the crystalline $Li_{15}Si_4$ phase is only partially formed during charging at 0.2 C rate. The formation of the $Li_{15}Si_4$ phase may be rate dependent. [33] It has been observed that amorphous silicon thin films can sustain high capacity even at high discharge rates with the good cyclability due to the facile lithium insertion and extraction into the single phase. Moreover, the volume expansion of amorphous alloy as a result of the lithium insertion is known to be homogeneous without pulverization as it occurs in the crystalline materials. [57]

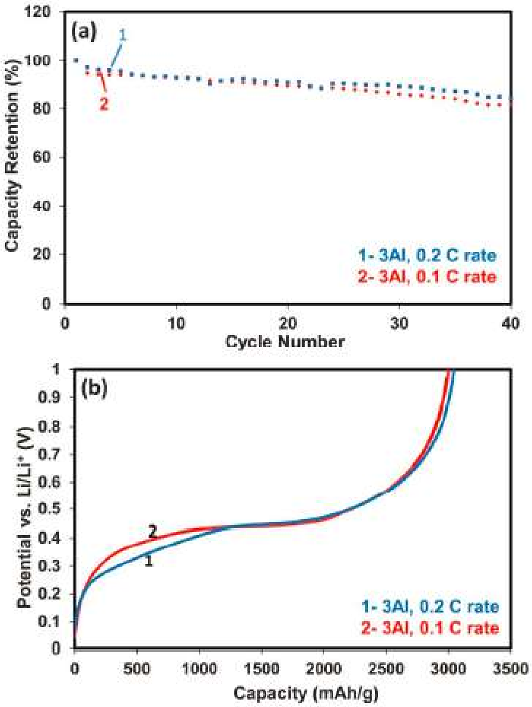

Figure 2.11: (a) Discharge capacity retention, and (b) first charging cycle of the 3Al/SiNWs at 0.2 and 0.1 C rate.

In order to determine whether the uncoated and coated SiNWs morphology changes after cycling, the cells were disassembled and the anode was further characterized. According to Figure 2.12(a), the uncoated SiNWs are completely disintegrated after 100 cycles, seem to have become porous, and extensive SEI formation is observed as flakes on the nanowires' surface (see inset). Essentially the same picture is obtained for the 1Al/SiNWs where the microstructure strongly resembles that of uncoated SiNWs after cycling. Figures 2.12(c-e) show SEM images of the 3Al/SiNWs electrode, which had the best electrochemical cycling properties, at different cycle numbers and magnifications. The original morphology is apparently retained, although there appear to be minor modifications to the surface compared to the as-made material (see Figure 3.2) possibly due to the repeated lithiation/delithiation of the Al layer and/or minor SEI deposits after 30 cycles (Figure 2.12(c)). Most importantly, even after 100 cycles, there are still areas in the material where the nanowires have retained their original morphology.

However, the higher magnification image in Figure 2.12(e) does show that closer to the substrate, there are areas where the nanowires have disintegrated to a similar extent as the uncoated and 1Al/SiNWs did. The same disintegration is observed for cycled 19Al/SiNWs in Figure 2.12(f). Similar to 3Al/SiNWs, there are areas where the original shape of the nanowires seems largely intact, but further down there is also evidence of disintegration. For this thicker Al coating, there is some evidence for agglomeration as larger particles are visible adjacent to the wires, indicating that thicker Al coatings are more vulnerable to agglomeration and breakup than thinner coatings. These images are in agreement with our cycling results in Figures 2.9 and 2.10. The Al coating can slow down, but not prevent capacity degradation and this is probably due to the uncoated parts of the material disintegrating close to the substrate. This strongly suggests that if more uniform coating could be achieved, for instance by growing the nanowires with better vertical alignment, the cycling stability would be improved further.

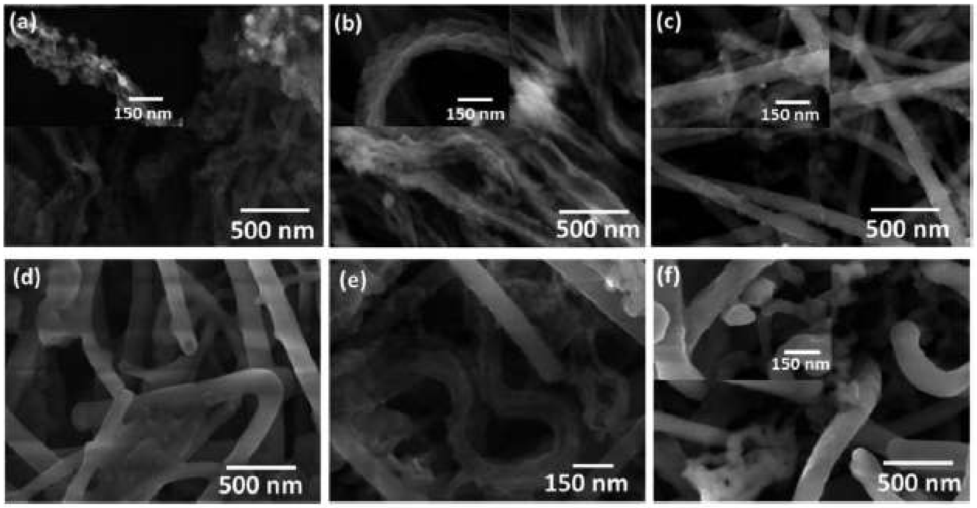

Figure 2.12: SEM images of the (a) bare SiNWs after 100 cycles, (b) 1Al/SiNWs after 100 cycles, 3Al/SiNWs after (c) 30, (d) and (e) 100 cycles, and (f) 19Al/ SiNWs after 55 cycles.

Figure 2.13 shows TEM images of 1Al/SiNWs, 3Al/SiNWs and 19Al/SiNWs after 100 cycles in the delithiated state. In Figure 2.13(a) and (b), a disintegrated 1Al/SiNW is shown. The morphology is rather similar to that observed in the SEM images in Figure 2.12. No SEI layer that was stable under the electron beam was observed. Figures 2.13(c-e) show TEM images of nanowires from the 3Al/SiNWs material. In this particular image, the Al coating seems to have peeled off from the NW's surface and has been replaced by an amorphous SEI layer that was stable under the electron beam. This means it likely consists of inorganic compounds such as LiF and Li_2CO_3. The outer part of this layer was observed to rapidly decompose under the TEM electron beam, indicating that the outer part had high organic content. The SiNW itself has also become amorphous as the SAD pattern and HRTEM image in Figure 2.13(c) and (e), respectively, show. The SAD pattern shows diffuse rings representative of an amorphous phase. For a different part of the same sample, presence of metallic Al on the surface could be confirmed by the simulation of the electron diffraction pattern shown in Figure 2.13(f). The dark field micrograph in Figure 2.13(g) is imaged by using a portion of the 111 Al ring. Figure 2.13(h) and (i) illustrate one of the particles on or adjacent to the 19Al/SiNWs in Figure 2.12f. As could be seen from the dark field image (Figure 2.13(i)) which has been taken from the g=200 Al reflection, the particles mostly consist of Al which has peeled off the SiNW.

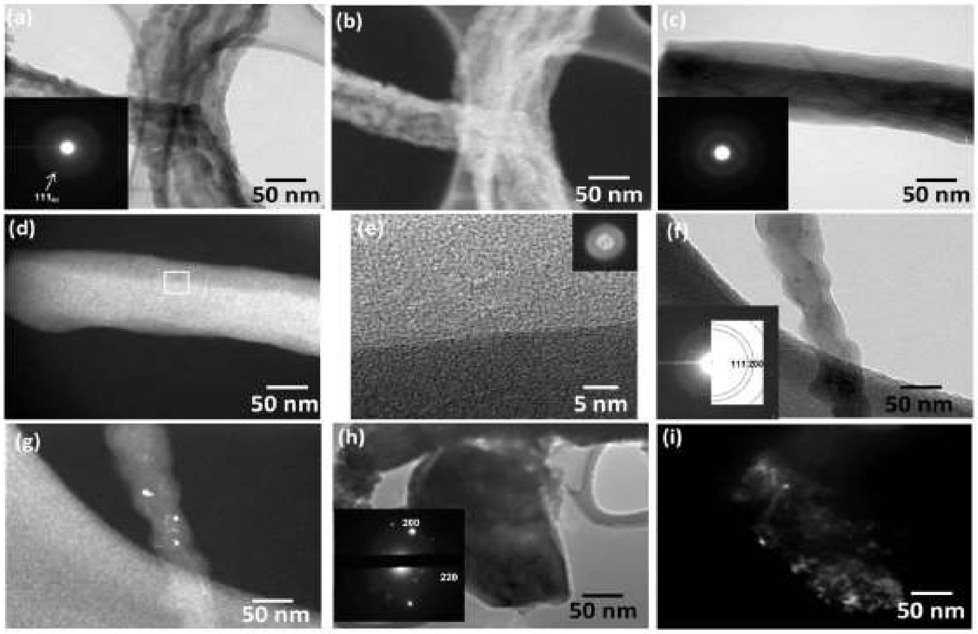

Figure 2.13: (a) and (b) show 1Al/SiNW. (a) bright field micrograph with corresponding SAD insert, (b) dark field micrograph taken from a portion of the 111Al ring. Fig. 2.13(c)–(g) show TEM micrographs of the 3Al/SiNW. (c) and (f) bright field micrograph with corresponding SAD insert, (d) dark field micrograph obtained using a portion of amorphous Si ring, (e) HRTEMimage of the SiNW structure, (g) dark field micrograph obtained using a portion of amorphous 111Al ring. Fig. 11 (h) and (i) show a particle adjacent to the 19Al/SiNWs. (h) bright field micrograph with corresponding indexed selected area diffraction (SAD) insert, (i) dark field micrograph, obtained using g ¼ 200Al reflection.

From the results presented so far we observe that

1): the initial coulombic efficiency, as well as the total capacity, is significantly higher for SiNWs grown on TiN than on SS and higher than previous reports on SiNWs.

2): after the first cycle, SiNWs on TiN and on SS degrade at approximately the same *rate*

3): sufficiently thick Al layers can mechanically stabilize the coated parts of the SiNWs and prevent them from pulverizing.

4): there is an optimum in the Al thickness where capacity degredation is slowed down but not prevented.

A coulombic efficiency < 100% can be due to SEI formation, irreversible reactions such as reduction of SiO_2 and loss of active material during lithiation due to pulverization. From XPS measurements by Chan et al, SiO_2 reduction was found to take place at potentials above 0.5 V[58]. It was found in Figure 2.9(g) that the capacities in the first cycle even down to a potential of 0.25 V are lower than 55 mAh/g for all our materials, which shows that the contribution of the native oxide layer is small. Besides Si, the Al probably has a (amorphous) native oxide layer as well. However, for all Al coated samples we found evidence for metallic Al in both as-made and cycled states. Furthermore, a native oxide layer on Al can be transformed upon lithiation to a ternary Li-Al-O glassy phase that is an excellent Li-ion conductor[59]. Therefore, partial oxidation of the Al surface is not expected to have a negative impact on the electrochemical properties of our SiNWs and from Figures 2.9 and 2.10 we indeed see no evidence for this. Incidentally, a *fully* oxidized Al shell in the form of Al_2O_3 has a negative influence on the cycling performance of SiNWs (see Figure 2.14).

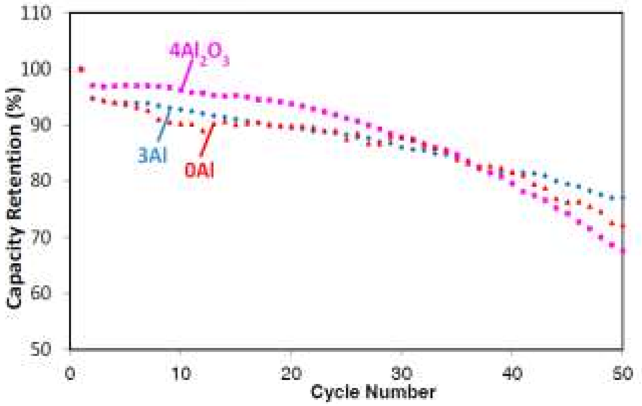

Figure 2.14: Cycling stability of bare SiNWs, 3Al/SiNWs and SiNWs coated with 4 wt.% Al2O3 deposited by ALD.

Because of the high volumetric expansion of Si upon lithiation, the SiNWs may be very sensitive to pulverization/cracking and contact loss with the substrate at the base. An earlier study by Ryu et al. showed that thick nanowires can disintegrate during the first lithiation. [60] Based on numerical modeling, combined with ex-situ TEM observations, a 'critical diameter' for fracture and pulverization was established in the range of 220 ~ 260 nm. The observed difference in total capacity and coulombic efficiency between SiNWs grown on TiN and SS, 3581 vs. 3050 mAh/g and 93.1 vs. 84.3%, respectively, may therefore be explained by differences in pulverization resistance. From the SEM images and size distributions in Figure 2.1, SiNWs/SS was observed to have a higher number of very thick nanowires and a significant fraction is above the 'critical size' of around 250 nm. Figure 2.15(a-e) depicts a series of SEM images of as-grown SiNWs/SS (a and b) and after one lithiation/delithiation cycle (c-e). Initially, some very thick nanowires are observed, the same as in Figure 2.1(a) and 2.15(a), but after only one cycle, no thick nanowires are observed either near the substrate (c and d) or in a top-down view (e). This is a strong indication that SiNWs above a critical size pulverize in the first lithiation cycle, leading to the relatively low coulombic efficiency that we observed.

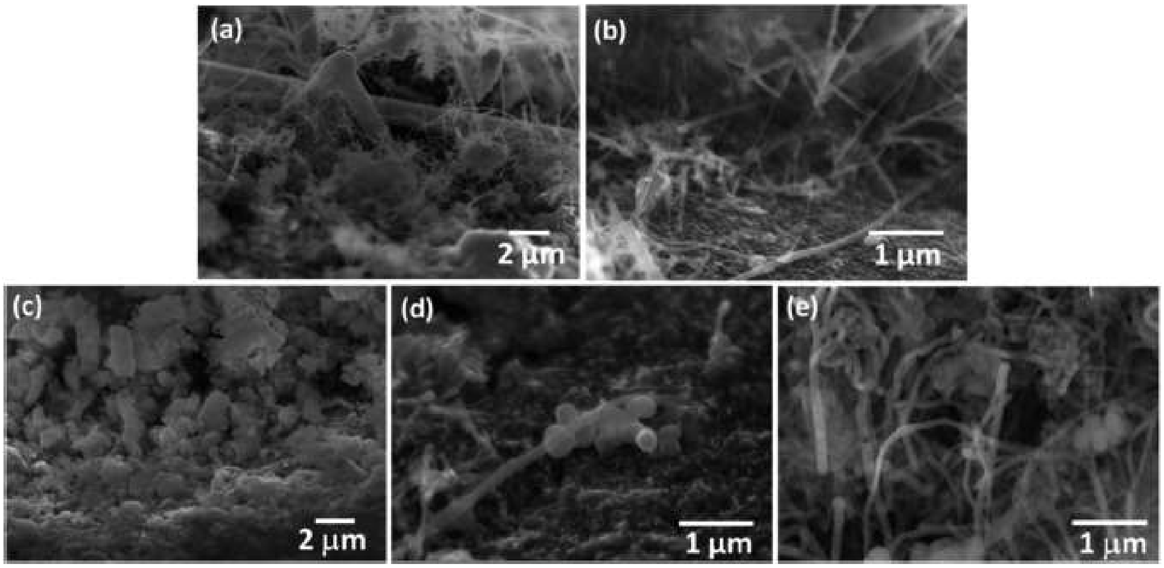

Figure 2.15: SEM micrographs of SiNWs/SS electrode (a) and (b) as-synthesized, (c)–(e) after the first cycle. (c) and (d) near the SS substrate, (e) top-down view.

Another contributing factor to capacity loss could be detachment of the SiNWs from the substrate, either abruptly in the first cycle or gradually in the course of cycling. It has been observed that FeSi alloys, which are formed at the interface between SS and SiNWs during the high temperature SiNW growth, can react with Li during electrochemical cycling. [61] The cycling stability of $FeSi_2$ powder turned out to be extremely poor, indicating the material is readily pulverized. Although formation of a small amount of $FeSi_2$ was confirmed by XRD (see Figure 2.7) it was still present in the lithiated and delithiated states, making it unlikely that Li reacting with iron silicides contributed to the first cycle capacity loss in SiNWs/SS. The other side reaction that is unique to the SS substrates is the conversion of Cr_2O_3 to Cr and Li_2O. However, given that this reaction is reversible (see Figure 2.4), one would expect the effects to be visible throughout the course of cycling and not only in the first cycle, but the degradation *rates* of SiNWs/SS and SiNWs/TiN were found to be similar in Figure 3.5. Although the SS substrate does show signs of surface damage in some places after removal of the SiNWs after 1 cycle (see Figure 2.16), the role of Cr_2O_3 in capacity degradation seems minor.

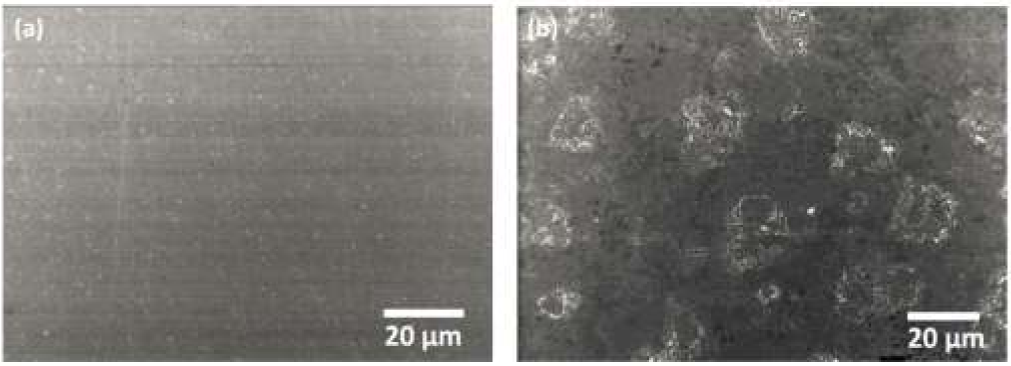

Figure 2.16: Surface of the stainless steel substrate after polishing steps (a) and after lithiation/delithiation cycle and removal of the Si nanowires (b).

Our third general observation relates to the observed mechanical stability of the nanowires during cycling. Radial expansion of SiNWs was found to be very large and highly anisotropic in in-situ TEM studies. [62] Upon lithiation, the initially cylindrical shape of the nanowires was transformed into a dumbbell-shape which could lead to rupture of the nanowire through the middle, effectively cutting its size in half. This can explain the disintegration we observed for the uncoated and 1Al-coated SiNWs in Figure 2.12 and 2.13. However, despite this large anisotropic expansion upon lithiation, our results clearly indicate that a thick enough Al coating can maintain the mechanical integrity of the nanowires during prolonged cycling. This means the Al coating likely does modify the expansion, either directing it more in the axial direction rather than radial or making radial expansion more isotropic by exerting a compressive stress on the SiNW during lithiation. The 1Al-coating appears to be too thin, and thus too vulnerable to rupture, to have this strong stabilizing effect.

A compressive stress on the SiNWs during lithiation could also help to keep SiNWs with near-critical diameters intact. Applying a 3 and 8 wt.% Al coating to SiNWs/SS resulted in improvement from 84.3 for bare SiNWs/SS to 88.7% and 91.5% coulombic efficiency, respectively, in the first cycle (see Figure 2.17) lending support to this hypothesis. This may also explain why the Al coating had so little influence on the coulombic efficiency in the first cycle for SiNWs on TiN. These had a relatively narrow size distribution around 100 nm and will not have any problems with pulverization related to their size. However, Chen et al. reported substantial improvement in coulombic efficiency in the first cycle for nanowires with diameters similar to ours; approximately 100 nm. [34, 41] However, a very high mass-loading, 0.6 mg/cm^2 compared to 0.18 mg/cm^2 for the present study, and long growth time (2 h) was reported, which means the nanowires should be very long. This may increase the mechanical vulnerability of the nanowires causing the coating layer to have a beneficial effect, despite the sufficiently small diameter. A way to test this hypothesis further would be to grow well-aligned SiNWs with narrow size distributions but different average diameters by controlling the size of the Au catalyst particles on TiN. A possible way to achieve this would be to adjust the Au layer thickness, as was recently demonstrated for Ni particles on SiO_2.[63]

Although 3Al/SiNWs and 8Al/SiNWs degrade more slowly than the other samples, all the materials eventually do degrade to what appears to be a ‘steady-state capacity’ that is between 28 and 38% of the initial capacity (see Figure 2.10(b)). Loss of active material should be evident as an increase in internal resistance of the electrodes. To investigate this, we performed electrochemical impedance spectroscopy on bare and coated SiNWs in their as-made and cycled states. The results are shown in Figure 2.18 in the form of a Nyquist plot. Another possibility is that over the course of cycling, more and more SiNWs gradually detach from the TiN substrate. The spectra are composed of one semicircular arc at high frequencies indicative of a charge transfer reaction where the diameter of the semicircle equals the charge transfer resistance (R_{ct}), followed by a nearly straight line at 45^o or higher angle with respect to the real axis at lower frequencies. The shift of the impedance spectra along the real axis is approximately 3 Ohm for all samples. This value is the sum of all electrical resistances within the electrodes, which includes the contact resistance between the current collector and the SiNWs. The bare SiNWs displays a very large semicircle, indicative of high charge transfer resistance that is likely due to the presence of native oxide. The xAl/SiNWs have significantly lower charge transfer resistance, similar to what was found for Cu and carbon coatings [34, 41] further highlighting the beneficial effects of the Al coating.

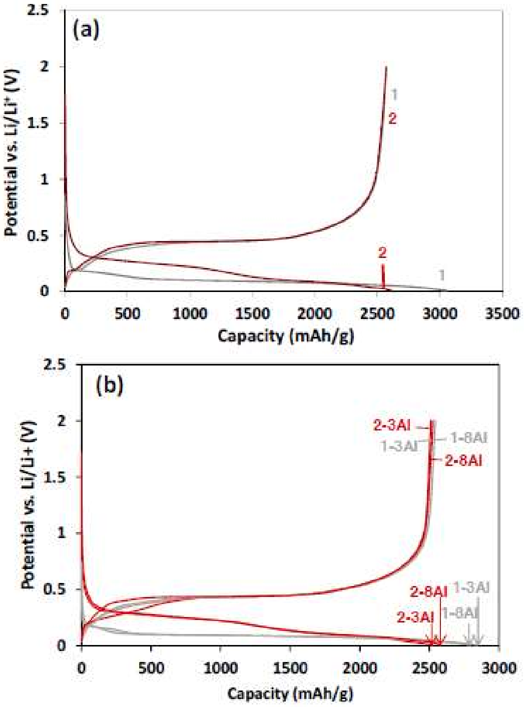

Figure 2.17: First and second cycles for SiNWs/SS (a) and 3Al/SiNWs/SS and 8Al/SiNWs/SS (b).

For all electrodes, there was an increase in the electrical resistance of approximately a factor of 4, which is indicative of contact loss between the active material, i.e. the SiNWs, and the current collector/substrate. Nanowire detachment from the substrate will reduce the number of conductive pathways for electrons and increase reaction resistances in the electrode. In principle, this should lead to an increase in R_{ct} by a similar factor, but the effect is much smaller, probably due to the presence of native oxides in the as-made materials that are reduced in the first lithiation cycle. As a result, for the bare SiNWs the charge transfer resistance is even lower in the cycled state than in the as-made state. R_{ct} is significantly higher for bare SiNWs and 13Al/SiNWs compared to 3Al and 1Al, which reflects a higher tendency for SEI formation for the uncoated SiNWs and for thick Al coatings sensitive to agglomeration and detachment from the nanowire surface.

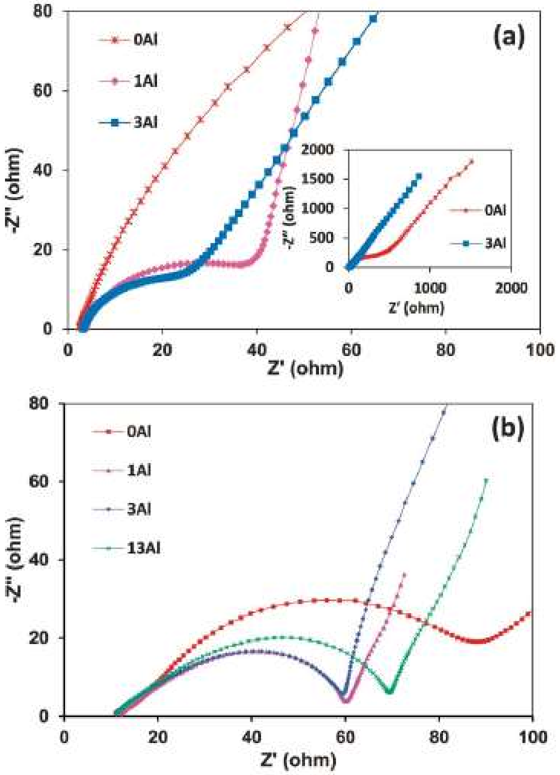

Figure 2.18: Impedance spectra of uncoated and Al coated SiNWs on TiN/SS substrate (a) as-synthesized, (b) after 100 cycles.

The most important benefit of the Al coating is the prevention of pulverization. The coated parts of the nanowires were clearly protected from degradation as seen from the SEM images in Figure 2.12. However, progressive pulverization of the parts near the substrate still leads to capacity degredation down to 28 to 38% of the original capacity, corresponding to between 785 (19Al/SiNWs) and 1292 mAh/g (3Al/SiNWs). However, the capacities seem to stabilize as the coulombic efficiency increases again in late stages of cycling, which means a certain fraction of the nanowires will remain attached to the substrate and remain electrochemically active. Furthermore, the material with optimum coating thickness, 3Al/SiNWs, seems to stabilize at a higher capacity than bare nanowires. This strongly suggests that the Al coating also has a positive influence on wire attachment to the substrate and that if coverage of the nanowires by the coating layer can be improved, the beneficial effects of the Al coating will be more pronounced. This can be achieved by growing the nanowires with a lower density and better vertical alignment, which may be possible by adjusting the Au layer thickness, in order to reduce shadowing effects during Al deposition. Also, transferring our SiNW growth process with TiN interlayers onto commercially available copper foils that are commonly used as current collectors in Li-ion batteries should be undertaken to bring these materials closer to practical application.

2.4 Conclusions

We compared the electrochemical performance of SiNWs grown on TiN and SS and investigated the effects of Al coating. Only the SiNWs grown on SS had a significant fraction of nanowires above a critical diameter (~250 nm) that pulverize upon lithiation leading to lower initial coulombic efficiency for SiNW/SS, 84.3%, compared to SiNW/TiN, 93.1% when cycling between 0.01 and 2V vs. Li/Li^+ at 0.1C rate. Such small amount of irreversible capacity loss for bare SiNWs during the first cycle has never been observed in previous studies. We therefore conclude that the size distribution has a large influence on the stability and should be optimized, preferably with an average diameter around 100 nm or less. Coating with Al showed no additional benefit to the initial coulombic efficiency, but improved the capacity retention when the thickness was within an optimum range between 3 and 8 wt.% by helping to maintain the mechanical integrity of the nanowires. When the coating was too thin, it was still too vulnerable to fracture, when it was too thick, it tended to agglomerate and peel off the surface of the nanowires. The biggest improvement was seen after 75 cycles where bare SiNWs retained 42% of their original capacity and 3Al/SiNWs 55%. After 100 cycles, the materials retained between 28 (19Al/SiNWs) and 38% (3Al/SiNWs) of their original capacity which showed Al coating slows down the capacity degredation but does not prevent it. This means the nanowires still disintegrate and detach from the substrate at their base. Nevertheless, the higher steady-state capacity after 100 cycles for 3Al/SiNWs suggests that Al coating also helps maintain contact with the substrate.

In summary, we have shown that SiNWs with an Al shell with an optimized thickness are promising anode materials for rechargeable lithium-ion batteries. Future research should concentrate on improving the coverage of the SiNWs by the coating layer and further investigating the effects of the nanowire diameter and density and finding ways to control them.

2.5 References

1. S. A. Freunberger, Y. Chen, Z. Peng, J.M. Griffin, L. J. Hardwick, F. Barde, P. Novak and P. G. Bruce, *Journal of the American Chemical Society*, 2011, **133**, 8040-8047.
2. R. Marom, S. F. Amalraj, N. Leifer, D. Jacob and D. Aurbach, *J. Mater. Chem.*, 2010, **21**, 9938.
3. J. S. Thorne, J. R. Dahn, M. N. Obrovac and R. A. Dunlap, *J. Alloys and Comp.*, 2011, **509**, 6705-6710.
4. A. Yu, H. W. Park, A. Davies, D. C. Higgins, Z. Chen and X. Xiao, *J. Phys. Chem. Lett.*, 2011, **2**, 1855-1860.
5. J. Danet, T. Brousse, K. Rasim and D. Guyomard, *Phys. Chem. Chem. Phys.*, 2010, **12**, 220–226.
6. S. Bijani, M. Gabas, G. Subias, J. Garcia, L. Sanchez, J. Morales, L. Martinez and J. R. Ramos-Barrado, *J. Mater. Chem.*, 2011, **21**, 5368-5377.
7. A.M.A. Hashem, A.E. Abdel-Ghany, A.E. Eid, J. Trottier, K. Zaghib, A. Mauger, C.M. Julien, *J. Power Sources*, 2011, **196**, 8632-8637.
8. C. Martin, O. Crosnier, R. Retoux, D. Belanger, D. M. Schleich and T. Brousse, *Adv. Funct. Mater.*, 2011, **21**, 3524-3530.
9. J. Danet, T. Brousse, K. Rasim, D. Guyomard and P. Moreau, *Phys. Chem. Chem. Phys.*, 2010, **12**, 220-226.
10. V. L. Chevrier, J. W. Zwanziger and J. R. Dahn, *J. Alloys and Comp.*, 2010, **496**, 25-36.
11. D. Mazouzi, B. Lestriez, L. Roue, D. Guyomard, *Electrochem. And Solid-State Lett.*, 2009, **12**, A215-A218.
12. T. D. Hatchard and J. R. Dahn, *J. Electrochem. Soci.,* 2004, **151**, A838-A842.
13. V. L. Chevrier, J. W. Zwanziger and J. R. Dahn, *Can. J. Phys.*, 2009, **87**, 625–632.
14. S. H. Ng, J. Wang, D. Wexler, K. Konstantinov, Z. P. Guo, and H. K. Liu*, Angew. Chem. Int. Ed.*, 2006, 45, 6896 –6899.
15. T. Zhang, J. Gao, L. J. Fu, L. C. Yang, Y. P. Wu and H. Q. Wu., *J. Mater. Chem.*, 2007, **17**, 1321–1325.
16. J. Guo, X. Chen and C. Wang, *J. Mater. Chem.,* **2010**, 20, 5035–5040.
17. D. Larcher, S. Beattie, M. Morcrette, K. Edstroem, J. C. Jumas and J. M. Tarascon, *J. Mater. Chem.*, 2007, **17**, 3759–3772.

18. S. Ohara, J. J. Suzuki, K. Sekine and T. Takamura, *Electrochemistry*, 2003, **71**, 1126–1128.

19. Y. Xu, G. Yin, Y. Ma, P. Zuo and X. Cheng, *J. Mater. Chem.*, 2010, **20**, 3216-3220.

20. L. Ji and X. Zhang, *Electrochem. Commun.*, 2009, **11**, 1146–1149.

21. M. H. Park, M. G. Kim, J. Joo, K. Kim, J. Kim, S. Ahn, Y. Cui and J. Cho, *Nano Lett.*, *2009*, **9**, 3844–3847.

22. T. Song, J. L. Xia, J. H. Lee, D. H. Lee, M. S. Kwon, J. M. Choi, J. Wu, S. K. Doo, H. Chang, W. Il Park, D. S. Zang, H. Kim, Y. G. Huang, K. C. Hwang, J. A. Rogers and U. Paik*,* *Nano Lett.*, 2010, **10**, 1710–1716.

23. J. R. Szczech and S. Jin, *Energy Environ. Sci.*, 2011, *4*, 56–72.

24. Y. Kumai, H. Kadoura, E. Sudo, M. Iwaki, H. Okamoto, N. Sugiyama and H. Nakano, *J. Mater. Chem.*, 2011, **21**, 11941–11946.

25. J. S. Xue, K. Myrtle and J. R. Dahn, *J. Electrochem. Soc.*, 1995, **142**, 2927–2935.

26. K. Wang, X. He, L. Wang, J. Ren, C. Jiang, C. Wan, *Solid State Ionics*, 2007, **178**, 115–118.

27. N. S. Choi, Y. Yao, Y. Cui and J. Cho, *J. Mater. Chem.*, 2011, **21**, 9825-9840.

28. J. L. Gómez-Cámer, J. Morales and L. Sánchez, *J. Mater. Chem.*, 2011, **21**, 811–818.

29. M. Holzapfel, H. Buqa, L. J. Hardwick, M. Hahn, A. Würsig, W. Scheifele, P. Novák, R. Kötz, C. Veit and F. M. Petrat, *Electrochim. Acta*, 2006, **52**, 973–978.

30. B. Laïk, L. Eude and J. P. Pereira-Ramos, *Electrochim. Acta*, 2008, **53**, 5528-5532.

31. T. Song, D. H. Lee, M. S. Kwon, J. M. Choi, H. Han, S. G. Doo, H. Chang, W. Park, W. Sigmund, H. Hansu Kim and U. Paik, *J. Mater. Chem.*, 2011, **21**, 12619–12621.

32. B. Laïk, D. Ung, A. Caillard, C.S. Cojocaru, D. Pribat and J.P. Pereira-Ramos, *J. Solid State Electrochem.*, 2010**, 14**, 1835-1839.

33. C. K. Chan, R. Ruffo, S. S. Hong, R.A. Huggins and Y. Cui, *J. Power Sources*, 2009,**189**, 34-39.

34. H. Chen, Y. Xiao, L. Wang and Y. Yang, *J. of Power Sources*, 2011, **196**, 6657–6662.

35. L. Hu, H Wu, S. Hong, L. Cui, J. R. McDonough, S. Bohy and Y. Cui, *Chem. Commun.*, 2011, **47**, 367-369.

36. T. Stephenson, A. Kubis, M. Derakhshesh, M. Hazelton, C. Holt, P. Eaton, B. Newman, A. Hoff, M. Gray and D. Mitlin, *Energy & Fuels*, 2011, **25**, 4540-4551.

37. S. Grugeon, S. Laruelle, L. Dupont, F. Chevallier, P. L. Taberna,-P. Simon,-L. Gireaud,-S. Lascaud, E. Vidal,-B. Yrieix and J-M. Tarascon, *Chem. Mater.*, 2005, **17**, 5041-5047.

38. L. Dupont, S. Laruelle, S. Grugeon, C. Dickinson, W. Zhou and J-M. Tarascon, *J. Power Sources*, 2008, **175**, 502-509.

39. L. Dupont, S. Grugeon, S. Laruelle and J-M. Tarascon, *J. Power Sources*, 2007, **164**, 839-848.

40. L.Q. Zhang, X. H. Liu, Y. Liu, S. Huang, T. Zhu, L. Gui, S.X. Mao, Z. Z. Ye, C. M. Wang, J. P. Sullivan and J. Y. Huang, *ACS Nano*, 2011, **5**, 4800-4809 and references therein.

41. H. Chen, Z. Dong, Y. Fu, Y. Yang, *J. Solid State Electrochem.*, 2010, **14**, 1829-1834

42. K. Xu and A. Cresce, *J. Mater. Chem.*, 2011, **21**, 9849–9864.

43. Y. Yu, L. Gu, C. Zhu, S. Tsukimoto, P. A. van Aken and J. Maier, *Adv. Mater.*, 2010, **22**, 2247-2250.

44. D. Favez, L. Deillon, J.-D. Wagnière, M. Rappaz, *Acta Mater.*, 2011, **59**, 6530-6537

45. C. Ophus, T. Ewalds, E. Luber, D. Mitlin, *Acta Mater.*, 2010, **58**, 5150-5159

46. M. Green, E. Fielder, B. Scrosati, M. Wachtler and J. S. Moreno, *Electrochem. Solid-State Lett.*, 2003**, 6**, A75-A79.

47. M. D. Fleischauer, M. N. Obrovac, J. D. McGraw, R. A. Dunlap, J. M. Topple and J. R. Dahn, *J. Electrochem. Soci.*, 2006, **153**, A484-A491.

48. D. Larcher, S. Beattie, M. Morcrette, K. EdstrÖm, J.C. Jumas and J. M. Tarascon, J. Mater. Chem., 2007, **17**, 3759–3772.

49. M. D. Fleischauer, J. Li, and M. J. Brett, *J. Electrochem. Soci.*, 2009, **156**, A33-A36.

50. G.L. Miller and W.A. Orr, *Appl. Phys. Lett.*, 1980, **37**, 1100-1101.

51. V. L. Chevrier, J. W. Zwanziger and J. R. Dahn, *Can. J. Phys.*, 2009, **87**, 625–632.

52. J. Li, A. Smith, R. J. Sanderson, T. D. Hatchard, R. A. Dunlap and J. R. Dahn, *J. Electrochem. Soci.,* 2009, **156**, A283-A288.

53. L. Baggetto, R. A. H. Niessen, F. Roozeboom, P. H. L. Notten, *Adv. Funct. Mater.*, 2008, **18**, 1057–1066.

54. M. D. Fleischauer, J. Li, and M. J. Brett, *J. Electrochem. Soci.*, 2009, **156**, A33-A36.

55. R. Krishnan, T. M. Lu and N. Koratkar, *Nano Letters*, 2011, **11**, 377–384.

56. C. Y. Wang, Y. S. Meng, G. Ceder and Y. Li, *J. Electrochem. Soci.*, 2008, **155**, A615-A622.

57. L. Y. Beaulieu, T. D. Hatchard, A. Bonakdarpour, M. D. Fleischauer, J. R. Dahn, *J. Electrochem. Soci.*, 2003, **150**, A1457-A1464.

58. C.K. Chan, R. Ruffo, S. S. Hong and Y. Cui., *J. Power Sources,* 2009, **189**, 1132-1140.

59. Y. Liu, N. S. Hudak, D. L. Huber, S. J. Limmer, J. P. Sullivan and J.Y. Huang, *Nano Letters*, 2011, **11**, 4188-4194.

60. I. Ryu, J. W. Choi, Y. Cui and W. D. Nix, J. *Mech. Phys. Solid*, 2011, **59**, 1717-1730.

61. N. Jayaprakash, N. Kalaiselvi, C. H. Doh, *Intermetallics*, 2007, **15**, 442-450.

62. X. H. Liu, J. Y. Huang, *Energy Environ. Sci.*, 2011, **4**, 3844-3860

63. E. J. Luber, B. C. Olsen, C. Ophus, D. Mitlin, *Phys. Rev. B*, 2010, **82**, 085407

3 ALD TiO_2 coated Silicon Nanowires for Lithium Ion Battery Anodes with enhanced Cycling Stability and Coulombic Efficiency

Material in this chapter has been published in:

E. Memarzadeh Lotfabad, P.Kalisvaart, K. Cui, A. Kohandehghan, M. Kupsta, B. Olsen, and D. Mitlin, *Phys. Chem. Chem. Phys.*, 2013, **15**, 13646-13657.

3.1 Introduction

Li-ion batteries (LIBs) are currently the most important energy storage device for a wide variety of applications such as cell phones, laptops and other portable electronics[1-6]. However, to meet the more demanding applications such as powering electrical vehicles, LIBs with higher energy density, longer cycle life, and faster discharge/charge rate than the existing ones are required. [7-10] Silicon is a promising anode material for LIBs owing to its large charge storage capacity of 3590 mAh/g, corresponding to $Li_{15}Si_4$, which is ten times higher than graphite (372 mAh/g). The main drawback of silicon is its large volume expansion/contraction (~300%) upon alloying/dealloying with lithium, resulting in high mechanical stress, pulverization and loss of electronic contact leading to severe capacity degradation. [11-15] In addressing this problem, several approaches have been tried to enhance the cycling performance of Si anodes in LIBs. Among them, Si-based nanostructures including nanoparticles, [16,17] thin films, [18,19] nanowires, [12,20-22] and nanotubes [23,24] have attracted the most attention. Silicon nanowires (SiNWs) can accommodate the generated volumetric change anisotropically in both longitudinal and radial directions. Furthermore, anchored SiNWs on a conductive, possible flexible, substrate have no need of binder and conductive additives, potentially increasing the capacity of a full cell.[25-27]

The high specific surface area of nanowires is both an advantage and a disadvantage. On the one hand they provide a large area available for charge transfer reactions and their small diameter keeps Li diffusion distances short. On the other hand, the electrolyte solvents are thermodynamically unstable below 1.5 V vs. Li/Li^+ and the decomposition products immobilize part of the lithium in the battery in the so-called solid-electrolyte interphase (SEI). SEI formation is generally irreversible and a material with higher surface area will therefore cause higher irreversible charge losses. Furthermore, the high volume expansion of Si will continuously fracture the SEI during lithiation, exposing fresh Si to the electrolyte. This will increase the amount of SEI with each cycle, as well as increase the charge transfer and diffusion resistances.[28,29]

Thus, researchers have been seeking ways to modify the surface of the electrodes to make the material less reactive with the electrolyte. Deposition of coatings onto silicon nanowires presents some challenges. They are usually grown using an Au-catalysed vapour-liquid-solid chemical vapour deposition process which produces poorly aligned nanowire forests. Highly directional deposition methods such as sputtering or thermal evaporation will result in incomplete coverage of the nanowires because of shadowing effects. Carbon, [30] copper, [31] and aluminium [22] coating of SiNWs using these methods have therefore had only limited success in improving the performance, although there is a marked improvement in the mechanical stability of the parts of the nanowires that do get conformally coated. [22, 32] Capacity degradation was slowed down, but not prevented, for SiNWs coated with 3-8 wt.% of Al, probably because the uncoated parts, near the nanowire base, are still subject to the same degradation mechanisms as bare SiNWs such as excessive SEI formation, agglomeration and delamination from the substrate. [33]

Atomic layer deposition (ALD) is a method capable of producing conformal coatings on substrates of any size or shape with very precise control over the coating thickness.[11] Deposition of a continuous layer inside etched features (trenches) with aspect ratio as high as 1:20 has been achieved. [34] Conversely, conformal coating on nano*pillars* made of Al has also been demonstrated using ALD. [35] However, to date, ALD has not been employed to coat silicon nanowires, despite its potential to achieve complete coverage and thus markedly improve upon the performance of sputter or evaporation-coated SiNWs, if a suitable coating material can be selected.

TiO_2 has been studied extensively as an anode material for LIBs in its own right. [36-42] Its volume expansion upon lithiation according to:

$$xLi^{+} + x\bar{e} + TiO_2 \leftrightarrow Li_xTiO_2 \qquad (4.1)$$

is less than 4%, which means its cycle life is excellent in general and the low expansion may be beneficial for adhesion of the coating to the underlying Si nanowire. Diffusion of lithium ions is found to be higher in a TiO_2-Si composite than in bare silicon. [43] Furthermore, 'x' is usually found to be ≤ 0.55 for anatase but can be close to 1 for amorphous TiO_2 and for very small anatase particles, turning the material from an insulator (bandgap ~3.5 eV) into an electronic conductor. Thus, TiO_2 coating on SiNWs is potentially beneficial for both structural integrity as well as the rate capability of the composite.

As mentioned before, an important purpose of the coating is to make the Si less reactive with the electrolyte. TiO_2 is usually tested between 1 and 3 V vs. Li/Li^+ and, as a result, little is known about the reactivity of TiO_2 with the electrolyte at low potentials. It was found that the cycling stability of TiO_2 is not affected by extending the potential range down to 0.1 V and that the SEI formed on TiO_2 is thermally more stable than that on graphite, [44] which reacts with Li in the same potential range as Si (< 0.5 V vs. Li/Li^+). Therefore, applying TiO_2 coating onto SiNWs can improve the safety of the battery.

In view of all the above, SiNWs coated with TiO_2 by ALD have great potential as a high performance Li-ion battery anode material. In the present paper, we study the influence of varying the ALD deposition parameters and TiO_2 layer thickness on the electrochemical properties and microstructure development of TiO_2-coated SiNWs during galvanostatic cycling. A factor two improvement in capacity retention at 0.1 C and factor three improvement in rate capability at 5 C over a bare SiNW baseline is achieved. The reasons for the improved performance are found to be related to improved structural integrity, reduced agglomeration and passivation of the surface of SiNWs towards electrolyte decomposition for the optimal TiO_2 coating.

3.2 Experimental

We prepared the SiNW electrodes by using a gold-catalyzed, vapour–liquid–solid growth on 316L stainless steel spacers (diameter 15.4 mm). In order to prevent penetration of Au into stainless steel, a Ti/TiN diffusion barrier with layer thicknesses of 50 and 200 nm, respectively, was deposited onto the substrates using magnetron sputtering (Orion 8, AJA international). Base pressure was always below $5x10^{-8}$ mbar and the argon pressure during sputtering was 4 mTorr. For reactive sputtering of TiN, a N_2:Ar ratio of 1:20 was used and the deposition temperature raised to 250°C. 10 nm Au was deposited using RF magnetron sputtering at a power of 45 W at a rate of ~0.4 Å/s after cooling the substrate down to room-temperature. SiNWs were grown in a commercial Tystar CVD furnace. Prior to growth, the samples were annealed in vacuum for 30 minutes before introducing a SiH_4:H_2 (ratio 1:4) mixture at a pressure of 100 Torr for a growth time of 2 minutes at the same temperature. Then, the substrates covered with SiNWs were placed in the ALD reactor. TiO_2 was deposited from titanium isopropoxides $Ti(OCH(CH_3)_2)_4$ as the titanium source and O_2 as the oxygen source. Argon was used as the carrier gas. We investigated the influence of the TiO_2 microstructure by varying the layer thickness and deposition temperature. Deposition of the coating was carried out at 200°C and 300°C and at 200°C followed by annealing treatment at 600 °C in vacuum for 1 h after deposition to get anatase TiO_2. The number of deposition/purge cycles required for 10 nm TiO_2 is 196 and 204 at 200 and 300°C, respectively. The TiO_2 thicknesses used were 5, 10 and 15 nm, equivalent to mass loadings of ~0.05, 0.1 and 0.16 mg per sample, respectively. For an average mass of ~0.35 mg Si per sample, this corresponds to 12, 22 and 31 wt% TiO_2 in the TiO_2/SiNWs nanocomposite, respectively. For the remainder of the manuscript the samples will be referred to as (x)TiO_2-y(A)/SiNWs, i.e. silicon nanowires coated with x nm TiO_2 at an ALD deposition temperature of y °C, where (A) indicates post-deposition annealing treatment. In order to separately investigate the electrochemical properties of the coatings, 10 nm planar films on stainless steel spacers including the Ti/TiN barrier layer were deposited under identical conditions. The mass loading of TiO_2 on (10)TiO_2-200/SiNWs is equivalent to a 120 nm thick planar film, which means the SiNWs have approximately 12 times more surface area in contact with the electrolyte than a planar Si film.

316 stainless steel-CR2032 button half-cells using the TiO_2/SiNW working electrodes and Li foil as counter electrodes were assembled in a glovebox filled with Ar with less than 0.2 ppm oxygen and moisture contaminations. A polyethylene (MTI technologies) separator (porosity of 36–44% and 0.03 μm pore size) soaked with a liquid electrolyte of 1 M $LiPF_6$ dissolved in a 1:1:1 volume ratio of ethylene carbonate (EC): dimethyl carbonate (DMC): diethylcarbonate (DEC) organic solvents was placed between the electrode and the lithium in the cell. The cells

were galvanostatically charged and discharged on a computer controlled BT2000 Arbin potentiostat between 0.01 and 2 V (vs. Li/Li$^+$) at various currents. Cyclic voltammetry (CV) was carried out using Versa STAT 3 potentiostat at 1 mV/s scan rate for SiNWs based anode materials and 0.2 mV/s for thin film materials in two different potential ranges (0.01-2 V and 1-3 V (vs. Li/Li$^+$)).

Electrochemical impedance spectroscopy (EIS) measurements were measured using Versa STAT3 frequency response analyser FRA) by applying an AC voltage of 10 mV amplitude over a frequency range of 0.01 Hz to 1 MHz.

After electrochemical testing, the coin cells were disassembled and the samples were rinsed thoroughly with acetonitrile and kept overnight in the glove box to remove the excess electrolyte. To characterize the morphology of the as-prepared and cycled samples, we used field emission scanning electron microscopy (FE-SEM) (Hitachi S-4800) and transmission electron microscopy (TEM) (JEOL 2010, 200 kV). Electron energy loss spectroscopy (EELS) analysis was conducted using a JEOL 2200FS TEM operated at 200 kV in a scanning TEM (STEM) mode with a nominal analytical beam size of 0.5 nm. High angle annular dark field (HAADF) images were recorded simultaneously with the EELS analysis. Compositional mapping was achieved with an in-column Ω filter. The software employed for signal collection and data extraction from EELS spectra was Digital Micrograph (Gatan, Inc.). The data extraction was performed by following the standard procedure of pre-edge background subtraction and integration on the edge. [45] Low-loss plasmon peaks at 60-70 eV have been used for EELS mapping of Li-K. We mapped Si, C, Ti, and O elements by integrating over core loss edges of Si-L, C-K, Ti-L, and O-K at ~100-120, 300-320, 470-490, and 530-550 eV, respectively. Cross-sectional samples of cycled materials were obtained using a Hitachi NB5000 dual beam FIB/SEM.

X-ray photoelectron spectroscopy (XPS) measurements were performed on an ULTRA (Kratos Analytical) spectrometer using monochromatic Al-K$_\alpha$ radiation (hν=1486.6 eV) run at 210 W. Data collection was conducted under ultrahigh vacuum (10^{-9} Torr) from an area of 300×700 μm^2. Spectra were collected with an energy window of 20 eV. A charge neutralizer was used to compensate for charging effects. The binding energy scale was calibrated from the universal hydrocarbon contamination using the C1s peak at 284.8 eV. The XPS data were analyzed using CasaXPS software. Background subtraction was done using a nonlinear Shirley-type background model.

3.3 Results and Discussion

SEM and TEM micrographs of as-made, VLS grown SiNWs coated with 10 nm of TiO_2 by ALD are presented in Figure 3.1 and 3.2. 10 nm was found to be the optimum coating thickness with regard to capacity and cycling stability (see Figure 3.3). All results presented hereafter were obtained with this coating thickness and it will therefore not be explicitly indicated anymore. The electrodes will be denoted as TiO_2-y/SiNWs, where y is the ALD deposition temperature in ^{o}C, from here on. The SAD patterns of TiO_2-200/SiNWs and TiO_2-300/SiNWs consist of an overlay of a single crystal spot pattern of Si and a diffuse halo around the primary beam associated with amorphous TiO_2. For TiO_2-200(A)/SiNWs (A=annealing at 600^{o}C for 1 h), a second spot pattern belonging to anatase TiO_2 appears besides that of Si.

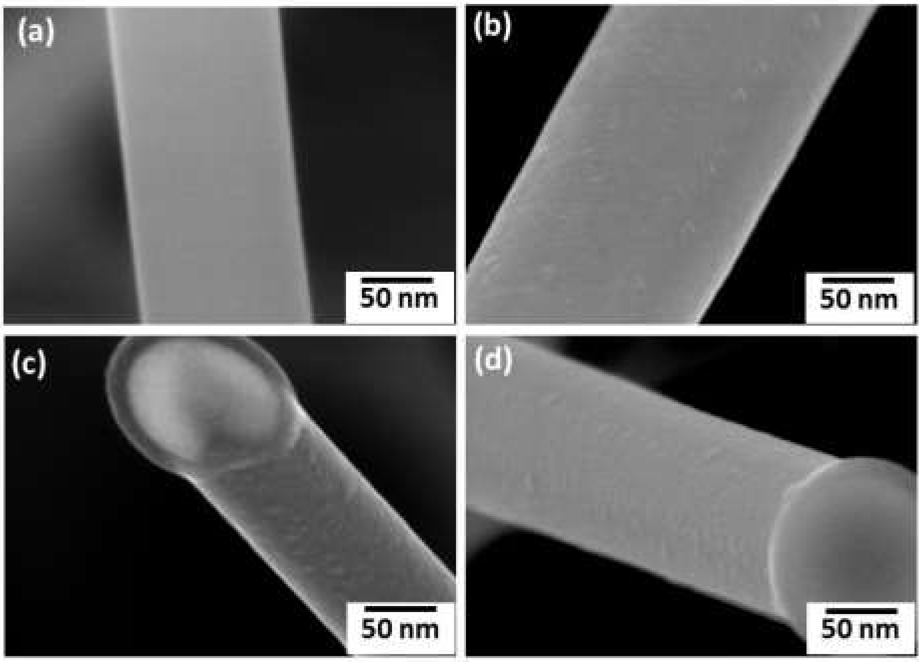

Figure 3.1: SEM images of (a) SiNWs, (b) (10)TiO_2-200/SiNWs, (c) (10)TiO_2-300/SiNWs, (d) (10)TiO_2-200(A)/SiNWs.

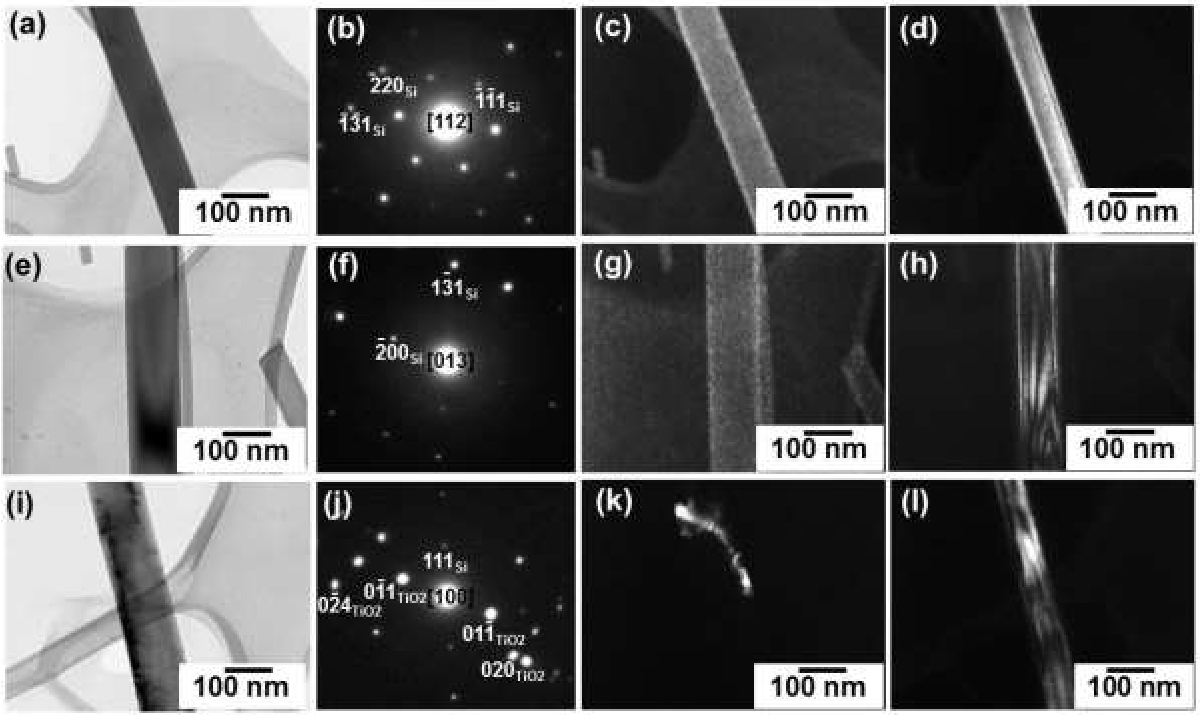

Figure 3.2: TEM micrographs of TiO_2 coated SiNWs. (a)-(d): (10)TiO_2-200/SiNWs. (a) Bright field micrograph, (b) corresponding indexed selected area diffraction (SAD), (c) dark field micrograph obtained using a portion of the diffuse halo of amorphous TiO_2 between the primary beam and the first set of Bragg reflections of Si, (d) dark field micrograph of the Si obtained using g =111_{Si} with the wire oriented near the 112 symmetric zone axis, (e)–(h): (10)TiO_2-300/SiNWs. (e) Bright field micrograph, (f) corresponding indexed SAD, (g) Dark field micrograph obtained using a portion of the diffuse halo of amorphous TiO_2 between the primary beam and the first set of Bragg reflections of Si, (h) dark field micrograph of the Si obtained using g=111_{Si}. (i)–(l): (10)TiO_2-200(A)/SiNWs. (j) Bright field micrograph, (j) corresponding indexed SAD showing the 011, 020 and 024 diffraction spots of anatase TiO_2, (k) dark field micrograph, obtained using g=011_{TiO2}, (l) dark field micrograph of the Si obtained using g =111_{Si}.

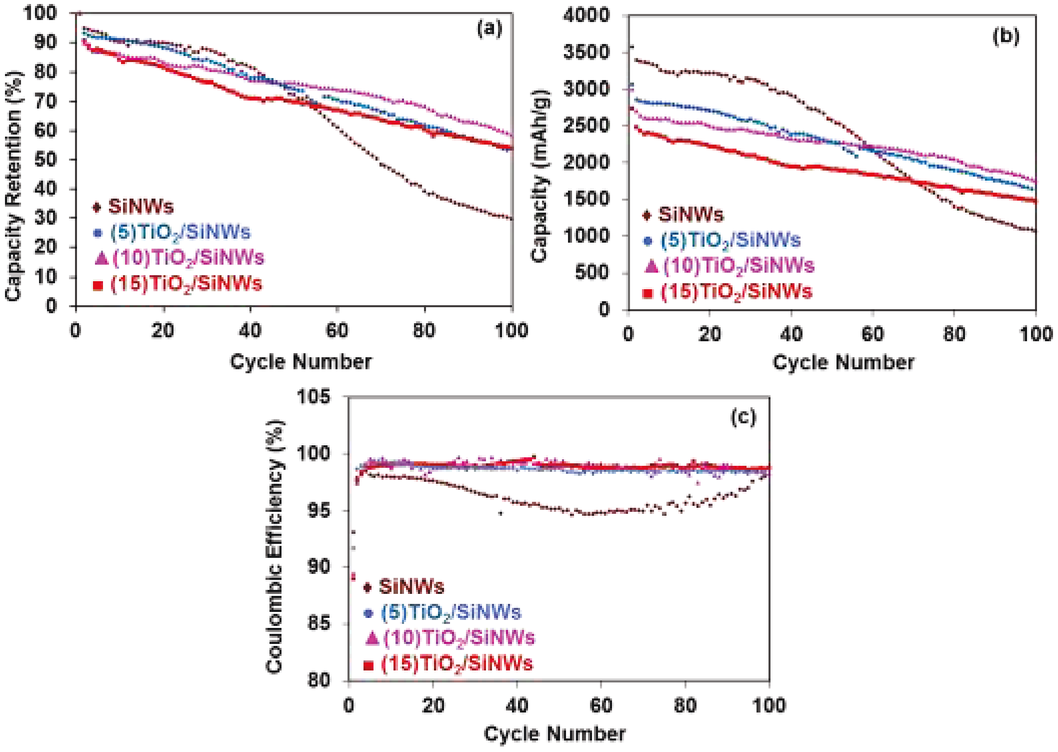

Figure 3.3: Capacity retention vs. cycle number, expressed as a percentage relative to the first cycle capacity, for bare and TiO_2-200/SiNWs nanocomposites at different TiO_2 thicknesses cycled at 0.1 C rate, (b) specific capacity in mAh/g and (c) corresponding coulombic efficiency.

High-resolution TEM images and EELS elemental maps of the TiO_2-coated SiNWs are shown in Figure 3.4. The TiO_2 coatings are seen to always be near the nominal thickness of 10 nm. The fast fourier transform (FFT) patterns show only the 111 spot of Si for the composites with TiO_2 deposited at 200 and 300 °C and the magnifications in Figure 3.4(b) and (e) show the lattice fringes of Si in the core and an amorphous structure in the coating. Only for the annealed TiO_2/SiNWs nanocomposite is the (101) reflection of anatase TiO_2, with interplanar spacing of 3.5 Å, observed in Figure 3.4(h) as well as the FFT pattern.

EELS maps of the as-prepared TiO_2/SiNWs nanocomposites showing the distribution of the elements are shown in Figure 3.4(c), (f) and (i). For all the TiO_2-coated composites, the Ti and O signals are strongest near the edges of the imaged area, where the signal is mainly originating from the TiO_2 shell, whereas the Si signal is clearly strongest in the centre of the nanowire. This confirms the core-shell structure of composites prepared with ALD and the coating thickness is again shown to be nominal (10 nm).

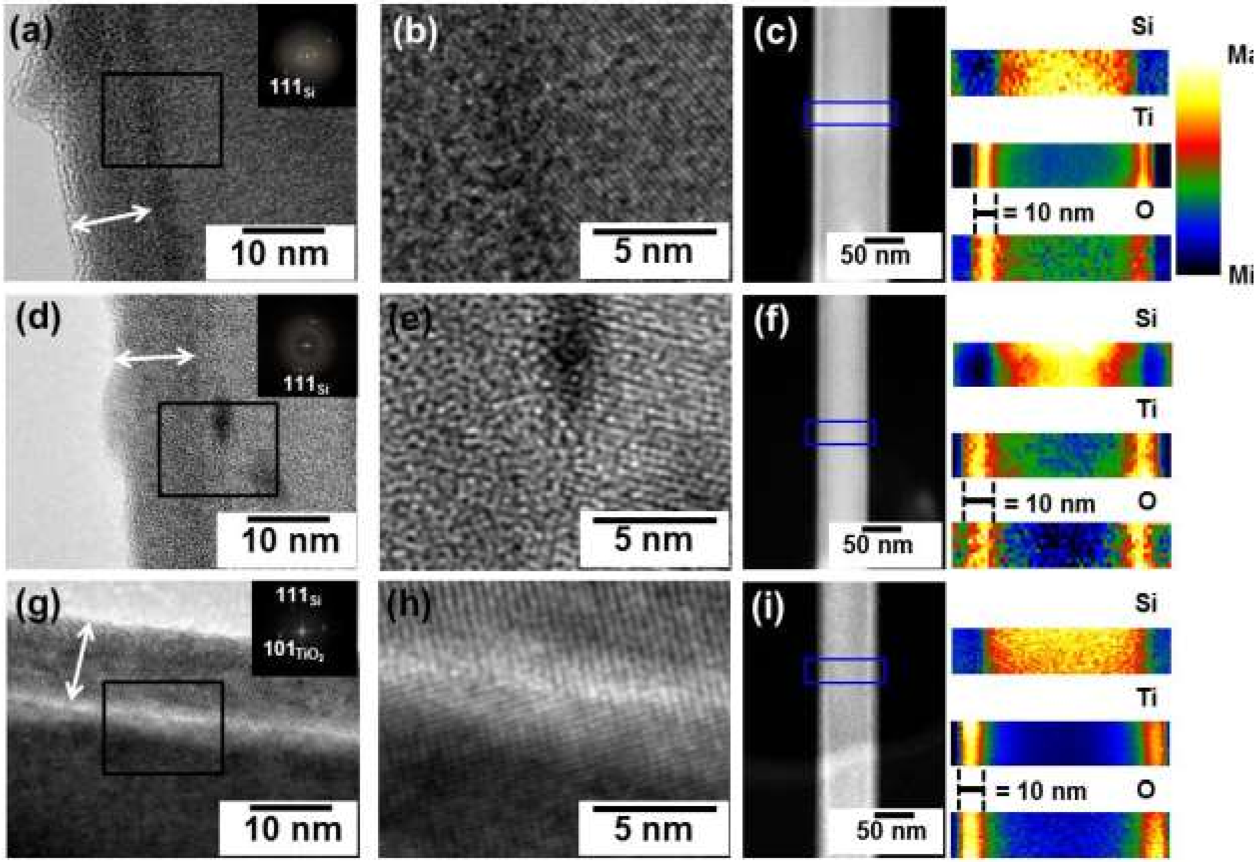

Figure 3.4: HRTEM images including fourier transforms (left and middle) and EELS maps (right) of (10)TiO_2-200/SiNWs, (a)-(c), (10)TiO_2-300/SiNWs (d)-(f), and (10)TiO_2-200(A)/SiNWs, (g)-(i). The areas delineated by the rectangles in (a), (d) and (g) are magnified by a factor 3 in (b), (e) and (h) which clearly show the lattice fringes for Si and, in the case of (10)TiO_2-200(A)/SiNWs, anatase TiO_2. The double-headed arrows in (a), (d) and (g) are the same length as the 10 nm scale bar. The HRTEM images and EELS maps show that the coating is at its nominal thickness.

XPS spectra for the as-made materials (see Figure 3.5) show native oxide for the bare SiNWs and TiO_2 for the coated nanowires. There is a slight variation in the peak position for the Ti2p spectra, where the Ti 2p1/2 peaks are centered at 464.2 eV, 464.4 eV and 464.5 eV and the Ti 2p3/2 peaks are centered at 458.4 eV, 458.5 eV and 458.8 eV for (10)TiO_2-200/SiNWs, (10)TiO_2-300/SiNWs and (10)TiO_2-200(A)/SiNWs, respectively. Differences in the Ti:O stoichiometry, due to differences in deposition temperature and annealing treatment, can shift the binding energy of Ti to lower values, but the presence of Ti in a lower valence state would lead to much more severe broadening than what is observed here. [46] For bare SiNWs, the $(CH_2)_n$ peak at 284.8 eV in the C1s spectra arises only from contamination and is substantially lower than for the TiO_2-coated materials. There is a downward trend in the intensity of the carbon signal with increasing deposition temperature and annealing treatment, indicating that for the coated SiNWs, part of the signal arises from residual organic groups from the ALD precursor (i.e. $OCH(CH_3)_2$) in the coating. The Ti binding energy in $Ti(OCH(CH_3)_2)_4$ is slightly lower than that in TiO_2[47] so it is likely that the observed variations are due to residual precursor and the crystallization of amorphous TiO_2 into anatase after annealing. The ‘tail’ in the O1s spectra possibly arises from silicon sub-oxide (SiO_x, $x < 2$) formed at the interface between the native oxide and the TiO_2 coating in the early stages of deposition as TiO_2 is thermodynamically more stable than SiO_2. [48]

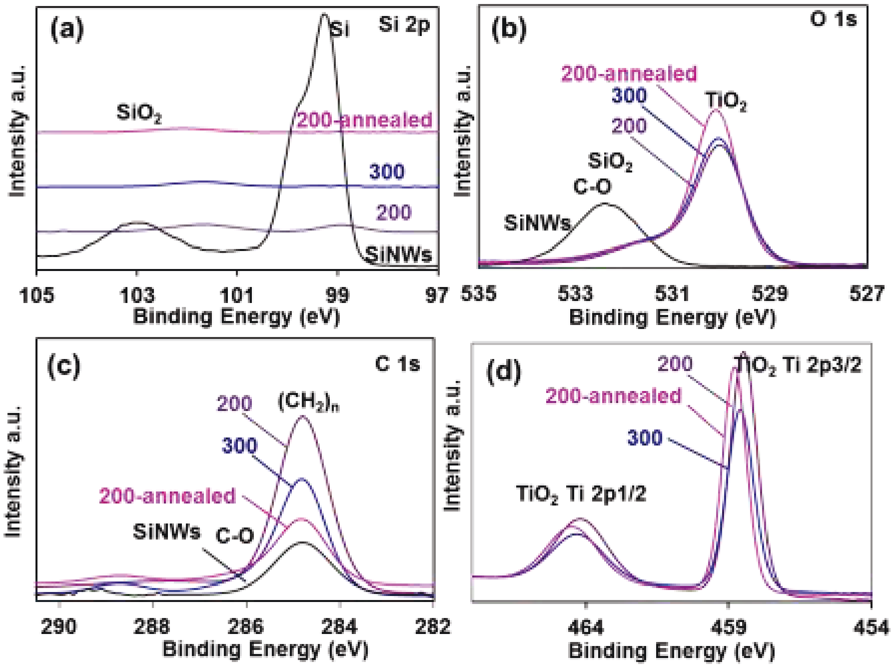

Figure 3.5: C1s, Si1s, O1s and Ti 2p XPS spectra of as-synthesized SiNWs, (10)TiO_2/SiNWs at ALD deposition temperatures of 200 and 300 °C and after annealing.

After deposition of the coatings at elevated temperatures, differences in thermal expansion coefficient between the TiO_2 coating, SiO_2 native oxide and Si nanowire core will result in stress when the material is cooled down to room temperature. The expansion coefficient of SiO_2 is approximately constant at $\sim 2\times10^{-6}\ K^{-1}$ and that of Si is 2.75-$3.75\times10^{-6}\ K^{-1}$ in the range between room-temperature and 300 °C. For amorphous TiO_2, the average thermal expansion coefficient is estimated to be about three times larger, $6x10^{-6}$ in the range between 0 and 250 °C. [49, 50] The resulting stress, as determined from Si substrate bending measurements on planar films, was reported by Huang et al. to be 682 MPa for an ALD deposition temperature of 300°C. This value decreased sharply for lower growth temperatures. Crystallization by annealing increased the stress even further. [51] Thus, given the different deposition and annealing temperatures and different levels of residual precursor, the coatings can be expected to perform quite differently from one another.

When the composites are electrochemically cycled, differences do indeed emerge. Table 3.1 summarizes the measured first discharge (lithiation) specific capacity, first-cycle capacity loss ([1st discharge capacity – 2nd discharge capacity]/[first discharge capacity]) and coulombic efficiency (CE), defined as CE = delithiation capacity/lithiation capacity. As expected, TiO_2/SiNWs nanocomposites show a reduced capacity, because the capacity of TiO_2 is much smaller than that of Si (330 vs. 3590 mAh/g). The first discharge capacity loss is higher and CE is lower for TiO_2/SiNWs nanocomposites, which is more pronounced for the amorphous coatings.

Table 3.1: Galvanostatic electrochemical results obtained for the bare and TiO_2 coated SiNWs nanocomposites at 0.1 C- rate

Electrode	First discharge specific capacity ($mAhg^{-1}$)	First cycle capacity loss (%)	Initial Coulombic efficiency (%)
SiNWs	3576	5	93
TiO_2-200/SiNWs	3000	11	89
TiO_2-300/SiNWs	2909	9	90
TiO_2-200(A)/SiNWs	2769	7	91

Figure 3.6(a) and (b) depict the voltage profiles of bare SiNWs and the TiO_2-200/SiNWs nanocomposite during constant-current (CC), or galvanostatic, charge/discharge in a voltage window of 0.01-2 V vs. Li/Li^+ at a rate of 0.1C. For both electrodes, phase transformation of crystalline Si into amorphous Li_xSi causes the appearance of a long voltage plateau located at

around 0.1 V during lithiation. [52, 53] The delithiation curves exhibit a single and flat plateau at about 0.4 V, corresponding to the two-phase reaction from crystalline $Li_{15}Si_4$ to amorphous Li_ySi. [54] After the first cycle, the lithiation curves exhibit several sloping plateaus related to multiple amorphous Li-Si phases with different Li/Si ratios. Magnification of the first 250 mAh/g in the voltage profiles of the first lithiation cycle (Figure 3.6(c)) shows there are differences in the electrochemical response of the TiO_2 coatings. The anatase coating clearly shows a small plateau around 1.7 V, whereas the curves for the amorphous coatings are rather featureless, in accordance with previous electrochemical studies on these different forms of TiO_2. [9, 55, 56]

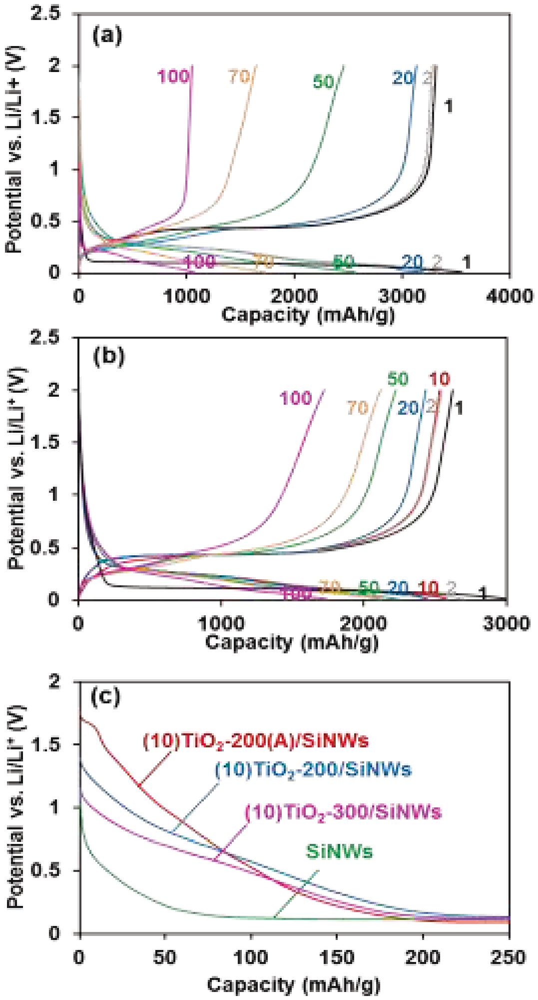

Figure 3.6: Galvanostatic discharge/charge voltage profiles of (a) SiNWs, (b) (10)TiO_2-200/SiNWs, (c) magnification of the first 250 mAh/g in the first discharging cycle at 0.1 C rate.

Constant-current measurements of identically prepared planar TiO_2 films are shown in

Figure 3.7 and show many of the same features. For the bare nanowires, the voltage profile drops quickly to 0.1 V in the lithiation process where the initial 50 mAh/g likely corresponds to reduction of the native oxide on silicon. [53] From Figure 3.6(a) and (b), it is already obvious that the specific capacity in cycle 100 is considerably higher for (10)TiO_2-200/SiNWs than it is for bare SiNWs. A more elaborate comparison of the cycle life and CE vs. cycle number between TiO_2/SiNWs nanocomposites and bare SiNWs is shown in Figure 3.8.

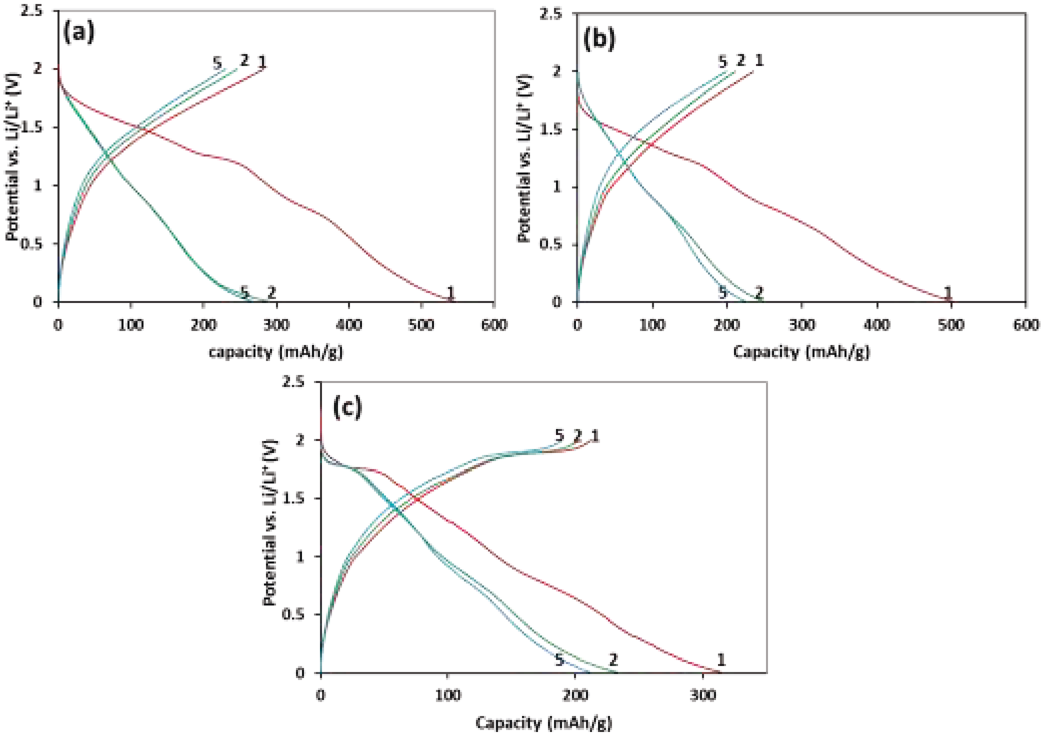

Figure 3.7: Galvanostatic discharge/charge curves of 10 nm TiO_2 at ALD deposition temperature of (a) 200 °C (b) 300 °C, (c) after annealing treatment at 600 °C for 1 hr at 0.1 C-rate.

The capacity retention after 100 cycles, as a percentage of the capacity in the first cycle, increases in the order bare SiNWs < (10)TiO_2-200(A)/SiNWs < (10)TiO_2-300/SiNWs < (10)TiO_2-200/SiNWs, from 30 to 40, 44 and finally 58%. The specific capacity at cycle 100 increases in the same order from 1065 mAh/g for bare SiNWs to 1112, 1275 and finally 1600 mAh/g for (10)TiO_2-200/SiNWs. The coulombic efficiency *vs.* cycle number of uncoated, amorphous and crystalline TiO_2-coated SiNWs is plotted in Figure 3.8(c). The trend is consistent with the one obtained from the cycle life (capacity) plots. CE decreases in the same order as the capacity retention and specific capacity after 100 cycles. Bare SiNWs initially have ~98% efficiency, but this becomes as low as 95% when capacity degradation is most rapid between cycle 40 and 80. For (10)TiO_2-200/SiNWs the CE is consistently between 98 and 99.5%, which is among the highest reported for SiNWs in standard, carbonate solvents-based electrolytes.

The rate capability of the bare and coated SiNWs was also tested and the results are shown in Figure 3.8(d). Up to 1 C rate, there is little difference between the three coated electrodes, although the bare SiNWs perform clearly worse. At 2 C and 5 C, however, clear differences between the coated materials emerge with (10)TiO_2-200/SiNWs coming out as clearly better than both (10)TiO_2-300/SiNWs and (10)TiO_2-200(A)/SiNWs which can cycle 34, 25 and 19%, respectively, of their initial capacity at 5 C. Thus, it is shown that crystallisation of the TiO_2 coating is detrimental to the electrochemical performance of the composite.

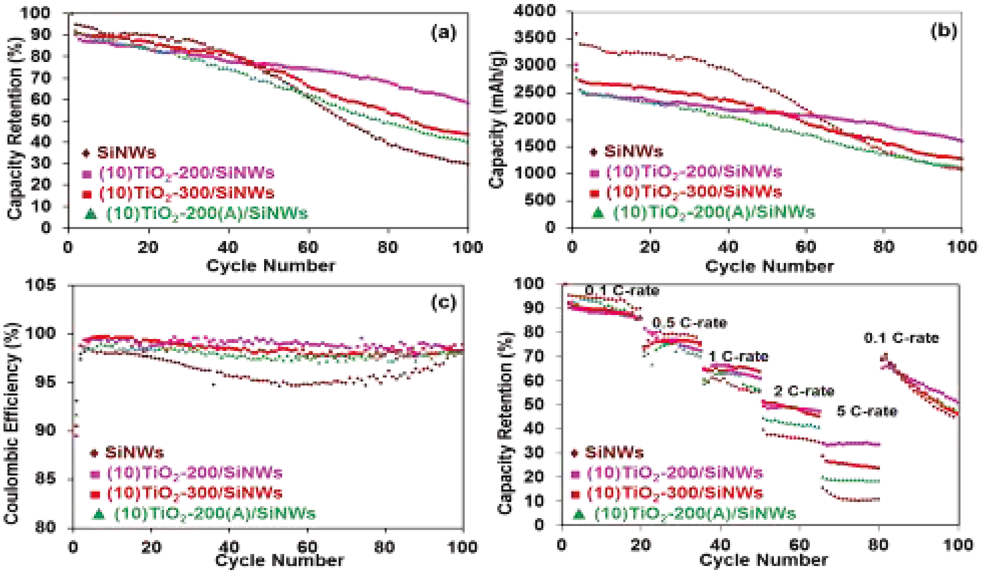

Figure 3.8: (a) Capacity retention vs. cycle number, expressed as a percentage of the first cycle capacity, for bare SiNWs and TiO_2/SiNWs nanocomposites deposited at different temperatures and with annealing treatment at 0.1 C rate, (b) cycle life expressed as specific capacity, (c) corresponding Coulombic efficiency, and (d) comparison of the rate capability of bare SiNWs and the nanocomposites expressed as apercentage of the initial capacity at 0.1 C.

The data in Table 3.1 show that the trend in coulombic efficiency in cycle 1 is opposite to the long-term trend. The reasons for this can be deduced from Figure 3.9. The single-crystal diffraction pattern of Si is no longer found in the SAD pattern of the TiO_2-200/SiNWs composite (Figure 3.9(a)) as nanowires become amorphous after 1 full lithiation/delithiation cycle. [22] A ring pattern corresponding to cubic $LiTiO_2$ is observed, despite the fact that the electrode is in the delithiated state. The calculated d-spacings are 0.204, 0.146 nm, similar to what was previously found for cubic lithium titanate ($LiTiO_2$). [56] The HRTEM image in Figure 3.9(b) confirms the presence of crystalline $LiTiO_2$ phase embedded in an amorphous phase. The lattice fringe spacing is 0.204 nm, corresponding to the (200) planes of cubic $LiTiO_2$. Also for (10)TiO_2-300/SiNWs, the $LiTiO_2$ phase is found with identical lattice spacings as for (10)TiO_2-200/SiNWs (see Figure 3.10).

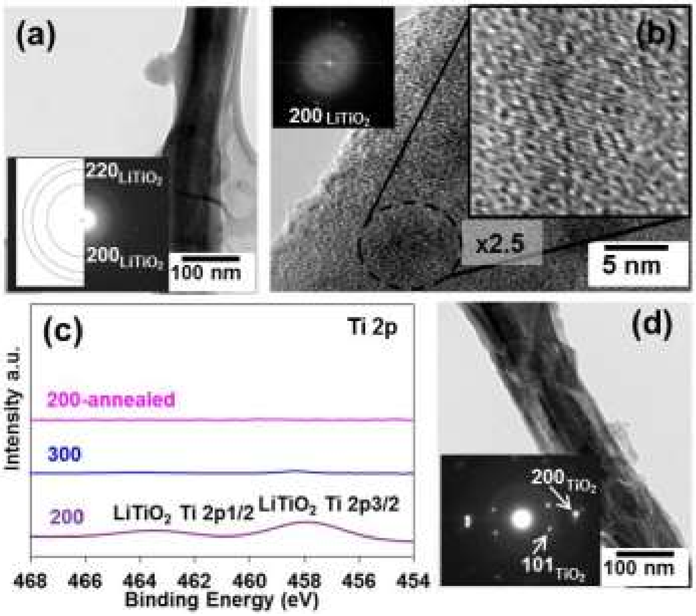

Figure 3.9: (a) Bright-field TEM and SAD pattern of TiO_2 -200/SiNWs, (b) HRTEM and FFT pattern of the same showing 200$LiTiO_2$ lattice spacing. (c) Ti XPS spectrum after 1 cycle of TiO_2 -200/SiNWs, TiO_2 -300/SiNWs and TiO_2 -200(A)/SiNWs and (d) bright-field TEM and SAD pattern of TiO_2 -200(A)/SiNWs.

In the Ti2p XPS spectrum for TiO_2-200/SiNWs in Figure 3.9(c), the peaks for TiO_2 are still visible, but have shifted to lower binding energies by ~0.75 eV. This shift reflects the change of Ti^{+4} to Ti^{+3} oxidation state upon formation of $LiTiO_2$. [57] The electrodes are in the delithiated state so the presence of $LiTiO_2$ indicates irreversible trapping of Li within the voltage range used, leading to a lower coulombic efficiency in the first cycle. Note that TiO_2-200/SiNWs is the only composite for which a signal from the original interface with the electrolyte is still detected, showing that despite the lowest first cycle efficiency, this composite forms the thinnest SEI layer, although individual nanowires are still easily distinguishable in SEM micrographs after 1 cycle for all four electrodes (see Figure 3.11).

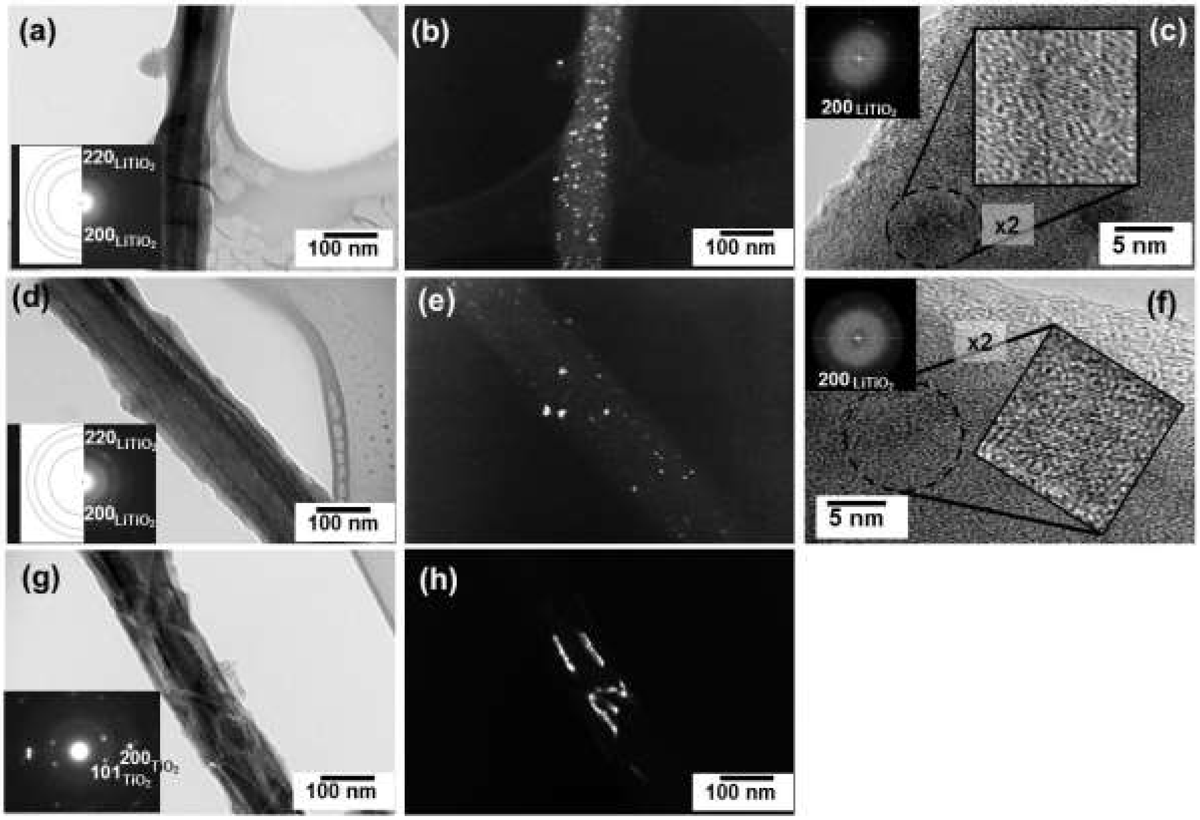

Figure 3.10: TEM micrographs of (a)-(c) (10)TiO_2-200/SiNWs, (c)-(f) (10)TiO_2-300/SiNWs, (g) and (h) (10)TiO_2-200(A)/SiNWs after 1 cycle (after delithiation to 2 V). (a), (d) and (g) bright field micrographs with corresponding selected area diffraction (SAD) insert. (b), (e) dark field micrographs using a portion of 200_{LiTiO2} ring pattern, highlighting coarser grain size of $LiTiO_2$ in (d). (f) dark field micrograph of the TiO_2 obtained using $g=101_{TiO2}$. HRTEM images of (c) (10)TiO_2-200/SiNWs, and (f) (10)TiO_2-300/SiNWs, highlighting partial crystallization of $LiTiO_2$ phase embedded in the amorphous region.

The SAD pattern of lithiated TiO_2-200(A)/SiNWs (35th cycle) does show evidence for $LiTiO_2$ (see Figure 3.12), but the amount is very small, consistent with the finding that anatase TiO_2 only transforms into $LiTiO_2$ in extremely small particles.[41] This is consistent with our CC

(Figure 3.7) and CV measurements (see Figure 3.13) on the planar TiO_2 films and previous findings on amorphous vs. crystalline TiO_2 [55] which show higher total and irreversible capacity for the amorphous material. The CC curve for the planar anatase film shows a small plateau both on lithiation, at 1.7 V, and delithiation, 1.9 V, which is consistent with the fact that the SAD pattern of TiO_2-200(A)/SiNWs in Figure 3.9(d) shows only anatase TiO_2 and shows no evidence of residual, trapped Li.

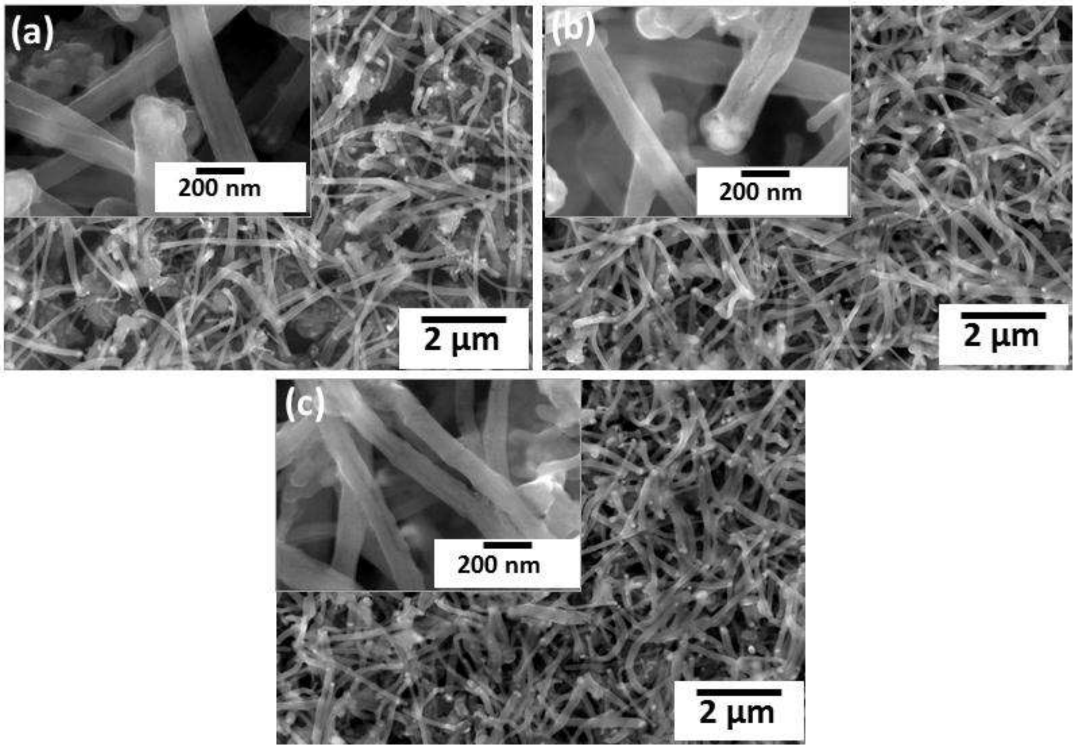

Figure 3.11: SEM images of (a) (10)TiO_2-200/SiNWs, (b) (10)TiO_2-300/SiNWs and (c) (10)TiO_2-200(A)/SiNWs after the first cycle at 0.1 C-rate.

The above findings also explain the improved rate capability of TiO_2-200/SiNWs compared to bare SiNWs and anatase-coated SiNWs as $LiTiO_2$ provides an electrically conductive pathway [42] and the amorphous fraction has favourable Li transport properties. Even when delithiation is continued up to 3 V vs. Li/Li^+, $LiTiO_2$ does not fully delithiate as Figure 3.12 shows. The (111) and (222) diffraction spots are also visible in the SAD pattern and definitively confirm that the structure is cubic. Dark-field images in Figure 3.10, taken using a portion the 200 $LiTiO_2$ diffraction ring, show a larger grain size of the $LiTiO_2$ phase for TiO_2-

300/SiNWs, likely due to the higher residual precursor content at 200 °C. Higher deposition temperatures are also reported to lead to slightly more dense coatings, irrespective of precursor residues, [51] which may also contribute to the difference in LiTiO$_2$ grain size. Measurements of the refractive index on the planar films also confirm this (see Figure 3.14).

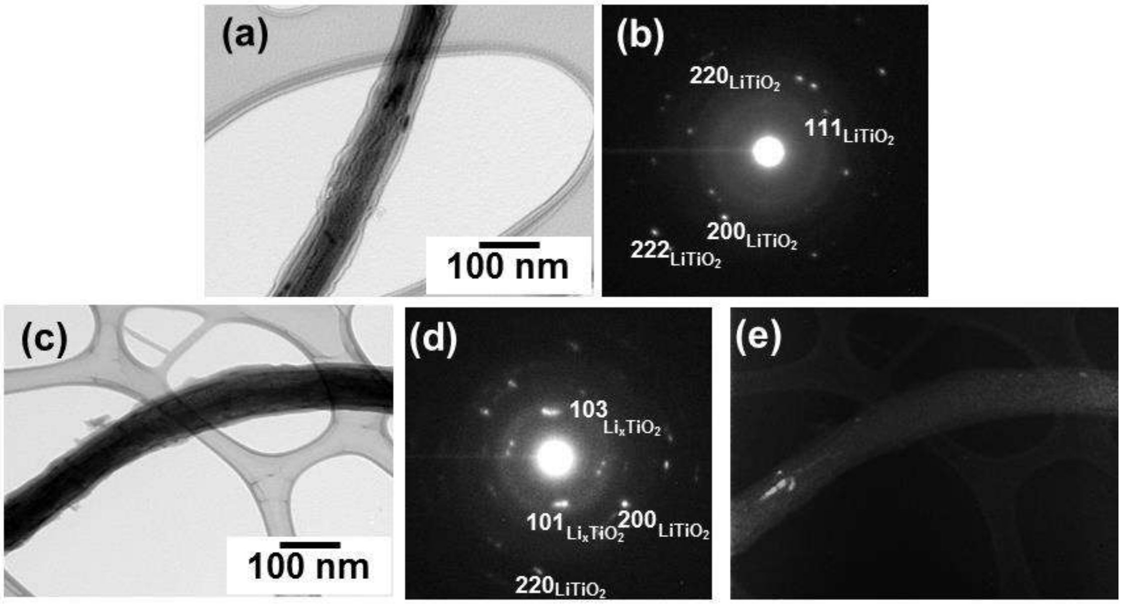

Figure 3.12: a) bright-field image of (10)TiO$_2$-200/SiNWs after 1 cycle between 0.01 and 3V vs. Li/Li$^+$ (b) corresponding SAD pattern confirming the cubic structure. (c)-(e) TEM micrographs of TiO$_2$-200(A)/SiNWs after 35 cycles (after lithiation to 0.01 V). (c) Bright field micrograph, (d) corresponding indexed selected area diffraction (SAD) pattern, (c) dark field micrograph using g=101$_{\text{LixTiO2}}$, (e) dark field micrograph obtained using g=200$_{\text{LiTiO2}}$.

Figure 3.15 presents a cross-sectional view of TiO$_2$-200/SiNWs and TiO$_2$-200(A)/SiNWs after 100 cycles obtained using a focussed ion beam, together with EDX elemental mappings of silicon, titanium, carbon, oxygen and fluorine. The Ti and Si signals are strongly correlated for both composites and increase towards the substrate, showing that the TiO$_2$ coating completely covers the SiNWs, once more highlighting the ability of ALD to conformally coat the nanowires. For TiO$_2$-200/SiNWs, contrary to TiO$_2$-200(A)/SiNWs numerous voids and some individual nanowires are visible in the top part of the cross-section, indicating less SEI formation and increased mechanical support and reinforcement by the TiO$_2$ coating, consistent with its higher coulombic efficiency compared to TiO_2- 200(A)/SiNWs. The Ti and Si signals also appear weaker whereas all other elements that generally make up the SEI are at least as strong, indicating the the SEI layer is indeed thicker inTiO_2-200(A)/SiNWs.

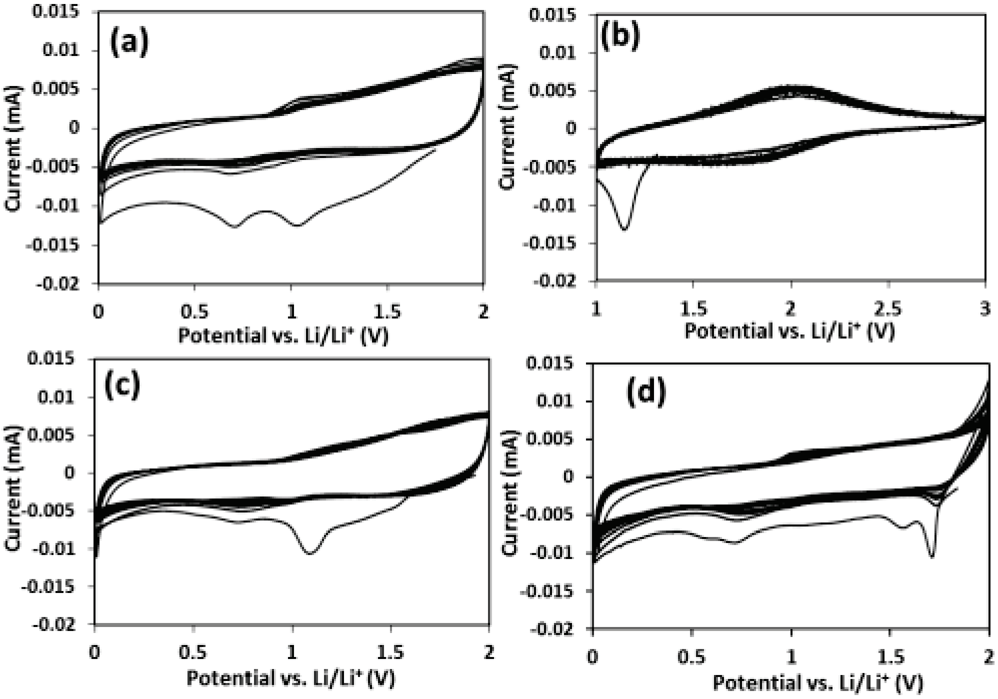

Figure 3.13: CV curves of planar TiO_2 films (a), deposited at 200°C between 0.01 and 2V and (b) between 1 and 3 V vs. Li/Li^+, (c) deposited at 300°C and (d) annealed at 600°C between 0.01 and 2V at a scan rate of 0.2 mV/s.

There are some small cracks beginning to form between the bottom of the nanowire agglomerate and the TiN layer on the substrate. This should account for part of the capacity decline that is still observed for TiO_2-200/SiNWs and shows that one of the degradation mechanisms that has been observed for SiNWs, delamination and formation of large voids near the substrate that has been observed for bare and Mg-coated SiNWs, [33] is not entirely prevented but greatly delayed. Again, this highlights the major improvement that is achieved by comformal coverage by the coating achieved with ALD as opposed to directional deposition methods such as sputtering.

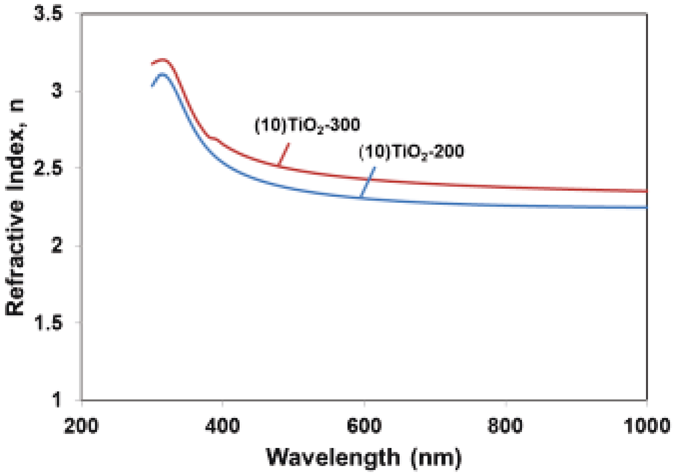

Figure 3.14: Refractive index as a function of wavelength for 10 nm planar TiO_2 films on Si deposited at 200 and 300°C.

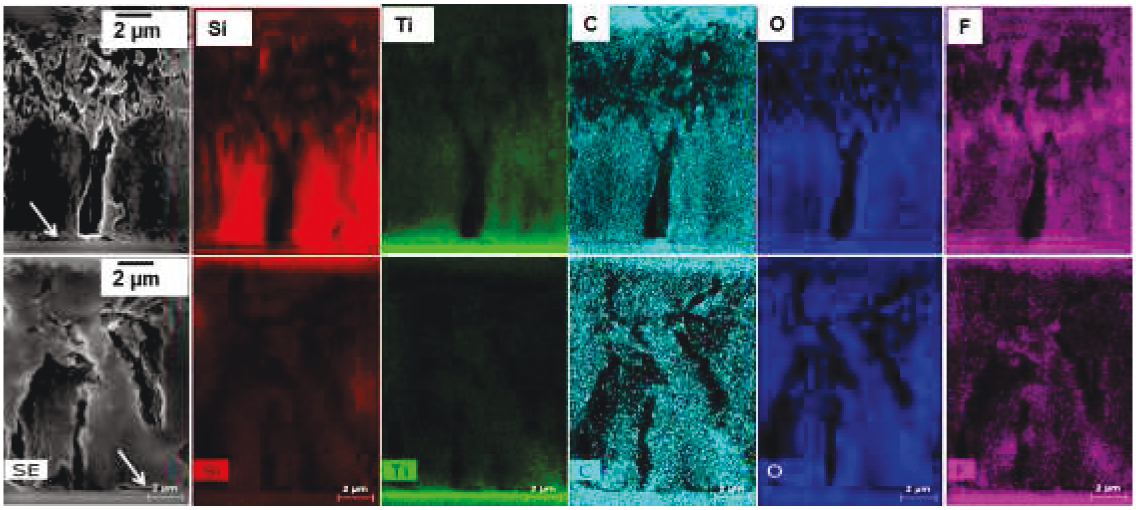

Figure 3.15: FIB cross-section SEM images of TiO_2-200/SiNWs, and TiO_2-200(A)/SiNWs together with elemental mappings of Silicon, Titanium, Carbon, Oxygen and Fluorine after 100 cycles at a rate of 0.1 C. The arrows indicate the locations of cracks that are forming between the nanowire agglomerate and the TiN layer on the substrate.

The SEM micrographs in Figure 3.16 and TEM micrographs in Figure 3.17 show the microstructure of the electrodes after 100 cycles. Bare nanowires form a porous agglomerate where the shape of individual nanowires is no longer recognizable. By contrast, for TiO_2-200/SiNWs the nanowires' original shape is essentially intact after 100 cycles, showing that the coating indeed helps maintain the mechanical integrity of the nanowires during cycling.

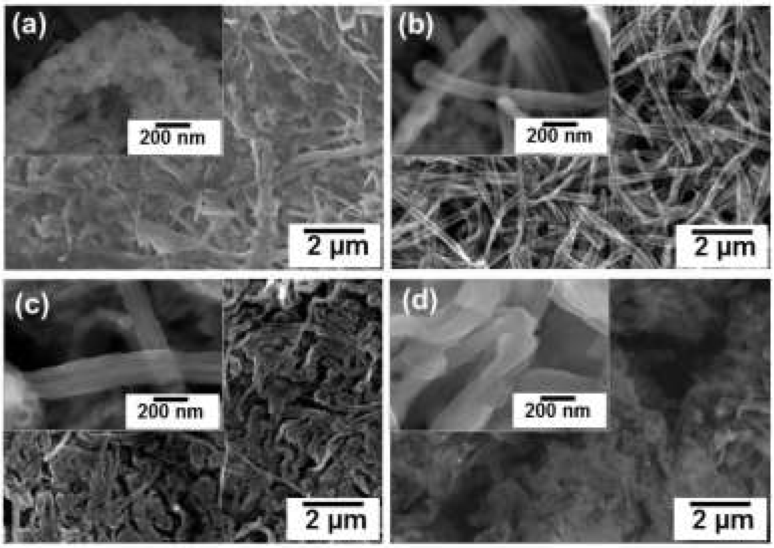

Figure 3.16: SEM images of (a) SiNWs, (b) TiO_2-200/SiNWs, (c) TiO_2-300/SiNWs (d) TiO_2-200(A)/SiNWs after 100 cycles at 0.1 C.

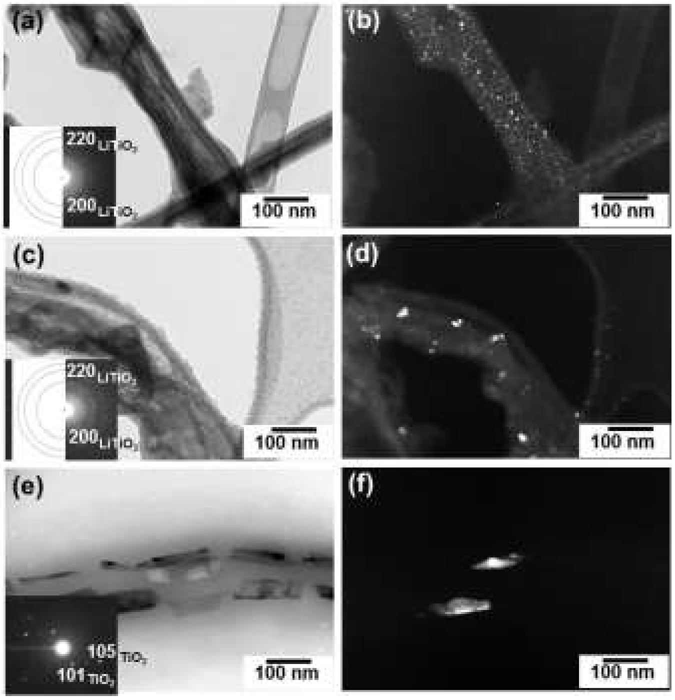

Figure 3.17: TEM micrographs of, (a) and (b),TiO_2-200/SiNWs, (c) and (d), TiO_2-300/SiNWs and (e) and (f), TiO_2-200(A)/SiNWs after 100 cycles (after delithiation to 2 V). (a), (c) and (e) are bright field micrographs with corresponding SAD inserts. (b), and (d) dark field micrographs using a portion of the 200_{LiTiO2} ring, (f) dark field micrograph using $g=101_{TiO2}$.

The picture is similar for the 5 and 15 nm coatings as Figs. 3.18 and 3.19 show. The degree of agglomeration observed in Figure 3.16 increases in the same order as the CE, electrochemical cycling stability and rate capability decrease. Consistent with the electrochemical measurements in Figs. 3.6 and 3.8, there is a very big difference between TiO_2-200/SiNWs and TiO_2-200(A)/SiNWs in Figure 3.16. From the TEM images taken after 100 cycles at 0.1 C-rate in Figure 3.17, a possible explanation for this can be found. The SAD pattern and dark field image (Figure 3.17(b)), which was obtained using a portion of the 200 $LiTiO_2$ diffraction ring, confirms the presence of $LiTiO_2$ also after 100 cycles. The $LiTiO_2$ phase looks to be homogeneously distributed over the entire width and length of the nanowire and has a very small grain size. A very different microstructure is found for TiO_2-200(A)/SiNWs where the anatase TiO_2 shell has cracked open and partially peeled off from the nanowire core. The dark-field image obtained from the 101 diffraction spot of anatase TiO_2, shows that each of the shell fragments is likely a single crystal. Because nanocrystalline materials can withstand higher deformation before fracturing, one would expect the anatase coating to be more vulnerable to fracture and delamination during cycling as the volume expansion of Si upon lithiation is very large. It can therefore be concluded that the two-phase nanostructure that has formed after the first cycle consisting of $LiTiO_2$ and amorphous TiO_2 is essential for obtaining good cycling stability. A similar argument applies for the difference between TiO_2-200/SiNWs and TiO_2-300/SiNWs that is evident in Figure 3.16(b) and 3.16(c). The $LiTiO_2$ grain size is clearly larger for the coating deposited at 300^{o}C (compare Figure 3.17(b)and 3.17(d)), although the difference is small compared to the annealed coating. That there is such a big difference in performance probably means the thermal stress in the as-made materials is also important.

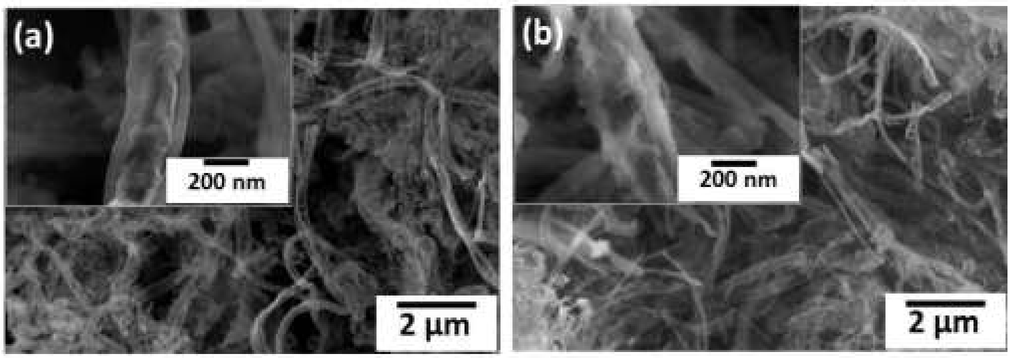

Figure 3.18: SEM images of (a) (5)TiO_2-200/SiNWs, (b) (15)TiO_2-200/SiNWs at 0.1 C-rate after 100 cycles.

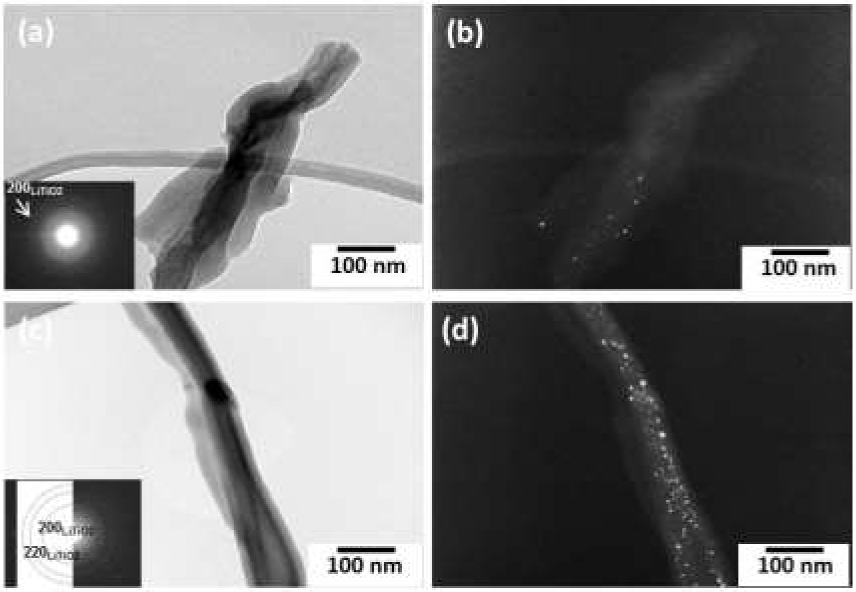

Figure 3.19: TEM micrographs of (a) and (b) (5)TiO_2-200/SiNWs, (c) and (d) (15)TiO_2-200/SiNWs after 100 cycles. (a) and (c) are bright field micrographs with corresponding SAD insert. (b), and (d) dark field micrographs obtained using a portion of the 200_{LiTiO2} ring pattern.

Figure 3.20 shows HAADF images and EELS elemental maps of bare SiNWs and the TiO_2 coated composites after 100 cycles. In this way, the spatial distribution of the SEI components across the nanowires can be visualized on the nanometre scale. Figure 3.20(a) shows that after 100 cycles, the bare SiNWs are completely covered by Li_2CO_3 or Li alkylcarbonate as there is nearly perfect overlap between the Li, C and O signals around a Si core. The Li, C and O signals are strong over the entire imaged area, indicating the Li_2CO_3 deposit is thick and that large amounts of SEI form on bare Si surfaces. For TiO_2-200/SiNWs (Figure 3.20(b)), there is a clear overlap between the Li and Ti-rich regions, indicating that also after 100 cycles, the $LiTiO_2$ phase is present as was also seen in TEM. Si is still concentrated in the core, in accordance with the SEM micrograph in Figure 3.16(b). At the outer surface of the structure depicted in Figure 3.20(b), there is a thin layer that is rich in Li and C, but this SEI layer is much thinner compared to bare SiNWs. For TiO_2-300/SiNWs and TiO_2-200(A)/SiNWs, the core region in the image is strongly depleted of Si and strong Si signal is found outside of the TiO_2 coating, indicating that the nanowire has broken up into several thinner strands as was already observed in Figure 3.17(c) and is also similar to what was observed for very thin Al coatings. [22]

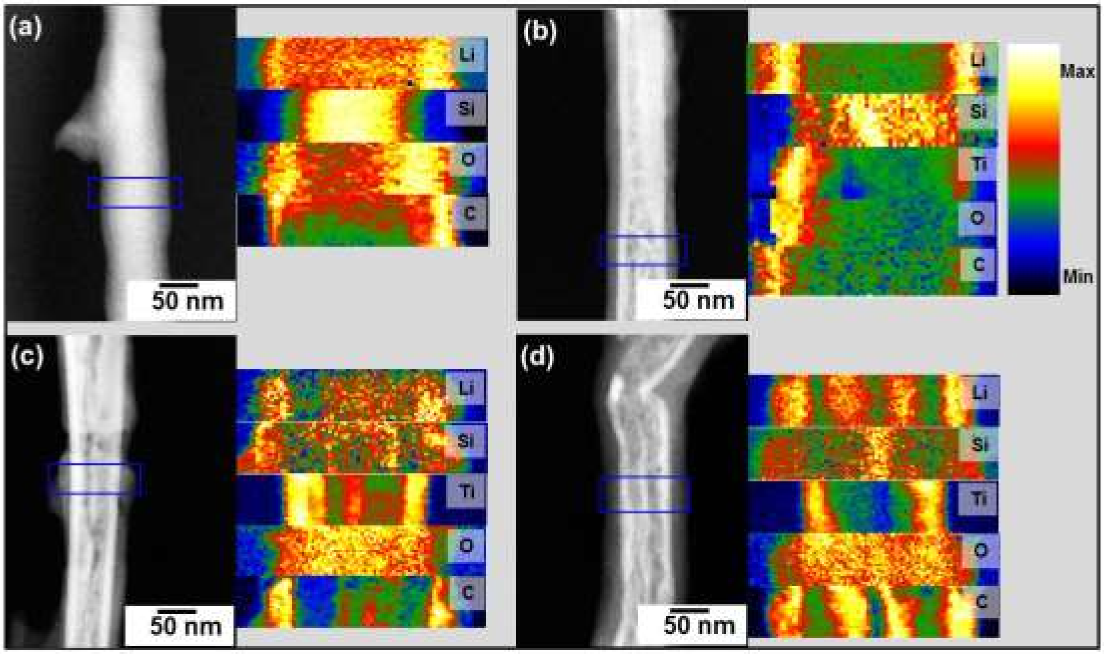

Figure 3.20: HAADF images and EELS elemental maps of Si, Ti, O, Li and C of cycled (a) SiNWs, (b) TiO_2-200/SiNWs, (c) TiO_2-300/SiNWs and (d) TiO_2-200(A)/SiNWs after 100 cycles in the delithiated state.

This observation can be explained by considering the effects of the forces exerted by the coating on the underlying Si. The parts of the nanowire that still have the TiO_2 coating attached will be under compressive stress after lithiation due to the large difference in volume expansion between the Si and TiO_2. From the rate capability data in Figure 3.8(d), it is clear that the coating improves the charge transfer kinetics which means the coated regions of the nanowire contract faster during delithiation than regions where the coating has delaminated. This would cause the uncoated Si(Li) to be 'extruded' through the gaps in the coating, leading to the microstructure consisting of thin strands of Si, parts of which are no longer enveloped by the coating, as is observed in Figure 3.20(c) and 3.20(d). It would then also be expected that higher charge and discharge rates exacerbate these effects and disintegration is indeed found to be much more severe, even for TiO_2-200/SiNWs, when cycling is performed continuously at higher rates (see Figure 3.21-3.24).

A material with a smaller grain size can sustain higher stress and deformation as a result of the larger volume expansion of SiNWs without delaminating and the observed trend in the mechanical stability of the coatings conforms to this. TiO_2-200/SiNWs developed the more fine-grained composite structure of $LiTiO_2$ and amorphous TiO_2 compared to TiO_2-300/SiNWs and the stability is improved accordingly. The grain size in the anatase coating after annealing is by far the largest, even after 100 cycles, and as a consequence has the worst cycling stability.

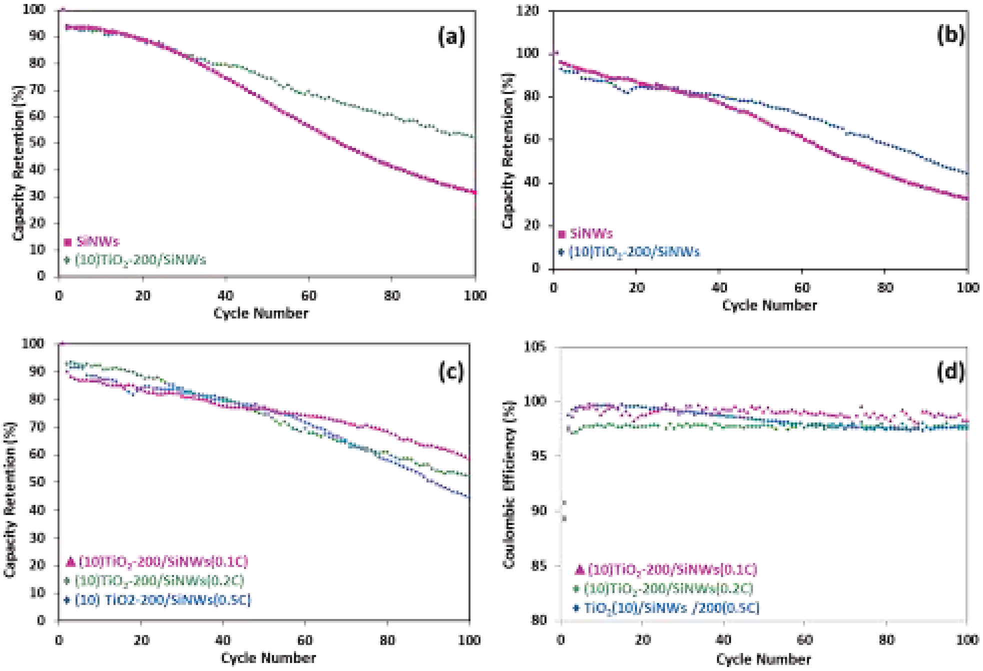

Figure 3.21: Capacity retention vs. cycle number for bare and (10)TiO_2-200/SiNWs nanocomposite at (a) 0.2 C-rate, (b) 0.5 C-rate, (c) Comparison of the % capacity retention of (10)TiO_2-200/SiNWs nanocomposite at different C-rates, and (d) comparison of the corresponding coulombic efficiency at different C-rates.

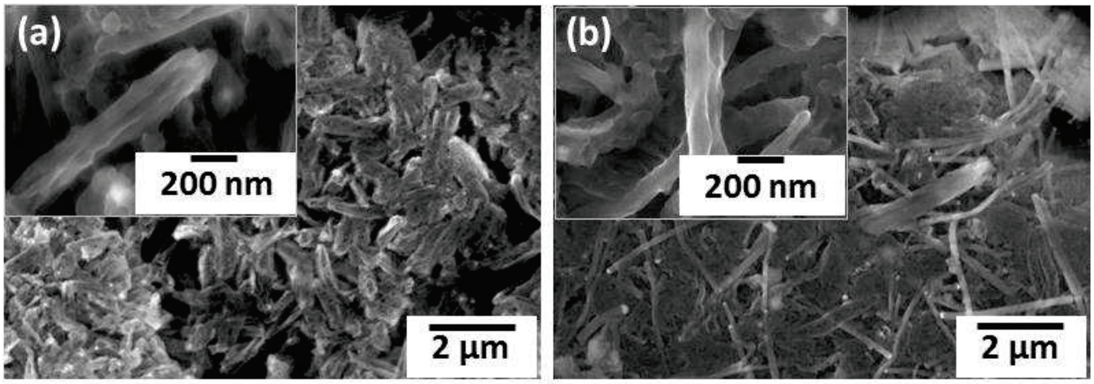

Figure 3.22: SEM images of (10)TiO_2-200/SiNWs at (a) 0.2 C-rate, (b) 0.5 C-rate after 100 cycles.

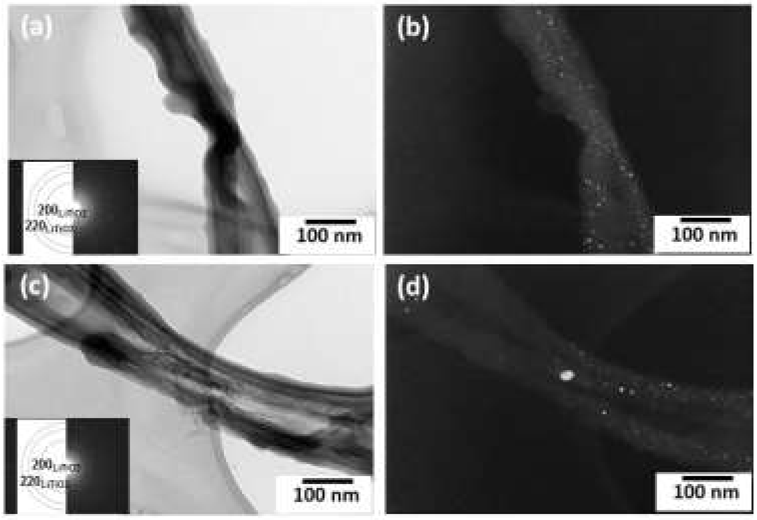

Figure 3.23: TEM micrographs of (10)TiO_2-200/SiNWs at (a) and (b) 0.2 C-rate, (c) and (d) 0.5 C-rate after 100 cycles. (a), and (c) bright field micrographs with corresponding SAD pattern insert. (b), and (d) dark field micrographs obtained using a portion of 200_{LiTiO2} ring pattern.

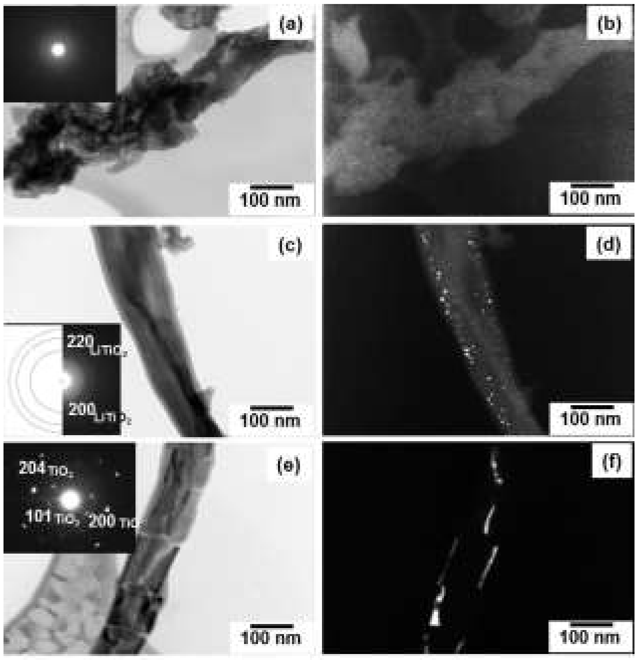

Figure 3.24: (a) TEM micrographs of (a) and (b) bare SiNWs, (c) and (d) (10)TiO_2-200/SiNWs and (e) and (f) (10)TiO_2-200(A)/SiNWs after 100 cycles at different rates according to Figure 3d (after delithiation to 2 V). (a), (c) and (e) bright field micrographs with corresponding SAD insert. (b), dark field micrograph using a portion of diffuse ring, (d) dark field micrographs using a portion of 200_{LiTiO2} ring pattern, and (f) dark field micrographs using $g=101_{TiO2}$.

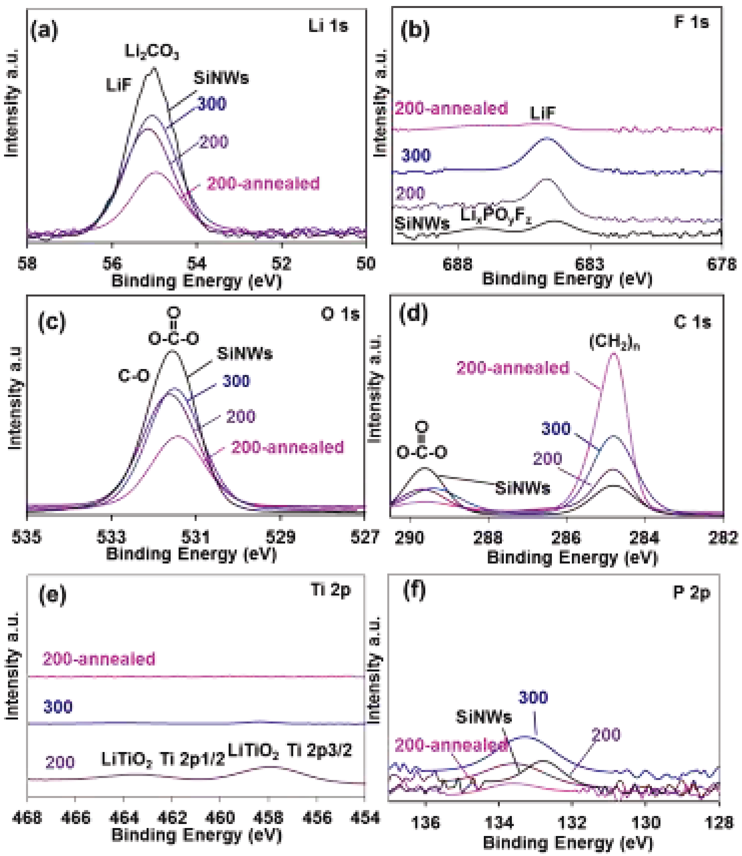

Figure 3.25: XPS spectra for bare SiNW electrode and electrodes coated with 10 nm TiO_2 after the first cycle.

The XPS spectra of the composites after 100 cycles are shown in Figure 3.26. Bare SiNWs have considerably higher Li signal, compared to the coated composites. The difference in the C1s and O1s spectra is smaller, although the trend is the same, and the peaks correspond to the signals of various carbonate species. [47, 58] Table 3.2 lists a summary of the XPS results expressed as atomic composition, in at.%, of the surface films. The Li content is shown to increase in the order TiO_2-200/SiNWs < TiO_2-300/SiNWs < TiO_2-200(A)/SiNWs< bare SiNWs from 15 to 23 at.%, despite the higher amount of LiF for the coated electrodes. This indicates that the SEI layer on the TiO_2 coated electrodes contains more single-electron reduction products such as $C_2H_5OCO_2Li$, whereas that on bare SiNWs has a higher amount of Li_2CO_3, consistent with the observed differences in coulombic efficiency.

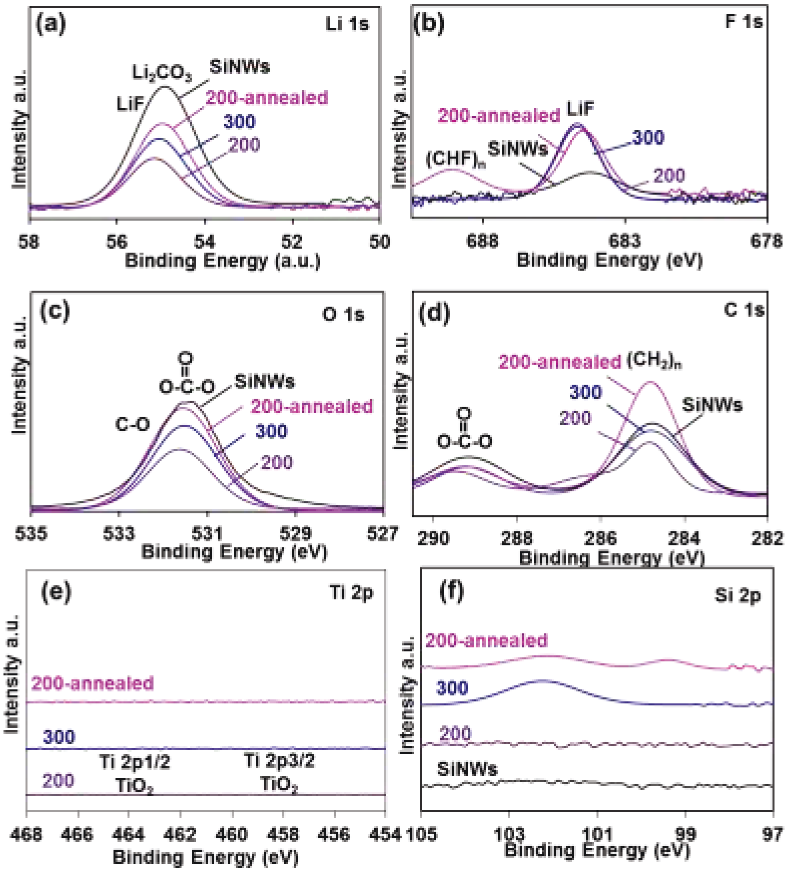

Figure 3.26: Li1s, F1s, O1s, C1s, Ti2p, P2p XPS spectra of 100 times-cycled SiNWs, TiO_2-y/SiNWs at ALD deposition temperatures of 200 and 300 °C and after annealing from the top surface of the electrodes in the delithiated state.

All the electrodes, except for TiO_2-200(A)/SiNWs, show lower relative Li content after 100 cycles, compared to after 1 cycle. This indicates that Li_2CO_3 is formed close to the original interface between the electrolyte and the SiNW or the TiO_2 coating layer and that the amount of Li alkoxides and alkylcarbonates is higher in SEI that forms in later stages of cycling. The fluorine content, mostly in the form of LiF is considerably higher for all the TiO_2-coated electrodes compared to bare SiNWs. For TiO_2-200(A)/SiNWs, the F1s spectra contain a peak around 689 eV in addition to LiF signal, indicating the presence of organofluorine compounds.[58] LiF is formed by electroless decomposition of the $LiPF_6$ salt [59] or a more complicated, but also electroless, reaction path involving trace water that is present in the electrolyte solvents. [60] For bare SiNWs, there is barely any detectable F1s signal, indicating that any LiF is completely covered by electrolyte reduction products formed on freshly exposed Si during lithiation. This is further evidence of the passivating effect of TiO_2 coating, especially for TiO_2-200/SiNWs. The fact that trace amounts of Si are detected for TiO_2-300/SiNWs and TiO_2-200(A)/SiNWs is consistent with the ‘extrusion’ mechanism described based on the EELS results.

Table 3.2: Surface composition, in atomic percentages, as derived from the XPS spectra in Fig Figure 3.24 and Figure 3.25 for 1 and 100 times cycled electrodes

Electrode	SiNWs		TiO_2-200/SiNWs		TiO_2-300/SiNWs		TiO_2-200(A)/SiNWs	
State	Cycle 1	Cycle 100	Cycle 1	Cycle 100	Cycle 1	Cycle 100	Cycle 1	Cycle 100
C1s	30	40	41	42	46	41	59	43
O1s	42	35	36	33	36	34	26	35
Li1s	27	23	19	15	20	17	14	18
F1s	<1	<1	1	6	1	5	<1	3
Other (Si, Ti, P)	1	2	3	4	<1	2	1	1

It should be noted here that as a way to improve coulombic efficiency and cycling stability, additions to, and wholesale reformulations of, the electrolyte have been studied as well. SiNWs cycled in dioxolane, which has a lower viscosity and a much higher resistance to reduction compared to carbonates, retain >2000 mAh/g after 100 cycles and 1250 mAh/g after 1000 cycles at 6 C. [58] However, ethers were abandoned early on in the development process of Li-ion batteries because of their poor oxidation resistance which makes them incompatible with conventional cathode materials.[59] Coatings have the distinct advantage that they are confined to one electrode only and therefore have no such compatibility issues.

A graphical representation of the microstructural evolution of bare and TiO_2 coated SiNWs is shown in Figure 3.27. Shown from left to right are an as-grown bare SiNW, a bare SiNW after 100 cycles including a thick SEI layer, an as-grown TiO_2-coated SiNW and finally a TiO_2-coated SiNW after 100 cycles. The picture illustrates how bare SiNWs disintegrate into thinner strands covered by thick SEI deposits as was shown in the inset of Figure 3.16(a) and previous in-situ microscopy studies. [32] For TiO_2-200/SiNWs, the coating adheres sufficiently strongly to the nanowire that the disintegration process that occurs for bare SiNWs is prevented and the SEI layer remains much thinner, as could be seen comparing Figure 3.20(b) and 3.20(c) and 3.20(d). The TiO_2-300/SiNWs and TiO_2-200(A)/SiNWs show a behaviour that is intermediate between those depicted in Figure 3.27. The EELS Si maps in Figure 3.20 clearly showed partial breakup into thinner strands, but the TiO_2 coating helps to retain better mechanical integrity than for bare SiNWs.

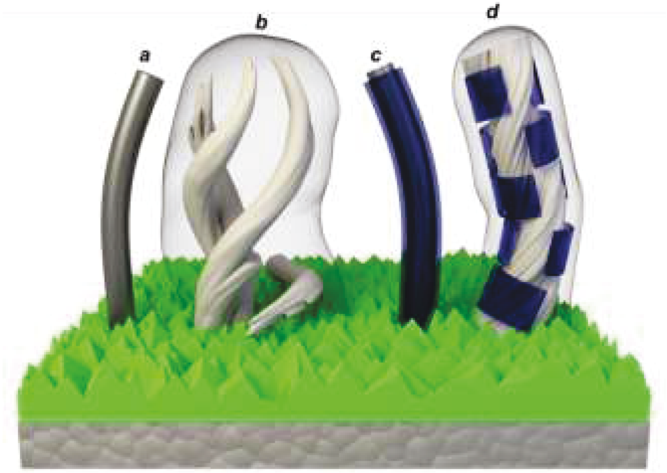

Figure 3.27: Schematic microstructural illustration of the (a) and (b) bare SiNWs, (c) and (d) TiO_2 coated SiNWs for (a) and (c) as-grown, (b) and (d) cycled samples.

Comparing the results presented here to previous studies on coated SiNWs, one of the most important findings is that the coating must be conformal and extend all the way to the substrate. Sputter coating improves coulombic efficiency, [22, 33] but the effects on cycling stability are not as clear. Because of the high directionality of sputtering, shadowing effects will reduce coverage of the SiNW significantly near the nanowire base. The fact that ALD can conformally coat a substrate of any shape is likely responsible for the significant improvement in all performance aspects for our TiO_2-coated silicon nanowires. The fact that a solution-based approach, where the nanowires were coated with a conducting polymer, was recently shown to achieve vast improvements in cycling stability as well, [61] further supports this.

We grew SiNWs on a rigid, planar substrate with relatively low mass loading of ~0.15 mg/cm^2. However, by dispersing Au nanoparticles onto a current collector/substrate with higher surface area such as Ni foam or hierarchically structured porous carbons, [62] the loading per geometric area could be much higher. ALD deposition of a TiO_2 coating would help improve the mechanical integrity of the contact points between the nanowire base and the substrate in the same way as we demonstrated here. PTFE and a conductive carbon additive are stable at our optimum ALD deposition temperature and direct deposition onto a powder electrode has also been shown to improve cycling stability to comparable levels as commercial graphite electrodes in a *binder-free* configuration.[63] For Si anodes, hollow nanospheres have already been shown to hold great promise as a binder-free system as well, [64] and ALD TiO_2 can be expected to help reduce the <10% capacity decay per 100 cycles even further. Thus, we have shown that ALD-deposited TiO_2 coatings greatly expand the number of ways in which the problematic cycling stability of Si can be improved. This is expected to become very important as Si anodes have been identified as the anode of choice for '3rd generation' automotive batteries by the US Department of Energy. [65]

3.4 Conclusions

Coating with TiO_2 not only improves the relative capacity retention by a factor two at 0.1 C and over a factor three at 5 C, but also increases the coulombic efficiency to 99%, compared to 95% for bare SiNWs, which is the highest value ever reported for SiNW-based electrodes in standard, carbonate-based electrolytes. Consistent with higher coulombic efficiency, SEM and XPS analysis showed less SEI formation overall and lower Li content compared to bare SiNWs for (10)TiO_2-200/SiNWs and (10)TiO_2-300/SiNWs, whereas crystallization of the TiO_2 into anatase by annealing is detrimental to the performance. EELS showed strongly reduced carbon signal in regions with intact TiO_2 coating, further confirming the passivating effect of TiO_2 towards SEI formation.

The best performance was found for electrodes where the TiO_2 coating is initially fully amorphous. The amorphous coatings develop a highly dispersed microstructure of crystalline $LiTiO_2$ and an amorphous phase during cycling that is highly resistant to delamination. Though $LiTiO_2$ was shown to also form from anatase, (10)TiO_2-200(A)/SiNWs does not develop the same fine-grained microstructure and as a consequence has inferior capacity retention.

The most important aspect of the coating seems to be that coverage should initially be 100%, all the way down to the nanowire base, as this was shown to be important in avoiding nanowire agglomeration followed by delamination from the conductive substrate. Future efforts can therefore be expected to concentrate on ALD and wet-chemical methods that are capable of producing conformal coatings on highly irregularly shaped substrates

3.5 Notes and references

[a] *University of Alberta, Chemical&Materials Engineering, 9107 116th Street, T6G 2V4, Edmonton AB, Canada, Tel: +1-780-850-2678; E-mail: pkalisvaart@gmail.com*

[b] *National Institute of Nanotechnology, 11421 Saskatchewan Drive, T6G 2M9, Address, Address, Town, Country.; Tel: +1-780-492-1542; E-mail: dmitlin@ualberta.ca*

†Electronic Supplementary Information (ESI) available: [details of any supplementary information available should be included here]. See DOI: 10.1039/b000000x/

1. J. M. Tarascon, and M. Armand, *Nature*, 2001, **414**, 359-367.
2. M. Armand, J. M. Tarascon, *Nature*, 2008, **451**, 652-657.
3. S. Bijani, M. Gabas, G. Subias, J. Garcia, L. Sanchez, J. Morales, L. Martinez and J. R. Ramos-Barrado, *J. Mater. Chem.*, 2011, **21**, 5368–5377.
4. D. Deng, M. G. Kim, J. Yang Lee and J. Cho, *Energy Environ. Sci.*, 2009, **2**, 818–837.
5. M. Pfanzelt, P. Kubiak, S. Jacke, L. Dimesso, W. Jaegermann and M.Wohlfahrt-Mehrens, *J. Electrochem. Soc.*, 2012, **159 (6)**, A809-A814.
6. B. J. Landi , M. J. Ganter , C. D. Cress , R. A. DiLeo, and R. P. Raffaelle, *Energy Environ. Sci.*, 2009, **7**, 638-654.
7. H. Wu, G. Chan, J. W. Choi, I. Ryu, Y. Yao, M. T.McDowell, S. W. Lee, A. Jackson, Y. Yang, L. Hu, and Y. Cui, *Nature Nanotechnology*, **7**, 2012, 310-315.
8. M. M. Thackeray, C. Wolverton, and E. D. Isaacs, *Energy Environ. Sci.*, 2012, **5**, 7854-7863.
9. W. H. Ryu, D. H. Nam, Y. S. Ko, R. H. Kim, H. S. Kwon, *Electrochemica Acta, 2012*, **61**, 19-24.
10. F. F. Cao, Y. G. Guo, and Li-Jun Wan, *Energy Environ. Sci.*, 2011, **4**, 1634-1642.
11. X. Meng, X. Q. Yang and X. Sun, *Adv. Mater.*, 2012, **24(27)**, 3589-615.
12. T. Song, D. H. Lee, M. S. Kwon, J. M. Choi, H. Han, S. G. Doo, H. Chang, W. Park, W. Sigmund, H. Kim and U. Paik, *J. Mater. Chem.*, 2011, **21**, 12619–12621.
13. T.D. Hatchard and J.R. Dahn, *J. Electrochem. Soc.*, 2004, **151**, A838.
14. V.L. Chevrier and J.R. Dahn, *J. Electrochem. Soc.*, 2010, **157**, A392.
15. L.Y. Beaulieu, T.D. Hatchard, A. Bonakdarpour, M.D. Fleischauer and J.R. Dahn, *J. Electrochem. Soc.*, 2003, **150**, A1457
16. J.L. Gómez-Cámer, J. Morales and L. Sánchez, *J. Mater. Chem.*, 2011, **21**, 811.

17. T. Zhang, J. Gao, L. J. Fu, L. C. Yang, Y. P. Wu and H. Q. Wu, *J. Mater. Chem.*, 2007, **17**, 1321–1325.

18. C. Yu, X. Li, T. Ma, J. Rong, R. Zhang, J. Shaffer,Y. An, Q. Liu, B. Wei and H. Jiang, *Adv. Energy Mater.* 2012, **2**, 68–73.

19. D. Larcher, S. Beattie, M. Morcrette, K. Edstroem, J. C. Jumas and J. M. Tarascon*, J. Mater. Chem*., 2007, **17**, 3759–3772.

20. A. Gohier, B. Laïk, J. P. Pereira-Ramos, C. S. Cojocaru, P. Tran-Van, *J. Power Sources*, 2012, **203**, 135-139.

21. K. Peng, J. Jie, W. Zhang and S. T. Lee, Appl. Phys. Lett., 2008, **93**, 033105.

22. E. L. Memarzadeh, W. P. Kalisvaart, A. Kohandehghan, B. Zahiri, C. M. B. Holt and D. Mitlin, *J. Mater. Chem*., 2012, **22**, 6655.

23. N. S. Choi, Y. Yao, Y. Cui and J. Cho, *J. Mater. Chem*., 2011, **21**, 9825–9840.

24. T. Song, J. L. Xia, J. H. Lee, D. H. Lee, M. S. Kwon, J. M. Choi, J. Wu, S. K. Doo, H. Chang, W. Il Park, D. S. Zang, H. Kim, Y. G. Huang, K. C. Hwang, J. A. Rogers and U. Paik, *Nano Lett*., 2010, **10**, 1710–1716.

25. R. Huang, X. Fan, W. Shen and J. Zhu, *Appl. Phys. Lett*., 2009, **95**, 133119.

26. T. Song, D. H. Lee, M. S. Kwon, J. M. Choi, H. Han, S. G. Doo, H. Chang, W. Park, W. Sigmund, H. Hansu Kim and U. Paik, *J. Mater. Chem*., 2011, **21**, 12619–12621.

27. B. Laïk, D. Ung, A. Caillard, C. S. Cojocaru, D. Pribat and J. P. Pereira-Ramos, *J. Solid State Electrochem*., 2010, **14**, 1835–1839.

28. K. Xu and A. Cresce, *J. Mater. Chem*., 2011, **21**, 9849–9864.

29. D. Liu, and G. Cao, *Energy Environ. Sci*., 2010, **3**, 1218-1237.

30. H. Chen, Z. Dong, Y. Fu and Y. Yang, *J. Solid State Electrochem*., 2010, **14**, 1829–1834.

31. H. Chen, Y. Xiao, L. Wang and Y. Yang, *J. Power Sources*, 2011, **196**, 6657–6662.

32. L. Q. Zhang, X. H. Liu, Y. Liu, S. Huang, T. Zhu, L. Gui, S. X. Mao, Z. Z. Ye, C. M. Wang, J. P. Sullivan and J. Y. Huang, *ACS Nano*, 2011, **5**, 4800–4809.

33. A. Kohandehghan, W.P. Kalisvaart, M. Kupsta, B. Zahiri, B. Shalchi Amirkhiz, Z. Li, E.L. Memarzadeh, L.A. Bendersky, D. Mitlin, *J. Mater. Chem. A*, 2013, **1**, 1600.

34. H. C. M. Knoops, M. E. Donders, M. C. M. van de Sanden, P. H. L. Notten, and W. M. M. Kessels, *J. Vac. Sci. Technol. A*, 2012, **30(1)**, 010801.

35. S. K. Cheah, E. Perre, M. Rooth, M. Fondell, A. Hårsta, L. Nyholm, M. Boman, T. Gustafsson, J. Lu, P. Simon and K. Edström, *Nano Lett.*, 2009, **9(9)**, 3230-3233.

36. X. Su, Q. Wu, X. Zhan, J. Wu, S. Wei, Z. Guo, *J. Mater. Sci.*, 2012, **47**, 2519–2534.

37. Z. Hong, M. Wei, T. Lan, L. Jiang and G. Cao, *Energy Environ. Sci.*, 2012, **5**, 5408–5413.

38. Y. Wang, X. Su and S. Lu, *J. Mater. Chem.*, 2012, **22**, 1969–1976.

39. H. W. Shim, D. K. Lee, I. S. Cho, K. S. Hong and D. W. Kim, *Nanotechnology*, 2010, **21**, 255706.

40. J. Wang, Y. Zhou, Y. Hu, R. O'Hayre and Z. Shao, *J. Phys. Chem. C*, 2011, **115**, 2529–2536.

41. M. Wagemaker, W.J.H. Borghols, F.M. Mulder, *J. Am. Chem. Soc.*, 2007, **129**, 4323

42. W.J.H. Borghols, D. Lützenkirchen-Hecht, U. Haake, E.R.H. van Eck, F.M. Mulder, M. Wagemaker, *Phys. Chem. Chem. Phys.*, 2009, **11**, 5742

43. Z. Y. Zeng, J. P. Tu, X. H. Huang, X. L. Wang, X. B. Zhao and K. F. Li, *Electrochem. Solid-State Lett.*, 2008, **11(6)**, A105-A107.

44. M. Pfanzelt, P. Kubiak, M. Fleischhammer, M. Wohlfahrt-Mehrens, *J. Power Sources*, 2011, **196**, 6815.

45. R.F. Egerton, Electron energy-loss spectroscopy in the electron microscope. 3rd ed2011, New York: Springer.

46. R. Methaapanon, R.F. Bent*, J. Phys. Chem. C*, 2010, **114**, 10498.

47. NIST XPS database at http://srdata.nist.gov/xps/Default.aspx

48. L. Brewer, *Chemical Reviews*, 1953, **52**, 1.

49. Y. Okada, Y. Tokumaru, *J. Apl. Phys.*, 1984, **56**, 314

50. T. Hanada, N. Soga, M. Ohkawa, *J. Non-Cryst. Solids,* 1986, **88**, 236

51. Y. Huang, G. Pandraud, P.M. Sarro, *J. Vac. Sci. Technol. A*, 2013, **31**, 01A148

52. V. L. Chevrier, J. W. Zwanziger and J. R. Dahn, *Can. J. Phys.*, 2009, **87**, 625–632.

53. X.H. Liu, J.W. Wang, S. Huang, F. Fan, X. Huang, Y. Liu, S. Krylyuk, J. Yoo, S.A. Dayeh, A.V. Davydov, S.X. Mao, S.T. Picraux, S. Zhang, J. Li, T. Zhu, J.Y. Huang, *Nature Nanotech.*, 2012, **7**, 749

54. L. Baggetto, R. A. H. Niessen, F. Roozeboom and P. H. L. Notten, *Adv. Funct. Mater.*, 2008, **18**, 1057–1066.

55. H. T. Fang, M. Liu, D. W. Wang, T. Sun, D. S. Guan, F. Li, J. Zhou, T. K. Sham and H. M. Cheng, *Nanotechnology*, 2009, **20**, 225701.

56. D. Wang, D. Choi, Z. Yang, V. V. Viswanathan, Z. Nie, C. Wang, Y. Song, J. G. Zhang and J. Liu, *Chem. Mater*., 2008, **20**, 3435–3442.

57. M. S. Wu, M. J. Wang, J. J. Jow, W. D. Yang, C. Y. Hsieh, H. M. Tsai, *J. Power Sources*, 2008, **185**, 1420–1424.

58. G. V. Etacheri, U. Geiger, Y. Gofer, G. A. Roberts, I. C. Stefan, R. Fasching and D. Aurbach, *Langmuir*, 2012, **28**, 6175−6184.

59. K. Xu, *Chemical Reviews*, 2004, **104**, 4303.

60. D. Aurbach, *J. Power Sources*, 2000, **89**, 206.

61. Y. Yao, N. Liu, M.t. McDowell, M. Pasta, Y. Cui, *Energy Environ. Sci*., 2012, **5**, 7927.

62. Z. Li, L. Zhang, B. Shalchi-Amirkhiz, X. Tan, H. Wang, B. C. Olsen, C. M. B. Holt, D. Mitlin, *Adv. Energy Mater*., 2012, **2**, 431-437.

63. Y. S. Jung, A. S. Cavanagh, L. A. Riley, S-H. Kang, A. C. Dillon, M. D. Groner, S. M. George, S-H. Lee, *Adv. Mater.,* 2010, **22**, 2172-2176.

64. Y. Yao, M. T. McDowell, I. Ryu, H. Wu, :L. Hu, W. D. Nix, Y. Cui, *Nano Lett.*, 2011, **11**, 2949-2954.

65. US Department of Energy Vehicle Technologies Program eere.energy.gov.

4 Si Nanotubes ALD Coated with TiO_2, TiN or Al_2O_3 as High Performance Lithium Ion Battery Anodes

Material in this chapter has been published in:

E. Memarzadeh Lotfabad, P.Kalisvaart, A. Kohandehghan, Kai Cui, Martin Kupsta, Behdokht Farbod, David Mitlin˒ *J. Mater. Chem. A*, 2014, **2**, 2504-2516.

4.1 Introduction

The specific energy storage capacity and the charge/discharge rate of lithium ion batteries are critical for their use in electric vehicles (EVs). [1,2] Increasing specific energy capacity remains a challenge despite the significant gains in rate capability and safety through the use of new materials. Replacing graphitic carbon with Si as the anode material can considerably increase the energy storage capacity of the battery. However commercialization remains limited by several factors, including the materials' accelerated failure relative to graphite. Mechanical failure is associated with the dramatic volume change during lithiation, which causes major stresses, fracture and contact loss of the active material, Si, with the current collector [3,4]. Consequently, relatively rapid capacity loss will occur. Studies show that mechanical failure can be mitigated by using Si-based nanostructures including solid nanoparticles, [5] thin films, [6,7] or hollow shapes such as nanotubes, hollow nanoparticles and related nanostructures. [3,8-15] These studies indicate that a key feature for electrode design is not only to provide sufficient free space during lithiation and to keep the dimensions of the structures well within the nano-scale regime, but also to tailor materials' active surface to remain primarily compressively stressed during lithiation. One outstanding example of such a strategy is to have hollow Si nanostructures where only the inner surface is active towards Li while the outer surface is passivated by a thick layer of native oxide. [11] In a hollow core-shell nanostructures, the confining oxide layer forces the core to expand inwards into the hollow space. The outer electrode interface with the electrolyte is mechanically constrained and remains static during both lithiation and delithiation. This makes the material cycle over 6,000 times in half cells while retaining more than 85% of their initial capacity at C/5.

Silicon nanotubes (SiNTs) is one attractive electrode configuration that improves electrochemical performance.[11,12,14] The axial void space within the nanotubes provides additional free space to accommodate the 300% volume expansion associated with lithiating Si to $Li_{15}Si_4$. Such electrodes exhibit initial coulombic efficiencies typically in the 85% range, and capacity retentions of near 80% for up to 50 cycles. [12,14,16] Typical cycling coulombic efficiencies are in the 95 - 97 % range, [14,16] which means that a full cell lithium ion battery with initially balanced anode/cathode capacity would last somewhere between 20 and 33 cycles before running out of Li ions. Moreover these cycling lifetimes would be even lower due to lower coulombic efficiency during the initial cycles. It would therefore be highly desirable to improve both the initial coulombic efficiency and the cycling columbic efficiency of such hollow nanostructures.

Poor coulombic efficiency is typically associated with the irreversible and continuous formation of a solid electrolyte interface (SEI). Both the solvent and salt of the electrolyte solution are thermodynamically unstable and undergo reduction on the anode, which operates at low potentials close to metallic lithium. [17,18] A material with a large surface-to-volume ratio will therefore cause higher irreversible capacity losses. [19,20] These surface films passivate the anode surface and prevent further decomposition of the electrolyte solution. However, high volume changes experienced by silicon during electrochemical cycling can continuously weaken and fracture the SEI layer, exposing fresh silicon to the electrolyte with each cycle. This will form a new SEI layer mostly composed of electrolyte reduction products such as Li_2CO_3 and increase the amount of SEI with each cycle. The instability of the SEI can eventually lead to overall capacity loss and failure of the battery. [21-24] Besides solvent reduction products such as Li_2CO_3 and alkyl carbonates, SEI also partially consists of LiF which is a (electroless) decomposition product of the $LiPF_6$ salt but can also be formed through reaction with trace amounts of water to HF and eventually LiF. [25,26]

Thin surface coatings have been shown to be effective for stabilizing the SEI layer, and hence improving the coulombic efficiency in Si. The use of functional coatings such as carbon, [27-29] conductive polymer, [30] Cu, [31] Ag, [32] Al, [33] Mg and Mg_2Si, [34] Al_2O_3, [26,35-37] TiO_2, [21,37-40] SnO_2, [41,42] and TiN [43] on the surface of silicon and of other anodes have shown promising outcomes.

Coatings can act as a buffer layer between the active electrode and electrolyte, and prevent the formation of excessive amounts of SEI. This approach has been explored in some detail for anode materials with solid (only an outer Li active surface) geometries such as solid nanowires, nanoparticles, nanorods, etc. However hollow (an outer and an inner Li active surface) nanostructures have been explored far less. The key difference between these two architectures is that in materials such as Si nanotubes there are potentially two, rather than one, surfaces where SEI may form from the get-go.

In this study we employ atomic layer deposition (ALD) to coat TiO_2, Al_2O_3 and TiN onto hollow Si nanotubes to demonstrate that it is not entirely correct to assume that passivating only the outer surface is enough to achieve optimum coulombic efficiency. Rather, we show that an additional improvement may be obtained by coating the inner surface as well. For example we achieve an average coulombic efficiency of 99.9% (among the highest ever reported for any hollow Si nanostructure) for Si nanotubes coated with TiO_2 both their inside and their outside, *versus* 99.1% with an outer coating only. While this difference seems small, with all else being equal in a real device it may mean a lifetime of 1000 cycles rather than 111 cycles. Since electrochemical reduction - based growth of SEI occurs preferentially on exposed fresh Si, rather than on pre-existing SEI, [21,44,45] a broader implication of our findings is that some material degradation occurs on the inner surfaces as well. Thus, lithiation-induced expansion (and hence the stress state) on the inside of such hollow structures may be more complex than originally envisioned.

4.2 Experimental

4.2.1 Synthesis of coated Si nanotubes

Si nanotubes (SiNTs) were grown using ZnO nanorods as sacrificial templates, similarly to what was originally done in ref 14. A 200-nm-thick ZnO seed layer was first deposited onto 316L stainless steel spacers (diameter 15.4 mm) using magnetron sputtering (Orion 8, AJA international). We used Ar gas with a purity of grade 5N at a sputtering pressure of $5 \text{ x}10^{-3}$ mbar, with a maximum base pressure of $5\text{x}10^{-8}$ mbar. ZnO nanorods (NRs) were then grown on the seed layer by incubating in an aqueous solution containing 0.025 M zinc nitrate hexahydrate and 0.025 M hexamethylenetetramine at 90 ºC for 24 hr. Then, samples were thoroughly rinsed with deionized water and dried at 90 °C. ZnO nanorods were transferred to a CVD chamber for deposition of the Si. Deposition of Si was achieved at 540 ºC for 15 min with the mixture of H_2 and SiH_4 at a pressure of 300 mTorr, producing 20-25 nm thick Si shells. In the same CVD furnace, after Si deposition, the ZnO was selectively removed by annealing at 600 ºC for 24 hr with 50% H_2 in Ar, first reducing the ZnO and then evaporating the Zn.

Atomic layer deposition (ALD) conformal coatings were applied before and/or after deposition of Si, so as to coat the inside of the SiNTs (ALD onto sacrificial ZnO, performed prior to Si deposition), the outside of the SiNTs (ALD after Si deposition), or both. The total thickness of the coatings was 3 nm, either as an individual 3 nm thick inner or outer layer, or as 1.5/1.5 nm inner and outer layer together. Since the inner and the outer nanotube surfaces have different areas, the actual mass loading was not exactly identical for each of the three cases. Each electrode has approximately 0.2 mg Si active mass. A 3 nm TiO_2 coating on the outside adds 0.036 mg to the sample mass. For 3 nm TiO_2 on the inside, this is 0.024 mg and for double-sided coating 0.037 mg. This is equivalent to ~ 0.11, 0.13, 0.12, 0.13 mg/cm^2 for bare SiNTs, TiO_2 on the outside, inside and double sides of the nanotubes, respectively. TiO_2 was deposited from titanium isopropoxides $Ti(OCH(CH_3)_2)_4$ as the titanium source and O_2 as the oxygen source. Argon was used as the carrier gas. The XPS spectra of the as-synthesized electrodes demonstrated that the relative intensity of the carbon signal was higher when TiO_2 was coated on the outside or both sides of the SiNTs compared to bare SiNTs and inner TiO_2 coating. The extra intensity over that of adventitious carbon comes from the residual organic groups in the ALD precursor that have not entirely volatilized. Trimethyl aluminium (TMA) and O_2 were employed as precursors for Al_2O_3. $TiCl_4$ and N_2 were employed as precursors for TiN. All coatings were deposited at 200^{o}C. The film thickness was confirmed both by ex-situ rate measurements on planar supports and by TEM analysis of the nanotube architectures.

4.2.2 Electrochemical testing

CR2032 button half-cells were assembled using the SiNTs as working electrodes and Li foil (15.4 mm diameter) as counter electrodes. Assembly was performed in an Ar-filled glove box with less than 0.1 ppm oxygen and moisture content. Lithium metal foil was separated from the working electrode with a polyethylene separator (MTI technologies, porosity of 36–44% and 0.03 µm pore size). The electrolyte was 1 M $LiPF_6$ dissolved in a 1:1:1 volume ratio of ethylene carbonate (EC): dimethyl carbonate (DMC): diethylcarbonate (DEC) organic solvents.

Galvanostatic discharge/charge cycling was carried out on a computer controlled BT2000 Arbin potentiostat in the voltage range of 0.01 to 2 V (vs. Li/Li^+). A constant current density was used for discharge/charge experiments at rates between 0.2 and 5C. Electrochemical impedance spectroscopy (EIS) of the half-cell electrodes was measured using a Princeton Applied Research VersaSTAT3 frequency response analyzer (FRA). An AC voltage of 10 mV amplitude was applied over a frequency range of 0.01 Hz to 1 MHz.

4.2.3 Microstructural Characterization

For post-cycling characterization the coin cells were disassembled in the same glove box. Subsequently, the cycled electrodes were rinsed thoroughly with acetonitrile to remove excess electrolyte and kept in the glove box to dry overnight. The samples were characterized using field emission scanning electron microscopy (FE-SEM) (Hitachi S-4800) and transmission electron microscopy (TEM) (JEOL 2010, 200 kV). Electron energy loss spectroscopy (EELS) measurements were conducted using a JEOL 2200FS TEM operated at 200 kV in a scanning mode (STEM) with a nominal analytical beam size of 0.5 nm. High angle annular dark field (HAADF) images were recorded simultaneously with the EELS analysis. The software employed for signal collection and data extraction from EELS spectra was Digital Micrograph (Gatan, Inc.). The data extraction was performed by following the standard procedure of pre-edge background subtraction and integration on the edge [46]. We mapped Silicon, Carbon, Titanium, and Oxygen by integrating over core-loss edges of Si-L, C-K, N-K, Ti-L, and O-K-edge, respectively. Lithium maps for cycled materials were obtained from Li-K edge at 60-70 eV. Cross-sectional SEM images of the as-prepared and cycled samples were acquired using a Hitachi NB5000 dual-beam focused ion beam (FIB)/SEM.

Surface composition of electrode materials is characterized via X-ray photoelectron spectroscopy (XPS) using an ULTRA (Kratos Analytical) spectrometer with Al K_α X-ray source (hv=1486.6 eV) run at 210 W. Data collection was conducted under ultrahigh vacuum (10^{-9} Torr) over an area of 300×700 μm^2. All XPS spectra were calibrated from the universal hydrocarbon contamination using the C1s peak at 284.8 eV. We used CasaXPS software was used to analyze XPS data. Background subtraction was done using a nonlinear Shirley-type model.

4.3 Results and Discussion

4.3.1 As-synthesized microstructures

We will employ a shorthand designation to label the various SiNTs samples that is based on the type and the location of the coating. As described in the experimental section, the three coatings TiO_2, Al_2O_3 and TiN were deposited either on the inside (3 nm) outside (3 nm), or on both sides (1.5 nm inner, 1.5 nm outer) of the nanotubes. When only the inside of the nanotubes was coated, the designation is TiO_2/SiNTs, Al_2O_3/SiNTs, TiN/SiNTs. When the outside is coated the designation is SiNTs/TiO_2, SiNTs/Al_2O_3, SiNTs/TiN. When both sides are coated, the designation is TiO_2/SiNTs/TiO_2, Al_2O_3/SiNTs/Al_2O_3, TiN/SiNTs/TiN.

Figure 4.1 shows representative top view SEM micrographs of the (a) SiNTs, (b) SiNTs/TiO_2, (c) SiNTs/Al_2O_3 and (d) SiNTs/TiN electrodes. Typical diameters of the SiNTs were in the 100 - 150 nm range. From cross section SEM and FIB (Figure 4.1(e)) we measured the nanotubes to be in the 2.5-3 μm range in length, and to be grown almost vertically with respect to the substrate.

Figure 4.2 presents TEM micrographs of the as-synthesized SiNTs electrodes, displaying bright field images and indexed selected area diffraction patterns for each material Figures 4.2(a) and 4.2(b) show the uncoated SiNTs. In all cases the SiNTs were polycrystalline, as highlighted in the dark field micrograph obtained using a portion of 111_{Si} ring pattern that shows the Si nanocrystallites within the tube walls. Such initial Si microstructure existed in all the samples, with no discernable sample-to-sample variation in the grain size. Figure 4.2(c-e) show bright field images and indexed SAD patterns of SiNTs/TiO_2, SiNTs/Al_2O_3 and SiNTs/TiN, respectively. The TiO_2 and Al_2O_3 coatings are amorphous while the TiN appears to be nanocrystalline and its most intense ring matches with the 200 reflection of the equilibrium cubic structure ($Fm\bar{3}m$) of TiN.

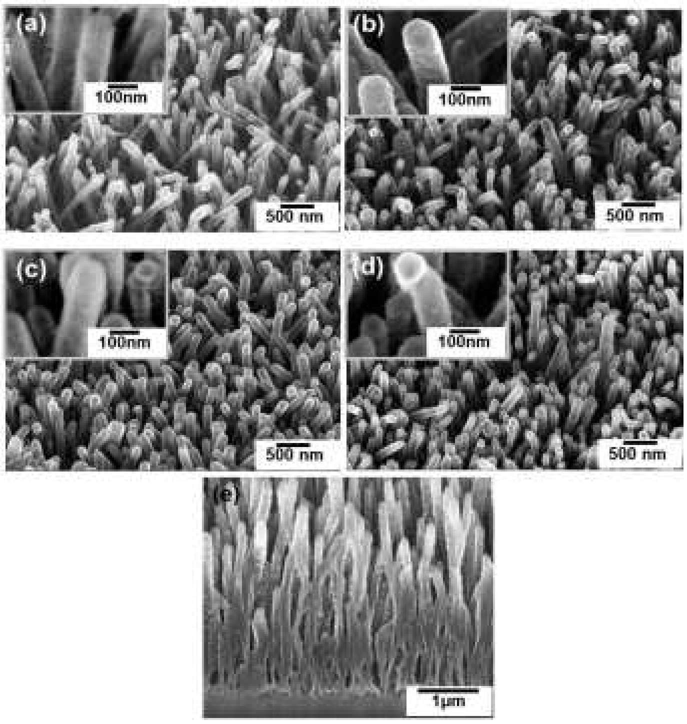

Figure 4.1: SEM micrographs of (a) SiNTs, (b) SiNTs/TiO_2, (c) SiNTs/Al_2O_3, (d) SiNTs/TiN electrodes. (e) FIB cross-section of SiNTs/TiO_2 showing the height of the nanotubes as approximately 3 μm.

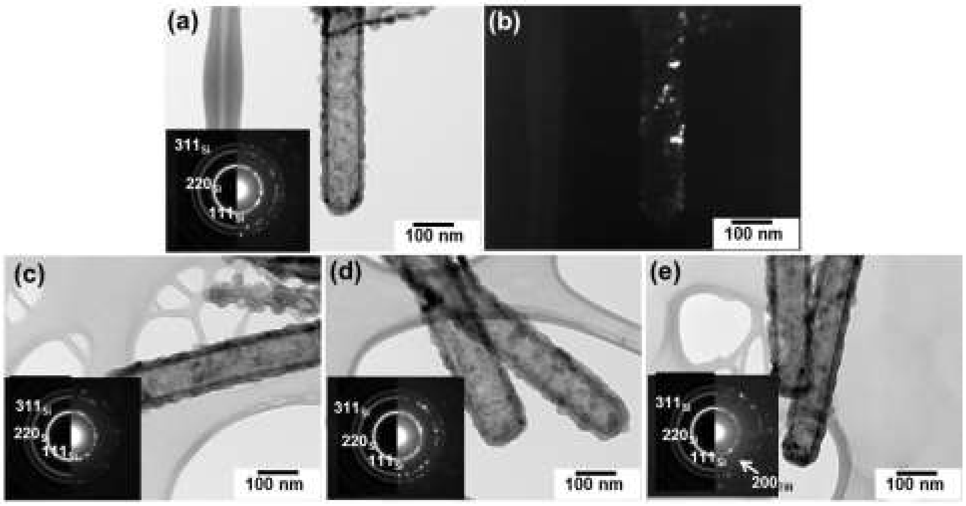

Figure 4.2: TEM micrographs of the as synthesized materials. (a) and (b) uncoated SiNTs showing a bright field micrograph with the corresponding indexed SAD pattern, and a dark field micrograph of the polycrystalline Si obtained using a portion of 111_{Si} ring pattern. (c) Bright field micrograph and indexed SAD pattern of SiNTs/TiO_2, (d) SiNTs/Al_2O_3, (e) SiNTs/TiN The TiO_2 and Al_2O_3 coatings are amorphous whereas TiN is nanocrystalline.

For TiO_2/SiNTs/TiO_2 and TiO_2/SiNTs shown in Figure 4.3(a-b) and 4.3(c-d), the anatase 101 reflection is visible as the inner coating is already present during the high-temperature Si deposition and the reduction step of ZnO, causing it to crystallize.

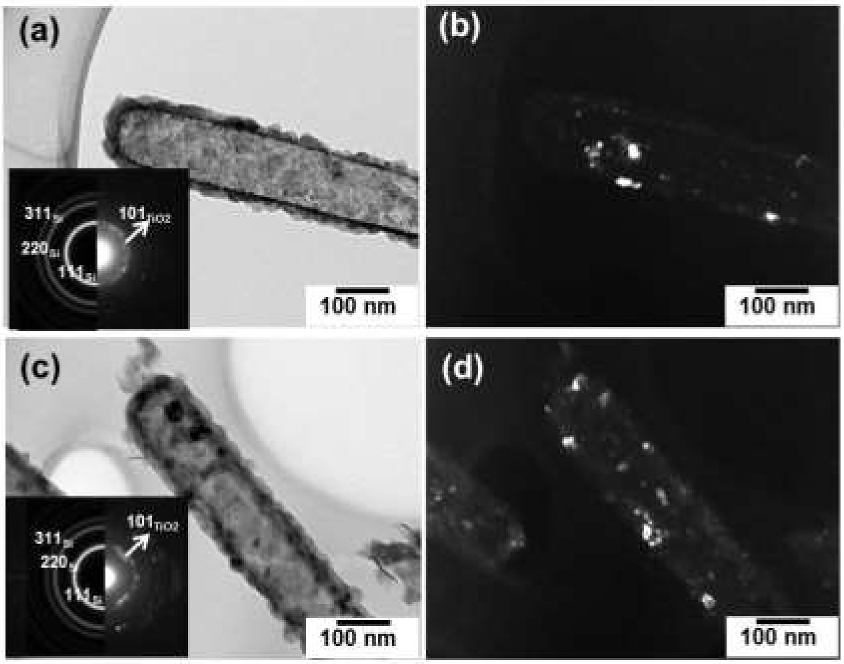

Figure 4.3: TEM micrograph of the as synthesized materials, showing a bright field micrograph with the corresponding indexed SAD pattern, and a dark field micrograph of the polycrystalline Si obtained using a portion of 111_{Si} ring pattern. (a) and (b) TiO_2/SiNTs/TiO_2; (c) and (d) TiO_2/SiNTs.

Figure 4.4 shows HRTEM micrographs, highlighting the walls of the uncoated and the coated as-synthesized SiNTs. Figure 4.4(a) shows the uncoated specimens, highlighting the wall thickness on one SiNT that is 22 nm. Most of the nanotubes we examined had wall thicknesses in this range. The fast fourier transform (FFT) pattern insert shows a 111 ring of Si, in agreement with the SAD analysis of Figure 4.2. The magnified images in Figures 4.4(b) and 4.4(c), taken from regions 1 and 2, highlight the lattice fringes of the polycrystalline Si walls, and the amorphous ~ 2 nm thick silicon oxide present on the inner and outer wall surfaces. Since in this case the micrograph was obtained from the inner tube wall, HRTEM image actually shows the oxide overlapping with the crystalline Si. Figures 4.4(d-f) show the wall of SiNTs/TiO_2, demonstrating the highly uniform and defect-free amorphous TiO_2 coating on the outer Si surface. The thickness of the TiO_2 is quite close to the nominal, i.e. 3 nm. For TiO_2/SiNTs/TiO_2, the magnified images in Figure 4.4(i) highlights lattice fringes of Si and 1.5 nm amorphous outer TiO_2.

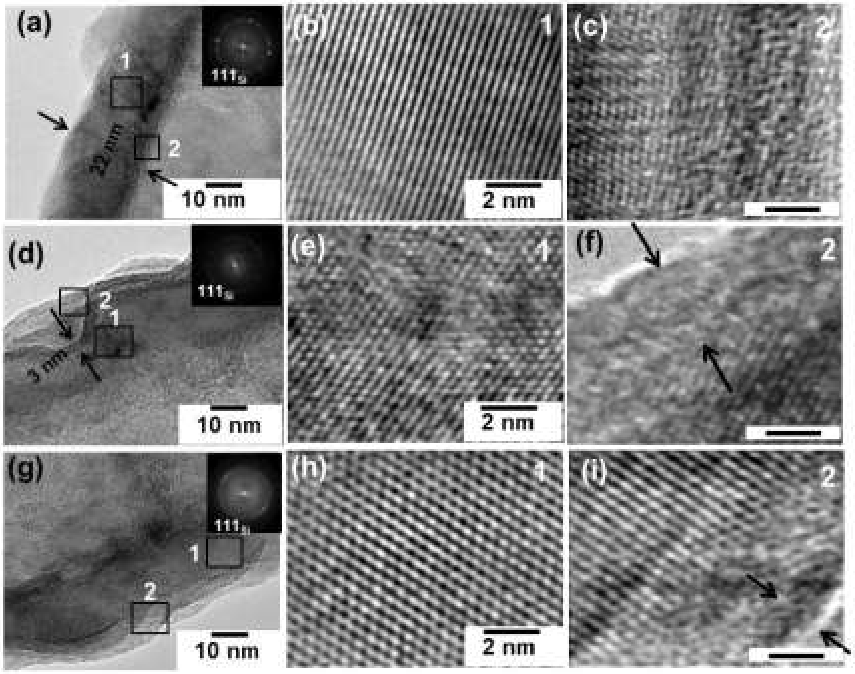

Figure 4.4: HRTEM images including fast fourier transforms (FFTs) of (a)-(c) uncoated SiNTs; (d)-(f) and (d) SiNTs/TiO_2; and (g) – (i) TiO_2/SiNTs/TiO_2. High magnification images of areas marked by rectangles 1 and 2 highlight the lattice fringes for Si and the amorphous structure of the outer TiO_2 coating.

Figure 4.5 shows the HAADF images and the EELS maps of (a) uncoated SiNTs, (b) SiNTs/TiO_2, and (c) TiO_2/SiNTs/TiO_2. In Figure 4.5(d) the line scan profile along the nanotube diameter (red dashed line) shows the hollow core-shell structure for TiO_2/SiNTs/TiO_2. As expected, no Zn signal was detected inside the tubes, as the metal is known to simultaneously evaporate during the reduction process. [14] The HAADF image and EELS maps of the uncoated SiNTs support the conclusion that Si is oxidized on the inner surface of the tubes as well as on the outer, as indicated by the arrows. The former occurs primarily due to the oxygen that is released during the decomposition of ZnO. The SiNTs/TiO_2 material shows an analogous relatively diffuse oxygen signal on the inner tube surface (there is no reason why it should differ), and a much sharper Ti and O signal on the outer tube walls. TiO_2 is thermodynamically more stable than SiO_2 [21,47], and should at least partially reduce the native oxide upon its deposition. The line scan in Figure 4.5(d) shows a 'double spike' in both the Ti and O signal at either end of the nanotube, confirming the presence of the 1.5 nm TiO_2 coating on both sides of the Si nanotube wall.

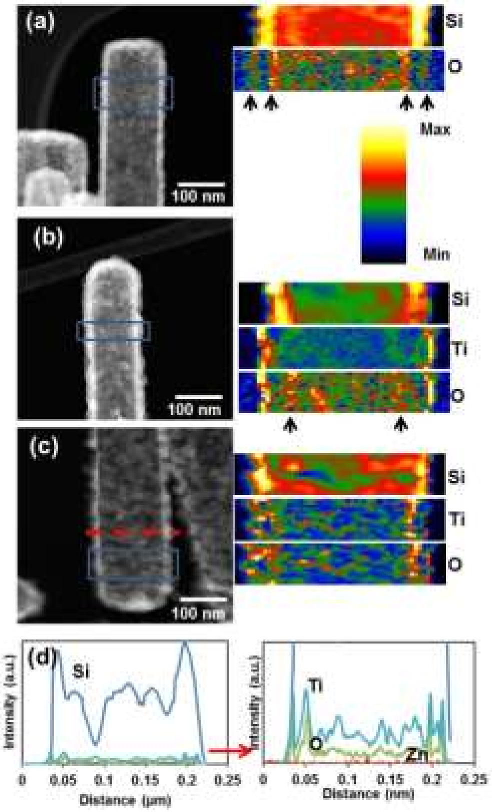

Figure 4.5: HAADF images and EELS maps of (a) uncoated SiNTs, (b) SiNTs/TiO_2, and (c) TiO_2/SiNTs/TiO_2. Native oxide layers on Si are indicated with arrows. (d) line scan profile along the nanotube diameter (red dashed line) shows the hollow core-shell structure for TiO_2/SiNTs/TiO_2 where 2 spikes in both the Ti and O signals spaced ~20 nm apart are visible on either end of the scanned area.

Figure 4.6 shows the XPS spectra for the as-synthesized materials. None of the samples showed any signal associated with the Zn 2p spectra. For uncoated SiNTs and TiO_2/SiNTs, the XPS spectra show the Si^{n+} peak at 103 eV. This binding energy is consistent with Si in its highest oxidation state (i.e. Si^{4+}) indicative of stoichiometric SiO_2. [48] However, for SiNTs/TiO_2 and TiO_2/SiNTs/TiO_2, the Si^{n+} peak shifts to a lower binding energy. This is indicative of lower Si oxidation states (Si^{3+} and Si^{2+}), and consistent with ALD titanium at least partially reducing the SiO_2 surface. A peak shift can also be observed in O1s spectra, going from 532.1 eV for uncoated SiNTs and TiO_2/SiNTs, to 531.6 eV for SiNTs/TiO_2 and TiO_2/SiNTs/TiO_2. The relative intensity of the carbon signal is higher for SiNTs/TiO_2 and TiO_2/SiNTs/TiO_2, originating from the residual organic groups in the ALD precursor (i.e. $OCH(CH_3)_2$) that have not volatalized. The SiNTs are sufficiently thick to block most of the XPS signal from the inner TiO_2 coatings of the TiO_2/SiNTs specimen. Lithium alkoxides are normally one of the main constituents of the SEI layer. [17] The residual isopropoxide ligands should convert to $LiOCH(CH_3)_2$ during the first lithiation and should not impair electrode reversibility.

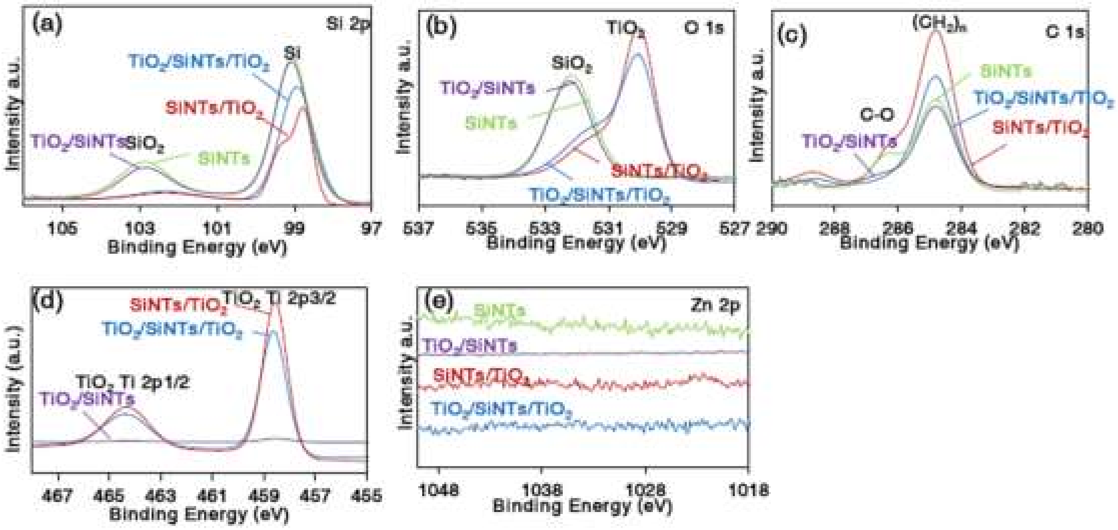

Figure 4.6: XPS spectra of the TiO_2-coated SiNTs electrodes in as-synthesized state.

4.3.2 Electrochemical performance and post-cycled microstructure

When the composites are electrochemically cycled substantial differences emerge in their performance. Table 4.1 lists the 1st discharge specific capacity, first-discharge capacity loss ([1st discharge capacity – 2nd discharge capacity]/[1st discharge capacity])x100%, and initial coulombic efficiency (CE), (1st delithiation capacity/ 1st lithiation capacity). The data is presented for electrodes tested at a rate of 0.2 C. Because the experimentally measured capacity of TiO_2 is more than an order of magnitude lower than that of Si (150 - 300 vs. 3590 mAh/g), the coated SiNTs electrodes show a slightly lower initial specific capacity. The first discharge capacity loss is lower and the coulombic efficiency is higher for TiO_2 - SiNTs nanocomposites, the improvement being the most pronounced when the TiO_2 is present on both surfaces of the SiNTs.

Table 4.1: Galvanostatic cycling results for the uncoated and coated SiNW electrodes, tested at 0.2

Electrode	First discharge specific capacity (mAhg^{-1})	First discharge capacity loss (%)	Initial Coulombic efficiency (%)
SiNTs	3064	17	84
SiNTs/TiO_2	2885	14	87
TiO_2/SiNTs/TiO_2	2822	12	89
TiO_2/SiNTs	2925	13.5	86
SiNTs/Al_2O_3	2951	13.5	86.5
Al_2O_3/SiNTs/Al_2O_3	2885	11.5	87.5
Al_2O_3/SiNTs	3027	12.5	86
SiNTs/TiN	3002	12	86
TiN/SiNTs/TiN	2952	11.9	87.5
TiN/SiNTs	3044	13	85.5

It is known that in the presence of oxygen the surface of Si naturally passivates to SiO_2 both at ambient and at higher temperatures, e.g. [49] The presence of SiO_2 contributes to the initial capacity loss since the conversion of SiO_2 into lithium oxides during the lithiation process is irreversible. [50,51] An irreversible conversion reaction of TiO_2 to Li_2O and Ti has not been directly observed. [52] However during the first discharge there is irreversible trapping of Li that is known to occur for nm-scale amorphous TiO_2 films that partially transform to stable $LiTiO_2$ nanocrystallites. [21] At voltages roughly below 0.7 V vs. Li/Li$^+$, the electrolyte reduction product SEI will still form on either surface. [21,53,54] However, since the highest initial CE (89% vs. 84% for uncoated) and lowest initial first-discharge capacity loss (12% vs. 17%) are achieved in TiO_2/SiNTs/TiO_2 electrodes, one can argue that on the balance a TiO_2 - electrolyte interface is more advantageous than a SiO_2 - electrolyte interface.

The overall trend for TiN and Al_2O_3 is the same as with TiO_2; a slight reduction of the first discharge capacity, but an improvement in the first discharge capacity loss and in the initial CE and the highest initial CE is found for double-sided coated SiNTs. The Al_2O_3 coating may partially reduce the SiO_2 (depending on the chemical activity of the Al during the ALD process), and forms a Li-Al-O glass film in the lithiated state. It has also been shown to possess excellent lithium ion conductivity (up to $3 \times 10^{-5}\ \Omega^{-1}cm^{-1}$) due to the partially occupied Li ion sites inside. The extent of SEI formation on Li-Al-O surfaces is known to be relatively low.[26] Bulk or thin film TiN does not store Li, though near-atomically thin TiN layers do permit lithium flux through the grain boundaries and other defects.[43] Interestingly, despite TiN not being expected to reduce the underlying SiO_2, it provides analogous positive improvement in both the CE and the first discharge capacity loss as does the TiO_2 and the Al_2O_3. This implies that it is the extent of the initial SEI formation on a given oxide or nitride surface that is critical for improving both factors.

Figure 4.7 shows the constant current (CC) voltage profiles and the differential capacity curves (dCapacity/dV) of the uncoated SiNTs and the coated specimens. The samples were tested at 0.2 C, and the data are shown for the 1st, 2nd, 20th, 50th and 100th cycles. Figures 4.7(a) and 4.7(b) represent the uncoated SiNTs while Figures 4.7(c) and 4.7(d) show the data for TiO_2/SiNTs/TiO_2. The same data for the rest of the specimens are shown in Figure 4.8-4.10. For all electrodes, there is a low voltage plateau during the first discharge, which can be assigned to the lithiation of crystalline Si into an amorphous Li_xSi phase with a progressively increasing Li content at lower voltages. This sloping plateau shows up as a peak in the differential capacity profile during cycle 1, centered at roughly at 0.12 V. During subsequent cycles the slope of this plateau begins to vary, leading to multiple peaks in the dC/dV plots. The multiple plateau slopes are attributed to amorphous Li_ySi phases with differing composition, and hence differing local atomic arrangements and free energies.[55] It is known that lithiation of Si to below 50 mV vs. Li/Li^+ results in the formation of a crystalline $Li_{15}Si_4$ phase.[56] This can be observed as a small peak in the differential capacity curves near this voltage. The anodic peak in the differential capacity during charging, centered at roughly 0.45 V, corresponds to the voltage plateau associated with the two-phase region where $Li_{15}Si_4$ phase converts back to a-Li_ySi.[57]

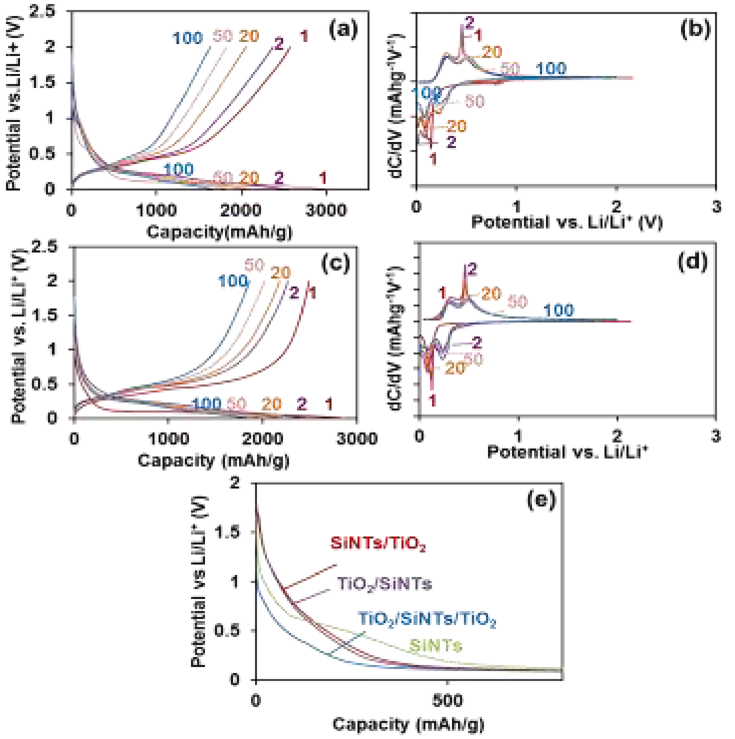

Figure 4.7: Constant current voltage profiles and differential capacity curves, tested at 0.2 C, at 1, 2, 20, 50 and 100 cycles. (a) and (b) SiNTs; (c) and (d) TiO_2/SiNTs/TiO_2. (e) Magnification of the first 800 mAh/g in the first discharging cycle at 0.2 C rate.

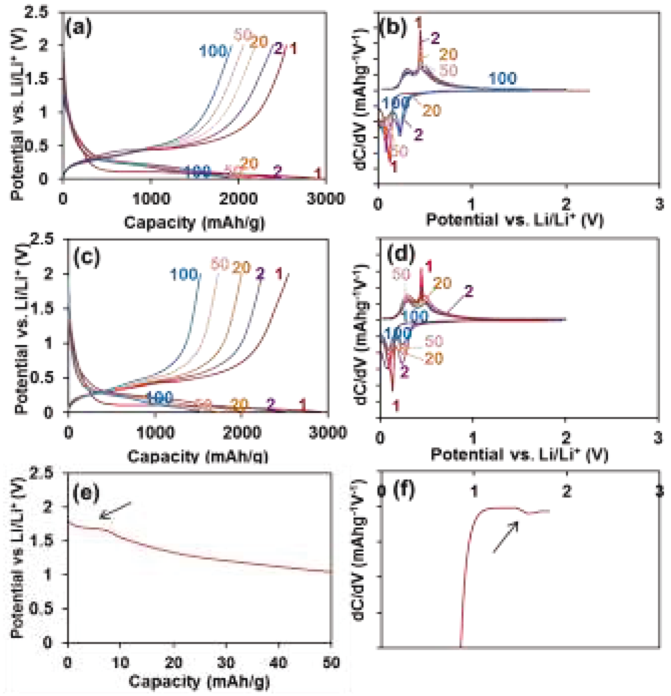

Figure 4.8: Constant current voltage profiles and differential capacity curves, tested at 0.2 C, at 1, 2, 20, 50 and 100 cycles. (a) and (b) SiNTs/TiO_2, (c) and (d) TiO_2/SiNTs. (e) Magnification of the first 50 mAh/g for TiO_2/SiNTs in the first discharging cycle at 0.2 C rate. (f) Magnification of the dC/dV for the TiO_2/SiNTs in the first discharging cycle at 0.2 C. They highlight the plateau and the related peak in the dC/dV profile for TiO_2/SiNTs sample corresponding to the lithiation of anatase TiO_2.

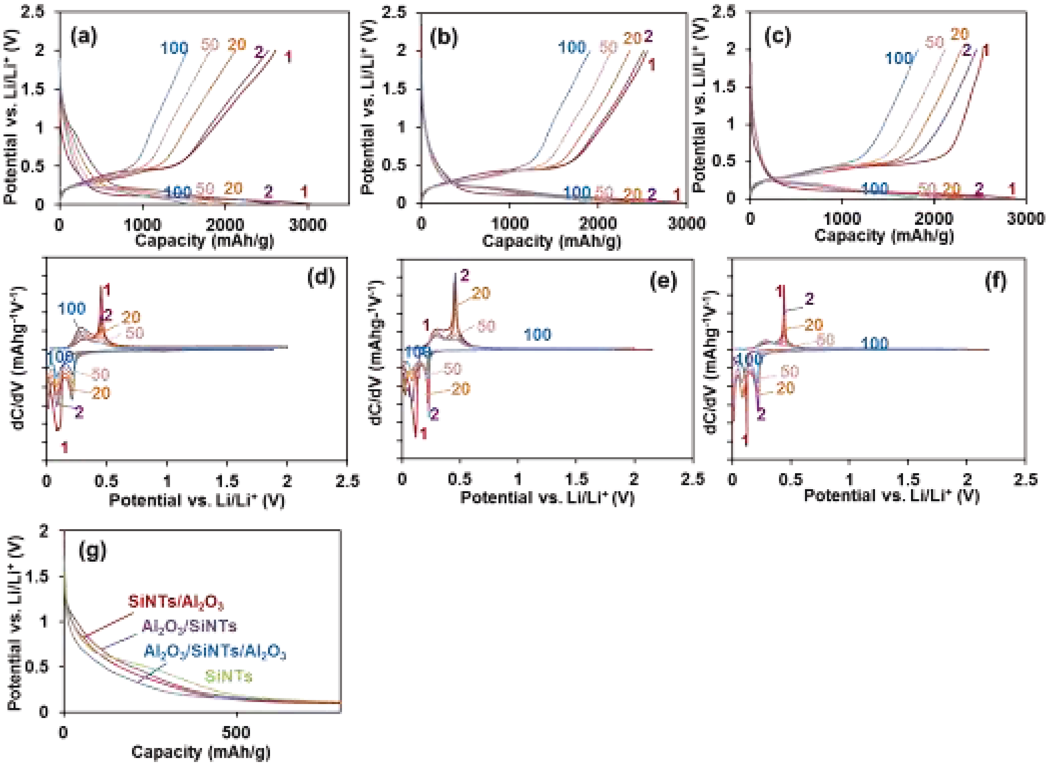

Figure 4.9: a) and (d) Al_2O_3/SiNTs, b) and (e) SiNTs/Al_2O_3, (c) and (f) /Al_2O_3/SiNTs/Al_2O_3. (g) Magnification of the first 800 mAh/g in the first discharging cycle at 0.2 C rate.

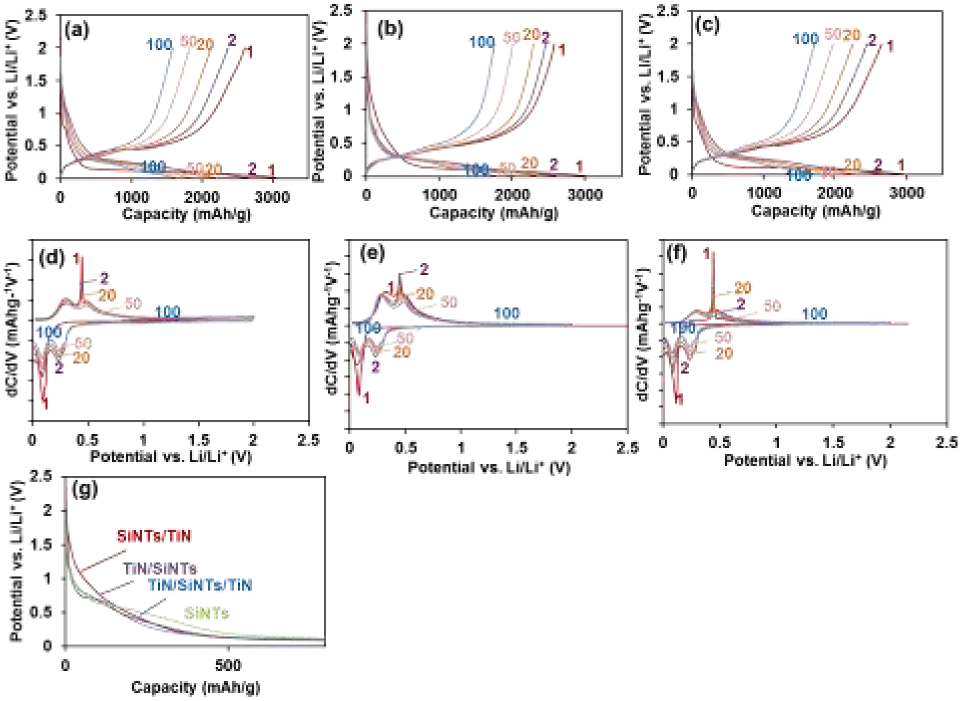

Figure 4.10: (a) and (d) TiN/SiNTs, (b) and (e) SiNTs/TiN, (c) and (f) /TiN/SiNTs/TiN. (g) Magnification of the first 800 mAh/g in the first discharging cycle at 0.2 C rate.

Figure 4.7(e) shows a magnified view of the voltage profile between 0 and 800 mAh/g during the first discharge of the TiO_2 coated specimens and of the uncoated baseline. The irreversible reduction of SiO_2 by Li should happen below 1 V. [58] For uncoated SiNTs, some capacity is indeed achieved between 0.7 and 1V, though the majority of the current is associated with the sloping plateau that initiates at about 0.7 V. This onset voltage is attributed to the formation of the SEI layer. [59] This feature is much less distinct for the TiO_2 coated samples, especially for the TiO_2/SiNTs/TiO_2, where most of the capacity gain is initiated at a lower reduction voltage (~ 0.5 V). The Al_2O_3 coated SiNTs show this trend too (see Figure 4.9), with the plateau being the least distinct and occurring at the lowest voltage for Al_2O_3/SiNTs/Al_2O_3. For TiN coatings (Figure 4.10) this effect is consistently less pronounced, with the SiNTs/TiN electrode in fact having the onset voltage at a higher value (~ 1.2 V). However, the distinct plateau-like feature indicating onset of SEI formation is absent in its voltage profile as well and is only clearly seen in TiN/SiNTs which has its outer surface exposed to the electrolyte. It should be noted here that the electrochemical response related to lithiation of the coating layers is only visible for TiO_2/SiNTs when the initial 50 mAh/g is magnified further and is typical for anatase TiO_2 (see Figure 4.8(e) and 5.8(f)). Al_2O_3 is amorphous, remains so upon lithiation [60] and does not produce a distinct response in either CC or dC/dV profiles.

Figures 4.11(a-c) compare the capacity retention and CE versus cycle number for the samples with the coating on the outside of the nanotubes. The electrodes were tested at a rate of 0.2 C. By cycle 2 all the electrodes exhibit similar specific capacities that are in the 2530 - 2617 mAh/g range. The bare SiNTs and SiNTs/TiO_2 were tied for the lowest, while SiNTs/TiN and SiNTs/Al_2O_3 were tied for the highest of these values. However by cycle 100 the differences were much more significant: The uncoated SiNTs possessed a capacity of 1665 mAh/g, SiNTs/TiN was at 1774 mAh/g, SiNTs/Al_2O_3 was at 1921 mAh/g, while SiNTs/TiO_2 was at 1936 mAh/g. On the basis of the percentage of the initial capacity retention, the differences were just as significant: The bare SiNTs retained 54% of the initial capacity, TiN coated retained 59%, while Al_2O_3 and TiO_2 coated nanotubes were both at 66%. Figure 4.11(c) demonstrates that the steady-state coulombic efficiency vs. cycle number data is consistently higher for all the coated electrodes. Taken at cycle # 50, the CE values are 97.5% for SiNTs, 99.3 % for SiNTs/TiN, 99.6% for SiNTs/TiO_2 and 99.8% for SiNTs/Al_2O_3. Of course there is some scatter in the data; however the trend is consistent at other cycle numbers.

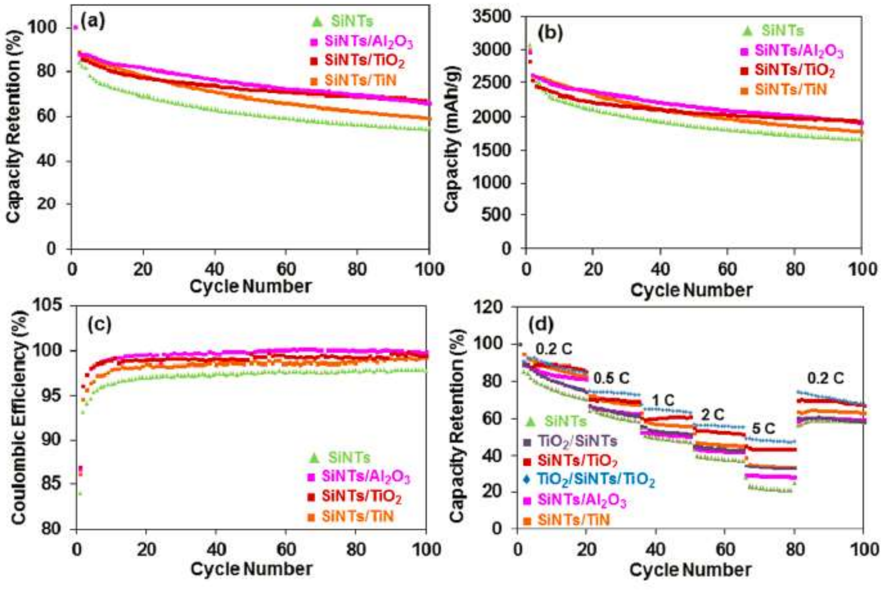

Figure 4.11: (a) and (b) Capacity retention vs. cycle number for SiNT's coated with 3 nm of Al_2O_3, TiN, and TiO_2 on their outer surface, tested at 0.2 C rate; (c) corresponding Coulombic efficiency; and (d) rate dependence of capacity retention as a percentage of capacity at 0.2 C.

The rate capability of the bare and outer-coated SiNTs was also tested and the results are shown in Figure 4.11(d). For TiO_2 coated SiNTs, the results of all three electrode configurations, inner, outer and double-sided, are included. The TiO_2/SiNTs/TiO_2 electrode demonstrates by far the best rate capability, with a capacity retention of around 50% at 5C, versus 20% for the uncoated baseline. Of the three coatings, the best rate capability is achieved with TiO_2. It has been demonstrated that a high electronic conductivity and a high Li-diffusion coefficient are both key for improving the rate capability of an electrode. [61] TiN offers excellent electrical conductivity [43,62] and a Li-Al-O glass offers excellent Li-ion conduction. Our recent study on TiO_2 coated silicon nanowires demonstrated that during lithiation cycling, the structure of amorphous ALD TiO_2 evolves into a nanocomposite composed of a highly Li - active amorphous TiO_2 and a highly electrically conducting but Li inactive $LiTiO_2$. [21] Thus, uniquely both objectives are achieved with the TiO_2 coating: the $LiTiO_2$ providing an electrically conductive pathway [63] and the amorphous fraction enhancing Li transport at the electrode-electrolyte interface. Therefore, we argue that it is the unique two-phase microstructure of lithiated TiO_2 that offers both high ionic and electrical conductivity that makes the rate capability of the outer-TiO_2-coated materials stand out as superior. The presence of the TiO_2 coating on both sides of the nanotube, versus just an outer or an inner coating, is also quite beneficial for further improving the rate capability. A straightforward argument may be made that this provides a larger electrical conduction pathway to the current collector and a higher surface area with fast Li transport.

Figure 4.12 shows the XPS data for all the coatings and the uncoated baseline, after 100 cycles. For the Al_2O_3 coating the Li 1s and O 1s spectra show a shift to higher binding energies confirming the formation of Li-Al-O film. [36] Li_2CO_3 is a well-known electrolyte reduction product, [26] the irreversible formation of which is associated with poor coulombic efficiency. Comparison of XPS spectra of SiNTs with different coating materials (Figure 4.12(a-e)) demonstrate that they all minimize the amount of cycling-induced carbonate formation during cycling as compared to the uncoated electrodes. Of the three coatings, the highest relative amount of Li_2CO_3 occurs in bare SiNTs followed by SiNTs/TiN and the lowest amount by far in SiNTs/Al_2O_3, agreeing with the CE results in Figure 4.11(c). The fact that strong Al signal is still detected for SiNTs/Al_2O_3 even after 100 cycles shows that the amount of SEI on the outer surface of the SiNTs is relatively low for this electrode. On the other hand, no Ti signal is detected anymore for cycled SiNTs/TiO_2 and SiNTs/TiN. We should also note that SEI is known to preferentially form on fresh Si surfaces exposed to the electrolyte rather than on the back of existing SEI. [21,59] The signal for LiF, which is considered an electroless decomposition product of the $LiPF_6$ salt that forms over time, [64] is relatively stronger in both SiNTs/Al_2O_3 and SiNTs/TiO_2, as compared to SiNTs/TiN and SiNTs, which is once again consistent with less fresh Si exposed and thus higher coulombic efficiency for the former two electrodes.

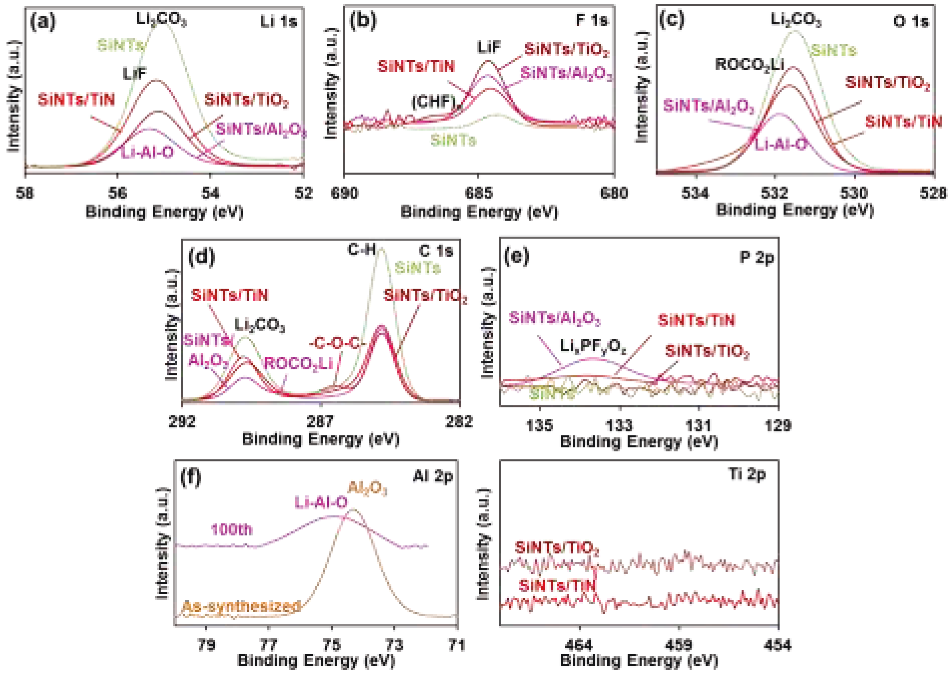

Figure 4.12: XPS spectra of the electrodes in the as-synthesized state and after 100 cycles. (a) - (e) SiNTs, SiNTs/Al_2O_3, SiNTs/TiN , SiNTs/TiO_2. (f) Al2p spectra for SiNTs/Al_2O_3, (g) Ti2p spectra for SiNTs/TiO_2 and SiNTs/TiN.

Figures 4.13(a) and 4.13(b) show the capacity retention vs. cycle number of SiNTs, TiO_2/SiNTs, SiNTs/TiO_2 and TiO_2/SiNTs/TiO_2 up to 200 or 100 cycles, tested at a rate of 0.2 C. Figure 4.13(c) shows the corresponding coulombic efficiency. Figure 4.14(a) and 4.14(b) show the capacity retention vs. cycle number up to 100 cycles in Al_2O_3 coated SiNTs, highlighting the role of coating location, i.e. inner surface, outer or both. Figure 4.14(c) shows the corresponding coulombic efficiency. Figure 4.15(a) and 4.15(b) show the capacity retention vs. cycle number up to 100 cycles of TiN coated SiNTs, highlighting the role of coating location. Figure 4.15(c) shows the corresponding coulombic efficiency. A comparison of the Figures shows that the double-coated electrodes perform the best out the three configurations, both in terms of capacity retention and coulombic efficiency, with outer coating being intermediate. The inner coated electrodes show consistently the least improvement. For the case of TiO_2/SiNTs/TiO_2 there is a substantial improvement even after 200 cycles: 60% capacity retention vs. 42% for the uncoated baseline and a coulombic efficiency of nearly 100% vs. 97-98%.

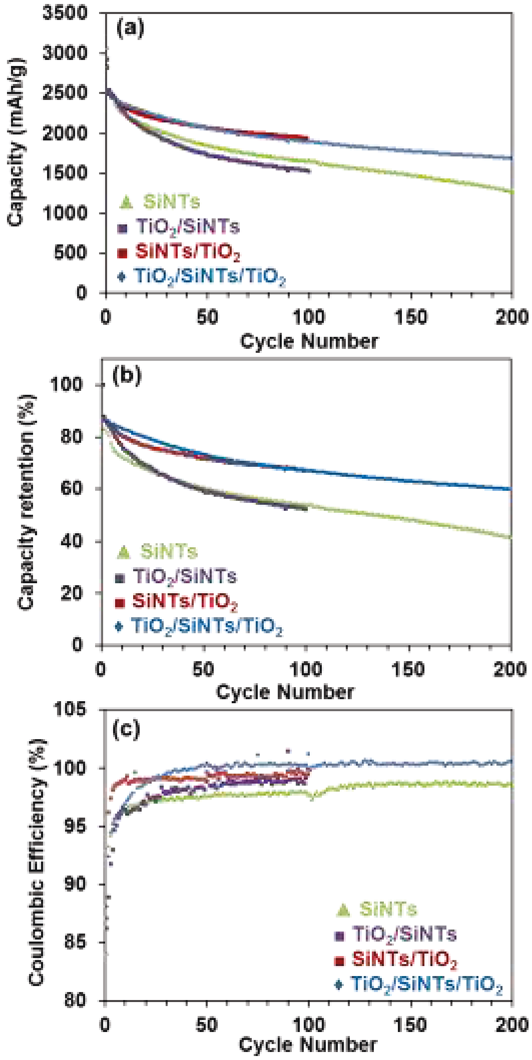

Figure 4.13: (a) and (b) Capacity retention vs. cycle number of TiO_2 coated SiNTs, highlighting the role of coating location, i.e. inner surface, outer or both. (c) corresponding Coulombic efficiency.

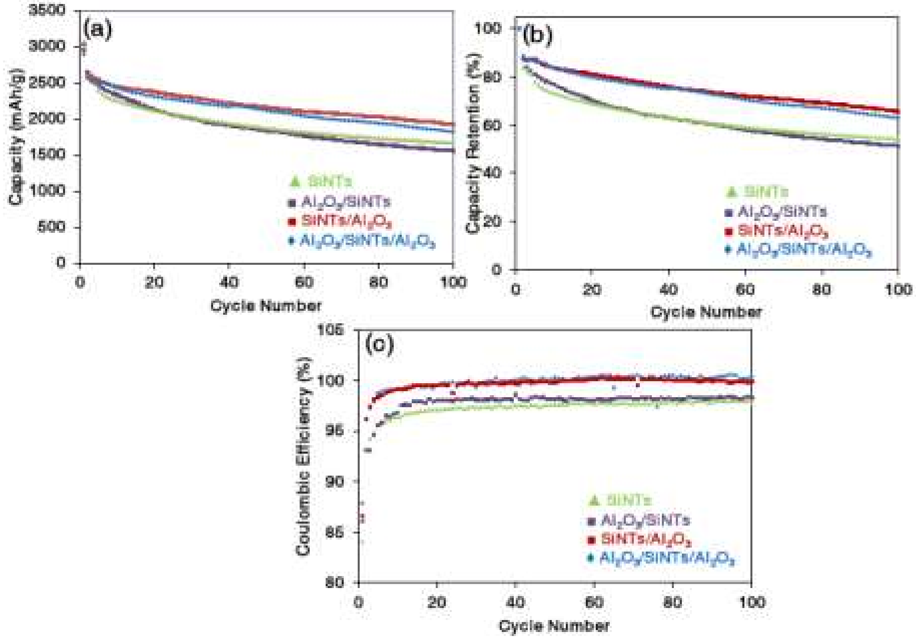

Figure 4.14: (a) and (b) Capacity retention vs. cycle number of Al_2O_3 coated SiNTs, highlighting the role of coating location, i.e. inner surface, outer or both. (c) corresponding coulombic efficiency.

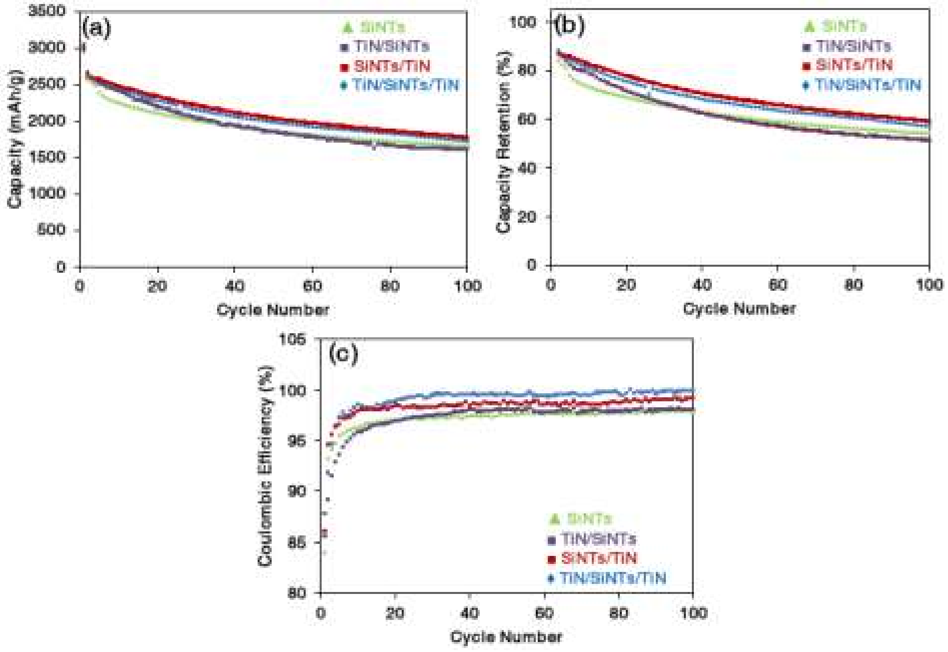

Figure 4.15: (a) and (b) Capacity retention vs. cycle number of TiN coated SiNTs, highlighting the role of coating location, i.e. inner surface, outer or both. (c) corresponding coulombic efficiency.

Electrochemical impedance spectroscopy (EIS) was utilized to examine the inner/outer/both TiO_2 coatings in more detail, again employing the bare SiNTs as a baseline. Figures 4.16(a) and 4.16(b) show the Nyquist plots for the as synthesized and the post-100 cycles electrodes, respectively. The spectra exhibit one semicircle in the high-frequency region followed by a straight sloping line in the low-frequency region, consistent with previous reports of cycled battery electrodes. [65] The semicircle at the high frequencies is associated with the charge transfer resistance R_{ct} of the electrodes, and is expected to grow in diameter with the accumulation of SEI during cycling. [66] In the as-synthesized state R_{ct} is consistently lower for the TiO_2 coated electrodes than for the uncoated baselines. The charge transfer resistance for as-synthesized samples increases in the order TiO_2/SiNTs/TiO_2 < SiNTs/TiO_2 < TiO_2/SiNTs < uncoated SiNTs. The same trend is actually magnified after 100 cycles, which is consistent with the CE and the XPS results that show least Li_2CO_3 and other electrolyte reduction products in the SEI in the double-sided coated sample.

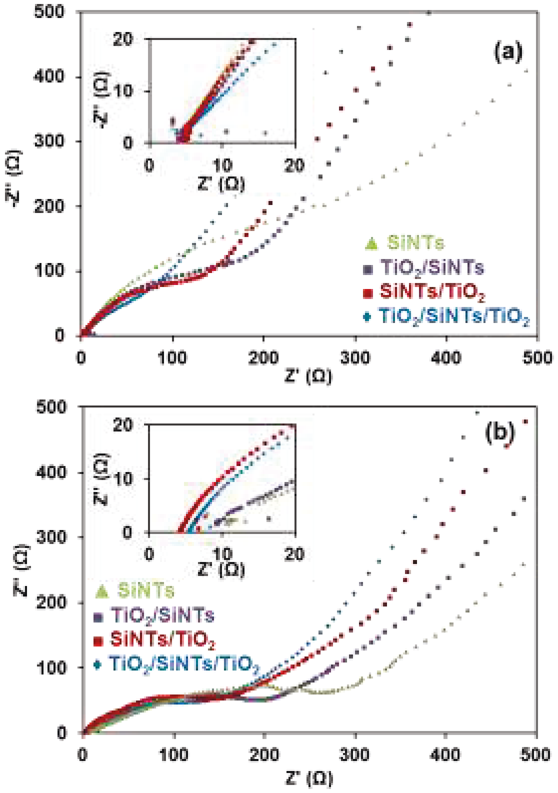

Figure 4.16: Impedance spectra for as-synthesized, (a), after 100 cycles in delithiated state, (b) for bare SiNTs and inner, outer and double-sided TiO_2-coated SiNTs.

The role of inner and/or outer coating layer and the influence on cycling performance can be explained by TEM and SEM analysis of the post cycled nanotubes. These results are shown in Figure 4.17 and 4.18, respectively. For all samples, the ring pattern of Si is no longer found in the SAD pattern as SiNTs becomes amorphous after the first lithiation.

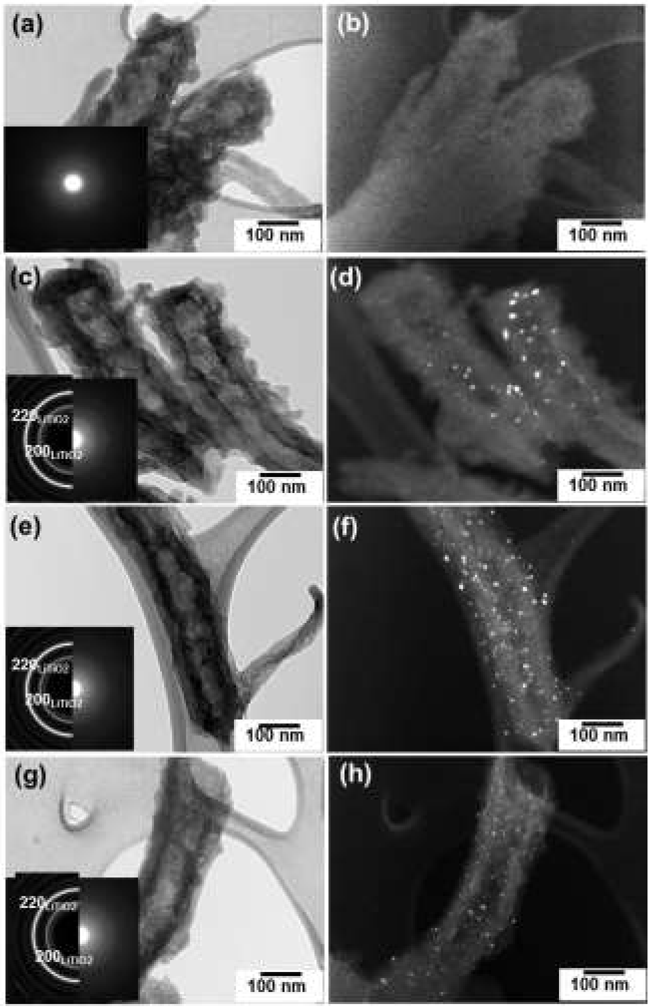

Figure 4.17. TEM micrographs of the post 100 cycles delithiated microstructures. (a) and (b) bare SiNTs. The dak field micrograph was taken using a portion of the diffuse “amorphous” ring. (c) and (d) TiO_2/SiNTs, (e) and (f) SiNTs/TiO_2, (g) and (h)TiO_2/SiNTs/TiO_2. In (d), (f) and (h) the dark field micrographs were taken using a portion of the 200_{LiTiO2} ring.

A ring pattern corresponding to cubic $LiTiO_2$ with d-spacings 2.04 and 1.46 Å is observed for all TiO_2-coated nanotubes in the delithiated state, [21] agreeing with the SAD analysis of Figure 4.2. The SAD pattern (insert of Figures 4.17(c), 4.17(e) and 4.17(g)) and dark field images (Figures 4.17(d), 4.17(f) and 4.17(h)), which have been taken using a portion of the 200 $LiTiO_2$ diffraction ring confirm the presence of this phase with a very small grain size. For the uncoated and the TiO_2/SiNTs electrodes there is clearly more degradation than for SiNTs/TiO_2 and TiO_2/SiNTs/TiO_2. The same trend is visible in the FIB-SEM cross-sections in Figure 4.18, where SiNTs/TiO_2 and TiO_2/SiNTs/TiO_2 clearly display the least amount of structural damage. For TiO_2/SiNTs the inner nanotube wall remains smooth, indicating that the coating is intact to some extent.

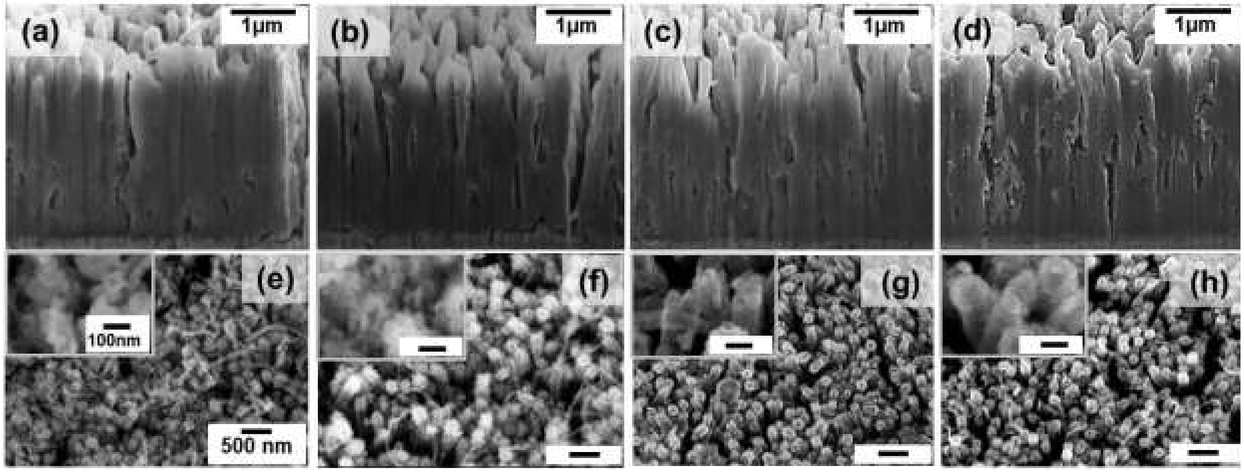

Figure 4.18: FIB cross-sections (top row) and plane-view SEM images (bottom row) after 100 cycles of bare SiNTs (a and e), TiO_2/SiNTs (b and f), SiNTs/TiO_2 (c and g) and TiO_2/SiNTs/TiO_2 (d and h) Despite the original structure of the nanotubes still being recognizable for all electrodes, SiNTs and TiO_2/SiNTs clearly show more structural damage compared to and TiO_2/SiNTs/TiO_2, in agreement with cycle life and CE data.

The same observation is made for the Al_2O_3 and TiN coatings in Figure 4.19. Especially SiNTs/Al_2O_3 shows remarkable structural integrity after cycling. Naturally, Si has become amorphous during cycling, but also the Al_2O_3 remains amorphous when it has been converted to Li-Al-O glassy phase. For SiNTs/TiN, the TiN coating remains crystalline. The dark-field image (Figure 4.19(d)) has been taken using a portion of 200_{TiN} ring pattern.

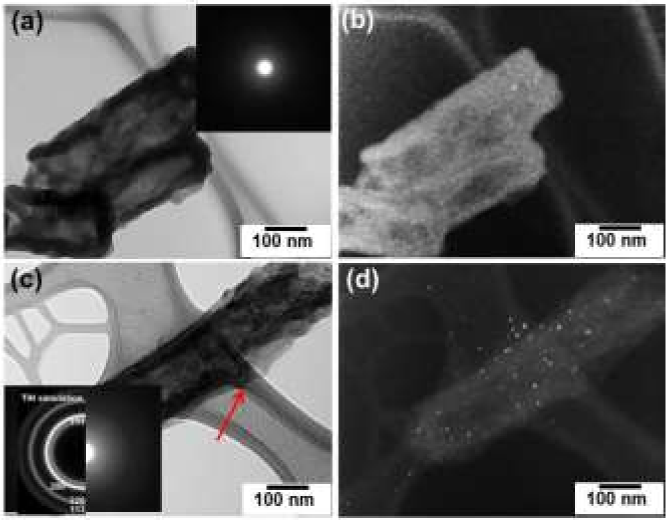

Figure 4.19: (a) and (b) SiNTs/Al_2O_3. For Al_2O_3, the dark-field micrograph was taken using a portion of the diffuse “amorphous” ring, (c) and (d), SiNTs/TiN, with the TiN nanocrystallites being imaged in dark field using a portion of 111_{TiN} ring pattern.

To better understand the distribution of the SEI components across the nanotubes and the effect on CE, the EELS elemental maps of uncoated SiNTs and TiO_2-coated nanocomposites after 100 cycles were acquired. These results are shown in Figure 4.20. Figure 4.20(a) shows that the uncoated SiNTs are mostly covered by Li, C, and O indicating the formation of Li_2CO_3 or Li alkylcarbonate, with a perfect overlap between Li, C and O signal throughout the whole nanotube’s length and width. This means that SEI layer mostly composed of Li_2CO_3 is quite thick and has grown directly inside and outside of the nanotube surface. The Si map also shows some evidence of fragmentation. For TiO_2/SiNTs, the SiNTs surface is similarly covered with SEI. Since the Si is directly exposed to the electrolyte when the coating is only on the inside, this is to be expected. Similar to bare SiNTs, the Si map shows evidence of fracturing, though the TiO_2 layer is seen as relatively intact. For SiNTs/TiO_2, there is little evidence of carbon outside of the TiO_2 shell. However, SEI signals are stronger inside of the nanotubes, where there is no coating and Si is, apparently, still directly exposed to the electrolyte. This is an important finding that explains why addition of an inner coating was experimentally observed to further improve the coulombic efficiency. It also indicates that one cannot assume that an inner surface of a hollow structure is entirely immune from continuing SEI formation during cycling. There is the least SEI in the double coated electrode i.e. TiO_2/SiNTs/TiO_2, which also shows the least mechanical degradation during cycling. This is consistent with its highest coulombic efficiency and cycling capacity retention. It is also worth noting that the relative signal strength of oxygen compared to carbon is lower than for bare SiNTs or inner coated SiNTs. This indicates a lower amount of Li_2CO_3, a 2-electron reduction product, and higher amounts of alkyl carbonates, which are single-electron reduction products, in agreement with XPS and CE data.

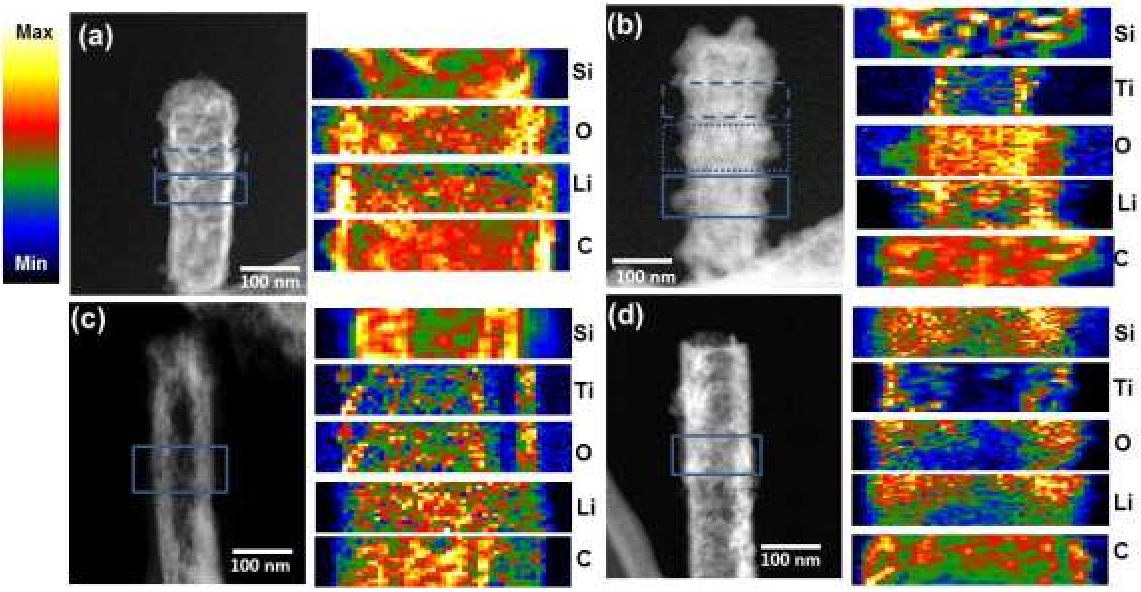

Figure 4.20: Microstructure after 100 cycles. HAADF images and EELS elemental maps of Si, Ti, O, Li and C of (a) SiNTs; (b) TiO_2/SiNTs. (c) SiNTs/TiO_2; (d) TiO_2/SiNTs/TiO_2; In (a) the Si map was obtained from the region marked by the dashed rectangle, while the other elements were obtained from the region marked by the solid rectangle. In (b) only Li, Si and C together, Ti and O together were obtained from the regions marked by the dashed rectangle, the dotted rectangle and solid rectangle, respectively.

As we mentioned before, the main problem using Si as an anode material is finding a way to accommodate the large volume expansion. An important asset of hollow structures in general is that part of that expansion can be directed inwards, making optimum use of that free space. Table 4.2 provides a comparison of the electrochemical performance of our best-performing electrode with that of previously reported hollow Si-based structures such as (coated) nanotubes,[11,14,16,24] hollow nanospheres[10] and 'yolk-shell'-type structures,[8,29,69,70] all of which aim to improve the accommodation of the volume changes of Si during cycling by introducing a large void fraction into the active material.

Table 4.2: Comparison of capacity at different rates and coulombic efficiency of different hollow Si-based structures

Electrodes	Capacity at 0.2C (unless indicated otherwise) Cycle nr:				Coulombic efficiency at 0.2 C (unless indicated otherwise) Cycle nr:				Rate capability at 2C (unless indicated otherwise)
	1st	50th	100th	200th	1st	50th	100th	200th	
TiO_2/SiNTs/TiO_2	2822	2070	1900	1700	~90	~100	~100	~100	~1700
SiNTs [14]	2924	~2000	N/A	N/A	90	~98	N/A	N/A	~1500
Hollow nanospheres[67]	2417	2250 (0.5C)	~2100 (0.5C)	1900 (0.5C)	77(0.5C)	99(0.5C)	99.5	99.5	N/A
Si-ATO-Si nanotubes[67]	2750* (0.05C)	~1540* (0.5C)	~1540* (0.5C)	N/A	73	>98	>98	N/A	1500 (0.5C)
hollow core–shell structured porous Si–C[29]	1400 (~0.13C)	~760 (~1.3C)	650 (1.3C)	N/A	~60	>98	>98	N/A	<600
SiNP@CT[8]	969(1C)	~920 (1C)	~920 (1C)	872 (1C)	71	~99	~99	~99	870
DWSiNT[11]	1780*	~1690 *	~1690 *	~1670 *	76 (12C)	99.9 (12C)	99.9 (12C)	99.9 (12C)	1000
SiNTs[68]	~1900 (0.5C)	<1200 (10th)	NA	N/A	~73	N/A	N/A	N/A	840
Si@void@C[69]	2833 (0.1)	~1500 (1C)	~1500 (1C)	~1500 (1C)	60 (0.1C)	~99 (1C)	~99 (1C)	~99.5 (1C)	~1100
Nest-like Si nanospheres[15]	3052 (0.5C)	~1000 (0.5C)	N/A	N/A	N/A	>99 (0.5C)	N/A	N/A	N/A
Si/Ge nanotubes[16]	~1700	~1300	N/A	N/A	88.5	~97	N/A	N/A	~1200
Si@HC_3[70]	3677 (0.05C)	1900 (0.05C)	1625 (0.05C)	N/A	64 (0.05C)	98-99 (0.05C)	98-99 (0.05C)	N/A	<1000 (2.5C)
Ni coated SiNTs[24]	760* (0.1-0.15C)	~646* (0.1-0.15C)	646* (0.1-0.15C)	N/A	71	~99	~99	N/A	N/A

*: delithiation capacity, N/A: not available

All the listed capacities are based on the total weight of the composite active material. Electrodes that use the active material in as-made form such as directly grown onto a current collector [10,14,16] or templated on carbon fibers [8,11,24] tend to have superior cycling stability and rate capability compared to when the electrodes are made in powder form using binders and conductive additives. [68,70] From the data listed in Table 4.2, it can be seen that our material stands out particularly in terms of rate capability and coulombic efficiency, which is seen as a general trend for coated Si materials.

Our results show that in terms of accommodating the Si expansion by directing it inwards, the Al_2O_3 coating is most suitable. The strong Al signal and relatively small amount of Li carbonate in the XPS spectra of SiNTs/Al_2O_3 indicate that hardly any fracturing of the coating occurs as exposure of fresh Si would lead to formation of electrolyte reduction products. The TEM images in Figure 4.19 also confirm this picture. This result is in good agreement with the findings of Baggetto et al. who proved that covering a Si thin film electrode with a thick layer of highly Li-ion conductive LiPON solid electrolyte largely prevents SEI formation. However, the Li-Al-O phase has such low electronic conductivity that the rate capability of SiNTs/Al_2O_3 is far inferior to that of SiNTs/TiO_2, despite the latter's tendency to form more SEI. Thus, there is always a compromise between optimizing coulombic efficiency, and thus battery lifetime, and achieving high rate performance and the actual application of device will determine which is more suitable. However, our amorphous ALD TiO_2 coating performs nearly equally well as Al_2O_3 in terms of CE and develops a microstructure upon lithiation that combines high electronic and ionic conductivity and is therefore universally applicable. Coating both sides of the SiNTs rather than only the outside boosts the CE by another ~1% for TiN and TiO_2-coated nanotubes, showing that the inside of the nanotubes is not entirely immune to SEI formation. Even though the inner TiO_2 coating crystallizes into the anatase structure during ZnO reduction and Si deposition, it is observed to form the electronically conductive $LiTiO_2$ phase (see Figure 4.17 (c)&(d), (g)&(h)), contrary to what we observed for thicker coatings,[21] and thus also helps to further improve the rate capability of the electrode.

4.4 Conclusions

We showed that atomic layer deposition (ALD) of TiO_2, TiN and Al_2O_3 on the outer, or both surfaces of hollow Si nanotubes can impart a remarkable positive influence on the cycling performance of Si nanotube electrodes. Coating only the inside of the nanotubes leaves Si exposed to the electrolyte and thus gives the smallest improvement in coulombic efficiency by ~1% while capacity retention is actually slightly worse for all three coatings. The optimum performance was achieved for nanotubes conformally coated on both sides with 1.5 nm of Li active TiO_2 with substantial improvement in capacity retention to 1700 mAh/g vs. 1287 mAh/g for the uncoated baseline, after 200 cycles at 0.2 C. Relative to their initial lithiation capacity, this corresponds to an improvement in capacity retention from 40 to 60%. Steady-state cycling coulombic efficiency improved from 97-98% to near 100% and high rate capability at 5C from 20 to 50% of the initial capacity at 0.2C. These results are among the best ever reported for hollow Si-based composite materials. In the case of TiO_2 and TiN, CE improves by an additional ~1% going from coating only the outside to both sides of the SiNTs, showing that the inner surfaces are not immune from SEI formation. The dual-phase structure of the TiO_2 coating consisting of amorphous TiO_2 and cubic $LiTiO_2$, combines high ionic and electronic conductivity and is therefore highly effective in enabling rapid lithiation and delithiation, as the rate capability data showed. Coatings with only high electronic (TiN) or only high ionic (Al_2O_3) conductivity are not nearly as effective. Furthermore, the coated composites show relatively little structural damage and good cycling stability (~7% degradation between 100 and 200 cycles) making them a promising material for Li-ion battery anodes.

4.5 References

1. J. M. Tarascon, and M. Armand,, *Nature*, 2001, **414**, 359-367.

2. M. M. Thackeray, C. Wolverton, and E. D. Isaacs, *Energy Environ. Sci.*, 2012, **5**, 7854-7863.

3. H. Wu, and Y. Cui, *Nano Today*, 2012, **7**, 414.

4. M. T. McDowell, S. W. Lee, W. D. Nix, and Y. Cui, *Adv. Mater.*, 2013.

5. X. Zhou, and Y.-G. Guo, *J. Mater. Chem. A*, 2013, **1**, 9019–9023.

6. S.K. Soni, B. W. Sheldon, X. Xiao, M. W. Verbrugge, D. Ahn, H. Haftbaradaran, and H. Gao*, J. Electrochem. Soc.*, 2012, **159**, A38.

7. C. Yu, X. Li, T. Ma, J. Rong, R. Zhang, J. Shaffer, Y. An, Q. Liu, B. Wei, and H. Jiang*, Adv. Mater.*, 2012, **2**, 68.

8. H. Wu, G. Zheng, N. Liu, T. J. Carney, Y. Yang, and Y. Cui, *Nano Lett.,*2012, **12**, 904−909.

9. B. Hertzberg, A. Alexeev, and G. Yushin, *J. Am. Chem. Soc.,* 2010, **132**, 8548–8549.

10. Y. Yao, M. T. McDowell, I. Ryu, H. Wu, N. A. Liu, L. B. Hu, W. D. Nix, J. W. Choi, and Y. Cui, *Nano Lett.*, 2011, **11**, 2949.

11. H. Wu, G. Chan, J. W. Choi, I. Ryu, Y. Yao, M. T.McDowell, S. W. Lee, A. Jackson, Y. Yang, L. Hu, and Y. Cui, *Nature Nanotechnology*, 2012, **7**, 310-315.

12. M-H Park, M. G. Kim, J. Joo, K. Kim, J. Kim, S. Ahn, Y. Cui, and J. Cho, *Nano Lett.*, 2009, **9(11)**, 3844-3847.

13. K. Zhao, M. Pharr, L. Hartle, J. J. Vlassak, and Z. Suo, *J. Power Sources*, 2012, **218**, 6-14.

14. T. Song, J. Xia, J.-H. Lee, D. H. Lee, M.-S. Kwon, J.-M. Choi, J. Wu, S. K. Doo, H. Chang, W. I. Park, D. S. Zang, H. Kim, Y. Huang, K.-C. Hwang, J. A. Rogers, and U. Paik, *Nano Lett.*, 2010, **10**, 1710.

15. H. Ma, F.Y. Cheng, J. Chen, J.Z. Zhao, C.S. Li, Z.L. Tao, and J. Liang, *Adv. Mater.*, 2007, **19**, 4067.

16. T. Song, H. Cheng, H. Choi, J.-H. Lee, H. Han, D. Hyun Lee, D. Su. Yoo, M.-S. Kwon, J.-M. Choi, S. Gwang Doo, H. Chang, J. Xiao, Y. Huang, W. Il Park, Y.-C. Chung, H. Kim, J. A. Rogers, and U. Paik, *ACS Nano*, 2012, **6 (1)**, 303–309.

17. D. Aurbach, B. Markovsky, M. D. Levi, A. Schechter, M. Moshkovich, and Y. Kohen, *J. Power Sources*, 1999, **81−82**, 95-111.

18. G. V. Etacheri, U. Geiger, Y. Gofer, G. A. Roberts, I. C. Stefan, R. Fasching, and D. Aurbach, *Langmuir*, 2012, **28**, 6175−6184.

19. M. W. Forney, M. J. Ganter, J. W. Staub, R. D. Ridgley, and Brian J. Landi, *Nano Lett.*, 2013, **13**, 4158−4163.

20. R. A. DiLeo, M. J. Ganter, M. N. Thone, M. W. Forney, J. W. Staub, R. E. Rogers, B. J. Landi, , *J. Power Sources*, 2013, **2(2)**, 268–275.

21. E. Memarzadeh Lotfabad, P.Kalisvaart, K. Cui, A. Kohandehghan, M. Kupsta, B. Olsen, and D. Mitlin, *Phys. Chem. Chem. Phys.*, 2013, **15**, 13646-13657.

22. K. Xu, and A. Cresce, Interfacing electrolytes with electrodes in Li ion batteries, *J. Mater. Chem*., 2011, **21**, 9849–9864.

23. D. Liu, and G. Cao, *Energy Environ. Sci*., 2010, **3**, 1218-1237.

24. K. Karki, Y. Zhu, Y. Liu, C.-F. Sun, L. Hu, Y. Wang, C. Wang, and J. Cumings, *ACS Nano*, 2013, **7 (9)**, 8295–8302.

25. C. K. Chan, R. Ruffo, S. S. Hong, Y. Cui, *J. Power Sources*, 2009, **189**, 1132–1140.

26. X. Xiao, P. Lu, and D. Ahn, *Adv. Mater.*, 2011, **23**, 3911–3915.

27. R. Huang, X. Fan, W. Shen, and J. Zhu, *Appl. Phys. Lett.*, 2009, **95**, 133119.

28. H. Chen, Z. Dong, and Y. Fu, and Y. Yang, *J. Solid State Electrochem.*, 2010, **14**, 1829-1834.

29. X. Li, P. Meduri, X. Chen,W. Qi, M. H. Engelhard, W. Xu, F. Ding, J. Xiao, W. Wang, C. Wang, J.-G. Zhang, and J. Liu, *J. Mater. Chem.*, 2012, **22**, 11014.

30. Y. Yao, N. Liu, M. T. McDowell, M. Pasta, and Yi Cui, *Energy Environ. Sci.*, 2012, **5**, 7927

31. M. T. McDowell, S. W. Lee, C. Wang, and Y. Cui, *Nano Energy*, 2012,**1** ,401–410.

32. Y. Yu, L. Gu, C. Zhu, S. Tsukimoto, and P. A. van Aken, J. Maier, *Adv. Mater.*, 2010 , **22**, 2247–2250.

33. E. L. Memarzadeh, W. P. Kalisvaart, A. Kohandehghan, B. Zahiri, C. M. B. Holt and D. Mitlin, *J. Mater. Chem*., 2012, **22**, 6655.

34. A. Kohandehghan, W.P. Kalisvaart, M. Kupsta, B. Zahiri, B. Shalchi Amirkhiz, Z. Li, E.L. Memarzadeh, L.A. Bendersky, and D. Mitlin, *J. Mater. Chem. A*, 2013, **1**, 1600.

35. Y. He, X. Yu, Y. Wang, H. Li and X. Huang, *Adv. Mater.*, 2011, **23**, 4938–4941.

36. H. T. Nguyen, M. R. Zamifir, L. D. Duong, Y. H. Lee, P. Bondavalli, and D. Pribat, *J. Mater. Chem.*, 2012, **22**, 24618.

37. X. Meng, X. Q. Yang and X. Sun, *Adv. Mater.*, 2012, **24**, 3589-615.

38. B. E. Kim, S. E. Park, J. C. Lim, and Joong Kee Lee, *Phys. Scr.*, 2010, **T139**, 014021.

39. S. K. Cheah, E. Perre, M. Rooth, M. Fondell, A. Hårsta, L. Nyholm, M. Boman, T. Gustafsson, J. Lu, P. Simon, and K. Edström, *Nano Lett.*, 2009, **9(9)**, 3230-3233.

40. G. Jeong, J.-H. Kim, Y.-U. Kim and Y.-J. Kim, *J. Mater. Chem.*, 2012, **22**, 7999.

41. Y. Hwa, W-S. Kim, B-C. Yu, HS. Kim, S-H. Hong, and H-J. Sohn, *J. Mater. Chem. A*, 2013, **1**, 3733.

42. X. Li, X. Meng, J. Liu, D. Geng, Y. Zhang, M. N. Banis , Y. Li , J. Yang, R. Li , X. Sun, M. Cai , and M. W. Verbrugge, *Adv. Funct. Mater.* 2012, **22**, 1647–1654.

43. A. Kohandehghan, P. Kalisvaart, K. Cui, M. Kupsta, E. Memarzadeh Lotfabad, and D. Mitlin, *J. Mater. Chem. A*, 2013, **1**, 12850-12861.

44. L.Y. Beaulieu, V.K. Cumyn, K.W. Eberman, L. J. Krause, and J.R. Dahn, *Rev. Sci. Instr.*, 2001, **72**, 3313.

45. V. A. Sethuraman, K. Kowolik, and V. Srinivasan, *J. Power Sources*, 2011, **196(1)**, 393-398.

46. R.F. Egerton, Electron energy-loss spectroscopy in the electron microscope. 3rd ed2011, New York: Springer.

47. L. Brewer, *Chemical Reviews*, 1953, **52**, 1.

48. K. Song, S. Yoo, K. Kang, H. Heo, Y.-M. Kang, M.-H. Jo, *J. Power Sources*, 2013, 229, 229-233.

49. S. Sim, P. Oh, S. Park, J. Cho, *Adv. Mater.,* 2013, **25**, 4498.

50. S. Xun, X. Song, L. Wang, M. E. Grass, Z. Liu, V. S. Battaglia and G. Liu, *J. Electrochem. Soc.*, 2011, **158 (12)**, A1260-A1266.

51. X. H. Liu, J. W. Wang, S. Huang, F. Fan, X. Huang, Y. Liu, S. Krylyuk, J. Yoo, S. A. Dayeh, A. V. Davydov, S. X. Mao, S.T. Picraux, S. Zhang, J. Li, T. Zhu, and J. Y. Huang, *Nat Nanotechnol.*, 2012, **7(11)**, 749-56.

52. H. Kim, M. G. Kim, and J. Cho, *Adv. Energy Mater.*, 2012, **2**, 1425–1432.

53. G. Zampardi, E. Ventosa, F. La Mantia, and W. Schuhmann, *Chem. Commun.,* 2013, **49**, 9347.

54. M. Pfanzelt, P. Kubiak, S. Jacke, L. Dimesso, W. Jaegermann, and M.Wohlfahrt-Mehrensa, *J. Electrochem. Soc.*, 2012, **159 (6)**, A809-A814.

55. V. L. Chevrier, H. M. Dahn, and J. R. Dahn, *J. Electrochem. Soc.,* 2011, **158(11)**, A1207-A1213.

56. M.N. Obrovac, L. Christensen, *Electrochem. Solid-State Lett.*, 2004, **7**, A93–A96.

57. L. Baggetto, R. A. H. Niessen, F. Roozeboom and P. H. L. Notten, *Adv. Funct. Mater.*, 2008, **18**, 1057-1066.

58. H. Kim and J. Cho, *Nano Lett.*, 2008, **8 (11)**, 3688-3691.

59. H. Tavassol, J. W. Buthker, G. A. Ferguson, L. A. Curtiss and A. A. Gewirth, *J. Electrochem. Soc.,* 2012, **159(6)**, A730-A738.

60. Y. Liu , N. S. Hudak , D. L. Huber , S. J. Limmer , J. P. Sullivan and J. Y. Huang, *Nano Lett.*, 2011, **11**,
4188–4194.

61. H. T. Fang, M. Liu, D. W. Wang, T. Sun, D. S. Guan, F. Li, J. Zhou, T. K. Sham and H. M. Cheng, *Nanotechnology*, 2009, **20**, 225701.

62. M. Q. Snyder, S. A. Trebukhova, B. Ravdel, M. C. Wheeler, J. DiCarlo, C. P. Tripp and W. J. DeSisto, *J. Power Sources*, 2007, **165**, 379.

63. W.J.H. Borghols, D. Lützenkirchen-Hecht, U. Haake, E.R.H. van Eck, F.M. Mulder, M. Wagemaker, *Phys. Chem. Chem. Phys*., 2009, **11**, 5742.

64. K. Xu, *Chemical Reviews*, 2004, **104**, 4303.

65. L. Kavan, M. Gratzel, J. Rathousky, A. Zukal, *J. Electrochem. Soc.*, 1996, **143**, 394.

66. M. M. Rao, J. S. Liu, W. S. Li, Y. H. Liao, Y. Liang and L. Z. Zhao, *J. Solid State Electrochem*, 2010, **191**, 255–261.

67. J. Rong, X. Fang, M. Ge, H. Chen, J. Xu, and C. Zhou, *Nano Research*, 2013, **6(3)**, 182–190.

68. Z. Wen, G. Lu, S. Mao, H. Kim, S. Cui, K. Yu, X. Huang, P. T. Hurley, O. Mao, J. Chen, *Electrochem. Commun*., 2013, **29**, 67-70.

69. N. Liu, H. Wu, M. T. McDowell, Y. Yao, C. Wang, and Y. Cui, *Nano Lett.*, 2012, **12**, 3315−3321.

70. S. Chen, M. L. Gordin, R. Yi, G. Howlett, H. Sohn and D. Wang, *Phys. Chem. Chem. Phys.*, 2012, **14**, 12741–12745.

5 High Density Sodium and Lithium Ion Battery Anodes from Banana Peels

Material in this chapter has been published in:

E. Memarzadeh Lotfabad, J. Ding, Kai Cui, Alireza Kohandehghan, Peter Kalisvaart, Michael Hazelton, D. Mitlin, ACS Nano 2014, DOI: 10.1021/nn502045y

5.1 Introduction

Sodium ion batteries (NIBs, NABs or SIBs) are highly promising for large-scale energy storage systems (ESS) due to sodium's natural abundance, a more democratic global distribution and much lower price as compared to Li. [1-4]. Graphite microparticles are the standard anode material in commercial lithium ion batteries (LIBs) due to their reasonable reversible capacity (up to 372 mAh/g), low and flat potential plateaus providing an optimum voltage window versus an opposing cathode, superior cycling behavior, high coulombic efficiency and low cost. [5-8] Unfortunately, conventional graphite is not suitable for NIB anodes. [9-11] Minimal Na ions may be intercalated into graphite, an effect mainly attributed to the larger ionic radii of the Na *vs.* Li (0.102 nm vs. 0.076 nm). [10] Substantial gains have been made to find suitable alternative anode materials for NIBs, including various carbonaceous materials, [12-16] phosphorous, [17,18] ternary ionic sodium compounds, [19-24] metal oxides, [25-30] metal nitrides, [31] alloys, [32-44] graphene and graphene-based composites. [45,46] An emerging strategy for Li ion batteries is to employ dense - low surface area materials that can store charge by rapid intercalation of ions between the atomic layers, analogous to graphite but with much higher charge storage capacity. This approach has been recently utilized to create a large family of high-performance 2D LIB anode materials, labeled "MXenes" where M is a transition metal and X is C or N. [47-50] Such an approach would be similarly beneficial for NIB applications but has to date not received the same level of scientific attention.

Carbons, along with various earth abundant oxides, are highly attractive for both NIBs and LIBs since in many forms they optimize both performance and cost. [12,51-54] High surface area nanostructured carbons have been utilized for Na storage. [51,52,55] Studies have focused on hard (poorly or non graphitizable) carbons due to their large interlayer distance that can accommodate Na insertion in a range of chemically and physically dissimilar storage sites. [51,52,55-57] Emerging approaches include porous cellulose fibers, [58,59] graphene foam, [60] hierarchical structures based on a combination of graphene, carbon nanotubes, and iron nanoparticles, [61] Fe_2O_3/graphene hybrids, [62] or highly reversible spherical carbons. [63] Additional noteworthy examples of high performance NIB carbons include refs. [12,51,52,54,56,64,65] Such materials are very promising from a specific capacity and rate capability viewpoint. However, in many cases the heterogeneous environment of the stored Na creates a distribution of site energies, with "supercapacitor-like" sloping voltage profiles that may be non-ideal for some applications. The highest free energy sites in the carbon will trap Na irreversibly or will require a substantial overpotential to have it extracted. This leads to poor cycling coulombic efficiency and large (1 V or higher) charge/discharge voltage hysteresis.

Bananas are the most commonly eaten fruit in the United States, making up more than 50% of total amount of fruit consumed per year. According to 2009 statistics approximately 3.5 of the total 6 million metric tons were bananas. [66] The banana peels, which make up 40% of the total weight of the fruit, are inedible to humans and serve little economic purpose apart from being ground into compost along with other biodegradable wastes. The majority of banana peels are placed in landfills or garbage dumps, where they release CO_2 along with noxious gases as they decay. In that sense they are an ideal precursor for value added carbons, possessing a negative value associated with their disposal. Banana peels have been employed to fabricate conventional activated carbons (AC) for wastewater treatment [67-69] and for supercapacitor applications where they also served as a template for aminophenol furfural resin-zinc complexes. [70,71] In this study set out to create a NIB carbon that behaves electrochemically like graphite in LIBs, which as will be demonstrated requires a fundamentally different structure compared to that of a commercial high surface area - highly disordered AC. While such a material will never hold as much charge (by weight) as ultra-high surface area carbons like defective or N-doped graphene, [72-74] it will demonstrate key commercial advantages such as a) maximizing the voltage window of a full cell due to a low and flat plateau; b) be volumetrically dense with a low surface area, resulting in excellent electrode packing characteristics, a high volumetric capacity, and low levels of SEI formation, and c) highly reversible with nearly 100% cycling coulombic efficiency and minimal voltage hysteresis. Our facile synthesis strategy combined with a precursor that is truly an abundant waste will make these electrodes both inexpensive and environmentally friendly.

5.2 Experimental

5.2.1 Material synthesis

The collected biomaterial was extensively washed with DI water, cut into small pieces and dried at 110 °C overnight in vacuum oven. Typically 10 g of banana peels precursor is loaded in a tubular furnace for the pyrolysis carbonization process (800-1400 °C for 5 hours, heating rate: 5°C min^{-1}) under argon atmosphere with the flow of 100 sccm min^{-1}. The obtained carbon is carefully washed in 20% KOH at 70 °C for 2 h and 2 M HCl at 60 °C for 15 h to remove the remaining impurities. The purified samples are collected by filtration after rinsing further with DI water. Then the carbon is dried at 110 °C overnight in a vacuum oven. Some of the carbonized banana peel pseudographite (BPPG) specimens are further activated at 300 °C for 3 h (at a heating rate of 5 °C min^{-1} in the tubular furnace) in a dry air flow of 50 sccm min^{-1}. The obtained activated banana peel pseudographite (BPPG-A) is first ground and then washed with 2 M HCl and DI water again before use. Commercially purchased battery-grade graphite powder (MTI) and high surface area high electrical conductivity activated carbon (NORIT Supra) were employed as baselines.

5.2.2 Material characterization

The surface area and porous texture of carbon materials are characterized by nitrogen adsorption at 77 K (Quantachrome Autosorb^{-1}). Prior to the gas sorption measurements, the samples were outgassed at 250 °C for 4 h under a vacuum. The pore size distributions were evaluated by a nonlocal DFT method using nitrogen adsorption data and assuming slit-pore geometry. To characterize the morphology of the carbon samples, field emission scanning electron microscopy (FE-SEM) (Hitachi S-4800) and transmission electron microscopy (TEM) (JEOL 2010, 200 kV) are used. X-ray photoelectron spectroscopy (XPS) measurements are performed on an ULTRA (Kratos Analytical) spectrometer using monochromatic Al-K$_{\alpha}$

radiation (hυ= 1486.6 eV) run at 210 W. Before XPS analysis, the samples were dried at 110 °C in vacuum oven overnight to remove the absorbed water. X-ray diffraction (XRD) analysis was performed using a Bruker AXS D8 Discover diffractometer with the Cu K_α radiation.

5.2.3 Electrochemical testing

A slurry of 80% BPPG, 10% carbon black (Super-P) and 10% PVDF (binder) in N-methylpyrrolidone was coated onto 316L stainless steel spacers of 1.86 cm^2 (around 1 mg active materials on one electrode) and then dried at 110 °C overnight in vacuum oven. The obtained electrode, polyethene separator and Na/Li metal counter electrode were assembled into a 2032 type button cell filled with electrolyte, in an Ar filled glove box with sub-0.1 ppm water and oxygen contents. The NIB electrolyte was 1 M $NaClO_4$ in 1:1 by volume ethylene carbonate (EC) and diethyl carbonate (DEC). The LIB electrolyte was 1 M $LiPF_6$ in a 1:1:1 volume ratio of EC:DMC:DEC (DMC is dimethyl carbonate). For the samples employed solely for ex-situ XRD analysis of sodiation/desodiation or lithiation/delithiation-induced lattice dilation/contraction, carbon black was not included, and the amount of binder was limited to 5 wt %. Cyclic voltammetry (CV) was carried out using a Solartron 1470 Multistat system at a scan rate of 0.1 mV s^{-1} (0.001–2.8 V). The charge/discharge measurements were performed using an Arbin BT2000 Potentiostat. Electrochemical impedance spectroscopy measurements were also performed using a Solartron 1470E Multichannel Potentiostat/ Cell Test System. All electrochemical tests were conducted at room temperature.

5.3 Results and Discussion

5.3.1 Structure of BPPG and BPPG-A

We employ a shorthand designation to label the various carbons. The as-pyrolyzed banana peel pseudographite is named BPPG-*x*, with *x* representing the carbonization temperature. The subsequently air activated carbon is termed BPPG-*x*-A. Battery-grade graphite, labeled CG and high surface area high electrical conductivity activated carbon labeled AC (both commercially purchased) were employed as baselines.

The heterogeneous structure of a banana peel consists of biopolymers in plant cell walls, and includes hemicelluloses, pectins, lignins, free-sugars, proteins, and some crystalline cellulose.[75] Both hemicellulose and lignin are highly cross-linked and non-crystalline, thus favoring formation of non-graphitic carbons at reasonable pyrolysis temperatures. Lignin is deemed especially important for converting biomass into porous carbons through pyrolysis. [76] The banana peels contain up to 20% pectin, which is another branched biopolymer molecule, being similar in structure to lignin and consisting of sugar monomers. Up to 35% of the peel dry mass is made up of free-sugars, although the exact composition varies between species and with ripening. [75,77] During pyrolysis, organic molecules emit gases such as CO and CH_4, while the remaining carbon cross-links and undergoes some aromatic ordering. If the precursor is rich in smaller molecules such as the free-sugars, a viscous liquid may form allowing the graphene sheets to partially align themselves in the pitch that precedes full carbonization. [78] As discussed in the Introduction, formation of equilibrium graphite has to be avoided as the interlayer spacing is too small to facilitate Na intercalation. The banana peel is an ideal precursor for NIB anodes, balancing the lignin and pectin fractions that prevent crystallization of equilibrium graphite with the free-sugars that enable partial ordering of the graphene layers. Such pseudographitic ordering allows for significant Na intercalation into the graphene interlayer spacings of the pyrolyzed carbon. However the resultant graphene sheets are also highly defective (e.g. divacancy defects). These reversibly bind to Li and thus allow for 3X more charge to be stored as compared to equilibrium graphite in LIBs.

Figure 5.1(a) shows an environmental SEM image of a cross-sectioned dried banana peel. In the as-dried state (pre-carbonization) the peels are effectively dense with little visible macro porosity. Figures 5.2(a), 1(b) and 1(c) show SEM micrographs of the BPPG specimens. As a result of the pyrolysis the materials develop limited macroporosity. The inset in Figure 5.2(a) compares the density of loose (not tapped) powders of BPPG-1100-A with that of commercial electrode grade graphite (CG) and with commercial supercapacitor electrode-grade activated carbon (AC). With the same mass loading (1.19 grams), the packed volume of BPPG-1100-A is substantially lower than that of activated carbon, being closer to that of graphite. Since the diameter (1.9 cm) of the glass vials is identical in each case, the relative densities of the loose powders are effectively the inverse of their packed height difference. The heights of the AC, GC and BPPG-1100-A powders are 1.2 cm, 0.7 cm and 0.8 cm, respectively.

Table 5.1 lists the relevant physical properties of the as-carbonized and carbonized and activated BPPG specimens. The pore size distributions, calculated using density functional theory (DFT) model from the adsorption branch, are shown in Figure 5.2(b). The actual experimental isotherms for BPPG-A specimens are shown in the inset, which show Type-I/IV behavior.

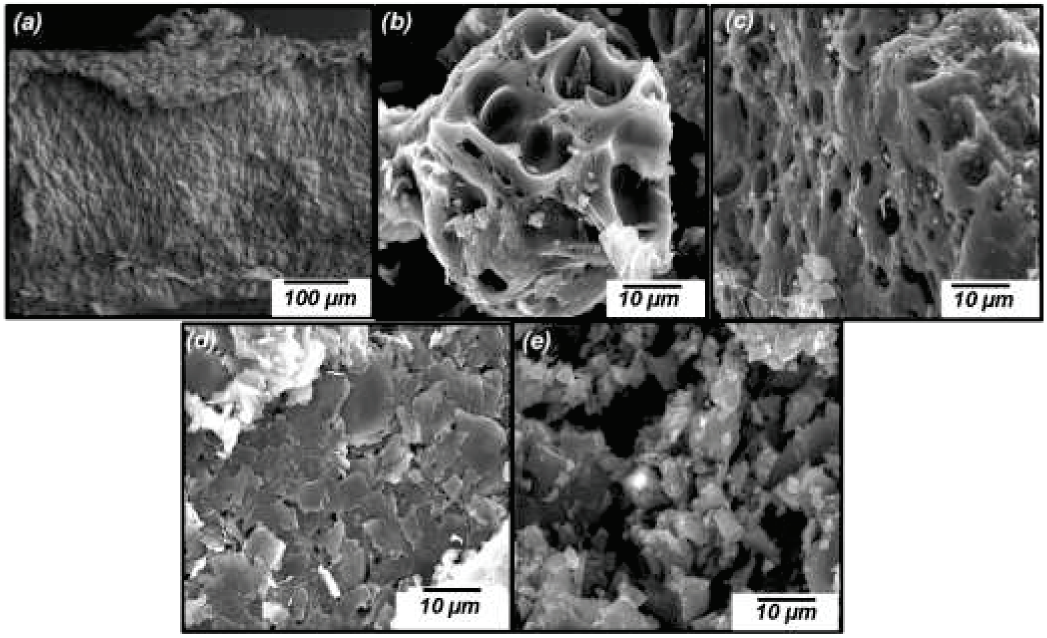

Figure 5.1: (a) Environmental SEM image of a cross-sectioned dried banana peel. (b)-(c) Low magnification SEM micrographs of banana peel pseudo graphite (BPPG) carbonized at 800°C and activated (b) and at 1400°C and activated (c). (d) SEM images of baseline commercial graphite (CG), and (e) baseline NORIT Supra activated carbon (AC), highlighting the overall morphology of the materials employed as electrochemical testing baselines.

Interestingly, increasing the carbonization temperature promotes a shift from microporosity to mesoporosity for an identical air activation treatment (300°C). For instance after carbonization at 1400 °C, the material is primarily mesoporous with the largest volume fraction of pores being centered 3.7 nm. Air activation is known to preferentially attack the disordered (less thermodynamically stable) portions of the carbon. One can argue that with increasing carbonization temperature and the enlargement of the pseudographitic domains (Table 5.1), there is a concomitant coarsening of the remaining disordered regions. This would lead to larger pores in the post-activated state. For the non-activated specimens the total surface areas range from 14.5 - 33 m^2/g, which is effectively the geometric surface area with an additional contribution from the macroporosity. Even after activation, the surface areas are relatively low, ranging from 62 to 217 m^2/g. The true density of the carbons may be estimated as

2 g / (1 cm^3 + volume of pores). The total pore volume for BPPG, BPPG-A and commercial high surface area activated carbon AC are listed in Table 5.1. While for the BPPG and BPPG-A the resultant density is still in the 2 g/cm^3 range, for the case of AC the density is half that value, i.e. 1 g/cm^3.

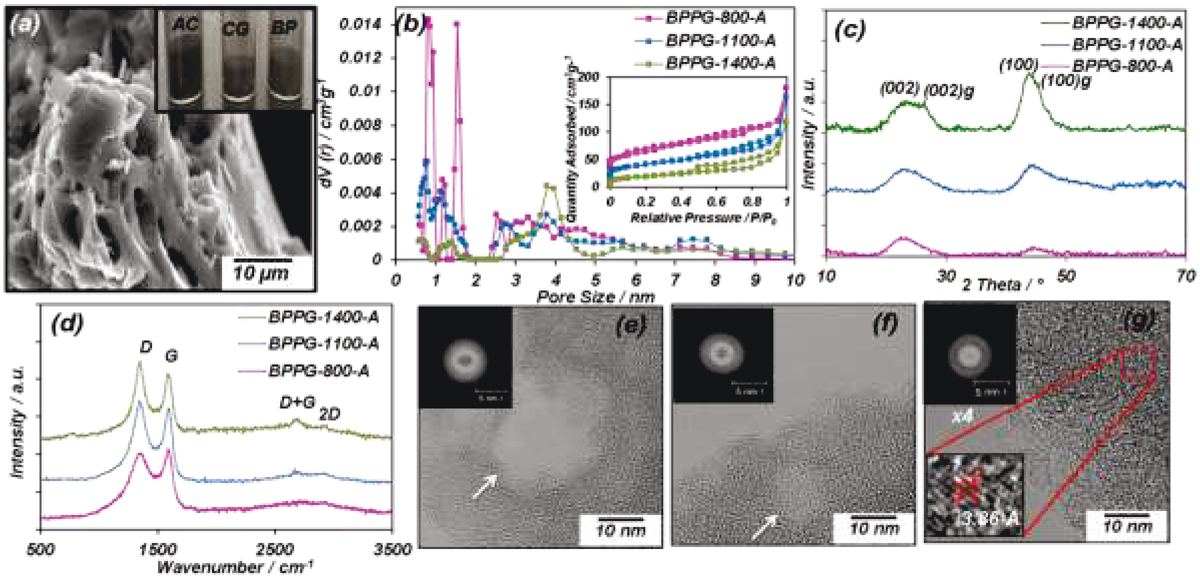

Figure 5.2: Structure of banana peel pseudo graphite (BPPG) in its activated state. (a) A SEM micrograph highlighting the general morphology of a BPPG particle (BPPG-1100-A), with the inset showing its volume difference in comparison with baseline commercial graphite (CG) and activated carbon (AC) of the same weight. (b) Pore size distribution (calculated from the adsorption isotherms using DFT method) with the inset showing nitrogen adsorption-desorption isotherms. (c) and (d) XRD and Raman spectra. (e)-(g) HRTEM micrographs of BPPG-800-A, BPPG-1100-A and BPPG-1400-A, respectively. The corresponding data for BPPG is shown in Figure 5.3(a)-5.3(b).

Table 5.1: Structure and textural properties of BPPG and BPPG-A

Samples	**d_{002} (Å)**	**L_a (nm)**	**L_c (nm)**	**I_G/I_D[a]**	**S_{BET} (m^2/g)[b]**	**V_t (cm^3/g)[c]**	**pore vol % (<2nm)**	**pore vol % (> 2nm)**
BPPG-800	3.97	2.12	1.56	0.78	33.0	0.059	20.3	79.7
BPPG-1100	3.91	4.15	1.59	0.91	19.3	0.052	10.1	89.9
BPPG-1400	3.84/3.35	7.30/10.91	2.04/5.56	0.93	14.5	0.047	6.2	93.8
BPPG-800-A	3.99	2.43	1.59	0.79	217.3	0.23	55.4	44.6
BPPG-1100-A	3.92	4.36	1.62	0.92	130.8	0.19	38.2	61.8
BPPG-1400-A	3.86/3.35	7.43/11.31	2.12/5.49	0.94	62.1	0.14	13.8	86.2
AC	3.72	4.2	1.84	0.26	2050	1.17	61.7	38.3

[a] I_D and I_G are the integrated intensities of D- and G-band. [b] Surface area was calculated with Brunauer_Emmett_Teller (BET) method. [c] The total pore volume was determined at a relative pressure of 0.98.

Figure 5.2(c) shows the XRD patterns of the BPPG-A specimens. The XRD patterns of the BPPG are shown in Figure 5.3(c). It can be seen that the 300°C activation will not appreciably alter the graphitic order/disorder. The results of the XRD analysis, along with the results of Raman and BET, are shown in Table 5.1. The average graphene interlayer spacing was calculated from the peak centers. The thickness and average width of the graphitic domains, L_c and L_a, are calculated based on the well-known Scherrer equation, using the FWHM values of (002) at $2\theta \sim 23^o$ and (100) at $2\theta \sim 43^o$. As Table 5.1 demonstrates, the integraphene layer (d_{002}) spacing gradually shifts toward lower values with increasing carbonization temperature. However, a comparison of the 800°C, 1100°C and 1400°C carbons indicates that this trend is quite weak, and that in all cases the spacing is significantly above that of equilibrium graphite (0.3354 nm). In the 800°C and 1100°C specimens the average thickness of the pseudographitic domains is ~ 1.6 nm, indicating that they are composed of ~ 4 stacked graphene layers (*i.e.*, 1.6/0.4 = 4). In the 1400°C specimens the domains are composed of ~ 5 stacked layers.

Carbonizing at 1400°C creates a bimodal distribution in the average *d* spacings, indicating that the temperature is finally high enough to form equilibrium graphite (c/2 measured as 0.3354 nm). The two overlapping peaks were mathematically deconvoluted using the Voigt function. Based on the deconvoluted areas of the peak doublets, the carbon to equilibrium graphite ratio for BPPG-1400-A is 8:1 by weight.

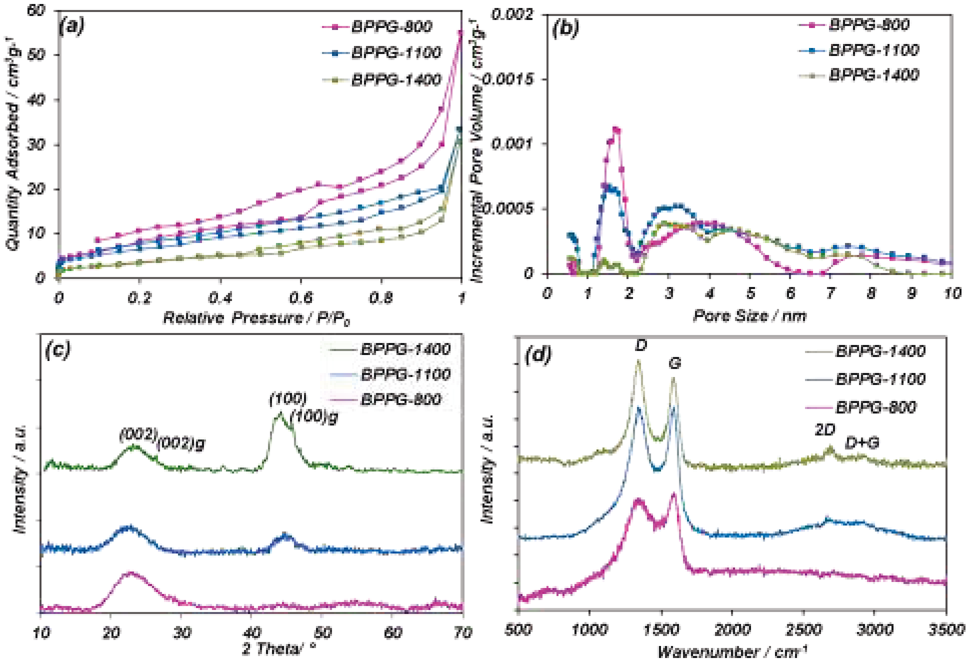

Figure 5.3: (a) Nitrogen adsorption-desorption isotherms of BPPG. (b) Pore size distribution calculated from the adsorption isotherms, using DFT method. (c) XRD patterns of the un-activated specimens (BPPG). (d) Raman spectra of BPPG.

Raman spectroscopy analysis results are shown in Figure 5.2(d) and Figure 5.3(d). In a Raman spectrum for carbon materials the G band is a characteristic feature of the graphitic layers and corresponds to the tangential vibration of the carbon atoms, while the D band corresponds to disordered carbon or defective graphitic structures. The integral intensity ratio of these two peaks scales with the degree of graphitic ordering in the carbons.[79] The integral intensity ratio of G band to D band rises with increasing carbonization temperature, agreeing with the XRD results. The fits of the spectra are shown in Figure 5.4(d), with the resultant I_G/I_D being shown in Table 5.1. For all synthesis conditions, the I_G/I_D ratio never goes above 1, indicating that the ordered graphene sheets in all the materials are highly defective.

High resolution transmission electron microscopy (HRTEM) micrographs of BPPG-800-A, BPPG-1100-A, and BPPG-1400-A are shown in Figure 5.2(e)-(g). For all three specimens, well defined larger (~ 3 nm and upwards) mesopores were observed throughout the structure, with individual ones being arrowed in Figures 5.2(e) and 5.2(f). The HRTEM micrographs show speckled contrast synonymous with the presence of microporosity. However due to the inevitable overlap of the individual sub-2 nanometer pores with the carbon along the beam path, it is not possible to resolve the micropores within the images. The HRTEM micrographs also show that with increasing carbonization temperature there is more aromatic ordering, agreeing with the XRD and the Raman results.

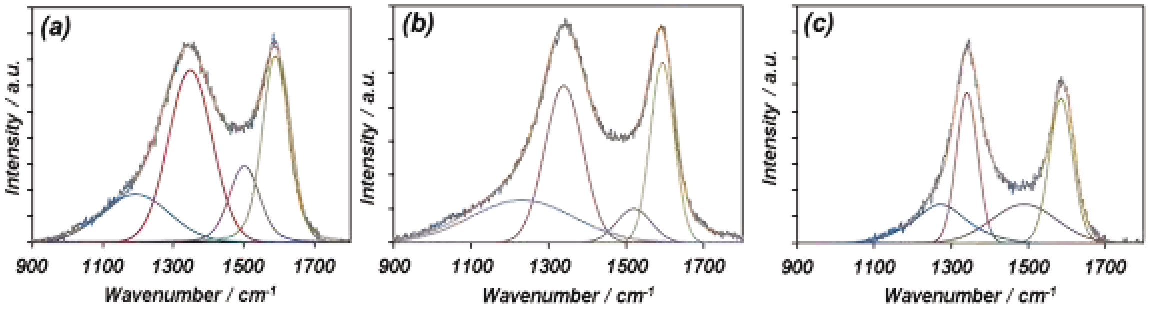

Figure 5.4: Fitted Raman spectra of BPPG-A specimens. (a) BPPG-800-A , (b) BPPGA-1100-A, and (c) BPPG-1400-A.

Figure 5.5, Tables 5.2 and 5.3 present X-ray photoelectron spectroscopy (XPS) results for BPPG and BPPG-A specimens. XPS data shown in Table 5.2 was from analysis performed on as-synthesized carbons. Table 5.3 shows XPS results on carbons that were mechanically ground after synthesis so as to expose bulk material to surface analysis. Combustion elemental analysis was also employed to obtain the bulk N, H and O content, the results being listed in Table 5.2. From both sets of XPS results it can be concluded that BPPG and BPPG-A contain nitrogen (0.48 - 2.82 wt.%) and oxygen (5.55 - 9.31 wt.%) heteroatoms, with minor amounts of Si (0.1 - 1.45 wt.%), Cl (0.14 - 0.38 wt.%), K (0.1 - 0.82 wt.%), Mg (0.1 - 0.17 wt.%), and P (0.06 - 0.13 wt.%). Elements K, Mg and P were detected only after grinding the powders, indicating that they are depleted from the as synthesized near-surfaces. Activation does somewhat increase the surface oxygen content of the materials, especially for the sample that was pyrolized at 800°C.

Since the carbons had low surface areas (19 - 217 m^2/g), it is not expected that O and N surface functionalities will have an appreciable impact on the electrochemical performance.

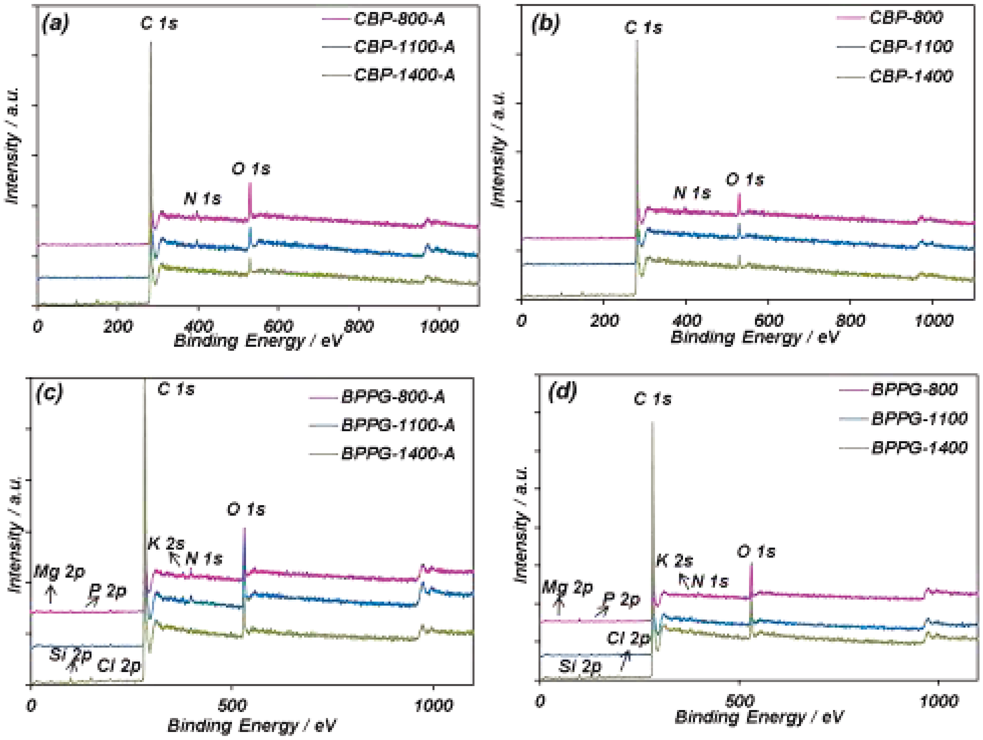

Figure 5.5: XPS survey spectra of the (a) and (b) as-synthesized, (c) and (d) mechanically ground BPPGA and BPPG specimens.

.

Table 5.2: Elemental composition information for BPPG and BPPG-A

	elemental analysis				**XPS**				
Samples	**C [wt%]**	**O [wt%]**	**N [wt%]**	**H [wt%]**	**C [wt%]**	**O [wt%]**	**N [wt%]**	**Si [wt%]**	**Cl [wt%]**
BPPG-800	82.44	8.12	1.93	1.03	88.47	7.83	2.10	1.45	0.15
BPPG-1100	87.44	5.24	0.76	0.39	92.02	6.10	1.06	0.57	0.25
BPPG-1400	92.42	3.98	0.19	0.16	92.53	5.55	0.48	1.3	0.14
BPPG-800-A	83.42	9.14	2.07	1.24	87.34	9.31	2.82	0.25	0.28
BPPG-1100-A	89.34	5.95	0.97	0.57	89.51	6.72	2.75	0.8	0.22
BPPG-1400-A	92.87	3.57	0.37	0.32	92.19	5.70	1.29	0.64	0.18

Table 5.2: XPS results on BPPG and BPPG-A that were mechanically ground after synthesis so as to expose bulk material to surface analysis

XPS (After grinding)								
Samples	**K [wt%]**	**Mg [wt%]**	**P [wt%]**	**C [wt%]**	**O [wt%]**	**N [wt%]**	**Si [wt%]**	**Cl [wt%]**
BPPG-800	0.1	0.17	0.08	87.95	8.02	2.17	1.31	0.2
BPPG-1100	0.18	0.15	0.13	92.03	5.83	1.01	0.42	0.25
BPPG-1400	0.82	0.1	0.06	91.82	5.53	0.39	1.08	0.2
BPPG-800-A	0.77	0.16	0.09	87.17	9.06	2.27	0.1	0.38
BPPG-1100-A	0.51	0.13	0.12	89.14	6.98	2.31	0.47	0.34
BPPG-1400-A	0.08	0.1	0.07	91.68	5.85	0.98	1.0	0.24

5.3.2 Electrochemical performance versus Na

We performed cyclic voltammetry (CV) and galvanostatic discharge/charge cycling on both the BPPG and BPPG-A, tested between 0.001 and 2.8 V *vs.* Na/Na$^+$. Figures 5.6(a) and 5.6(b) show the CV curves and the galvanostatic discharge/charge profiles for BPPG-1100-A, at cycle 1, 2, 5 and 10. The CV and galvanostatic data for the other materials are shown in Figures 5.7, and 5.8. The inset in Figure 5.6(b) is the dQ/dV curve, which has a similar shape to the CVs. Two small reduction peaks at ~0.5 and ~ 0.7 V are observed in the first CV scan and disappeared in the subsequent scans. The formation of a solid electrolyte interface (SEI) would occur at these potentials. However due to the carbons' low surface area, we attribute these two peaks more to irreversible Na insertion into the bulk. Table 5.3 shows the cycle 1 coulombic efficiency (CE) of the BPPG and BPPG-A specimens. There is a notable improvement in the cycle 1 CE with increasing order in the carbons (going from 63% to 73% for 800°C *vs.* 1400°C carbonization) but only a marginal decrease in the CE with increased surface area (e.g. dropping to 61% for 800°C + activation). This indicates the cycle 1 irreversible trapping of Na is associated with carbon disorder, be it at the highly defective graphene sites or in the amorphous regions between the pseudographitic domains. However during steady state cycling the CE is 100%, hence minimal additional permanent trapping of Na occurs.

A pair of highly reversible (minimal voltage hysteresis) oxidation/reduction peaks are present at 0.3-0.01 V, similar to lithium insertion in graphite. [5,7] As Table 5.4 points out, at an intermediate charging rate (50 mA/g) the reversible capacity of the as-carbonized and the activated specimens is very similar. For instance, for BPPG-1100 versus BPPG-1100-A the total capacity difference is 23 mAh/g (362 mAh/g vs. 385 mAh/g). As Figure 5.6(c) shows, all the BPPG and BPPG-A display a sloping-voltage region, and a nearly flat plateau at potentials lower than 0.2 V. The effect of carbonization temperature on the fraction of the total capacity associated with the plateau below 0.1 V is summarized in the histogram shown in Figure 5.6(d). The sub-0.1 V capacities increase with higher degree of ordering, being 106 mAh/g for BPPG-800-A, 200 mAh/g for BPPG-1100-A and 238 mAh/g for BPPG-1400-A. The low voltage capacity is fully independent of activation, indicating that it is not due to nanopore filling by Na metal, aka "nanoplating".

Charge storage in carbons for LIBs and NIBs has been ascribed to the following mechanisms, chemisorption on surface heteroatoms, [80] metal nanopore filling, i.e. "nanoplating", [52,78,81] intercalation between graphene layers, [12,54] and reversible adsorption at structural defect sites in the graphene. [82-86] The charge-discharge profiles in high surface area carbons with high O and N contents have a substantial voltage hysteresis, often being on the order of 1 V or more throughout the entire capacity range. [56,57,80] Below 0.2 V the 1100 °C and 1400 °C BPPG and BPPG-A have hysteresis that is less than 0.05 V. As we will demonstrate in the subsequent analysis, the key low voltage charge storage mechanism for BPPG is the reversible intercalation of Na between the graphene planes of the pseudographtic domains. In all the BPPG specimens the graphene sheets also contain a high content of defects. We attribute the sloping high voltage charge storage behavior to reversible binding of Na at graphene divacancies defects, as has been recently predicted by ab initio calculations. [83]

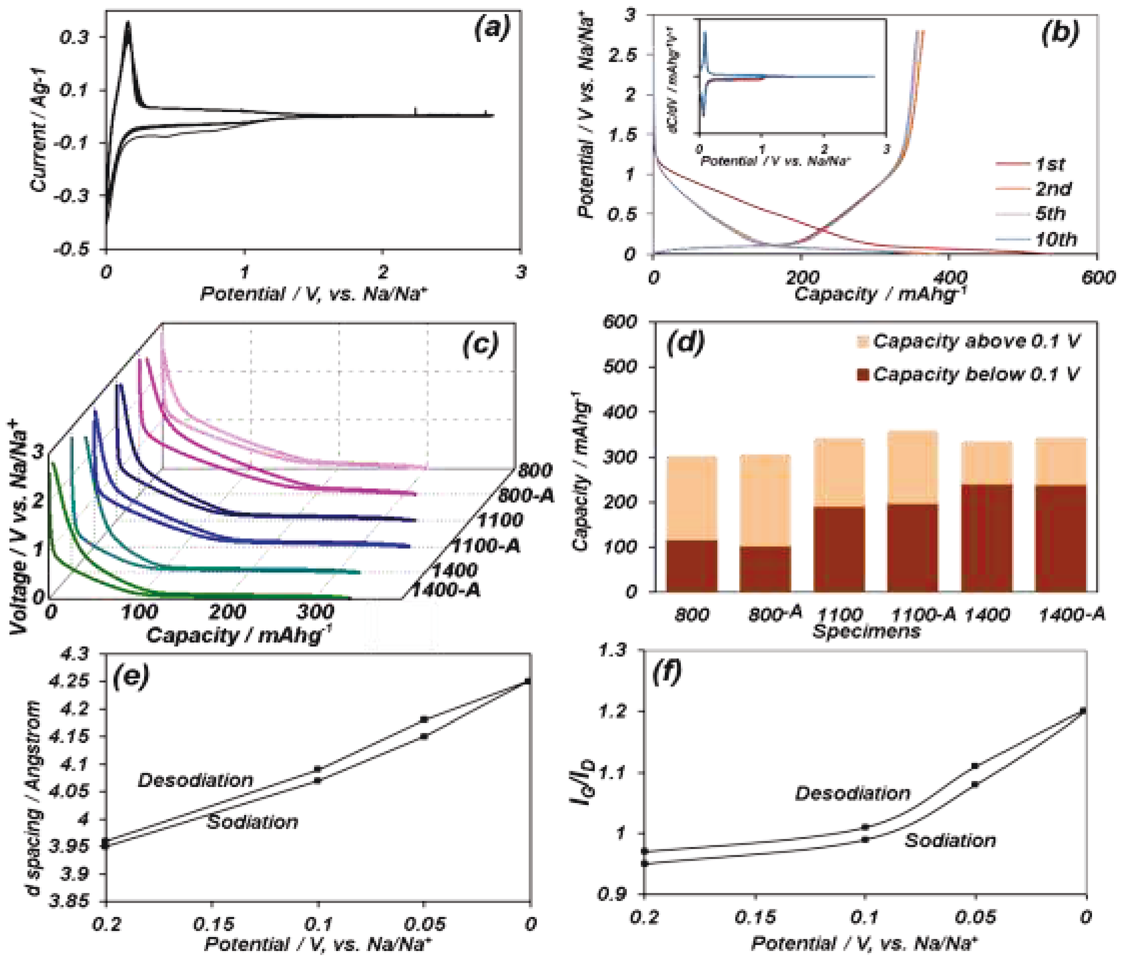

Figure 5.6: Electrochemical performance of BPPG, tested in a half cell against Na. (a) Cyclic voltammogram (CV) of BPPG-1100-A, tested at 0.1 mV s^{-1}. (b) Galvanostatic discharge/charge curves of BPPG-1100-A at a current density of 50 mAg^{-1}. (c) Potential profiles of BPPG and BPPG-A electrodes, (d) Summary of capacity versus potential distribution of BPPG and BPPG-A , 10^{th} cycle at 50 mA/g. (e) Dependence of the mean graphene interlayer spacing of BPPG-1400-A on discharge/charge voltage, demonstrating reversible Na intercalation-induced dilation of the mean intergraphene spacing. The electrodes were galvanostatically discharged/charged to 0.2, 0.1, 0.05, and 0.001 V, with dilation values derived from XRD spectra shown in Figures 5.10. (f) The Raman integral intensity ratio (I_G/I_D) of BPPG-1400-A as a function of discharge/charge voltage demonstrating intercalation-induced ordering of the carbon, values derived from Raman spectra in Figure 5.10.

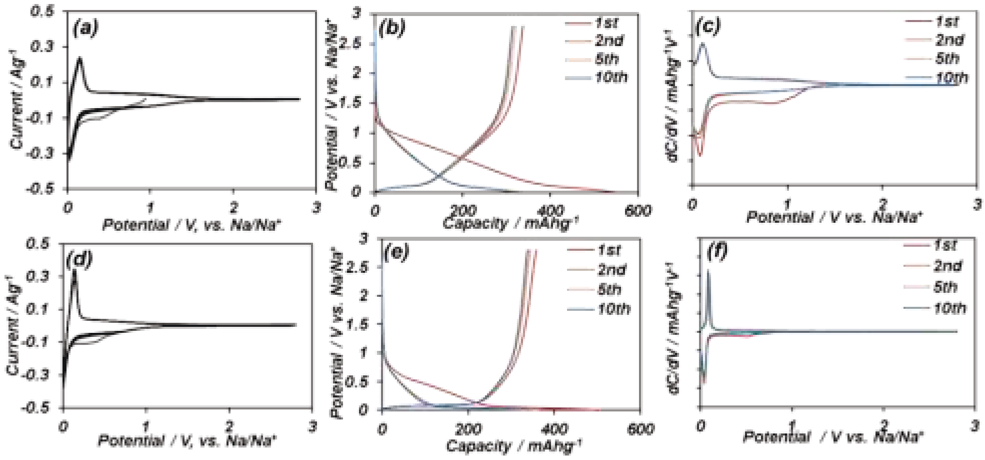

Figure 5.7.: CV and galvanostatic discharge/charge profiles of (a)-(c) BPPG-800-A, and (d)-(f) BPPG-1400-A electrodes. CVs were done between 0.001 and 2.8 V vs. Na/Na^{+} at a scanning rate of 0.1 mVs^{-1}. Galvanostatic discharge/charge profiles are obtained at current density of 50mA/g.

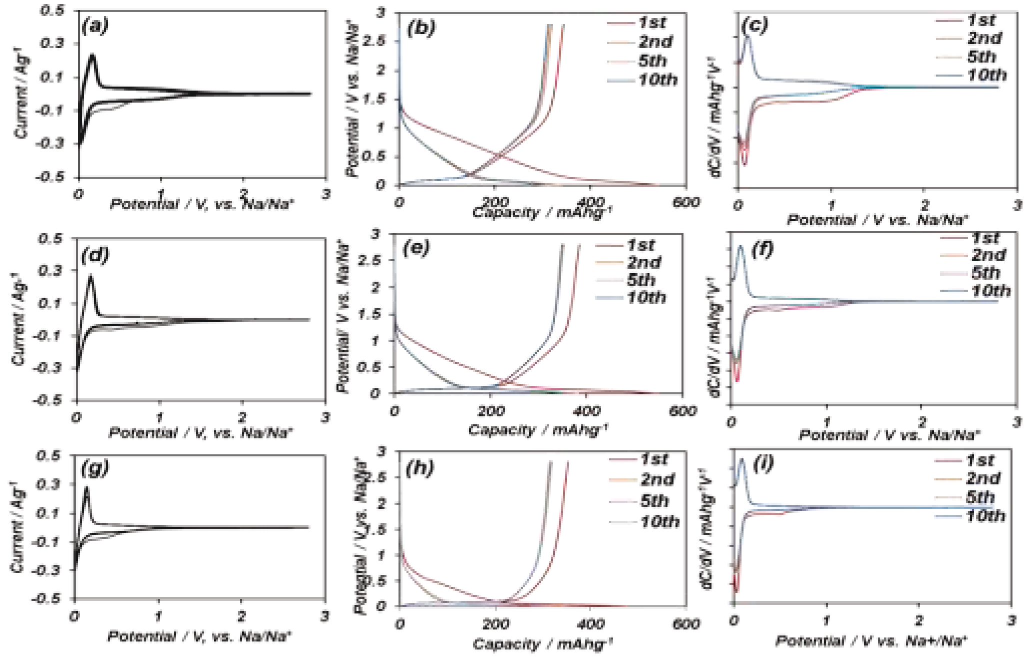

Figure 5.8: CV and galvanostatic discharge/charge profiles of (a)-(c) BPPG-800, (d)-(f) BPPG-1100, and (g)-(i) BPPG-1400 electrodes versus Na.

Table 5.4: Coulombic efficiency and cycling capacity of BPPG and BPPG-A, versus Na. Samples were activated at 0.05 A/g for 10 cycles and were subsequently tested at 0.1 A/g

Samples	Initial CE (%)	Cycle 2 (mAh/g)	Cycle 50 (mAh/g)	Cycle 300 (mAh/g)
BPPG-800 (Na)	63	328	277	254
BPPG-1100 (Na)	70	362	316	288
BPPG-1400 (Na)	73	351	292	245
BPPG-800-A (Na)	61	336	288	254
BPPG-1100-A (Na)	68	384	330	299
BPPG-1400-A (Na)	71	371	304	239

The relatively high density of BPPG also delivers a high volumetric charge capacity. Figure 5.9 provides this result for BPPG-1100-A, as a function of cycle number. For all experiments we employed a mass loading of ~1 mg cm^{-2} giving an average electrode thickness of 14 µm (see cross section SEM image in Figure 5.9). This results in an electrode with a packing density of ~ 0.75 g cm^{-3}. Thus the reversible volumetric capacity obtained for BPPG-1100-A is ~ 700 mAh cm^{-3} by active material (i.e. based on the true density of the carbon), and ~ 270 mAh cm^{-3} by electrode volume. It is difficult to make a one-to-one volumetric comparison with commercial LIB graphite since professionally manufactured commercial electrodes are both thicker (with correspondingly higher mass loading) and are roll-pressed rather than drop cast onto a current collector. The details of manufacturing process are almost always proprietary. However, it is possible to increase the packing density and the mass loading of BPPG to be closer to commercial systems. We employed a Carver ™ laboratory press (4000 psi) to achieve electrodes with a mass loading of ~ 6.2 mg. The resultant electrode thickness was 39 µm on a geometric area of 1.54 cm^2. This electrode is also shown in Figure 5.9.

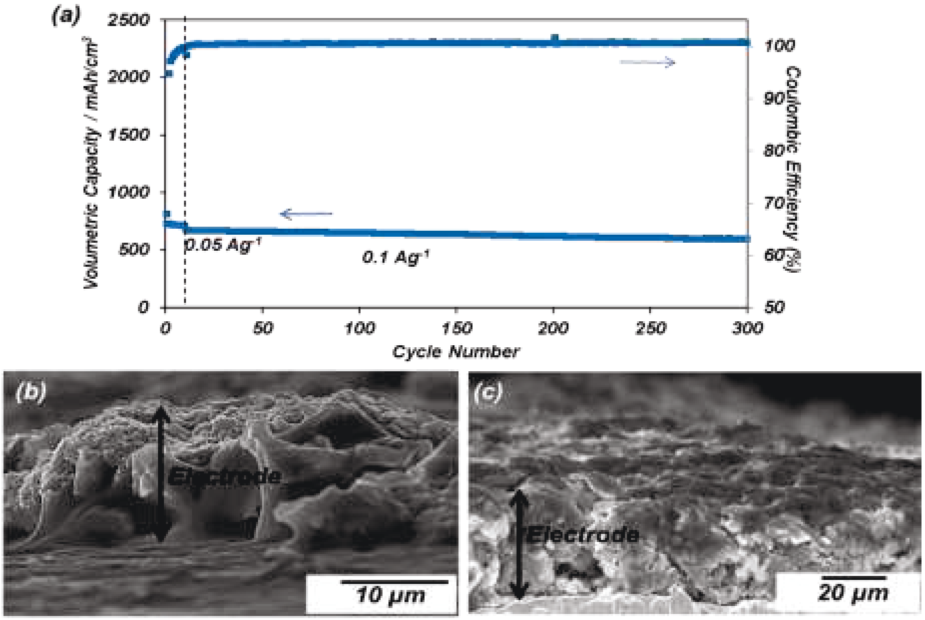

Figure 5.9: (a) Volumetric capacity of BPPG-1100-A tested against Na, at a current density of 50mA/g. Capacity calculation is based on the true density of BPPG, which is ~ 2 g cm^{-3}. (b) Cross section SEM image of a drop-cast BPPG-1100-A electrode, as electrochemically tested in this study. (c) Cross section SEM image of a pressed high mass loading BPPG-1100-A electrode.

We employed XRD and Raman spectroscopy to further understand the changes that occur in BPPG-1400-A during Na insertion/extraction. The results are shown in Figures 5.6(e) and 5.6(f), with the raw data being presented in Figure 5.10(a) and 5.10(b). To obtain a "steady-state" microstructure, the half-cells first received 10 galvanostic charge/discharge cycles at 30 mA/g. Upon cycle 11, the electrodes were discharged to (a) 0.2, (b) 0.1, (c) 0.05, and (d) 0.001 V and then charged to (e) 0.05 V, (f) 0.1 V and (g) 0.2 V. The cells were then disassembled in a glovebox with the active material being removed from the current collector, cleaned, and immediately analyzed. Figure 5.6(e) shows a plot of the mean d spacing *versus* voltage. The broad (002) pseudographitic peak shifts to lower angles as the electrode is sodiated. The d spacing is progressively expanded from the initial 3.96 Å to the final 4.25 Å at 0.001 V. The measured dilation has to be due to Na intercalation between the graphene layers, similar to Li in graphite. It has been reported that the equilibrium interplanar distance for NaC_6 is about 0.45 nm, while that for LiC_6 is 0.37 nm. [52,87] Based on the capacity achieved at this cycle number

(~330 mAh/g), the stoichiometric factor x in Na_xC_6 is ~ 0.88. Examining the interlayer upon subsequent desodiation indicates that the process is highly reversible, agreeing with the electrochemical testing. As indicated by the Raman spectra (Figure 5.6(f)), BPPG-1400-A becomes progressively more ordered during sodiation and subsequently disordered during the reverse process. Similar to the XRD results, the ordering is highly reversible with voltage. This Na insertion-induced ordering phenomena has not been previously reported.

Neither XRD nor XPS show evidence of Na metal nanopore filling even at 0.001 V. Metal peaks were not detected in the XRD patterns for any of the BPPG. We followed the XPS - scotch tape methodology employed in ref. 84 to analyze Na bonding in the interior of BPPG-1400-A. The C1s spectrum shown in Figure 5.10(d) shows minimal (Na)carbonates, indicating that the SEI layer was successfully removed along with the top of the carbon. Figure 5.10(c) demonstrates a strong binding peak of Na at 1071.1 eV, which almost entirely disappears at 2.8 V. We attribute this peak to C - Na bonds within the pseudographitic domains, although prior experimental evidence for this interpretation is unavailable. The binding energy for metallic sodium is 1071.7 eV, while for Na_2O it is 1072.5 eV, both of which are conspicuously absent. The fact that the Na signal almost entirely disappears at 2.8 V is also a strong indication that the SEI is removed. XPS results on samples without using the scotch tape approach show a strong peak in Na 1s spectra at ~1071 eV at both 0.001 and 2.8 V but with lower signal intensity after desodiation to 2.8 V. This indicates that some of the decomposition products that are formed can be partially dissolved. The presence of considerable (Na)carbonate peaks after desodiation to 2.8 V in both Na 1s and C 1s spectra indicates that these peaks could be related to the decomposition products rather than Na inside the electrode. This was further confirmed by SEM images of electrodes after desodiation to 2.8 V before and after using the scotch tape method (Figure 5.11). The morphology of the electrode after using the scotch tape method is almost identical to the as-prepared one with clean surfaces and sharp boundaries. By contrast, without using this method the surface is no longer smooth but rather rough in appearance with SEI layer covering the surface.

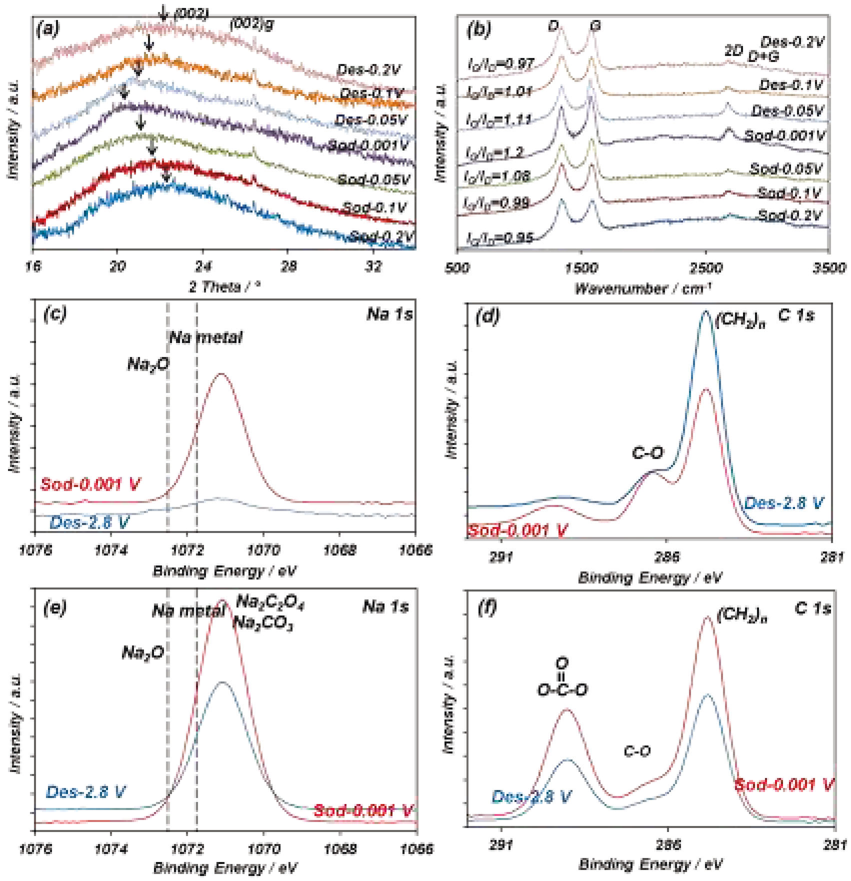

Figure 5.10: (a) XRD spectra for BPPG-1400-A at different discharge and charge voltages *versus* Na. (b) Raman spectra for BPPG-1400-A at different discharge and charge voltages *versus* Na. (c)-(f) High resolution Na 1s, and C 1s XPS spectra for sodiated and desodiated BPPG-1400-A, analyzed after 10 cycles. 5.10(c) and 5.10(d) show spectra for samples where the electrode's top SEI covered surface was removed by the scotch tape method. 5.10(e) and 5.10(f) show spectra for samples without the top layer removed, *i.e.* intact electrode covered by SEI. (a) XRD spectra for BPPG-1400-A at different discharge and charge voltages versus Na. (b) Raman spectra for BPPG-1400-A at different discharge and charge voltages versus Na. Na 1s, and C 1s high resolution XPS spectra for sodiated and desodiated BPPG-1400-A after 10 cycles.

Figure 5.12(a) shows the cycling capacity retention performance of BPPG-A and BPPG specimens, activated at 50 mA/g for the first 10 cycles and subsequently tested at 100 mA/g for the subsequent 290 cycles. The BPPG-1100-A and BPPG-1100 electrodes show the best combination of total capacity and capacity retention. BPPG-1100-A and BPPG-1100 possess a reversible capacity of 339 mAh/g and 318 mAh/g at cycle 11, and 298 mAh/g and 286 mAh/g at cycle 300. In BPPG-800, BPPG-800-A, BPPG-1100 and BPPG-1100-A the coulombic efficiency increases dramatically upon cycling, reaching over 98% after 5 cycles and ~ 100% (within measurement accuracy of the instruments) after 10 cycles. BPPG-1400-A and BPPG-1400 demonstrate slightly lower cycling CE (98.5-99%) and degrade faster during cycling than the rest. The cycle 11 capacities of BPPG-1400-A and BPPG-1400 are 310, and 295, respectively. After 300 cycles these numbers are reduced to 240 and 242, i.e. 22 % and 18% degradation. We believe that both the lower CE and the faster degradation are related to the presence of the secondary graphite phase. Upon attempted insertion of the misfitting Na ions, the graphite begins to exfoliate creating new surfaces and resulting in limited local pulverization of the electrode. Any fresh surfaces exposed to electrolyte will cause new SEI formation and subsequent loss of cycling CE, while local pulverization would lead to a capacity decay due to loss of electrical contact. We cycled the best overall performing material (BPPG-1100-A) up to 600 cycles at a rate of 500 mA/g. These results are also shown in Figure 5.12(b). The electrode exhibits a stable capacity of 210 mAh/g at cycle 600, corresponding to a capacity retention of 93%. It also demonstrates a cycling CE of ~ 100%.

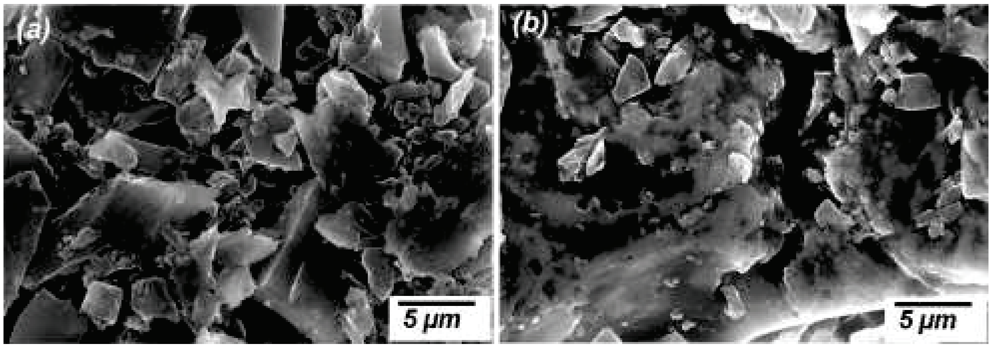

Figure 5.11: Low magnification SEM micrograph of BPPG-1400-A desodiated to 2.8 V, after 10 cycles. 5.11(a) shows the electrode morphology after the electrode's top layer was removed by the scotch tape method, 5.11(b) shows the morphology of an intact electrode that is covered by SEI.

Figures 5.12(c) and 5.12(d) show the rate capability of BPPG-A and BPPG electrodes. At high rates (1 A/g), the BPPG-800-A and BPPG-800 carbons demonstrate superior capacity. BPPG-1100-A and BPPG-1100 show the overall best performance at current densities of

0.5 A/g and lower. BPPG-1400-A and BPPG-1400 show the overall worst rate capability, having the lowest capacities at rates 0.5 A/g and higher. Comparing 5.12(c) and 5.12(d) shows a major effect of activation on the high rate performance of the carbons. These trends may be explained by considering the role of activation in introducing porosity in each of the materials, and the subsequent role of porosity in reducing solid-state Na diffusion distances within the carbons. It is reasonable to assume that at higher charging/discharging rates the extent of sodiation will become solid-state diffusion limited. This is a key difference between batteries and electrical double layer (EDL) capacitors, where in the latter case the ion diffusional limitations will occur within the electrolyte. [58,88] Assuming electrolyte contact on both sides of a carbon wall, the Na diffusion distance may be approximated as half the wall thickness.

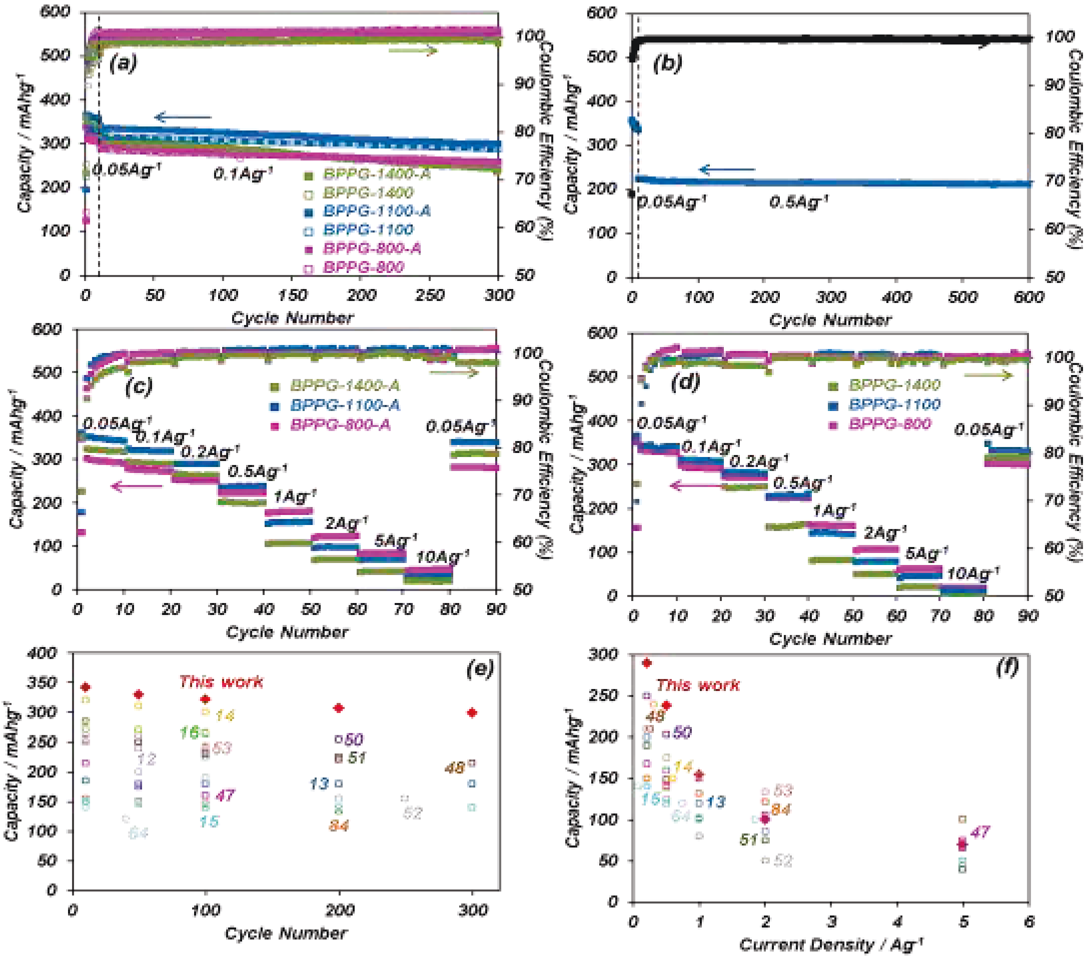

Figure 5.12: (a) Cycling performance of the BPPG and BPPG-A electrodes tested in a half cell against Na, with the corresponding coulombic efficiency (CE) being displayed on the right axis.

(b) Extended cycling performance and CE of the BPPG-1100-A electrode. (c) Rate performance of BPPG-A electrodes. (d) Rate performance of BPPG electrodes. (e) – (f) Cycling capacity retention and rate capability comparison of BPPG-1100-A with the state-of-the-art in literature, tested versus Na. Red diamonds are our results.

The introduction of limited micro and mesoporosity into the BPPG is therefore essential for reducing the solid diffusional limitations by creating carbon walls that are in effect much thinner than their macroscopic dimensions. At high rates every activated carbon (SA's of 62 - 217 m^2 g^{-1}) outperforms its unactivated counterpart (SA's of 14.5 - 33 m^2 g^{-1}). Among the as-carbonized materials BPPG-800 demonstrates the highest surface area (33 m^2 g^{-1}) and rate performance, while BPPG-1400 shows the lowest surface area (14.5 m^2 g^{-1}) and rate performance.

Electrochemical impedance spectroscopy (EIS) was employed to further examine the cycling behavior of BPPG-A and BPPG specimens. The impedance spectra of the electrodes before and after cycling were modeled, with the equivalent circuit depicted in Figure 5.13. Figure 5.14 shows the Nyquists plots for samples before cycling and after 300 cycles, respectively. The spectra consist of a depressed semicircle in the high- and middle-frequency regions and a straight line in the low-frequency region. R_{el} represents the sum of electrical resistances (contacts, etc.), C_{dl} the electrical double layer capacitance, R_{ct} is the charge transfer resistance and Z_W Warburg-type element associated with ion diffusion in the carbon electrode. For the cycled electrodes an additional parallel combination of a resistor and capacitor are added to represent ion transport through the SEI layer, [89] denoted as R_f and C_f, respectively. The numerical values obtained from modeling are listed in Table 5.5.

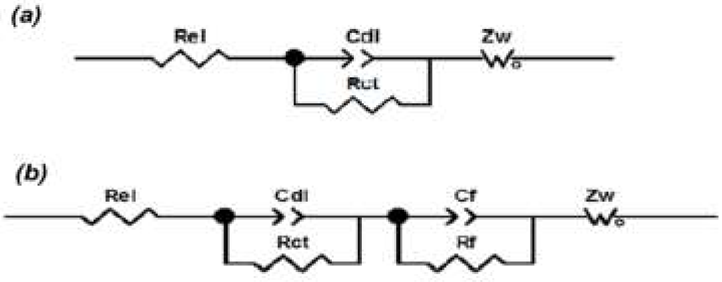

Figure 5.13: Equivalent electronic circuits used to simulate the electrochemical impedance

spectra (EIS) results. For the spectra of all the as- prepared specimens, equivalent circuit (a) was used. For the cycled specimens with an SEI layer formed, equivalent circuit (b) was used.

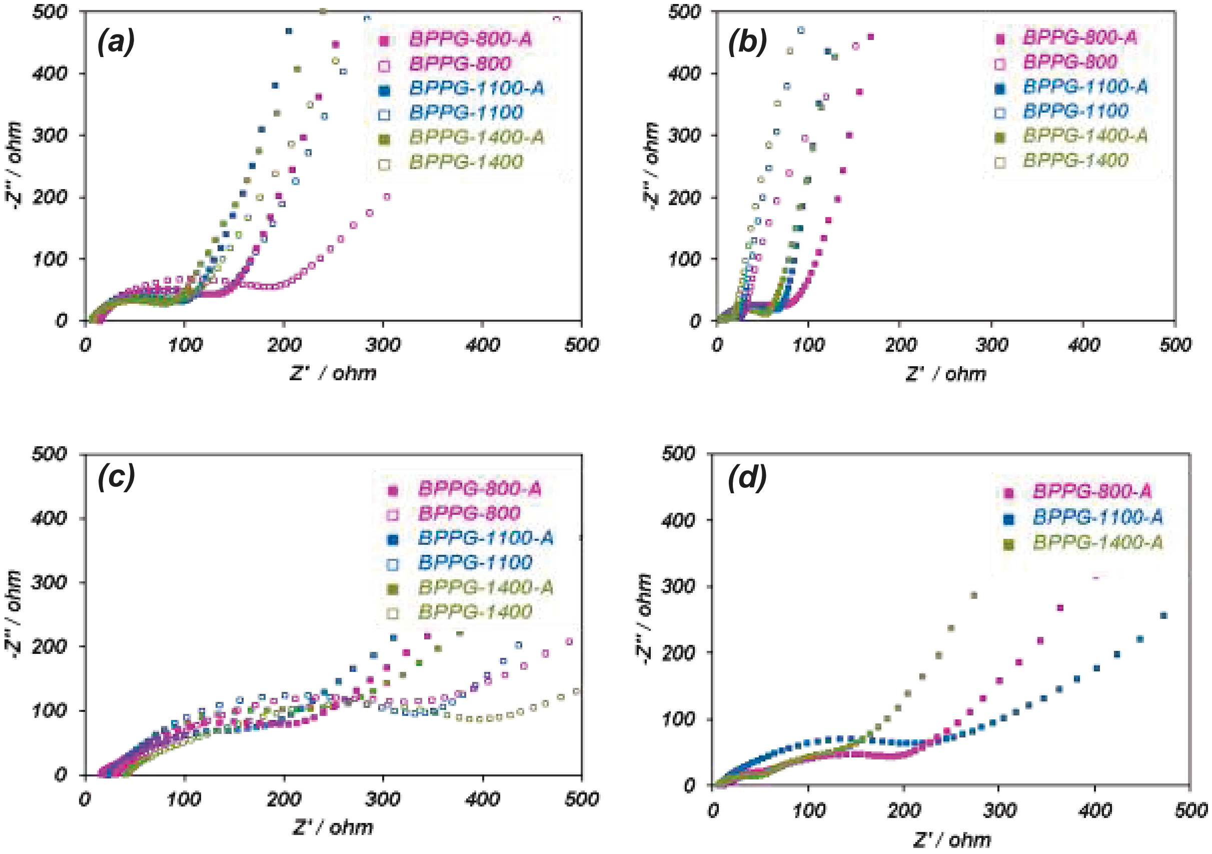

Figure 5.14: Experimental EIS of as-prepared BPPG-A, and BPPG electrodes versus (a) Na, (b) Li. Experimental EIS of BPPG-A, and BPPG electrodes after 300 cycles versus (c) Na, (d) Li.

Table 5.5: Resistance values simulated from modeling the experimental impedance (Figure 5.13) using the equivalent circuits shown in Figure 5.12

	As-prepared		**After 300cycles**	
Samples	**R_{el}**	**R_{ct}**	**R_{el}**	**R_{ct}+R_f**
BPPG-800-A (Na)	10.1	102.1	16.8	166.1
BPPG-1100-A (Na)	8.3	94.7	14.5	124
BPPG-1400-A (Na)	6.4	79.7	23.6	202.2

BPPG-800 (Na)	8.3	175.5	30.3	302.6
BPPG-1100 (Na)	8.6	126.4	24.6	246.4
BPPG-1400 (Na)	7.7	94.6	38.8	381.5
BPPG-800-A (Li)	4.6	80.3	9.4	232.4
BPPG-1100-A (Li)	4.3	65.3	8.9	262.4
BPPG-1400-A (Li)	6	50.5	7.1	210.1
BPPG-800 (Li)	5.9	19.5		
BPPG-1100 (Li)	4.1	18.2		
BPPG-1400 (Li)	4.5	14.2		

For the as-prepared samples, the trend in the charge transfer resistance, which is roughly equal to the diameter of the semicircle in the spectra, indicates that the lower carbonization temperature gives higher charge transfer resistance (Figure 5.14(a)-(b)). After 300 cycles the charge transfer resistance is substantially larger for BPPG-1400-A and BPPG-1400 specimens (Figure 5.14(c) and Table 5.5), supporting the argument that the samples' inferior cycling coulombic efficiency is associated with higher rates of SEI formation. The cycling-induced increase in the charge transfer resistance is on par for the BPPG-1100-A and BPPG-800-A specimens. However the total charge transfer resistance of BPPG-800-A remains higher than for BPPG-1100-A, an effect probably associated with the underlying structure of the carbon. It is plausible that Na insertion into a more disordered carbon from the electrolyte will be less facile than for a more ordered counterpart. Thus there would be a higher charge transfer resistance both in the as-synthesized state, before there is any SEI, and after extensive cycling. As Figure 5.15(e) indicates, past the first several charge/discharges, the cycling induced increase in the charge transfer resistance in both BPPG-1100-A and BPPG-800-A is quite minimal.

A comparison of the performance of the BPPG-1100-A specimen with state-of-the-art carbons is presented in Table 5.6 and in Figures 5.12(e) and 5.12(f). Figures 5.12(e) and 5.12(f) show the cycling performance and the rate capability comparison, respectively, with the solid red diamonds being our results. Table 5.6 emphasizes the plateau capacity (below 0.1 V) comparison of BPPG-1100-A with literature, an essential metric not captured in the total capacity plots presented in Figures 5.12(e) and 5.12(f). Carbons included in the comparison are carbon nanosheets,[52] carbon nanofibers, [13,16,53,57,80] hard carbon, [12,14] templated carbon, [64] highly disordered carbon, [55] hollow carbon nanowires, [52] hollow carbon nanospheres,[51] carbonized peat moss,[54] and nanocellular carbon foams, [15] all of them being primarily high surface area materials. To the best of our knowledge, the combination of high reversible volumetric and gravimetric capacities, the flat low voltage and low hysteresis plateaus, the extended cycling performance, and high rate capability have seldom been achieved in previous reports on sodium ion battery anode carbons.

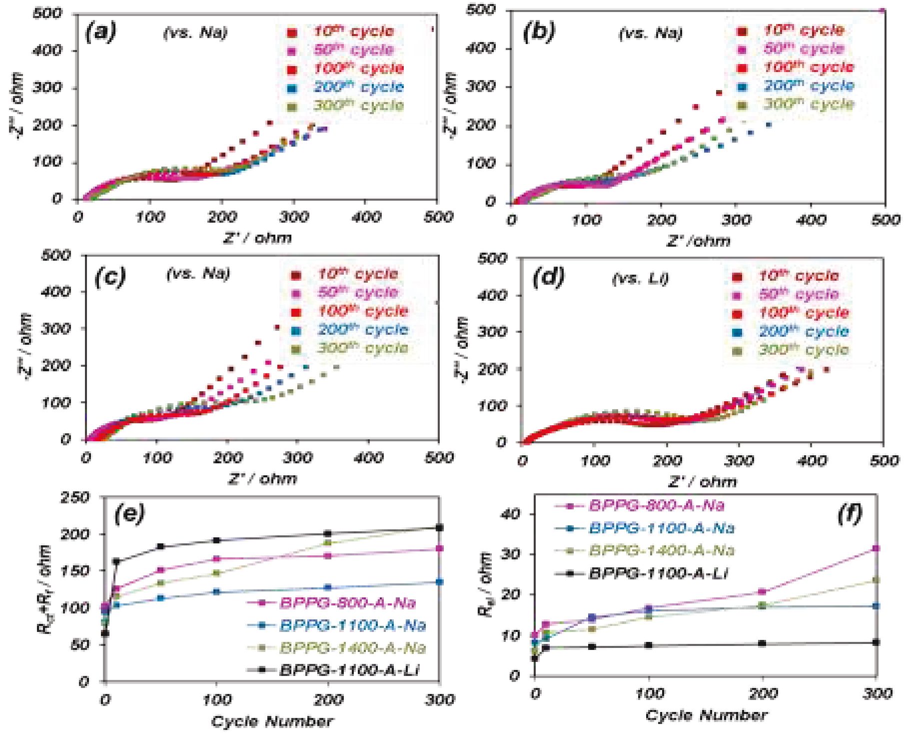

Figure 5.15: (a)-(c) EIS of BPPG-800-A, BPPG-1100-A, and BPPG-1400-A versus Na, for cycles 20 – 300. (d) EIS of BPPG-1100-A versus Li for cycles 10 - 300. (e) The total charge transfer resistance within all the interfaces (R_{ct}+R_f), as a function of cycle number. (f) R_{el} as a function of the cycle number.

Table 5.6: Plateau capacity (below 0.1 V) comparison of BPPG-1100-A versus state-of-the-art NIB carbons

Material	**Initial coulombic efficiency (%)**	**Plateau capacity (capacity below 0.1 V *vs* Na/Na$^+$)**	**Cyclability (discharge capacity)**	**Rate performance**
BPPG-1100-A (this work)	*67.8*	*200 mAg^{-1}* *At 50 mAg^{-1} (10th*	*342 mAhg^{-1} at 11th cycle* *298 mAhg^{-1} at 300th cycle*	*290 mAhg^{-1} at 200 mAg^{-1}* *238 mAhg^{-1} at 500 mAg^{-1}*

		cycle)	*88% capacity retention over 290 cycles at 100 mAg^{-1}*	*155 mAhg^{-1} at 1 Ag^{-1}* *100 mAhg^{-1} at 2 Ag^{-1}* *70 mAhg^{-1} at 5 Ag^{-1}*
Carbon Nanosheets (Ref. 56)	34.8	*ca*. 40 mAhg^{-1} at 50mAg^{-1} (10th cycle)	*ca*. 260 mAhg^{-1} at 10th cycle *ca*. 155 mAhg^{-1} at 200th cycle 60% retention over 190 cycles at 50 mAg^{-1}	*ca*. 190mAhg^{-1} at 200mAg^{-1} *ca*. 125mAhg^{-1} at 500mAg^{-1} *ca*. 80 mAhg^{-1} at 1Ag^{-1} 50 mAhg^{-1} at 2 Ag^{-1} 45 mAhg^{-1} at 5 Ag^{-1}
Interconnected Carbon nanofibers (Ref. 80)	41.8	Not reported	151 mAhg^{-1} at 10th cycle 134.2 mAhg^{-1} at 200th cycle 88.7% retention over 190 cycles at 200mAg^{-1}	150 mAhg^{-1} at 200 mAg^{-1} 139 mAhg^{-1} at 500 mAg^{-1} 132 mAhg^{-1} at 1 Ag^{-1} 121 mAhg^{-1} at 2 Ag^{-1} 100 mAhg^{-1} at 5 Ag^{-1}
Hard carbon particles (Ref. 12)	78	*ca*. 150 mAhg^{-1} at 25mAg^{-1}	250 mAhg^{-1} at 2nd cycle 225 mAhg^{-1} at 100th cycle 88% retention over 98 cycles at 25 mAg^{-1}	Not reported
Templated carbon (Ref. 64)	20	*ca*. 20 mAhg^{-1} at 74mAg^{-1} (10th cycle)	180 mAhg^{-1} at 2nd cycle, 120 mAhg^{-1} at 40th cycle 66.7% retention over 38 cycles at 74 mAg^{-1}	*ca*.140mAhg^{-1} at 74mAg^{-1} *ca*.120mAhg^{-1} at 740mAg^{-1} *ca*. 100mAhg^{-1} at 1.85 Ag^{-1}
Carbon fibers (Ref. 57)	46	Not reported	*c*a. 350 mAhg^{-1} at 2nd cycle 243 mAhg^{-1} at 100th cycle 70% retention over 98 cycles at 50 mAhg^{-1}	210 mAhg^{-1} at 200 mAg^{-1} 175 mAhg^{-1} at 500 mAg^{-1} 153 mAhg^{-1} at 1Ag^{-1} 134 mAhg^{-1} at 2 Ag^{-1} 101 mAhg^{-1} at 5 Ag^{-1}
Highly disordered carbon (Ref. 55)	57.6	*ca*. 110 mAhg^{-1} at 100 mAg^{-1} (3rd cycle)	255 mAhg^{-1} at initial cycles 234 mAhg^{-1} at 180th 92% retention over 170 cycles at 100 mAg^{-1}	190 mAhg^{-1} at 200 mAg^{-1} 139 mAhg^{-1}at 500 mAg^{-1} 102 mAhg^{-1} at 1 Ag^{-1} 75 mAhg^{-1} at 2 Ag^{-1} 40 mAhg^{-1} at 5 Ag^{-1}
Hollow carbon Nanowires (Ref. 52)	50.5	*ca*. 150 mAhg^{-1} at 50mAg^{-1}(10th cycle)	*ca*. 255 mAhg^{-1} at 10th cycle *ca*. 220 mAhg^{-1} at 200th cycle 86% retention over 190 cycles at 50 mAg^{-1}	210mAhg^{-1} at 250 mAg^{-1} 149 mAhg^{-1} at 500mAg^{-1}
Hollow carbon nanospheres (Ref. 51)	41.5	*ca*. 20 mAhg^{-1} at 50 mAg^{-1} (10th cycle)	250 mAhg^{-1} at 10th cycle, 160 mAhg^{-1} at 100th cycle 64% retention over 90 cycles at 100mAg^{-1}	168mAhg^{-1} at 200mAg^{-1} 142mAhg^{-1} at 500mAg^{-1} 120 mAhg^{-1} at 1Ag^{-1} 100mAhg^{-1} at 2Ag^{-1} 75mAhg^{-1} at 5Ag^{-1}
Carbonized peat moss (Ref. 54)	57.5	161 mAhg^{-1} at 50 mAg^{-1} (10th cycle)	284 mAhg^{-1} at 11th cycle 255 mAhg^{-1} at 210th cycle 90% retention over 200 cycles at 100 mAg^{-1}	250 mAhg^{-1} at 200 mAg^{-1} 203 mAhg^{-1} at 500 mAg^{-1} 150 mAhg^{-1} at 1Ag^{-1} 106 mAhg^{-1} at 2Ag^{-1}

				66 mAhg^{-1} at 5Ag^{-1}
Carbon nanofibers (Ref. 13)	58.7	*ca.* 130 mAhg^{-1} at 40 mAg^{-1} (10th cycle)	200 mAhg^{-1} at 2nd cycle 180mAhg^{-1} at 300th cycle 90% retention over 298 cycles at 200mAg^{-1}	200 mAhg^{-1} at 200 mAg^{-1} 160 mAhg^{-1} at 500 mAg^{-1} 120 mAhg^{-1} at 1 Ag^{-1} 85 mAhg^{-1} at 2 Ag^{-1}
Nanocellular carbon foams (Ref. 15)	Not reported	Not reported	153 mAhg^{-1} at 2nd cycle 137mAhg^{-1} at 300th cycle 90% retention over 298 cycles at 100mAg^{-1}	140 mAhg^{-1} at 200mAg^{-1} 120 mAhg^{-1} at 500mAg^{-1} 100 mAhg^{-1} at 1Ag^{-1} 50 mAhg^{-1} at 5Ag^{-1}
Porous carbon nanofiber (Ref. 16)	53.5	*ca.* 170 mAhg^{-1} at 50 mAg^{-1} (10th cycle)	280 mAh g^{-1} at 10th cycle 266 mAh g^{-1} at 100th cycle 95% retention over 90 cycles at 50 mAg^{-1}	225 mAhg^{-1} at 500mAg^{-1} 200 mAhg^{-1} at 1Ag^{-1} 164 mAhg^{-1} at 2Ag^{-1} 90 mAhg^{-1} at 5Ag^{-1}
Carbon fibers (Ref. 53)	< 40	184 mAh g^{-1} (1st cycle)	Not reported	Not reported
Hard carbon (Ref. 14)	61	>170 mAh g^{-1} (1st cycle)	340 mAh g^{-1} at 2nd cycle 300mAh g^{-1} at 120th cycle 88% retention over118 cycles at ~30mA g^{-1}	310 mAhg^{-1} at ~60mAg^{-1} 240 mAhg^{-1} at ~300mAg^{-1} 150 mAhg^{-1} at ~600mAg^{-1}

5.3.3 Electrochemical performance versus Li

The dense BPPG carbons are also uniquely promising for LIB applications, as the highly defective graphene sheets within the pseudographic domains will reversibly bind with Li, while the near-surface nanopores will provide sites for underpotential metal deposition. Figure 5.16(a) shows the cycling performance of the BPPG-A electrodes, with the coulombic efficiency of the electrodes also being displayed. The cycling CE is close to 100%. Figure 5.16(b) shows the rate performance of BPPG-1100-A electrode. BPPG-800-A, which is the most disordered carbon, demonstrated by far the highest overall cycling capacity, being at 800 mAh/g at cycle 300 when tested at 100 mA/g. This is direct evidence for the necessity of graphene defects in achieving a reversible capacity with Li that far surpasses that of commercial graphite. It has been shown that a divacancy is the thermodynamically most stable defect [84, 90, 91] and will also act as a preferential Li adsorption site. [84]

The CV curve of the BPPG-1100-A specimens is shown in Figure 5.17(a). Lithiation/delithiation demonstrates a pronounced reduction peak at 0 - 1 V during the 1st cycle and at 0 - 0.5 V during the subsequent cycles. The discharge - charge profiles for BPPG-A and BPPG are shown in Figures 5.17 and 5.18. The initial CEs are slightly lower when employing Li (Table 5.7) rather than Na (Table 5.4), which may be accounted for the difference in the structure and in the formation kinetics of SEI. [64,92] The degree of irreversible trapping of Li within the bulk of the carbon would also affect the cycle 1 CE values.

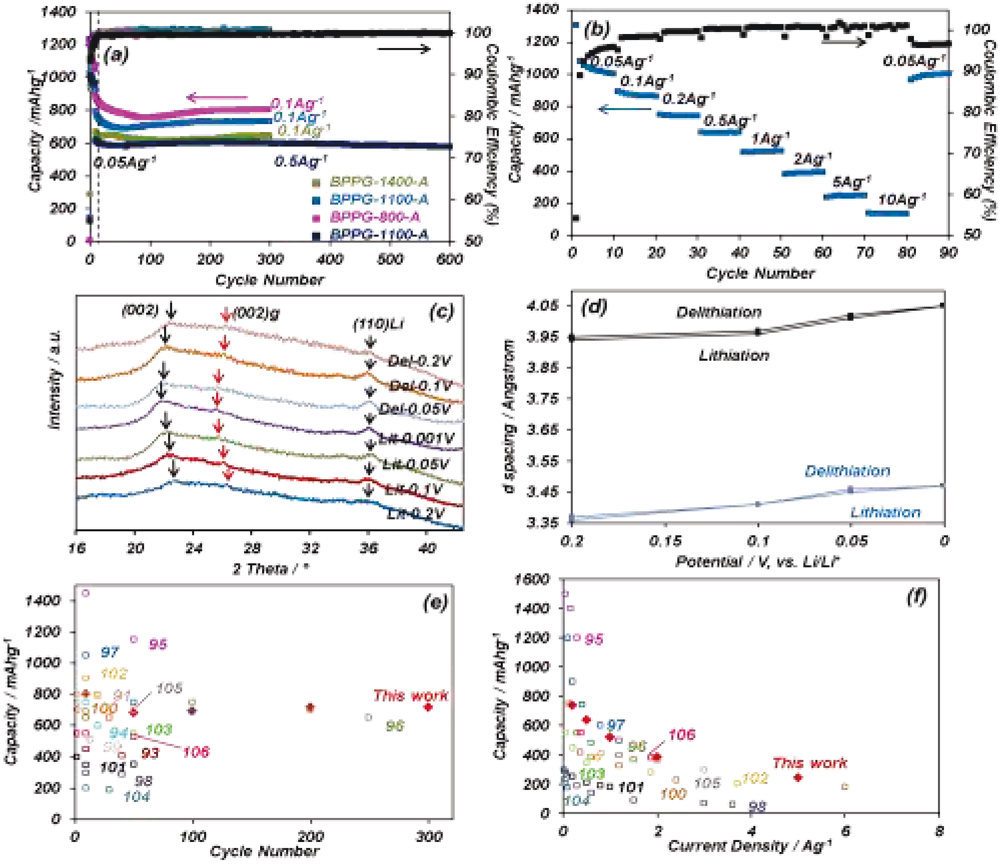

Figure 5.16: Electrochemical performance of BPPG, tested in a half cell against Li. (a) Cycling performance of the BPPG-A electrodes, with coulombic efficiency of electrodes being displayed. (b) Rate performance of BPPG-1100-A electrode. (c) XRD spectra for BPPG-1400-A at different discharge and charge voltages (vs. Li/Li$^+$). (d) Dependence of the mean graphene interlayer spacing of pseudo graphite (black line) and graphite (blue line) phases in BPPG-1400-A on the discharge/charge voltage. The electrodes were galvanostiatically discharged/charged to 0.2, 0.1, 0.05, and 0.001 V, 10th cycle at 50 mA/g. (e) – (f) Cycling capacity retention and rate capability comparison of BPPG-1100-A with the state-of-the-art in literature, tested versus Li. (The current density in reference 99 and 102 is based on A cm^{-2}). Red diamonds are our results.

Figure 5.19(a) compares the capacity versus voltage profiles for BPPG and BPPG-A versus Li, while Figure 5.19(b) shows a summary of capacity versus voltage. The galvanostatic profiles are less flat than they are with Na, and do show a marked hysteresis. These features are in accord with other reports on Li insertion/extraction into non-graphitic carbons. [52,72,93] The EIS data for BPPG-1100-A, presented in Figure 5.15(d), shows a similar trend as for the case of Na. Early during cycling the charge transfer resistance increases somewhat and remains essentially invariant during subsequent testing up to 300 cycles.

There is a major difference in the reversible capacity with Li versus with Na, the former being up to 3X higher. Activation has a substantial effect when testing against Li, while a negligible effect when testing against Na (at intermediate and low charging rates where diffusional limitations are not significant). This is one source of the capacity discrepancy between LIBs and NIBs, and will be shown to be direct outcome of Li metal nanopore filling. Reversible capacities are 1109 mAh/g for BPPG-800, 1225 mAh/g for BPPG-800-A; 1007 mAh/g for BPPG-1100, 1199 mAh/g for BPPG-1100-A; and 819 mAh/g for BPPG-1400, 1021 mAh/g for BPPG-1400-A. In all three cases the extra capacity due to activation is achieved below 0.1 V (Figure 5.19). We also hypothesize that the much higher > 0.1 V capacity in LIBs vs. NIBs, and the more sloping charge/discharge profiles with a larger hysteresis, are directly related to a wider abundance adsorption sites for Li in the defective graphene layers. The stronger binding sites will have Li absorption occur at a higher voltage (ΔG = -nFE) and will require a large overpotential upon subsequent delithiation of the half-cell.

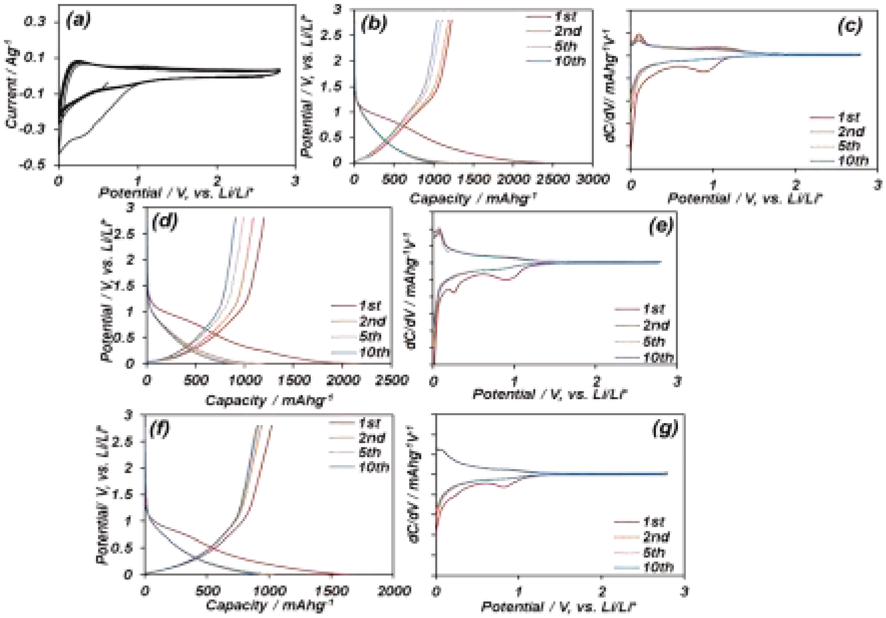

Figure 5.17: Electrochemical performance of BPPG-A, tested in a half cell against Li metal

from 0.001 and 2.8 V. (a) CV of BPPG-1100-A, tested at 0.1 mV/s. Galvanostatic discharge/charge curves of (b) and (c) BPPG-800-A, (d) and (e) BPPG-1100-A, (f) and (g) BPPG-1400-A at a current density of 50 mA/g.

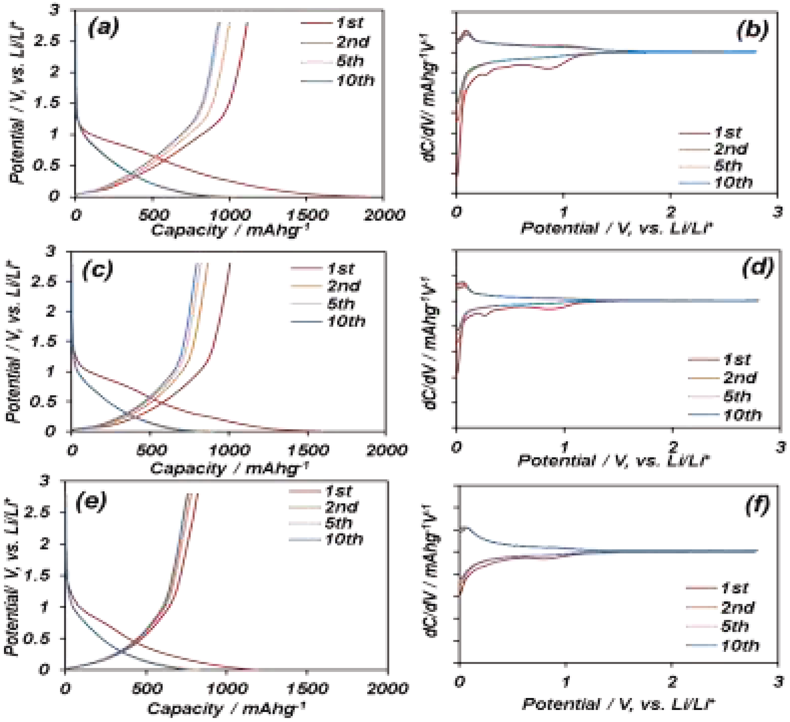

Figure 5.18: Galvanostatic discharge/charge curves of (a) and (b) BPPG-800, (c) and (d) BPPG-1100, (e) and (f) BPPG-1400, versus Li.

Table 5.7: Coulombic efficiency and cycling capacity of BPPG and BPPG-A, versus Li. Samples were activated at 0.05 A g^{-1} for 10 cycles and were subsequently tested at 0.1 A/g

Samples	**Initial CE (%)**	**Cycle 2 (mAh/g)**	**Cycle 50 (mAh/g)**	**Cycle 300 (mAh/g)**
BPPG-800-A (Li)	50	1268	779	801
BPPG-1100-A (Li)	55	1184	681	717
BPPG-1400-A (Li)	61	1020	637	641
BPPG-800 (Li)	58	1029	730	
BPPG-1100 (Li)	63	901	652	
BPPG-1400 (Li)	69	826	593	

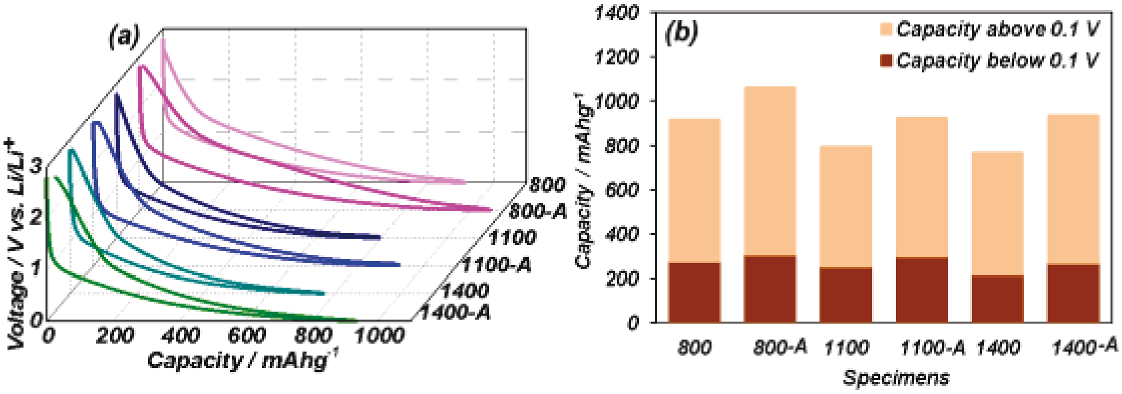

Figure 5.19: Electrochemical performance of BPPG, tested in a half cell against Li, 10th cycle at 50 mA/g. (a) Potential profiles of BPPG and BPPG-A electrodes, (b) Summary of capacity above and below 0.1 V in BPPG and BPPG-A.

Figures 5.16(c) and 5.16(d) show the dependence of the mean graphene interlayer spacing in the pseudographitic domains and in the equilibrium graphite on the charge/discharge voltage. The sample that was analyzed is BPPG-1400-A. Li intercalation-induced dilation in the pseudographite occurs to a lesser extent than with Na. This difference is in part due to the smaller radius of the Li. We argue that this also another manifestation of proportionally more Li being adsorbed on graphene defects, rather than being intercalated, as the former would add to the overall capacity but not induce systematic lattice dilation. Figure 5.20(a) and (b) shows the Raman integral intensity ratio as a function of discharge/charge voltage, demonstrating some Li intercalation-induced ordering of the carbon. The degree of ordering, however, is much less than for Na.

Figure 5.16(c) shows a strong lithium metal peak centered at 2θ ~ 36°, corresponding to (110)Li. This peak appears upon the reduction of the electrode to 0.2 V and grows more prominent at lower potentials. It also symmetrically shrinks upon delithiation. The unambiguous presence of a (110) metallic Li reflection is a direct evidence of a key contribution of metal nanopore filling to the overall capacity, and agrees with the earlier findings of Ref. 84. To further confirm this mechanism we employed XPS (Figure 5.21), using the same scotch tape technique to remove the SEI and the top carbon layer. Upon reducing the electrode to 0.001 V there is a prominent lithium metal peak. Conversely at 2.8 V the metal peak is effectively disappeared. Similarly without using the scotch tape approach, the presence of the peak with binding energy of ~55 eV and a considerable intensity in Li 1s spectra even after delithiation to 2.8 V indicates that this peak is attributed to the (Li)carbonate rather than Li metal inside the electrode. SEM images (Figure 5.22) also confirm that SEI layer has been successfully removed using scotch tape method with a smooth surface compared to the rough one in Figure 5.22(b).

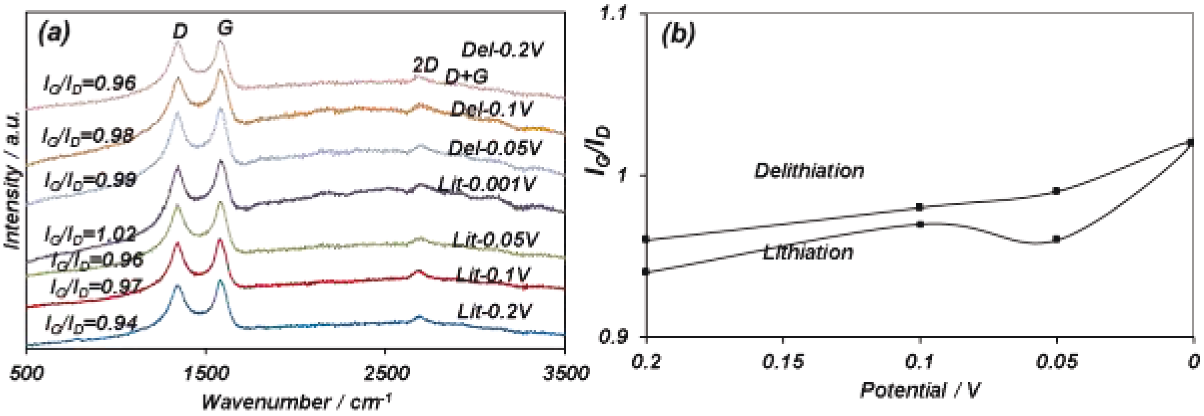

Figure 5.20: (a) Raman spectra for BPPG-1400-A at different discharge and charge voltages versus Li. The electrodes were galvanostiatically discharged/charged to 0.2, 0.1, 0.05, and 0.001 V. (b) The Raman integral intensity ratio (I_G/I_D) as a function of discharge/charge voltage demonstrating intercalation-induced ordering of the carbon, values derived from Raman spectra in Figure 5.20(a).

A comparison of the performance of BPPG-1100-A with state-of-the-art carbons is presented in Table 5.8 and in Figures 5.16(e) and 5.16(f). Extensive research has been done on carbon based anode materials for LIBs. [94] Carbons included in the comparison are mesoporous carbon, [93] graphene and graphene nanosheets, [95-97,99] carbon nanotubes/graphene, [98] carbon nanotube on graphene paper, [100] graphene nanoribbons, [101] graphene/carbon nanofibers, [102] monolithic carbon, [103] mesoporous carbon, [104] carbon nanotube on carbon fibre, [105] macroporous carbon, [106] carbon nanospheres, [107] and photothermally reduced graphene, [108] all of them being primarily high surface area materials. We did not include highly doped (e.g. by N, O, or B) carbons into the comparison since these store Li by several additional fundamentally different mechanisms related to reversible ion absorption at the heteroatom functionalities or at the associated defects. [72-74,109] Because of this extra Li storage contribution, the total capacities in such materials are always higher than that for "pure" carbons such the BPPG specimens, undoped graphene or carbon nanotubes. For instance, recently a 10% N doped medium surface area carbon was able to achieve a reversible capacity of 1780 mAh/g in the 2nd cycle. [72] Judging from the Table and the Figures, the overall performance of BPPG-A specimens is quite favorable both in terms of cycling and high rate capacity retention. This is especially true considering that materials presented in the comparison are all high surface area structures.

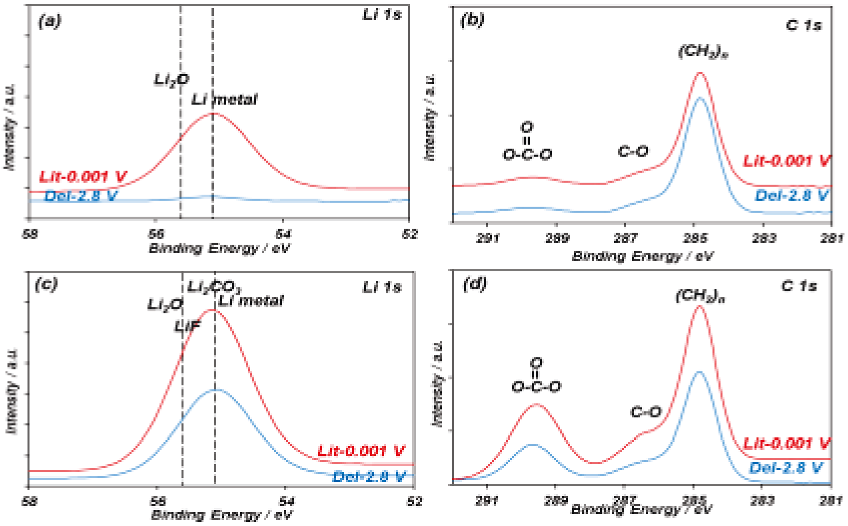

Figure 5.21: Li 1s, and C 1s high resolution XPS spectra for lithiated and delithiated BPPG-1400-A after 10 cycles.

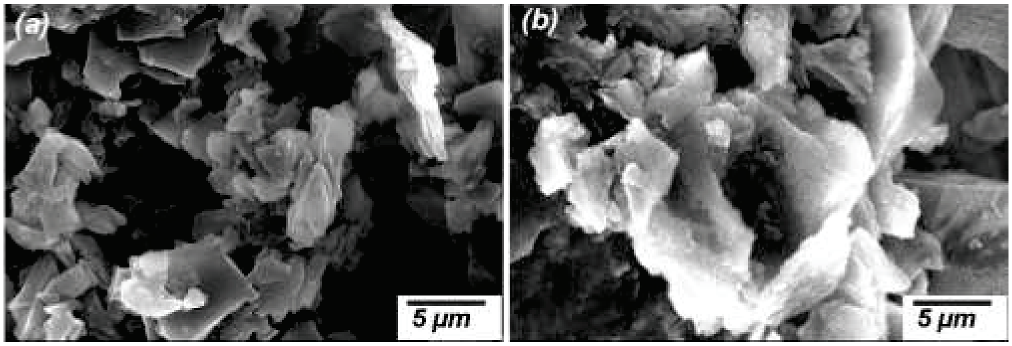

Figure 5.22: Low magnification SEM micrograph of BPPG-1400-A delithiated to 2.8 V, after 10 cycles. 5.22(a) shows the electrode morphology after the electrode's top layer was removed by the scotch tape method, 5.22(b) shows the morphology of an intact electrode covered by SEI.

Table 5.8: Performance comparison of BPPG-1100-A *versus* state of the art LIB carbons reported in literature

Material	**Initial coulombic efficiency (%)**	**Cyclability (discharge capacity)**	**Rate performance**
BPPG-1100-A (this work)	55	790 mAhg^{-1} at11th cycle 717 mAhg^{-1} at300th cycle 91% capacity retention over 290 cycles at 100 mAg^{-1}	738 mAhg^{-1} at 200 mAg^{-1} 634 mAhg^{-1} at 500 mAg^{-1} 518 mAhg^{-1} at 1 Ag^{-1} 385 mAhg^{-1} at 2 Ag^{-1} 243 mAhg^{-1} at 5 Ag^{-1}
Mesoporus carbon (Ref. 91)	35	900 mAhg^{-1} at 10th cycle 800 mAhg^{-1} at 20th cycle 89% retention over 10 cycles at 100 mAg^{-1}	Not reported
Graphene (Ref. 92)	38	580 mAhg^{-1} at 2nd cycle, 410 mAhg^{-1} at 40th cycle 71% retention over 38 cycles at 25 mAg^{-1}	Not reported
Graphene nanosheets (Ref. 93)	Not reported	784 mAhg^{-1} at 2nd cycle 600 mAhg^{-1} at 22th cycle 76% retention over 20 cycles at 50 mAg^{-1}	Not reported
Graphene sheets (Ref. 94)	53	1450 mAhg^{-1} at 10th cycle, 1150 mAhg^{-1} at 50th cycle 79% retention over 40 cycles at 50 mAg^{-1}	1500 mAhg^{-1} at 50 mAg^{-1} 1400 mAhg^{-1} at 150 mAg^{-1} 1200 mAhg^{-1} at 300 Ag^{-1}
CNTs/graphene (Ref. 95)	50	650 mAhg^{-1} at 10th cycle 650 mAhg^{-1} at 20th cycle At 600 mAg^{-1}	750 mAhg^{-1} at 100 mAg^{-1} 550 mAhg^{-1} at 300 mAg^{-1} 480 mAhg^{-1} at 600 mAg^{-1} 420 mAhg^{-1} at 900 mAg^{-1} 400 mAhg^{-1} at 1.2 Ag^{-1} 370 mAhg^{-1} at 1.5 Ag^{-1}
Graphene nanosheets (Ref. 96)	48	1050 mAhg^{-1} at 10th cycle 691 mAhg^{-1} at 100th cycle 66% retention over 90 cycles at 100 mAhg^{-1}	1200 mAhg^{-1} at 100 mAg^{-1} 900 mAhg^{-1} at 200 mAg^{-1} 740 mAhg^{-1} at 400 mAg^{-1} 600 mAhg^{-1} at 800 mAg^{-1} 500 mAhg^{-1} at 1.2 Ag^{-1}
CNTs on graphene paper (Ref. 97)	Not reported	300 mAhg^{-1} at 10th cycle 290 mAhg^{-1} at 40th cycle 97% retention over 30 cycles at 30 mAg^{-1}	290 mAhg^{-1} at 30 mAg^{-1} 275 mAhg^{-1} at 60 mAg^{-1} 190 mAhg^{-1} at 300 mAg^{-1} 140 mAhg^{-1} at 600 mAg^{-1} 90 mAhg^{-1} at 1.5 Ag^{-1} 70 mAhg^{-1} at 3 Ag^{-1}

			60 mAhg^{-1} at 3 Ag^{-1}
Graphene nanoribbons (Ref 98)	53	750 mAhg^{-1} at 2nd cycle 510 mAhg^{-1} at 14th cycle 68% retention over 12 cycles at 0.1C	Not reported
Graphene/carbon nanofibers (Ref. 99)	55	700 mAhg^{-1} at 2nd cycle 650 mAhg^{-1} at 30th cycle 93% retention over 20 cycles at 0.12 mAcm^{-2}	420 mAhg^{-1} at 0.36 mAcm^{-2} 385 mAhg^{-1} at 0.6 mAcm^{-2} 329 mAhg^{-1} at 1.2 mAcm^{-2} 229 mAhg^{-1} at 2.4 mAcm^{-2} 180 mAhg^{-1} at 6 mAcm^{-2}
Monolithic carbon (Ref. 100)	47	400 mAhg^{-1} at 2nd cycle 352 mAhg^{-1} at 50th cycle 88% capacity retention over 48 cycles at 100 mAg^{-1}	250 mAhg^{-1} at 200 mAg^{-1} 210 mAhg^{-1} at 500 mAg^{-1} 190 mAhg^{-1} at 800 mAg^{-1} 180 mAhg^{-1} at 1 Ag^{-1}
Mesoporous carbon (Ref. 101)	59	900 mAhg^{-1} at 10th cycle 786 mAhg^{-1} at 20th cycle 87% capacity retention over 10 cycles at 37.2 mAg^{-1}	190 mAhg^{-1} at 372 mAg^{-1} 140 mAhg^{-1} at 744 mAg^{-1} 90 mAhg^{-1} at 1.86 Ag^{-1} 70 mAhg^{-1} at 3.72 Ag^{-1}
CNTs on carbon fibre (Ref. 102)	>80	550 mAhg^{-1} at 10th cycle 550 mAhg^{-1} at 50th cycle at 0.05 mAcm^{-2}	550 mAhg^{-1} at 0.05 mAcm^{-2} 450 mAhg^{-1} at 0.2 mAcm^{-2} 350 mAhg^{-1} at 0.5 mAcm^{-2}
Macroporous carbon (Ref. 103)	43	200 mAhg^{-1} at 10th cycle 190 mAhg^{-1} at 30th cycle 95% capacity retention over 20 cycles at 40 mAg^{-1}	300 mAhg^{-1} at 15 mAg^{-1} 230 mAhg^{-1} at 32 mAg^{-1} 200 mAhg^{-1} at 61 mAg^{-1} 175 mAhg^{-1} at 90 mAg^{-1}
Carbon nanospheres (Ref. 104)	72	800 mAhg^{-1} at 2nd cycle 700 mAhg^{-1} at 50th cycle 88% capacity retention over 48 cycles at 50 mAg^{-1}	750 mAhg^{-1} at 48 mAg^{-1} 410 mAhg^{-1} at 82 mAg^{-1} 360 mAhg^{-1} at 2 Ag^{-1} 300 mAhg^{-1} at 3 Ag^{-1}
Photothermally reduced grapheme (Ref. 105)	95.3 (at 14.8 Ag^{-1})	550 mAhg^{-1} at 2nd cycle 540 mAhg^{-1} at 50th cycle 98% capacity retention over 48 cycles at 50 mAg^{-1}	550 mAhg^{-1} at 372 mAg^{-1} 380 mAhg^{-1} at 1.86 Ag^{-1} 160 mAhg^{-1} at 14.8 Ag^{-1} 90 mAhg^{-1} at 37.2 Ag^{-1} 88 mAhg^{-1} at 44.6 Ag^{-1} 60 mAhg^{-1} at 55.8 Ag^{-1}

5.4 Conclusions

We created a unique low surface area carbon that was derived from banana peels, termed Banana Peel Pseudo Graphite "BPPG". The materials are composed of pseudographitic arrays possessing a mean graphene interlayer spacing that is 17% dilated with respect to graphite, allowing for facile Na intercalation between the layers. For NIBs, the carbons actually perform as a direct electrochemical analogue to graphite in LIBs in terms of the overall charge storage capacity, superior cycling stability, coulombic efficiency, a large and nearly flat voltage plateau below 0.1 V, and minimal charge-discharge hysteresis. A wide comparison with literature shows BPPG to possess among the most promising electrochemical performances for a sodium ion battery carbon-based anode. BPPG also serves as a superb electrode for lithium ion batteries, achieving 3X the capacity of graphite. This may be attributed to a combination of the highly defective graphene in the pseudographitic arrays that reversibly binds Li, and to ample near-surface nanopores available for facile underpotential metal deposition.

5.5 References

1. J.M. Tarascon, *Nat. Chem.* 2010, **2**, 510
2. H. Pan, Y.S. Hu, L. Chen, *Energy Environ. Sci.,* 2013, **6**, 2338.
3. V. Palomares, M. Casas-Cabanas, E. Castillo-Mart´ınez, M.H. Han, T. Rojo, *Energy Environ. Sci.,* 2013, **6**, 2312.
4. M.D. Slater, D. Kim, E. Lee, C.S. Johnson, *Adv. Funct. Mater*., 2013, **23**, 947–958.
5. Y. Cao, L. Xiao, X. Ai, H. Yang, *Electrochem. Solid-State Lett.,* 2003, **6(2)**, A30-A33.
6. Y. Lin, Z.-H. Huang, X. Yu, W. Shen, Y. Zheng, F. Kang, *Electrochim. Acta,* 2014, **116**, 170-174.
7. L. Wang, Y. Huang, D. Jia, *Electrochimica Acta*, 2006, **51**, 4950–4955.
8. E. Peled, C. Menachem, D. BarTow, A. Melman, *J. Electrochem. Soc*., 1996, **143**, L4–L7.
9. P. Ge, Fouletier, *Solid State Ionics*, 1988, **28–30**, 1172-1175.
10. D.A. Stevens, J.R. Dahn, *J. Electrochem. Soc.*, 2001, **148**, A803-A811.
11. R.C. Asher, *J. Inorg. Nucl. Chem.,* 1959, **10**, 238 -249.
12. S. Komaba, W. Murata, T. Ishikawa, N. Yabuuchi, T. Ozeki, T. Nakayama, A. Ogata, K. Gotoh, K. Fujiwara, *Adv. Funct. Mater.* 2011, **21**, 3859–3867.
13. W. Luo, J. Schardt, C. Bommier, B. Wang, J. Razink, J. Simonsen, X. Ji, *J. Mat. Chem. A*, 2013, **1**, 10662-10666.
14. A. Ponrouch, A.R. Goni, M.R. Palacin, *Electrochem. Commun*., 2013, **27**, 85-88.
15. Y.Y. Shao, J. Xiao, W. Wang, M. Engelhard, X.L. Chen, Z.M. Nie, M. Gu, L.V. Saraf, G. Exarhos, J.G. Zhang, J. Liu, *Nano Lett.,* 2013, **13**, 3909-3914.
16. W. Li, L. Zeng, Z. Yang, L. Gu, J. Wang, X. Liu, J. Cheng, Y. Yu, *Nanoscale*, 2014, **6**, 693-698.
17. Y. Kim, Y. Park, A. Choi, N.-S. Choi, J. Kim, J. Lee, J.H. Ry, S.M. Oh, K.T. Lee, *Adv. Mater.,* 2013, **25**, 3045–3049.
18. W.J. Li, S.-L. Chou, J.-Z. Wang, H.-K. Liu, S.-X. Dou, *Nano Lett*., 2013, **13**, 5480−5484.
19. P. Senguttuvan, G. Rousse, M.E. Arroyo y de Dompablo, H. Vezin, J.M. Tarascon, M.R. Palac´ın, *J. Am. Chem. Soc.*, 2013, **135**, 3897-3903.
20. L. Zhao, J.M. Zhao, Y.S. Hu, H. Li, Z.B. Zhou, M. Armand, L.Q. Chen, *Adv. Energy Mater.*, 2012, **2**, 962-965

21. S. Il Park, I. Gocheva, S. Okada, J.-I. Yamaki, *J. Electrochem. Soc.,* 2011, **158**, A1067-A1070.
22. Y. Park, D.S. Shin, S.H. Woo, N.S. Choi, K.H. Shin, S.M. Oh, K.T. Lee, S.Y. Hong, *Adv. Mater.*, 2012, **24**, 3562-3567.
23. W. Wang, C. Yu, Z. Lin, J. Hou, H. Zhu, S. Jiao, *Nanoscale,* 2013, **5**, 594-599.
24. H.L. Pan, X. Lu, X.Q. Yu, Y.S. Hu, H. Li, X.Q. Yang, L.Q. Chen, *Adv. Energ. Mater*., 2013, **3**, 1186-1194.
25. L. Wu, D. Buchholz, D. Bresser, L.G. Chagas, S. Passerini, *J. Power Sources.,* 2014, **251**, 379–385.
26. R. Alcántara, M. Jaraba, P. Lavela, J.L. Tirado, *Chem. Mater.,* 2002, **14**, 2847-2848.
27. H. Xiong, M.D. Slater, M. Balasubramanian, C.S. Johnson, T. Rajh, *J. Phys. Chem. Lett.*, 2011, **2 (20)**, 2560–2565.
28. Y. Xu, E.M. Lotfabad, H.L. Wang, B. Farbod, Z.W. Xu, A. Kohandehghan, D. Mitlin, *Chem. Commun.,* 2013, **49**, 8973-8975.
29. K.-T. Kim, G. Ali. K.Y. Chung, C.S. Yoon, H. Yashiro, Y.K. Sun, J. Lu, K. Amine, S.-T. Myung, *Nano Lett.*, 2014, **14**, 2, 416–422.
30. S. Hariharan, K. Saravanan, V. Ramar, P. Balaya, *Phys. Chem. Chem. Phys*., 2013, **15**, 2945-2953.
31. X. Li, M.M. Hasan, A.L. Hector, J.R. Owen, *J. Mater. Chem. A*, 2013, **1**, 6441-6445.
32. L. Baggetto, P. Ganesh, C.N. Sun, R.A. Meisner, T.A. Zawodzinski, G.M. Veith, *J. Mater. Chem. A*, 2013, **1**, 7985-7994.
33. H.L. Zhu, Z. Jia, Y.C. Chen, N. Weadock, J.Y. Wan, O. Vaaland, X.G. Han, T. Li, L.B. Hu, *Nano Lett.*, 2013, **13**, 3093-3100.
34. L., Baggetto, P., Ganesh, R.P., Meisner, R.R., Unocic, J.C., Jumas, C.A., Bridges, G.M., Veith, *J. Power Sources,* 2013, **234**, 48-59.
35. L.F. Xiao, Y.L. Cao, J. Xiao, W. Wang, L. Kovarik, Z.M. Nie, J. Liu, *Chem. Comm.* 2012, **48**, 3321-3323.
36. J.W., Wang, X.H. Liu, S.X. Mao, J.Y. Huang, *Nano Lett.*, 2012, **12**, 5897-5902.
37. L. Wu, X. Hu, J. Qian, F. Pei, F. Wu, R. Mao, X. Ai, H. Yang, Y. Cao, *Energy Environ. Sci.*, 2014, **7**, 323.

38. Y. Zhu, X. Han, Y. Xu, Y. Liu, S. Zheng, K. Xu, L. Hu, C. Wang, *ACS Nano,* 2013, **7(7)**, 6378-6386.

39. X. Han, Y. Liu, Z. Jia, Y.-C. Chen, J. Wan, N. Weadock, K.J. Gaskell, T. Li, L. Hu, *Nano Lett*., 2014, **14**, 139−147.

40. Y. Liu, Y. Xu, Y. Zhu, J.N. Culver, C.A. Lundgren, K. Xu, C. Wang, *ACS Nano* 2013, **7(4)**, 3627-3634.

41. S.C. Jung, D.S. Jung, J.W. Choi, Y.-K. Han, *J. Phys. Chem. Lett*., 2014, **5**, 1283−1288.

42. B. Farbod, K. Cui, W.P. Kalisvaart, M. Kupsta, B. Zahiri, A. Kohandehghan, E. Memarzadeh, Z. Li, E.J. Luber, D. Mitlin, *ACS Nano*, 2014, DOI: 10.1021/nn4063598.

43. J. Qian, Y. Xiong, Y. Cao, X. Ai, H. Yang, *Nano Lett.,* 2014*,* DOI: 10.1021/nl404637q.

44. L. Ji, M., Gu, Y. Shao, X. Li, M.H. Engelhard, B.W. Arey, W. Wang, Z. Nie, J. Xiao, C. Wang, J.-G. Zhang, J. Liu, *Adv. Mater*. 2014, DOI: 10.1002/adma.201304962.

45. L. David, R. Bhandavat, G. Singh, *ACS Nano,* 2014, ***8*** **(2)**, 1759–1770.

46. D. Datta, J. Li, V.B. Shenoy, *ACS Appl. Mater. Interfaces*, 2014, **6(3)**, 1788–1795.

47. M. Naguib, V.N. Mochalin, M.W. Barsoum, Y. Gogotsi, *Adv. Mater.,* 2014, **26**, 992–1005.

48. M.R. Lukatskaya, O. Mashtalir, C.E. Ren, Y. Dall'Agnese, P. Rozier, P.L. Taberna, M. Naguib, P. Simon, M.W. Barsoum, Y. Gogotsi, *Science,* 2013, **341**, 1502-1505.

49. M. Naguib, J. Halim, J. Lu, K.M. Cook, L. Hultman, Y. Gogotsi, M.W. Barsoum, *J. Am. Chem. Soc*., 2013, **135**, 15966−15969.

50. O. Mashtalir, M. Naguib, V.N. Mochalin, Y. Dall'Agnese, M. Heon, M.W. Barsoum, Y. Gogotsi, *Nature Communications,* 2013, **4**, 1716.

51. K. Tang, L.J. Fu, R.J. White, L.H. Yu, M.M. Titirici, M. Antonietti, J. Maier, *Adv. Energy Mater*., 2012, **2**, 873–877.

52. Y. Cao, L. Xiao, M.L. Sushko, W. Wang, B. Schwenzer, J. Xiao, Z. Nie, L.V. Saraf, Z. Yang, J. Liu, *Nano Lett*., 2012, **12**, 3783–3787.

53. P. Thomas, D. Billaud, *Electrochim. Acta,* 2000, **46**, 39–47.

54. J. Ding, H., Wang, Z. Li, A. Kohandehghan, K. Cui, Z. Xu, B. Zahiri, X. Tan, E. Memarzadeh Lotfabad, B.C. Olsen, D. Mitlin, *ACS Nano*, 2013, **7 (12)**, 11004–11015.

55. X. Zhou, Y.-G. Guo, *ChemElectroChem*., 2014, **1**, 83–86.

56. H.-G. Wang, Z. Wu, F.I. Meng, D.-L. Ma, X.-L. Huang, L.-M. Wang, X.-B. Zhang, *ChemSusChem.,* 2013, **6**, 56–60.
57. L. Fu, K. Tang, K. Song, P.A. van Aken, Y. Yu, J. Maier, *Nanoscale*, 2014, **6**, 1384-1389.
58. Z. Gui, H. Zhu, E. Gillette, X. Han, G.W. Rubloff, L. Hu, S.B. Lee, *ACS Nano,* **2013**, **7(7)**, 6037-6046.
59. X. Chen, H. Zhu, C. Liu, Y.-C. Chen, N. Weadock, G. Rubloff, L. Hu, *J. Mater. Chem. A*, 2013, **1**, 8201–8208.
60. N. Li, Z. Chen, W. Ren, F. Li, H.M. Cheng, *PNAS,* 2012, **109(43)**, 17360-17365.
61. S.-H. Lee, V. Sridhar, J.-H. Jung, K. Karthikeyan, Y.-S. Lee, R. Mukherjee, N. Koratkar, I.-K. Oh, *ACS Nano,* 2013, **7(5)**, 4244-4251.
62. L. Li, G. Zhou, Z. Weng, X.-Y. Shan, F. Li, H.-M. Cheng, *Carbon,* 2014, **6 7**, 500–507.
63. V.G. Pol, E. Lee, D. Zhou, F. Dogan, J.M. Calderon-Moreno, C.S. Johnson, *Electrochim. Acta,* 2014, **127**, 61–67.
64. S. Wenzel, T. Hara, J. Janek, P. Adelhelm, *Energy Environ. Sci*., 2011, **4**, 3342–3345.
65. Y.-X. Wang, S.-L. Chou, H.-K. Liu, S.-X. Dou, *Carbon*, 2013, **57**, 202–208.
66. B.H. Lin, S.T. Yen, C.L. Huang, T.A. Smith, *Sustainability*, 2009, **1(3)**, 464-478.
67. G. Annadurai, R.-S. Juang, D.-J. Lee, *Water Science & Technology,* 2003, **47**, 185-190.
68. G. Annadurai, R.-S. Juang, D.-J. Lee, *J. Hazard. Mater*., 2002, **92**, 263-274.
69. M. Achak, A. Hafidi, N. Ouazzani, S. Sayadi, L. Mandi, *J. Hazard. Mater*., 2009, ***166***, 117–125.
70. V. Subramanian, C. Luo, A.M. Stephan, K.S. Nahm, S. Thomas, B. Wei, *J. Phys. Chem. C,* 2007, **111 (20)**, 7527–7531.
71. Y. Lva, L. Gana, M. Liua, W. Xionga, Z. Xua, D. Zhua, D.S. Wright, *J. Power Sources,* 2012, **29**, 152–157.
72. Z. Li, Z. Xu, X. Tan, H. Wang, C.M.B. Holt, T. Stephenson, B.C. Olsen, D. Mitlin, *Energy Environ. Sci.*, 2013, **6**, 871-878.
73. Z.S. Wu, W.C. Ren, L. Xu, F. Li, H.M. Cheng, *ACS Nano,* 2011, **5**, 5463-5471.
74. H. Wang, C. Zhang, Z. Liu, L. Wang, P. Han, H. Xu, K. Zhang, S. Dong, J. Yao, G. Cui, *J. Mater. Chem.*, 2011, **21**, 5430-5434.

75. T.H. Emaga, C. Robert, S.N. Ronkart, B. Wathelet, M. Paquot, *Bioresour. Technol.,* 2008, **99**, 4346–4354.
76. M.M. Titirici, A. Thomas, S.-H. Yu, J.-O. Müller, M. Antonietti, *Chem. Mater.,* 2007, **19**, 4205–4212.
77. T. Emaga, J. Bindelle, R. Agneesens, A. Buldgen, B. Wathelet, M. Paquot, *Trop. Anim. Health Prod.,* 2011, **43**, 171–177.
78. J.R Dahn, T. Zheng, Y. Liu, J.S. Xue, *Science,* 1995, **270**, 590–593.
79. C. Portet, G. Yushin, Y. Gogotsi, *Carbon,* 2007, **45**, 2511–2518.
80. Z. Wang, L. Qie, L. Yuan, W. Zhang, X. Hu, Y. Huang, *Carbon,* 2013, **55**, 328–334.
81. D.A. Stevens, J.R. Dahn, *J. Electrochem. Soc.*, 2000, **147**, 1271-1273.
82. C.S. Wang, G.T. Wu, W.Z. Li, *J. Power Sources,* 1998, **76**, 1–10.
83. D. Datta, J. Li, V.B. Shenoy, *ACS Appl. Mater. Interfaces,* 2014, **6 (3)**, 1788–1795.
84. R. Mukherjee, A.V. Thomas, D. Datta, E. Singh, J. Li, O. Eksik, V.B. Shenoy, N. Koratkar, *Nature Communications,* 2014, **5**, 3710.
85. Y. Liu, V.I. Artyukhov, M. Liu, A.R. Harutyunyan, B.I. Yakobson, *J. Phys. Chem. Lett.,* 2013, **4 (10)**, 1737–1742.
86. L.-J. Zhou, Z.F. Hou, L.-M. Wu, *J. Phys. Chem. C,* 2012, **116 (41)**, 21780–21787.
87. D. Billaud, F.X. Henry, P. Willmann, *Mater. Res. Bull.,* 1993, **28**, 477-483.
88. P. Simon, Y. Gogotsi, B. Dunn, *Science,* 2014*,* **343**, 1210-1211.
89. M.D. Levi D. Aurbach, *J. Phys. Chem. B,* 1997, **101(23)**, 4641-4647.
90. F. Banhart, J. Kotakoski, A.V. Krasheninnikov, *ACS Nano,* 2011, **5**, 26–41.
91. J.M. Carlsson, M. Scheffler, *Phys. Rev. Lett.,* 2006, **96**, 046806.
92. R. Alcantara, J.M. Jimenez-Mateos, P. Lavela, J.L. Tirado, *Electrochem. Commun.,* 2001, **3**, 639–642.
93. H. Zhou, S. Zhu, M. Hibino, I. Honma, M. Ichihara, *Adv. Mater*., 2003, **15(24)**, 2107-2111.
94. R. Mukherjee, R. Krishnan, T.-M. Lu, N. Koratkar, *Nano Energy,* 2012, **1**, 518–533.
95. A. Kumar, A.L.M. Reddy, A. Mukherjee, M. Dubey, X. Zhan, N. Singh, L. Ci, W.E. Billups, J. Nagurny, G. Mital, P.M. Ajayan, *ACS Nano,* 2011, **5(6)**, 4345-4349.
96. E. Yoo, J. Kim, E. Hosono, H.-S. Zhou, T. Kudo, I. Honma, *Nano Lett*., 2008, **8(8)**, 2277-2282.

97. S. Yin, Y. Zhang, J. Kong, C. Zou, C.M. Li, X. Lu, J. Ma, F.Y.C. Boey, X. Chen, *ACS Nano,* 2011, **5(5)**, 3831-3838.
98. W. Wang, I. Ruiz, S. Guo, Z. Favors, H. Hosseini Bay, M. Ozkan, C.S. Ozkan, *Nano Energy,* 2014, **3**, 113-118.
99. X. Li, Y. Hu, J. Liu, A. Lushington, R. Li, X. Sun, *Nanoscale*, 2013, **5**, 12607-12615.
100. S. Li, Y. Luo, W. Lv, W. Yu, S. Wu, P. Hou, Q. Yang, Q. Meng, C. Liu, H.-M. Cheng, *Adv. Energy Mater.,* 2011, **1**, 486–490.
101. T. Bhardwaj, A. Antic, B. Pavan, V. Barone, B.D. Fahlman, *J. Am. Chem. Soc*., 2010, **132**, 12556–12558.
102. Z.J. Fan, J. Yan, T. Wei, G.-Q. Ning, L.-J. Zhi, J.-C. Liu, D.-X. Cao, G.-L. Wang, F. Wei, *ACS Nano,* 2011, **5(4)**, 2787-2794.
103. G.-P. Hao, F. Han, D.-C. Guo, R.-J. Fan, G. Xiong, W.-C. Li, A.-H. Lu, *J. Phys. Chem. C,* 2012, **116**, 10303−10311.
104. B. Guo, X., Wang, P.E. Fulvio, M. Chi, S.M. Mahurin, X.G. Sun, S. Dai, *Adv. Mater*., 2011, **23**, 4661–4666.
105. J. Chen, J.Z. Wang, A.I. Minett, Y. Liu, C. Lynam, H. Liu, G.G. Wallace, *Energy Environ. Sci.*, 2009, **2**, 393–396.
106. B.K.T. Lee, J.C. Lytle, N.S. Ergang, S.M. Oh, A. Stein, *Adv. Func. Mater.,* 2005, **15(4)**, 547-556.
107. Y. Chen, Z. Lu, L. Zhou, Y.-W. Mai, H. Huang, *Nanoscale*, 2012, **4**, 6800-6805.
108. R. Mukherjee, A.V. Thomas, A. Krishnamurthy, N. Koratkar, *ACS Nano,* 2012, **6(9)**, 7867–7878.
109. L. Qie, W.M. Chen, Z.H. Wang, Q.G. Shao, X. Li, L.X. Yuan, X.L. Hu, W.X. Zhang, Y.H. Huang, *Adv. Mater.*, 2012, **24**, 2047-2050.

6 Concluding Remarks

6.1 Conclusions

In this thesis the effect of sputtered and ALD coatings on the electrochemical performance of Si nanowires and nanotubes was investigated. Moreover, the electrochemical performance of a bio-mass derived carbon as NIB anode which behaves electrochemically nearly identically to graphite in LIBs was investigated. This carbon was also examined for LIB applications. Chapter 2 was mainly focused on utilization of the support growth substrate as well as a mechanical constraining coating layer (Al) in order to improve the electrochemical performance of the Si nanowires. We observed that Si nanowires grown on TiN/SS exhibited higher initial coulombic efficiency (92.1%) and lower discharge capacity loss (4%) compared to nanowires grown on SS (84.3% and 14.5%, respectively). This was attributed to the size distribution, in which a significant fraction of nanowires grown on SS was above a critical diameter (~250 nm) that pulverize upon lithiation. We also observed that nanowires coated Al within an optimum range between 3 and 8 wt.% improved the capacity retention by maintaining the mechanical integrity of the nanowires.

Although Al coating with optimum thicknesses helps reduce the degradation rate, all the materials eventually do degrade to what appears to be a 'steady-state capacity' that is between 25 and 38% of the initial capacity. This was probably attributed to the uncoated parts of the Si nanowires disintegrating close to the substrate. This made us find a way in order to achieve more uniform coating. In chapter 3, we coated our nanowires with TiO_2 using ALD method due to its self-limiting nature allowing for very good control over thickness and uniformity. W showed that a 10 nm TiO_2 coating deposited with ALD improved the capacity retention of SiNW electrodes by a factor 2 at 0.1 C and a factor 3.5 at 5 C by greatly reducing one of the most important degradation mechanisms for this type of electrode: mass delamination of the nanowire assembly from the substrate. At the same time, the coulombic efficiency was improved from 95% for bare SiNWs to 99% for SiNWs coated with 10 nm TiO_2 at 200^oC. The mechanical integrity of the nanowires was better maintained for amorphous TiO_2 coatings that developed a highly dispersed two-phase nanostructure consisting of $LiTiO_2$ and amorphous TiO_2. The larger grain size of the annealed, anatase coating made it much more vulnerable to fracture and delamination. We showed ALD to be an effective method to apply coatings for cycle life improvement of LIB anodes and expect it to be applied much more frequently in the near future.

In order to further improve the cycling performance of Si anodes to better accommodate the large volume expansion, in chaper 4 we used another Si configuration with more hollow structure. We also coated nanotubes with different ALD coating on different locations. We showed that when nanotubes were conformally coated on both sides, the optimum performance could be achieved with an improvement in capacity retention from 40% for uncoated Si nanotube to 60% for double-sided TiO_2 coated nanotubes. Moreover, the steady-state cycling coulombic efficiency improved from 97-98% to near 100% and high rate capability at 5C was improved from 20 to 50% of the initial capacity at 0.2 C. Compared to double-sided coated SiNTs, coating only the inner surface or only the outer surface yield markedly smaller improvements in coulombic efficiency. This was achieved by the application of conformal outer coating, forcing nanotubes to expand into the internal hollow space and at the same time passivating both inner and outer surface to achieve optimum coulombic efficiency. We also demonstrated that a unique two-phase microstructure of lithiated TiO_2 offering both a high electronic conductivity and a high Li-diffusion is beneficial for improving the rate performance.

Finally in chapter 5, we used a biomass-derived carbon as an anode material for both NIBs and LIBs. Banana peel pseudographite in an optimized state possed a low surface area (130 m^2 g^{-1}) and a relatively high electrode packing density (0.75 g cm^{-3} vs. ~ 1 g cm^{-3} for graphite). BPPG delivered a high reversible gravimetric (and volumetric) capacity of 355 mAh/g (by active material ~ 700 mAh/cm^3, by electrode volume ~ 270 mAh/cm^3) after 10 cycles at 50 mA/g. Importantly there was a nearly flat ~ 200 mAh/g plateau below 0.1 V *vs* Na/Na^+ and a minimal charge/discharge voltage hysteresis. The electrodes also displayed an excellent combination of rate capability and cycling stability. A charge capacity of 221 mAh/g at 500 mA/g was degraded by 7% after 600 cycles, while a capacity of 336 mAh/g at 100 mA/g was degraded by 11% after 300 cycles, in both cases with ~ 100% cycling coulombic efficiency.

The key to achieving these properties was the carbons' unique structure consisting of highly ordered graphite-like arrays with an inter graphene spacing of 0.392 nm (vs. 0.3354 nm for graphite) that could accommodate Na intercalation. By coupling a tailored synthesis treatment with a unique structure of the banana peel precursor we were able to create carbons that are in-fact intermediate between the classic soft graphitic carbons and of hard non-graphitizeable carbons. A comparison of the performance our materials with previously published state-of-the-art carbons for NIB applications showed that the obtained combination of a high reversible volumetric and gravimetric capacities, the flat low voltage and low hysteresis plateaus, the extended cycling performance, and high rate capability has not been achieved in literature.

Banana peel pseudographite also showed an excellent electrochemical performance for LIB applications. The material's capacity in Li based electrolyte was approximately three times higher than graphite albeit with much larger hysteresis. We demonstrated that for Li metal nanopore filling is primarily responsible for the sub - 0.1 V capacity, with adsorption of Li on graphene defects being important at higher voltages.

These exceptional results demonstrated that the banana peel-derived carbons presented were a promising candidate for the construction of low-cost sodium ion battery systems that perform on a competitive level with Li-ion systems.